Title

Pyrotechnology through a zooarchaeological perspective: experimental data on burned bone and their application to Neanderthal fire use at Roc de Marsal (France)

Author

Gallo, Giulia Theresa

Publication Date

2022

Pyrotechnology through a zooarchaeological perspective: experimental data on burned bone and their application to Neanderthal fire use at Roc de Marsal (France)

By

GIULIA THERESA GALLO

DISSERTATION

Submitted in partial satisfaction of the requirements for the degree of

DOCTOR OF PHILOSOPHY

in

Anthropology

in the

OFFICE OF GRADUATE STUDIES

of the

UNIVERSITY OF CALIFORNIA

DAVIS

Approved:

Teresa E. Steele, Co-Chair

Nicolas Zwyns, Co-Chair

Vera Aldeias

Committee in Charge

2022

Pyrotechnology through a zooarchaeological perspective: experimental data on burned bone and their application to Neanderthal fire use at Roc de Marsal (France)

Abstract

A central point for nearly all disciplines of paleoanthropology remains the desire to describe, understand, and contextualize the diverse behavior of hominins and the emergence of modern human behavior. These compelling questions are at the forefront of studies which consider the archaeology of *Homo sapiens* and Neanderthals, our close genetic cousins, and prompt us to reconsider what it means and what it has meant to be human.

Neanderthals are estimated to be phenotypically extinct around 40,000 years ago, despite sharing a genetic legacy with all non-exclusively African populations of modern *Homo sapiens* (Prüfer et al., 2014). It is currently reconstructed through genetic and archaeological data that the last Neanderthals shared a landscape with contemporaneous *Homo sapiens* groups in Western Europe (overlap estimated to be between 2,000 and 10,000 years, but likely the former), but the exact nature and timing of their depopulation and eventual extinction remain an active research question.

One aspect of Neanderthal lifeways which has recently brought attention to potential adaptations that could have impacted their survival is the nature of Neanderthal control, use, and maintenance of fire. Control, meaning hominin production of fire, is here distinguished from use, which can include the management of fire naturally occurring in landscapes to alter materials (Goldberg et al., 2017; Sandgathe et al., 2017; Stahlschmidt et al., 2020). The maintenance of fire additionally includes the curation of and different technologies which intersect with anthropogenic fire (i.e., heat-treatment of lithics; Goldberg et al., 2017; Sandgathe et al., 2017;

Stahlschmidt et al., 2020). Due to fire acting as a mechanism to control one's environment it has been suggested to be deeply linked to human's evolutionary history and survival. Fire has been associated with many benefits, including the ability to cook, to preserve food, to modify wood and stone implements, to create birch tar, to offer protection from predators, to clear refuse, to create light, and to maintain a source of heat (Binford, 1978; Kozowyk et al., 2017, Sandgathe et al., 2011). Indeed, some researchers have proposed that fire use to increase caloric, and therefore energetic, returns through cooking could have contributed to the exponential increases in brain size seen 2 million years ago and again at ~400,000-500,000 years ago (Wrangham, 2009; Wrangham et al., 2017), while others have suggested that for migrations of hominins out of Africa, fire use would be necessary to survive in more northern latitudes (Gowlett, 2006). Despite these early predictions of fire's importance, it is not reflected in the visible archaeological record (Roebrocks and Villa, 2011). Instead, the timing of habitual fire use in Europe, as predicted by more frequent presence of reputable fire evidence, is estimated to be ~400,000 years ago (Roebrocks and Villa, 2011).

Neanderthal's ability to make and have pyrotechnology was most starkly called into question when researchers noted patterns of fire absence, remarkably during relatively cold periods, at several occupational sites within a constrained geographical area that could not be described by post-depositional processes (Dibble et al., 2017; Sandgathe et al., 2011). This is despite these periods occurring well after 400,000 years ago, when anthropogenic fire is more commonly occurring (Roebrocks and Villa, 2011; Sandgathe et al., 2011). Therefore, the consideration of Neanderthal occupations without fire presents a few scenarios for researchers: 1) Neanderthals could be adapted to living without fire; 2) some Neanderthals could not make fire due to intellectual limitations or having lost the knowledge (through social learning); 3)

Neanderthals in strained environmental conditions (i.e. limited fuel resources) did not always make fire or sparingly used fire as a resource, or 4) Neanderthals made fires elsewhere, potentially related to the organization of activities.

As the absence of evidence presents a challenge to investigate further, this project instead addresses the ways in which Neanderthal combustion feature properties, when present, can be studied and described with faunal assemblages. I aim here to address with zooarchaeological analyses aspects of fire temperature, location, duration, and atmosphere which can contribute to greater knowledge of how Neanderthal populations utilized and curated fire.

To achieve this goal, I use faunal remains to monitor changes which are induced by thermal alteration. Transformations to bone mineral are also demonstrated here by a large body of experimental studies, conducted as a sequence of collaborations to better understand the exact conditions under which bones are heated. I focus here on the chemical and structural changes to bone through spectroscopic analyses produced through Fourier Transform Infrared Spectroscopy (FTIR) and X-Ray diffraction (XRD). These data support traditional zooarchaeological standards of heated bone categorization to recommend a holistic strategy for sampling and studying archaeological burnt bone.

Chapter 2 introduces bone as a biomineral and presents a large experimentally produced referential dataset of bones heated from 100-1200 ˚C. FTIR and XRD are used here to demonstrate the changes in crystallite growth sizes, in addition to other aspects of thermal alteration. Bone which is charred and combusted (~ 300 ˚C) but has not yet experienced calcination (~700 ˚C) is demonstrated to be extremely porous with heightened solubility compared to both unburnt and calcined bone, and therefore it is vulnerable to differential preservation. The experimental bone is also compared to an archaeological assemblage of bone from the Upper Paleolithic (~30,000 years ago) site of Tolbor, Mongolia, to contextualize experimental observations and describe burning behaviors from an open air zooarchaeological assemblage.

Chapter 3 isolates the variables of time and duration to better understand the heat induced changes to bone. In this study I specifically address the misleading nature of coloration as a primary indicator of high temperatures, as well as suggest criteria for discerning long-time durations within archaeological assemblages. This is particularly valuable because ethnoarchaeologically, duration time has been demonstrated to be connected to fire function and because natural grass fires are documented to primarily be rapid and ephemeral (Bellomo, 1993; Mallol et al., 2007; Mallol and Henry, 2017; Pyne et al., 1996; Scott, 2000). Eight experimental trials were conducted as a part of this experiment, heating bone to temperatures of 300˚, 550˚ and 750 ˚C for time durations of 10 minutes, 9 hours, and 48 hours. I describe bone in this study using coloration (Munsell color chart, 2010), FTIR, and XRD. Results indicate that bone can be depigmented and light in color at low temperatures for long durations, which is similar (and potentially misleading) to what is recognized as calcined bone heated at high temperatures. These bones exposed to low temperatures for long durations are not, however, structurally and chemically calcined, and the bioapatite crystallites and crystal lattice do not experience the growth or transformations that accompany high heat. This does positively indicate that bones burnt at low temperatures for long durations can be recognized in the archaeological record.

Chapter 4 combines all observations from the experimental studies and applies this knowledge to the archaeological Middle Paleolithic (MP) faunal assemblage of Roc de Marsal (RDM) layer 9 from southwestern France. I utilize traditional zooarchaeological techniques alongside spectroscopic FTIR and mFTIR analyses on screened fragment and micromorphological thin sections to describe the properties of different Neanderthal fires within this depositional layer which have been previously described with lithic, geoarchaeological, and paleobotanical evidence (Aldeias et al., 2012; Goldberg et al., 2012; Reeves et al., 2019; Wroth et al., 2019). The abundance of thermally altered bone and well preserved combustion features in this layer provides an ideal environment to speak towards Neanderthal pyrotechnology. The burnt faunal assemblage of Roc de Marsal layer 9 and variability of burning conditions within that assemblage is consistent with differences between individual fires features inside the ancient dripline and those located in the cave exterior. This is a previously undescribed quality of fires at RDM, and the standardized methodology developed for this study can be used to address larger scale questions of Neanderthal fire use and curation with the future inclusion of additional assemblages.

Chapter 5 provides directions for future research and concluding remarks.

References

Aldeias, V., Goldberg, P., Sandgathe, D., Berna, F., Dibble, H. L., McPherron, S. P., ... & Rezek, Z. (2012). Evidence for Neandertal use of fire at Roc de Marsal (France). *Journal of Archaeological Science*, *39*(7), 2414-2423.

Bellomo, R. V. (1993). A methodological approach for identifying archaeological evidence of fire resulting from human activities. *Journal of Archaeological Science*, *20*(5), 525-553.

Binford, L. R. (1978). *Nunamiut ethnoarchaeology*. New York: Academic Press.

Dibble, H. L., Abodolahzadeh, A., Aldeias, V., Goldberg, P., McPherron, S. P., & Sandgathe, D. M. (2017). How did hominins adapt to ice age Europe without fire?. *Current Anthropology*, *58*(S16), S278-S287.

Goldberg, P., Dibble, H., Berna, F., Sandgathe, D., McPherron, S. J., & Turq, A. (2012). New evidence on Neandertal use of fire: examples from Roc de Marsal and Pech de l'Azé IV. *Quaternary International*, *247*, 325-340.

Goldberg, P., Miller, C. E., & Mentzer, S. M. (2017). Recognizing fire in the Paleolithic archaeological record. *Current Anthropology*, *58*(S16), S175-S190

Gowlett, J. A. (2006). The early settlement of northern Europe: fire history in the context of climate change and the social brain. *Comptes Rendus Palevol*, *5*(1-2), 299-310.

Kozowyk, P. R., Soressi, M., Pomstra, D., & Langejans, G. H. (2017). Experimental methods for the Palaeolithic dry distillation of birch bark: implications for the origin and development of Neandertal adhesive technology. *Scientific reports*, *7*(1), 1-9.

Mallol, C., Marlowe, F. W., Wood, B. M., & Porter, C. C. (2007). Earth, wind, and fire: ethnoarchaeological signals of Hadza fires. *Journal of Archaeological Science*, *34*(12), 2035-2052.

Mallol, C., & Henry, A. (2017). Ethnoarchaeology of Paleolithic fire: methodological considerations. *Current Anthropology*, *58*(S16), S217-S229.

Munsell Color (Firm). (2010). Munsell soil color charts : with genuine Munsell color chips. Grand Rapids, MI :Munsell Color.

Prüfer, K., Racimo, F., Patterson, N., Jay, F., Sankararaman, S., Sawyer, S., ... & Pääbo, S. (2014). The complete genome sequence of a Neanderthal from the Altai Mountains. *Nature*, *505*(7481), 43-49.

Pyne, S. J., Andrews, P. L., & Laven, R. D. (1996). Introduction to wildland fire, revised 2nd edn.

Reeves, J. S., McPherron, S. P., Aldeias, V., Dibble, H. L., Goldberg, P., Sandgathe, D., & Turq, A. (2019). Measuring spatial structure in time-averaged deposits insights from Roc de Marsal, France. *Archaeological and Anthropological Sciences*, *11*(10), 5743-5762.

Roebroeks, W., & Villa, P. (2011). On the earliest evidence for habitual use of fire in Europe. *Proceedings of the National Academy of Sciences*, *108*(13), 5209-5214.

Sandgathe, D. M., Dibble, H. L., Goldberg, P., McPherron, S. P., Turq, A., Niven, L., & Hodgkins, J. (2011). On the role of fire in Neandertal adaptations in Western Europe: evidence from Pech de l'Azé IV and Roc de Marsal, France. *PaleoAnthropology*, *2011*, 216-242.

Scott, A. C. (2000). The Pre-Quaternary history of fire. *Palaeogeography, palaeoclimatology, palaeoecology*, *164*(1-4), 281-329.

Stahlschmidt, M. C., Mallol, C., & Miller, C. E. (2020). Fire as an artifact—advances in paleolithic combustion structure studies: Introduction to the special issue. *Journal of Paleolithic Archaeology*, *3*(4), 503-508.

Stiner, M. C., Kuhn, S. L., Weiner, S., & Bar-Yosef, O. (1995). Differential burning, recrystallization, and fragmentation of archaeological bone. *Journal of archaeological science*, *22*(2), 223-237.

Wrangham, R. (2009). *Catching fire: how cooking made us human*. Basic books.

Wrangham, R. (2017). Control of fire in the Paleolithic: evaluating the cooking hypothesis. *Current Anthropology*, *58*(S16), S303-S313.

Wroth, K., Cabanes, D., Marston, J. M., Aldeias, V., Sandgathe, D., Turq, A., ... & Dibble, H. L. (2019). Neanderthal plant use and pyrotechnology: phytolith analysis from Roc de Marsal, France. *Archaeological and Anthropological Sciences*, *11*(8), 4325-4346.

Acknowledgements

There are a great number of researchers who have assisted me from the start of my academic journey to now. Forging these collaborative relationships has meant so much to me, and it has been the ultimate privilege to be a part of this community and to have received so much help at every stage. I must first acknowledge my academic advisors for their tremendous amount of work and dedication training me. There is no doubt that I would not be here without their patience, care, and trust. It is very powerful to work with advisors who are the types of researchers I aspire to be, both professionally and personally.

To begin, I must thank Dr. Teresa Steele. Dr. Steele, I moved my life to California because I wanted to work with you, and I am so lucky that you took a chance on me. I now have not only seen California, but so much of this world. The opportunity to be your student has changed everything for me. There is no doubt my retention in this field and any success I have as a researcher and archaeologist is due to being a part of your lab and having your mentorship. Thank you for your continued patience with me as I continue to learn and make mistakes, for creating the safest space I have found in this field, and for always being willing to listen to any concern. To see how every student trusts your confidence and advice speaks to how you are a pillar of our department and field. I know what I have learned from your example I will carry with me into everything I do next. You have connected me to opportunities I could have only dreamed of, and to support networks that have helped me through the most difficult periods. It is such a privilege to be a part of your lab and community you have built. Thank you, a thousand times.

To Dr. Nicolas Zwyns, thank you for trusting me, making me a part of your projects, and always sharing the absolute best advice. Thank you for never hesitating to invite me into your communities, including Liege, and integrating me fully into such dynamic and exciting projects. I have always felt completely welcome to jump into your teams, a gift that I know not every student can get. I also am fully aware that it is the accepting, honest, and warm cultures of your teams are directly from your example and the shared values you cultivate. I hope that I can continue to work with you long after the PhD, simply because you are a great boss. In addition to fieldwork, I also must thank you for the opportunity you provided me with the Center of Experimental Research at Davis (CEAD). With the freedom you allowed I truly was able to test myself, grow as a project developer, and learn leadership skills. You also remained very gracious and forgiving every time I misstep, and were always willing to nonjudgmentally help me fix whichever scenario I found myself in.

In addition to my advisors, there are many others at UC Davis I must thank and acknowledge for teaching me, supporting me, and giving me the tools necessary to complete my dissertation. This includes so many within the Evolutionary Anthropology wing at UC Davis. To Drs. Timothy Weaver and Damien Caillaud, thank you for so many excellent discussions and sharp questions. To Dr. Mark Grote, I dearly appreciate your time, sound advice, and tremendous amount of emotional and intellectual support. To Drs. Christyann Darwent and Jelmer Eerkens, thank you for allowing me to process samples within your labs (and, learn *how* to process samples, no matter how messy it got). I would also like to thank the student and faculty members of the Paleogroup and Early Human Technology journal clubs for creating spaces which allowed me to freely share my opinions, articulate my thoughts, and expose me to different viewpoints and knowledge bases. Attending, and baking for, our journal clubs were a highlight of my time in graduate school.

I owe so many thanks to so many UC Davis students, both members of my cohort and many amongst other cohorts. First, to the members of the Steele Lab, including Sara Watson, Trisha McNeill, and Drs. Naomi Martisius and Susan Lagle, it has been so special to go through graduate school with you as the backbone of my support network. I know I will always be able to turn to you for advice and edits, and hope there can be many collaborations in the future. To my fellow members of the Zwyns Lab, notably Peiqi Zhang and Corey Johnson. Thank you for your patience with my experimental materials all over the lab, and Peiqi, thank you for being my travel companion- I have so enjoyed working on projects together. To Neetha Iyer, I consider myself so lucky that graduate school put me in your path. Your encouragement, advice, brilliance, companionship, and sympathetic ear has been so important to me. Thank you for keeping my bowls safe and, also, for teaching me how to formulate a hypothesis. To Roshanne Bakiarty, Chelsea Cataldo-Ramirez, Dana Al-Hindi, and Drs. Mayowa Odegboyega, Kevin Smith, and Jason Miszaniec, I am so grateful to been together to figure our academia at your sides. Finally, to Sarah Marie Foley and Marigold Fyhrie, thank you for believing in my ideas, and I am looking forward to collaborations to come. I am so proud of you all.

Outside of the Evolutionary wing of the Anthropology department, UC Davis has so many others who I must attribute for so much of my growth as a researcher and educator. For those within the Teaching Assistant Consultant (TAC) program, both students who overlapped in my years there and our program manager Dr. Monica Esqueda, but also the continuing students and their commitment to effective and compassionate teaching. To Dr. Andrea Schreier, who was a line of support for me when I could not see how managing chronic illness and continuing as an archaeologist was possible. To Dr. Sanjai Parikh, thank you for letting me into your lab and allowing me access to instrumentation which has changed the direction of my research. Finally, to Drs. Alexandra Navrotsky and Sergey Ushakov, training this archaeologist in methods and concepts core to Materials Science has absolutely reformed my scholarship and research program. I owe you and your research team so much for providing me the opportunity to sink my teeth into and test my largest questions. Thank you for both your tremendous intellectual contributions to my projects and generous use of instruments, including the XRD work featured here.

From my undergraduate home department, New York University, I must thank Drs. Pam Crabtree, Rita Wright, Scott Williams, and Randy White. I am so grateful you allowed an undergraduate into those graduate courses. Despite being the most challenging learning environment I had ever found myself in, I learned as much in those years as the rest of my graduate education. To Dr. Milena Shattuck and Scott, thank you for making New York still feel like home. To Rita, you have always been a main inspiration for me, and the lifeline you found for me as your research assistant in between undergraduate and graduate school was a considerable gift to keep me within the Anthropology world in a difficult transition. To Randy, while I am sad that I will never be able to tell you, I attribute so much of my most pressing questions and deep love for Paleoanthropology from hearing your stories. Thank you for training me on your teams where I was able to witness the discovery of truly precious treasures.

Fieldwork is my first archaeological love and an aspect of my archaeological practice that keeps me tied to the material and landscapes which anchor my behavioral questions. I must thank those and their teams who have accepted me in the field, trained me, occasionally taken me to the hospital, and kept me safe by ensuring safe foods and environments: Drs. Marie Soressi, Tamara Dogandzic, Damien Flas, Marcel Weiss, Harald Floss, Roman Mensan, Francois Bon, Deb Olszewski, Dennis Sandgathe, Mohsen Zeidi, and Nicolas Conard. Additional thanks to Dr. Claire Heckel, who provided me my first chance to get connected to fieldwork, and to Christian Hoyer, Virginie Sinet-Mathoiot, Danielle Kelm, who I learned so much from and am so privileged to have worked with. In addition to fieldwork, it is a joy to acknowledge a department so important to me who both welcomed and, later, protected me in the pandemic. To Drs. Pierre Noiret, Veerle Rots, Damien Flas, Noora Taipale, Dries Knuts, Sonja Tomasso, Justin Coppe, Marine Michel as well as Christian Lepers, Timothee Libois, and Lola Tydgadt, un grand merci. Your hospitality, thoughtfulness, and community gave me an example of how I would like to conduct collaborative science. It has meant so much to me to have your continued support, even after I have left your city.

I would like to especially thank Drs. Shannon McPherron, Mareike Stahlschmidt, Paul Goldberg, and Vera Aldeias for their tremendous contributions to my growth as a researcher and providing such large opportunities for a student in my position. Your confidence, consideration, knowledge, and kindness has transformed my research platform. Thank you, Dr. McPherron, for helping me join excavation teams, for providing me with access to data, and for helping me navigate databases and data collection. I am so grateful for Dr. Stahlschmidt, whose consistent, thoughtful, and supportive mentorship has given me a platform to address some of my most pressing questions. Dr. Goldberg, thank you for allowing me access to micromorphological material. I believe this methodological direction has such great potential, and I appreciate your trust. To Dr. Aldeias: in addition to your encouragement, time, access to instrumentation and materials, I would additionally like to recognize and acknowledge your feedback and support as a member of my committee. It is a pleasure to have a chance to work with you, and your insight is invaluable.

Through my travels I have been graciously hosted by number of research institutions and provided access to many museum collections. I would like to therefore thank the curators and staff of the Musee d’Archeologie Nationale, the Campagne research facility, and the Musee de Mas d’Azil. I would like to additionally highlight the tremendous kindness and assistance given to me by the security crew, staff, and researchers at the Musee Nationale de Prehistoire through my data collection during the pandemic. To Bernard Nicolas, Stephane Madelaine, Catherine Cretin, Peggy Bonnet-Jacquement, and Pauline Rolland, thank you for both keeping me safe, helping me with equipment and collections, and keeping me company during a very isolating time. Your professional assistance and friendships transformed this difficult experience. Similarly, I must thank Isabelle Petrini and the staff of the Maison Bordes for your hospitality and care, transforming this iconic researcher housing into a home in the storm of the pandemic. Finally, I am so grateful to acknowledge Marie and Chris of Li**è**ge, for welcoming me into your home and assisting me with the Belgian visa process.

My project has been funded by a number of institutions, without which this work would not be possible. Thank you to UC Davis Graduate Studies and the UC Davis Anthropology department, the Sacramento Archaeology Society (SAS), and the Belgian American Education Foundation (BAEF). Financial support was also provided by the Leakey Foundation, who I must thank both for providing this opportunity for me to complete my project, but for also advancing a cause very important to me: increasing public knowledge and understanding of human origins, evolution, and behavior.

I have had a chance to meet, work with, and be hosted by so many supportive labs and communities across the discipline of Paleoanthropology. So many project ideas, theoretical concerns, and discussions of equity and inclusion have been discussed in these circles and I am so grateful to be considered your colleague. A huge thank you to the students, staff, researchers, faculty, and facilities of New York University (NYU), the New York Consortium in Evolutionary Primatology (New York, USA), the Max Planck Institute for Evolutionary Anthropology (Leipzig, Germany), the Interdisciplinary Center for Archaeology and the Evolution of Human Behavior (Faro, Portugal), the prehistory department of Tubingen University (Tubingen, Germany), and the prehistory department of the University of Liege (Liege, Belgium). It is from conversations within and around these intellectual spaces that I can see the future of the teams I would like to build and be a part of. I would like to specifically highlight and personally thank Drs. Li Li and Sarah Pederzani for your absolute willingness to support me, provide advice on figures, and for your friendship. I have learned so much from you both, it is motivating to see the excellent work that you do.

Dedication

This project, and, frankly, my deepest dream to be a working archaeologist (cultivated since I obsessed over Greek and Roman mythology in my beloved Metropolitan Museum), coming to fruition is due to the sacrifices and encouragement of my family. The unconditional love and support I have received is the most precious gift and means more to me than any degree or title I will ever achieve. To my family, this is our doctorate, and I am so proud to be your partner, sister, cousin, daughter, niece, and granddaughter. This project is dedicated to you all.

I must first thank my parents, who have never questioned my choices and have repeatedly saved me in the hardest moments. They have given everything they could to give me the best chance, and here we are. Thank you for never denying any of my curiosities, first in all the books I consumed, then the city, and now abroad. I hope to have a fraction of your work ethic, commitment, team building, problem solving skills, and warmth. You are both reflected in my work at every site I excavate, every team I manage, and every meal I cook! People from around the world have now tried your recipes (including the emergency carbonara). I love you both so much. We did it… was that the worst part?

To my Aunt Chris and Uncle Alan, thank you for supporting me with the gift of my education. There is no doubt that the path I have been set on began with my undergraduate degree, and there is in fact no way I can ever properly thank you for your support. You have given me my future, which, coincidentally, now means giving me the past. I was so happy and proud to volunteer at Turning Point (now Brooklyn Community Services) to follow your footsteps, and lessons from teaching there became the basis of my teaching practice today. To see your continued work with bringing books and opportunities to Brooklyn is so inspiring. I hope to keep community commitment and fighting for inclusive and equitable education is at the base of every action I do as an educator, and that will always be dedicated to you both.

To my Aunt Mary and Uncle Ricky, your interest, time, and care, and check ups have meant so much to us. Knowing you are on our team and always in our corner has given us confidence in the hardest times. Your emergency support and thoughtful gestures have literally meant the world to us. I wish we had a photo of you helping me set up a tent on the streets of

Bay Ridge; thank you for getting me my first gear and teaching me how to camp. It ended up being extremely useful!

To Uncle Greg and Aunt Sue, you have no idea how useful my organizational skills, (formed at Southeastern!), are for archaeological data collection. I am so grateful for all the tremendous support you have given us for all these years. To have the comfort of our support network and knowing family was close most certainly gave me the confidence to take risks.

To my Nana, if you remember, Dad once said Poppop built this house. That is true, but you have done the work of keeping us woven together as we left our homes and spread across states, cities, and countries. My entire life and having the privilege of this wonderful family is due to the work and sacrifices you and Poppop made for us, even before I was born. Thank you for being the thread between us and thank you for keeping us together. I have grown up on your stories, and now I get to tell a small portion of our human story.

To Remy, I'm pretty lucky to have had you as a best friend for a lifetime now. I hope you know how much I appreciate your support, and how grateful I am that you have my back. To Nick, Chris, Larissa, Alanna, Andrew, Caroline, Kate and Kevin, it is inspiring to see the incredible work you are all doing and putting out into this world. You all have such incredible creativity, drive, authenticity, and empathy. Nick, you allowing me to tag along with you and your friends let me see the diverse ways to express my own individual creativity, and I hope you know how much I use that every day. Chris, I am so grateful you are the family scientist, I hope I can continue to bother you about chemistry and spectroscopy for the rest of my career. Caroline, your commitment to supporting vulnerable communities is so powerful, and Andrew I have so much to learn from your teaching practice! Larissa, thank you for making sure I am safe in the field season by answering my bug bite questions and sending extra pairs of leggings so I would not be cold, and Kate thank you for sneaking into the library to be my study buddy all those years ago.

For my Cody, your encouragement, conversations, and unwavering support have been instrumental in absolutely every part of my scholarship, research, and pedagogy. You are reflected in all of my projects. Your inquisitive nature, your resilience, and your hunger for the difficult questions has taught me so much. To be on this journey at your side has been the greatest gift. What a beautiful life we have built, we have already won. It is so easy to find this field still so fascinating and full of mysteries by listening to you think aloud, and it also is so motivating to want to work on seemingly insurmountable problems by seeing you approach your work. Thank you for taking care of me regardless of where I am, picking me up and dropping me off for a thousand field seasons, and being my closest companion even when we are countries apart. Knowing you have my back has allowed me to be brave. There is much more to say than can fit here but with all (hopefully not tacky) sincerity you literally make me want to be a better scientist, and, more importantly, a better person.

Table of contents

Chapter 1

Introduction and Project Overview

Background

Special question of Neanderthal fire use

The overall role fire played in human evolution is uncertain. This includes the timing of habitual fire use by hominins, despite the benefits of environmental control and the ability to modify foods and other materials. Anthropogenic fire, or human made and curated fire, is indeed rare before 400,000 years (ka) ago, and while it is more archaeologically visible after 400 ka, there is still striking absences of fire visibility within the Middle Paleolithic (MP). Such absences of fire evidence has prompted researchers to suggest that not all hominins were obligate fire users, especially for Neanderthals in Southwest France in the relatively colder periods of Marine Isotope Stages (MIS) 4-3 (Roebroeks and Villa, 2011a; Dibble et al., 2017; Sandgathe et al., 2011a, 2011b). These observations call into question the presumed relationship between Neanderthals and fire and suggest that local environmental factors influenced the pattern of fire use in the European Late Pleistocene (Abdolahzadeh et al., 2022; Dibble et al., 2017; Roebroeks and Villa, 2011b; Sandgathe et al., 2011b; Sorenson, 2017).

The presence of Neanderthal fire has been attested at multiple MP sites, with specific attention to the recognition of burnt sediments (Aldeias et al., 2012; Courty et al., 2012; Leierer, 2021; Mallol et al., 2019), lithics (Abdolahzadeh et al., 2022, Aldeias et al., 2012; Dibble et al., 2009, 2018; Reeves et al., 2019), charcoal, phytoliths, and seeds (Albert et al., 2012; Cabanes et al., 2010; Henry et al., 2011; Rodriguez-Cintas et al., 2017; Shahack-Gross et al., 2014; Thery-Parisot, 2002a; Vidal-Matutano et al., 2015; 2017, 2018; Wroth, 2018; Wroth et al., 2019), and archaeomagnetic evidence (Carrancho et al., 2016, 2019; Herrejon Lagunilla et al., 2017; Leierer et al., 2020). Zooarchaeological approaches to Neanderthal fire technology have described accumulations of burnt bone (Rosell and Blasco, 2019) and have measured burnt faunal remains with traditional techniques (weights, counts, and percentages of cancellous or cortical tissue) to construct indices of bone likely used as a fuel source in an assemblage (Thery-Parisot, 2002b; Costamagno et al., 2009). However, the determination of MP Neanderthal fire function and properties, and variability within fire technology, has yet to be addressed and explored in a zooarchaeological standardized comparative context.

Aspects of fire technology which are most important to discerning different fire using behaviors have been highlighted in ethnoarchaeological studies relating to temperatures reached, fuel type and management, spatial positioning, and length of duration of a given firing event (Henry, 2017; Henry et al. 2018; Mallol et al., 2007; Mallol and Henry, 2017). Zooarchaeological approaches have the potential to specifically identify and discern between these behaviors of interest, as integrated changes to the bone organic and mineral components are temperature, atmosphere, and duration dependent and can be identified with a combination of macroscopic and spectroscopic analyses (Ellingham et al., 2015; Gallo et al., 2021; Reidsma et al., 2016; Mamede et al., 2018; Thompson et al., 2013).

Roc de Marsal (RDM)

Roc de Marsal (RDM) is a cave in the southwest of France, approximately 5km south of Les Eyzies in a tributary river valley of the Vézère (Aldeias et al., 2012; Sandgathe et al., 2011a). RDM has been extensively excavated since 1953, first under the direction of Jean Lafille, who unearthed the remains of a Neanderthal child in 1961 and continued work until 1971, and subsequently with multidisciplinary excavations from 2004-2010 (Aldeias et al., 2012; Goldberg et al., 2012) directed by Harold Dibble. RDM is composed of thirteen stratigraphic layers from a

2-meter sequence, spanning from Marine Isotope Stages (MIS) 5-3 (Goldberg et al., 2012; Guerin et al., 2012; Sandgathe et al., 2011). The most basal layers at RDM, likely dating from the temperate and wooded MIS 5a, have prevalent evidence for fire (Goldberg et al., 2012). Copious amounts of burnt bone, heat altered lithics, charcoal, ash units, and rubified sediments have been described for both layers 7 and 9, providing a striking signature of fire which was absent in the overlaying layers at RDM associated with colder and more arid MIS 4 and MIS 3 (Goldberg et al., 2012; Sandgathe et al., 2011a). The question of the pervasiveness and nature of MP Neanderthal fire using behaviors has highlighted a gap in the knowledge of Neanderthal's relationship with fire and necessitates future studies to move beyond documenting the presence of fire.

RDM is an excellent candidate to study variability in Neanderthal pyrotechnology for several reasons, as layer 9 exhibits minimal post-depositional movement, a large percentage of the site has been excavated with modern methodologies, and complementary studies have been completed considering other aspects of RDM fire properties, including through spatial analyses of lithic discard and geoarchaeological analyses (Aldeias et al., 2012; Goldberg et al., 2012; Sandgathe et al., 2011a; Reeves et al., 2019).

The research presented here will address fire properties from layer 9 of RDM with quantitative and qualitative faunal analyses alongside spectroscopic methods and spatial analyses. This high resolution zooarchaeological approach will speak to properties of combustion features not yet addressed and provide perspectives that cannot be answered with lithic or geochemical studies.

Theoretical significance

Historically, Neanderthal behavior has been documented through the study of their subsistence through faunal analyses, and investigations into their technological processes have focused on lithic artifacts. This study proposes a third perspective into Neanderthal lifeways: utilizing fauna to determine the technological processes of fire use and maintenance to characterize variation in Neanderthal fire technology. This approach draws heavily on observations of modern hunter-gatherer fire technology and use and integrates many scales of empirical evidence with larger theoretical frameworks for interpreting Neanderthal fire behavior. Finally, future work will aim to reconstruct this history of fire use and technology within the river valleys of the Dordogne and Vézère in Southwest France, especially of interest due to outstanding questions regarding Neanderthal competency for fire in this region. This includes the fire evidence from Pech de l'Azé IV (PIV) layer 8, which exhibits anthropogenic fire evidence roughly contemporaneous to Roc de Marsal, and the site of Le Moustier, which preserves an archaeological record for late Pleistocene Neanderthal populations. Establishing the types and variability of Neanderthal fire technology can therefore allow future research to formulate and test hypotheses considering fire technology adaptations between the closely related hominins to contextualize their behavioral similarities and differences.

Zooarchaeological approaches to the study of fire technology

Prior research investigating burnt bone has resulted in advances made in the study of behaviors related to cooking, waste disposal, bone fuel use, and the recognition of natural wildfire, indicating that burnt bone is an excellent proxy for archaeological anthropogenic fire (Clark and Ligouis, 2010; Costamagno et al., 2005; Gifford-Gonzalez et al. 1989; Speth and Clark, 2006; Stiner et al., 1995; Theory-Parisot et al., 2005). The macro-, micro-, and nano-scale changes that accompany the thermal alteration of bone are well documented, with many studies focusing on the visible color, texture, and mass changes to bone burnt to different temperatures (Ellingham et al., 2015; Stiner et al., 1995; Thompson, 2004; Zazzo et al., 2009). More recent developments in burnt bone research have documented primary structural and chemical changes in bone with exposure to heat at different temperatures, including: the rate of organic loss, the varying degrees of porosity, the presence of different compounds based on burning atmosphere, and the mineral bioapatite recrystallization and crystallite size growth (Ellingham et al., 2015; Gallo et al., 2021; Reidsma et al., 2016; van Hoesel et al., 2019).

Codifying burnt assemblages using common practice zooarchaeological scales of heating intensity, such as the seven category scale proposed by Stiner et al. (1995), alongside high-resolution spectroscopic analyses has the potential to directly address aspects of fire technology related to construction and maintenance such as if bone was used a fuel, if bone was burned as a part of a site maintenance strategy, the light and heat properties of fires, if bone was burned in the presence of oxygen,and primary and secondary locations of hearths (Barkai et al., 2017; Costamagno et al., 2009; Ellingham et al., 2015; Hoare, 2020; Thompson et al., 2013; Reidsma et al., 2016). With thermal alteration, bone loses organics and water, and the size and relative order of the mineral crystals change dramatically. The use of spectroscopic analyses such as Fourier-Transform Infrared Spectroscopy (FTIR) and X-Ray Diffraction (XRD) can monitor these transformations, informing true heat exposure and elucidating maximum temperature thresholds and different burning conditions that cannot be mistaken for macroscopic staining by sun bleaching (Ellingham et al., 2015; Piga et al., 2008; Shahack-Gross et al., 1997; Thompson, 2004). FTIR and XRD have also recently been demonstrated to distinguish between aspects of fire technology related to burning atmosphere (with access to oxygen or in a reduction environment) and long duration burning under temperatures of calcination (> 680 °C) (Gallo et al., in press; Reidsma et al., 2016). Finally, the orientation and shape of bone fragments on the microscopic scale, visible in micromorphological thin section slides, can identify the degree of preservation and actions such as hearth trampling and sweeping. Recently developed techniques using micro-FTIR (mFTIR) can be utilized directly on such micromorphological slides to attribute specific temperatures for each individual bone within their original depositional context (Aldeias et al., 2012; Miller et al., 2010).

Although faunal remains have been demonstrated to be powerful proxies for the study of ancient fire residues, numerous discrepancies have been reported between different studies, highlighting the intricate roles of variables such as time, temperature, initial status of bone material (e.g. fleshed or defleshed), and atmospheric and sedimentary conditions (Aldeias et al., 2016; Bennett, 1999; Reidsma et al., 2016; Speth and Clark, 2006; Stiner et al., 1995; Van Hoesel et al., 2019). These aspects of the thermal alteration of bone must be accounted for before researchers draw conclusions regarding fire types and functions, especially for Neanderthals, whose contested abilities regarding fire use and knowledge have great behavioral implications.

Project Overview

This project aims to: 1) describe the transformations to bone bioapatite crystallites and crystal lattices with heat and the applicability of knowledge of these transformation to archaeological assemblages; 2) identify the independent roles of both duration time and temperature for the thermal alteration of bone; and 3) apply data relevant to aspects of fire properties to interpret the remains of anthropogenic combustion features from the MP assemblage of RDM layer 9. For the RDM evidence of fire, the goals of this project also are to fully assess aspects of fire properties including A) fire temperatures, B) fire placement and distribution, C) inferred fuel, and D) variability between treatments of different features. This research establishes novel methodological approaches to analyze and interpret archaeological burnt and heated bone for the purpose of better contextualizing anthropogenic fire using behaviors while expanding knowledge on the different processes which impact thermally altered bone, both during and after the initial heating event.

Chapter 2 uses a robust experimental referential dataset to explore the structural characteristics of heated bone in oxygen atmospheres. This study demonstrates the timing of organic loss, changes in porosity, degree of bioapatite recrystallization, and bioapatite size growth in samples heated at 100˚-1200˚C, in 100˚C incremental steps. Spectroscopic analyses, specifically FTIR-ATR and XRD, are used here to measure relevant structural and chemical compositions. We find that the small and reactive crystallites of bones which are heated but not yet calcined are the most soluble of faunal remains at any stage of burning, and calcination accompanies much greater thermodynamic stability, and therefore, likelihood to preserve. This pattern is especially relevant due to the opposing mechanical properties of burnt bone, in which calcined bone exhibits the greatest amount of physical fragility and is susceptible to fragmentation with little added energy. This study compares experimental samples to an open-air archaeological assemblage 30,000 years ago to ensure changes are recognizable after active diagenetic agents. This paper was presented at the 9th meeting of the European Society for Human Evolution in 2019 (Liege, Belgium) and published in *PLoS ONE* in July 2021 (Gallo et al., 2021).

Chapter 3 continues investigations into the properties of thermally altered bone, here documenting how the duration and temperature affect specific alterations to bone mineral. Duration is a variable of utmost importance to investigate, as ethnoarchaeological observations of combustion features by modern hunting and gathering populations highlight duration as a very significant aspect of combustion features and deeply linked to fire function and fire curation behaviors. Traditional zooarchaeological categories of macroscopic observations are taken into consideration for this study alongside detailed spectroscopic analyses, including FTIR-ATR and XRD. This combined approach outlines several visual and compositional cues to identify long duration fires at low temperatures, and suggests methods to also recognize long durations above calcination temperatures. Our conclusions, for the first time, describe the interplay between color, burning temperature, and structural properties of heated bone and establish quantitative methods to distinguish heating duration in the archaeological record. This research was presented at the 2022 annual Paleoanthropology meetings in Denver, Colorado, and was submitted to the Journal of *Archaeological and Anthropological Sciences* as a part of a special issue on Pyrotechnology in October, 2022 (Gallo et al., n.d.).

Chapter 4 applies methods (described in Chapters 2-4) to a the full zooarchaeological assemblage from layer 9 of Roc de Marsal (RDM) in southwest France. This Middle Paleolithic Neanderthal site has excellent preservation and exceptional examples of burnt residues, including burnt and heated bone. Several combustion features have been previously identified, and the study of burnt fauna from RDM layer 9 presents here a complementary study to the described lithic, paleobotanical, and geoarchaeological evidence for fire proxies. The focus of this chapter is to fully describe the temperatures reached in specific fire events, combustion feature placement, and fuel used by Neanderthals in layer 9. These data allow a comparison between anthropogenic features to advance our understanding of Neanderthal fire using behaviors. Data collection includes three scales of analyses: bones from piece plotted material (> 2.5 cm), coarse screened fraction (< 2.5 cm- 6 mm), and bone identified within micromorphological slides.

Spectroscopic testing, here FTIR-ATR and micro-FTIR, is further used to characterize the temperatures, transformations, and properties of sampled bone across the screened and micromorphological evidence. Blue bone is additionally described here, present only in the screened fraction, as an indicator of potential site maintenance behaviors relevant to Neanderthal organization of space and construction of fire events. These data will be presented at the 2023 Paleoanthropology meeting (Portland, Oregon) and will be prepared for publication in 2023.

Chapter 5 provides the continuation of this research, including the extension to different Neanderthal sites in MIS 5 as well as MIS 3, future experimental work, and concluding remarks.

References

Abdolahzadeh, A., McPherron, S. P., Sandgathe, D. M., Schurr, T. G., Olszewski, D. I., & Dibble, H. L. (2022). Investigatingvariability in the frequency of fire use in the archaeological record of Late Pleistocene Europe. Archaeological and AnthropologicalSciences, 14(4), 1-26.

Albert, R. M., Berna, F., & Goldberg, P. (2012). Insights on Neanderthal fire use at Kebara Cave (Israel) through high resolution study of prehistoric combustion features: Evidence from phytoliths and thin sections. *Quaternary International*, *247*, 278-293

Aldeias, V., Goldberg, P., Sandgathe, D., Berna, F., Dibble, H. L., McPherron, S. P., Turq,A., & Rezek, Z. (2012). Evidence for Neandertal use of fire at Roc de Marsal (France). Journal of Archaeological Science, 39(7), 2414–2423. https://doi.org/10.1016/j.jas.2012.01.039

Barkai, R., Rosell, J., Blasco, R., & Gopher, A. (2017). Fire for a Reason: Barbecue at Middle Pleistocene Qesem Cave, Israel. Current Anthropology, 58(S16), S314–S328. https://doi.org/10.1086/691211

Bennett, J. L. (1999). Thermal alteration of buried bone. *Journal of Archaeological Science*, *26*(1), 1-8.

Bonnichsen & M. Sorg (Eds.), Bone Modification. Institute for Quarternary Studies, U. of Maine, Orono.

Cabanes, D., Mallol, C., Expósito, I., & Baena, J. (2010). Phytolith evidence for hearths and beds in the late Mousterian occupations of Esquilleu cave (Cantabria, Spain). *Journal of Archaeological Science*, *37*(11), 2947-2957.

Carrancho, Á., Lagunilla, Á. H., & Vergès, J. M. (2016). Three archaeomagnetic applications of archaeological interest to the study of burnt anthropogenic cave sediments. Quaternary International, 414, 244-257.

Clark, J. L., & Ligouis, B. (2010). Burned bone in the Howieson's Poort and post-Howieson's Poort Middle Stone Age deposits at Sibudu (South Africa): Behavioral and taphonomicimplications. Journal of Archaeological Science, 37(10), 2650–2661.

Costamagno, S., Théry-Parisot, I., Brugal, J.-P., & Guibert, R. (2005). Taphonomic consequences of the use of bones as fuel. Experimental data and archaeological applications.In Biosphere to lithosphere: New studies in vertebrate taphonomy (pp. 51–62). Oxbow Books Oxford.

Costamagno, S., Théry-Parisot, I., Castel, J.-C., & Brugal, J.-P. (2009). Combustible ou non? Analyse multifactorielle et modèles explicatifs sur les ossements brûlés paléolithiques: Vol. Gestion des combustibles au Paléolithique et au Mésolithique: nouveaux outils, nouvelles interpretations (I. Théry-Parisot, S. Costamagno, & A. Henry, Eds.). British Archaeological Reports International Series 1914. Oxford: Archaeopress.

Courty, M. A., Carbonell, E., Poch, J. V., & Banerjee, R. (2012). Microstratigraphic and multi-analytical evidence for advanced Neanderthal pyrotechnology at Abric Romani (Capellades, Spain). *Quaternary International*, *247*, 294-312.

Dibble HL, Berna F, Goldberg P, McPherron S, Mentzer S, Niven L, Richter D, Sandgathe DM, Tháry-Parisot I, Turq A (2009) A preliminary Report on Pech de I'Azé IV, layer 8 (Middle Paleolithic, France). Paleoanthropol Soc 2009:182–219

Dibble, H. L., Abodolahzadeh, A., Aldeias, V., Goldberg, P., McPherron, S. P., & Sandgathe,D. M. (2017). How Did Hominins Adapt to Ice Age Europe without Fire? Current Anthropology, 58(S16), S278–S287. https://doi.org/10.1086/692628

Dibble HL, McPherron SJP, Goldberg P, Sandgathe D (2018) The Middle Paleolithic site of Pech de l'Azé IV. Springer, Berlin, pp 221–227

Discamps, E., Muth, X., Gravina, B., Lacrampe-Cuyaubère, F., Chadelle, J. P., Faivre, J. P., & Maureille, B. (2016). Photogrammetry as a tool for integrating archival data in archaeological fieldwork: Examples from the Middle Palaeolithic sites of Combe–Grenal, Le Moustier, and Regourdou. Journal of Archaeological Science: Reports, 8, 268-276.

Discamps, E., & Royer, A. (2017). Reconstructing palaeoenvironmental conditions faced by Mousterian hunters during MIS 5 to 3 in southwestern France: A multi-scale approach using data from large and small mammal communities. Quaternary International, 433,64-87.

Discamps, E., & Lemeur, C. (2019). Variability of hunted prey and methods of exploitation of deer in the Mousterian: the contribution of recent collections from Moustier (Dordogne, France, Layers G and H). PALEO. Review of Prehistoric Archaeology , (30-1), 318-329.

Ellingham, S. T. D., Thompson, T. J. U., & Islam, M. (2015). Thermogravimetric analysis of property changes and weight loss in incinerated bone. Palaeogeography, Palaeoclimatology, Palaeoecology, 438, 239–244. https://doi.org/10.1016/j.palaeo.2015.08.009

Gallo, G., Fyhrie, M., Paine, C., Ushakov, S. V., Izuho, M., Gunchinsuren, B., ... & Navrotsky, A. (2021). Characterization of structural changes in modern and archaeological burnt bone: Implications for differential preservation bias. PloS one, 16(7),e0254529.

Gifford-Gonzalez, D. (1989). Ethnographic Analogues for Interpreting Modified Bones: Some Cases from East Africa. In R.

Gravina, B., & Discamps, E. (2015). MTA-B or not to be? Recycled bifaces and shifting hunting strategies at Le Moustier and their implication for the late Middle Palaeolithic in southwestern France. Journal of Human Evolution, 84, 83-98.

Guérin, G., Discamps, E., Lahaye, C., Mercier, N., Guibert, P., Turq, A., ... & Soulier, M. C. (2012). Multi-method (TL and OSL), multi-material (quartz and flint) dating of the Mousterian site of Roc de Marsal (Dordogne, France): correlating Neanderthal occupations with the climatic variability of MIS 5–3. *Journal of Archaeological Science*, *39*(10), 3071-3084.

Henry, A. G., Brooks, A. S., & Piperno, D. R. (2011). Microfossils in calculus demonstrate consumption of plants and cooked foods in Neanderthal diets (Shanidar III, Iraq; Spy I and II, Belgium). *Proceedings of the National Academy of Sciences*, *108*(2), 486-491.

Henry, A. G. (2017). Neanderthal cooking and the costs of fire. *Current Anthropology*, *58*(S16), S329-S336.

Henry, A. G., Büdel, T., & Bazin, P. L. (2018). Towards an understanding of the costs of fire. *Quaternary International*, *493*, 96-105.

Herrejón Lagunilla, Á., Carrancho, Á., José Villalaín, J., Mallol, C., Hernández, C. M., & Galván, B. (2017, April). Archaeomagnetic evidence of temporal diachronies in Middle-Palaeolithic palimpsests. A case study from El Salt (SE Spain). In *EGU General Assembly Conference Abstracts* (p. 1311).

Hoare, S. (2020). Assessing the Function of Palaeolithic Hearths: Experiments on Intensity of Luminosity and Radiative Heat Outputs from Different Fuel Sources. Journal of Paleolithic Archaeology. https://doi.org/10.1007/s41982-019-00047-z

Hodgkins, J. (2011b). On the Role of Fire in Neanderthal Adaptations in Western Europe: Evidence from Pech de l’Azé and Roc de Marsal France. PaleoAnthropology, 2011. https://doi.org/doi:10.4207/PA.2011.ART54

Leierer, L., Alonso, Á. C., Pérez, L., Lagunilla, Á. H., Herrera-Herrera, A. V., Connolly, R., ... & Mallol, C. (2020). It's getting hot in here–Microcontextual study of a potential pit hearth at the Middle Paleolithic site of El Salt, Spain. *Journal of Archaeological Science*, *123*, 105237.

Leierer, L. (2021). Approaching neanderthal behavior through the geoarchaeological study of combustion structures: investigations in soil micromorphology and lipid biomarkers (Doctoral dissertation, Universidad de La Laguna (Canary Islands, Spain)).

Mallol, C., Marlowe, F. W., Wood, B. M., & Porter, C. C. (2007). Earth, wind, and fire: ethnoarchaeological signals of Hadza fires.Journal of Archaeological Science, 34(12), 2035-2052.

Mallol, C., & Henry, A. (2017). Ethnoarchaeology of Paleolithic fire: methodological considerations. Current Anthropology, 58(S16),S217-S229.

Mallol, C., Hernández, C., Mercier, N., Falguères, C., Carrancho, Á., Cabanes, D., ... & Galván, B. (2019). Fire and brief human occupations in Iberia during MIS 4: Evidence from Abric del Pastor (Alcoy, Spain). Scientific reports, 9(1), 1-11.

Mamede, A. P., Gonçalves, D., Marques, M. P. M., & Batista de Carvalho, L. A. (2018). Burned bones tell their own stories: A review of methodological approaches to assess heat-induced diagenesis. *Applied Spectroscopy Reviews*, *53*(8), 603-635.

Miller, C. E., Conard, N. J., Goldberg, P., & Berna, F. (2010). Dumping, sweeping and trampling: experimental micromorphological analysis of anthropogenically modified combustion features.

Piga, G., Malgosa, A., Thompson, T. J. U., & Enzo, S. (2008). A new calibration of the XRD technique for the study of archaeological burned human remains. Journal of Archaeological Science, 35(8), 2171–2178. https://doi.org/10.1016/j.jas.2008.02.003

Reeves, J. S., McPherron, S. P., Aldeias, V., Dibble, H. L., Goldberg, P., Sandgathe, D., & Turq, A. (2019). Measuring spatial structure in time-averaged deposits insights from Roc de Marsal,France. Archaeological and Anthropological Sciences, 11(10), 5743– 5762. https://doi.org/10.1007/s12520-019-00871-y

Reidsma, F. H., van Hoesel, A., van Os, B. J. H., Megens, L., & Braadbaart, F. (2016). Charred bone: Physical and chemical changes during laboratory simulated heating under reducing conditions and its relevance for the study of fire use in archaeology. Journal of Archaeological Science: Reports, 10, 282–292. https://doi.org/10.1016/j.jasrep.2016.10.001

Roebroeks, W., & Villa, P. (2011a). On the earliest evidence for habitual use of fire in Europe. Proceedings of the National Academy of Sciences, 108(13), 5209– 5214. https://doi.org/10.1073/pnas.1018116108

Roebroeks, W., & Villa, P. (2011b). Reply to Sandgathe et al.: Neandertal use of fire. *Proceedings of the National Academy of Sciences*, *108*(29), E299-E299.

Rosell, J., & Blasco, R. (2019). The early use of fire among Neanderthals from a zooarchaeological perspective. *Quaternary Science Reviews*, *217*, 268-283.

Sandgathe, D. M., Dibble, H. L., Goldberg, P., McPherron, S. P., Turq, A., Niven, L., & Hodgkins, J. (2011a). Timing of the appearance of habitual fire use. Proceedings of the National Academy of Sciences, 108(29), E298–E298.https://doi.org/10.1073/pnas.1106759108 Sandgathe, D., Dibble, H. L., Goldberg, P., McPherron, S. P., Turq, A., Niven, L., &

Sandgathe, D. M., Dibble, H. L., Goldberg, P., McPherron, S. P., Turq, A., Niven, L., & Hodgkins, J. (2011b). On the role of fire in Neandertal adaptations in Western Europe: evidence from Pech de l'Azé IV and Roc de Marsal, France. *PaleoAnthropology*, *2011*, 216-242.

Shahack-Gross, R., Bar-Yosef, O., & Weiner, S. (1997). Black-Coloured Bones in Hayonim Cave, Israel: Differentiating Between Burning and Oxide Staining. Journal of Archaeological Science, 24(5), 439–446. https://doi.org/10.1006/jasc.1996.0128

Sorensen, A. C. (2017). On the relationship between climate and Neandertal fire use during the Last Glacial in south-west France. *Quaternary International*, *436*, 114-128.

Speth, J., & Clark, J. (2006). Hunting and overhunting in the Levantine Late Middle Palaeolithic. Before Farming, 2006(3), 1–42. https://doi.org/10.3828/bfarm.2006.3.1

Speth, J. D. (2017). Putrid Meat and Fish in the Eurasian Middle and Upper Paleolithic: Are We Missing a Key Part of Neanderthal and Modern Human Diet? 29. NOT COMPLETE

Stiner, M. C., Kuhn, S. L., Weiner, S., & Bar-Yosef, O. (1995). Differential Burning, Recrystallization, and Fragmentation of Archaeological Bone. Journal of Archaeological Science, 22(2), 223–237. https://doi.org/10.1006/jasc.1995.0024

Texier, JP, Discamps, E., Gravina, B., & Thomas, M. (2020). Filling deposits of the lower rock shelter of Moustier (Dordogne, France): lithostratigraphy, formation process and evolution of the geomorphological system. PALEO. Review of PrehistoricArchaeology , (30-2), 320-345.

Théry-Parisot, I. (2002a). Gathering of firewood during the Palaeolithic. *Charcoal analysis. Methodological approaches, palaeoecological results and wood uses. BAR International Series*, *1063*, 243-249.

Théry-Parisot, I. (2002b). Fuel management (bone and wood) during the Lower Aurignacian in the Pataud rock shelter (Lower Palaeolithic, Les Eyzies de Tayac, Dordogne, France). Contribution of experimentation. *Journal of Archaeological Science*, *29*(12), 1415-1421.

Théry-Parisot, I., Costamagno, S., Brugal, J.-P., Fosse, P., & Guilbert, R. (2005). The use of bone as fuel during the Palaeolithic, experimental study of bone combustible properties.

Thompson, T. (2004). Recent advances in the study of burned bone and their implications for forensic anthropology. Forensic Science International, 146, S203–S205.

Thompson, T. J. U., Islam, M., & Bonniere, M. (2013). A new statistical approach for determining the crystallinity of heat-altered bone mineral from FTIR spectra. Journal of Archaeological Science, 40(1), 416–422. https://doi.org/10.1016/j.jas.2012.07.008

van Hoesel, A., Reidsma, F. H., van Os, B. J., Megens, L., & Braadbaart, F. (2019). Combusted bone: Physical and chemical changes of bone during laboratory simulated heating under oxidising conditions and their relevance for the study of ancient fire use. Journal of Archaeological Science: Reports, 28, 102033.

Vidal-Matutano, P., Hernández, C. M., Galván, B., & Mallol, C. (2015). Neanderthal firewood management: evidence from stratigraphic unit IV of Abric Del Pastor (eastern Iberia). *Quaternary Science Reviews*, *111*, 81-93.

Vidal-Matutano, P., Henry, A., & Théry-Parisot, I. (2017). Dead wood gathering among Neanderthal groups: charcoal evidence from

Vidal-Matutano, P., Pérez-Jordà, G., Hernández, C. M., & Galván, B. (2018). Macrobotanical evidence (wood charcoal and seeds) from the Middle Palaeolithic site of El Salt, Eastern Iberia: Palaeoenvironmental data and plant resources catchment areas. *Journal of archaeological science: reports*, *19*, 454-464.

White, R., Mensan, R., Clark, A. E., Tartar, E., Marquer, L., Bourrillon, R., Goldberg, P.,Chiotti, L., Cretin, C., Rendu, W., Pike-Tay, A., & Ranlett, S. (2017). Technologies for the Control of Heat and Light in the Vézère Valley Aurignacian. Current Anthropology, 58(S16), S288–S302. https://doi.org/10.1086/692708

Wroth, K. (2018). *Neanderthal plant use and phytolith taphonomy in the Middle Paleolithic of Southwest France* (Doctoral dissertation, Boston University).

Wroth, K., Cabanes, D., Marston, J. M., Aldeias, V., Sandgathe, D., Turq, A., ... & Dibble, H. L. (2019). Neanderthal plant use and pyrotechnology: phytolith analysis from Roc de Marsal, France. *Archaeological and Anthropological Sciences*, *11*(8), 4325-4346.

Zazzo, A., Saliege, J. F., Person, A., & Boucher, H. (2009). Radiocarbon dating of calcined bones: Where does the carbon come from?. Radiocarbon, 51(2), 601-611.

Chapter 2

Characterization of structural changes in modern and archaeological burnt bone: implications for differential preservation bias

Abstract

Structural and thermodynamic factors which may influence burnt bone survivorship in archaeological contexts have not been fully described. A highly controlled experimental reference collection of fresh, modern bone burned in temperature increments 100-1200˚C is presented here to document the changes to bone tissue relevant to preservation using Fourier transform infrared spectroscopy and X-ray diffraction. Specific parameters investigated here include the rate of organic loss, amount of bone mineral recrystallization, and average growth in bone mineral crystallite size. An archaeological assemblage ca. 30,000 years ago is additionally considered to confirm visibility of changes seen in the modern reference sample and relate changes to commonly used zooarchaeological scales of burning intensity. The timing of our results indicates that the loss of organic components in both modern and archaeological bone burnt to temperatures up to 700˚C are not accompanied by growth changes in the average crystallite size of bone mineral bioapatite, leaving the small and reactive bioapatite crystals of charred and carbonized bone exposed to diagenetic agents in depositional contexts. For bones burnt to temperatures of 700˚C and above, two major increases in average crystallite size are noted which effectively decrease the available surface area of bone mineral crystals, decreasing reactivity and offering greater thermodynamic stability despite the mechanical fragility of calcined bone.

Introduction

Anthropogenic burnt bones can be indicative of many social and economic behaviors and can contribute to studies identifying evidence for ritual activity [1], cremations [2-4], bone fuel [5-9], hygienic practices [5,9], cooking and marrow warming [10], and locations of combustion features [11]. Burnt bones undergo substantive structural and compositional changes at different burning intensities, however, and the implications of these changes for differential bone survivorship in an archaeological fauna assemblage is of critical importance for studies utilizing burnt material.

Bone diagenesis can result in bone mineral disintegration or dissolution [12]. The rate, sequence, and extent of diagenetic processes are determined by many factors, including the nature of the depositional environment and the age, element, and species of the bone tissue. Postmortem bone preservation is well described in regards to the differences between compact and cancellous bone [13-16], juvenile and adult bone [17,18], intra- and interspecies variation in bone size and density [19-21], and different environmental conditions [12, 22-26]. However, zooarchaeological evaluations of burnt bone preservation have resulted in varied interpretations and have not addressed the different structural properties of bone burnt to different temperatures [5, 27].

The aim of this study is to describe the range of structural modifications to bone mineral produced by burning at different temperature intensities, and to relate such changes to standardized scales utilized in zooarchaeological methods, specifically here the Stiner et al. [27] scale of burning intensity. This is done with the intention of describing differences between categories of burnt bone, including any vulnerabilities to diagenetic processes that could result in assemblage biases within burnt bone in archaeological contexts. Here we present the results of a controlled experimental reference library of fresh, modern bone burnt in increments of 100-1200˚C and analyzed with Fourier transform infrared spectroscopy (FTIR) with Attenuated Total Reflectance (ATR) attachment and X-ray diffraction (XRD). We additionally compare spectroscopic measurements to a sample of burnt fauna dated to ca. 30 ka to verify visibility of alterations in an archaeological assemblage.

Bone

Bone is comprised of organic proteins primarily of collagen, inorganic mineral, and water, creating a composite material organized in compact bone in cylindrical structures of concentric lamellae surrounding an interior channel for a central blood canal [28,29]. This hierarchical arrangement provides and maintains the biological roles of skeletal tissue: mechanical strength to transmit force and protect organs, and the regulation of homeostasis through ionic regulation [28-31].

Living bone is very porous, with around 12% of bone volume comprised of open spaces [2]. The concentric systems, known as Haversian systems, constitute a large percentage of the bone matrix porosity, with the remainder composed of resorption bays and voids created between the organic and inorganic components [29-32]. The amount, size, and density of pores in bone is variable across elements, species, and ages, although trabecular bone does exhibit a higher porosity than compact bone due to its more open structure [21, 29, 32].

Inorganic bone constituent, bioapatite, is isostructural to mineral hydroxyapatite $Ca_5(PO_4)_3OH$. The specific chemical compositions of bioapatite reflect diet, biological age through history of bone remodeling, and variation can exist both within species and within the skeletal elements themselves [29]. Bioapatite contains 5-8 wt% carbonate which can substitute either phosphate or hydroxyl group in hydroxyapatite structure [33]. Bioapatite has a high degree of nonstoichiometry, and its composition can be described as $Ca_{10-x}(PO_4)_{6-x}(HPO_4, CO_3)x(OH,1/2CO_3)_{2-x}$ with $0<x<2$ [31, 34, 35].

In vivo bioapatite has extremely small, thin, plate-like morphologies (1-7 nm thick, 15-200 nm in length, and 10-80 nm in width) which are cross-linked to organic collagen fibrils [34-36]. Water is found in bone as loose mobile water in the extracellular matrix, in void spaces to facilitate movement, and integrated within and around the organic and mineral components [31, 37]. Bioapatite crystallites have typical surface areas above 200 m^2g and are heavily hydrated [30, 31, 35-38]. These surface layers of ions play a key role in the regulation of homeostasis, as they can be easily exchanged and provide a necessary capacity to regulate ionic concentrations in living tissue [3, 28, 38-41].

Bone diagenesis

Diagenesis, the postmortem changes to bone tissue in burial environments, includes the integrated processes of microbial attack, water activity, and mineral recrystallization and can result in the complete disintegration of bone material [12]. The arrangement and size distribution of pores at the time of burial are large predictors of bone decay or bone survival, as pores mediate the access and extent of destructive agents such as bacteria and water [18, 22-24, 42-44]. Microbial attack itself is an active and immediate process accounting for a large amount of initial organic destruction, especially in warmer environments [42]. Microbial access to collagen degrades the protein chains, effectively removing the organic component of bone [19, 24, 32, 42, 44, 45]. The removal of the collagen component results in a more brittle biomaterial on the macroscale, and leaves bioapatite crystals unprotected on the micro- and nanoscale [46].

Exposed bioapatite is vulnerable to the incorporation of impurities and to disintegration, as postmortem crystals initially retain the specific morphology, reactivity, and thermodynamic instability of living bioapatite [47, 48]. The reaction between bone mineral and water is the most significant predicate of bioapatite disintegration at this stage of diagenesis, and bones buried in environments with active water movement are highly vulnerable to leeching and dissolution, noted to be heightened when bioapatite is exposed and easily accessible after organic removal [24, 48]. There is no universal thermodynamic model of bioapatite solubility due to the complexity of bone as a biomaterial, and rather each crystal domain is assigned its own Metastable Equilibrium Solubility (MES): a distribution phenomenon dependent on aspects of bone quality such as carbonate substitutions, ion vacancies, low crystallinity, and small crystal sizes [48, 49]. Uptake of contamination from the burial environment, such as rare earth elements and secondary calcite, has been noted to reduce as bone mineral spontaneously recrystallizes without in-vivo regulation and larger crystals grow at the expense of smaller crystals [18, 50, 51]. This process results in bone mineral with a slightly higher crystallinity, effectively decreasing the available reactive surface area of bioapatite and therefore the overall solubility compared to fresh bone [18, 36, 50, 51].

Burnt bone

Burning bone results in the decomposition of the organics and loss of water, as well as in massive changes to bioapatite crystal dimensions and structure. The extent and degree of these alterations are correlated to temperature and burning atmosphere, producing bones with different mechanical and thermodynamic properties dependent on the extent of burning. These micro- and nano- scale transformations have a notable impact on visible macroscopic changes to heat altered bone, including color changes, cracking, shrinkage, weight loss, and fragmentation [27, 41, 52-

55]. Burnt bone coloration is generally correlated to burning intensity, and the ease of color identification has assisted in the proliferation and use of zooarchaeological scales of coding heat alteration, such as the Stiner et al. [27] classification of burning intensity (Table 1).

Table 1: Burning intensity scale based on macroscopic visual qualities following Stiner et al. [27]

Burning Scale	Description
0	Not burnt
1	Slightly burnt, < 50% carbonized
2	Majority burnt, > 50% carbonized
3	Fully carbonized
4	Slightly highly burnt, < 50% calcined
5	Majority highly burnt, > 50% calcined
6	Fully calcined

Scales of burning based on macroscopic visual cues are tremendously beneficial for processing archaeological assemblages of burnt fauna, but do not reflect the sequence of changes in the composition and structural properties of burnt bone. Observations on the nano- and micro-scale have therefore led to the definition of four stages of burning which are correlated to the transformation of bone mineral and removal of organics on the nano- and microscale: dehydration, decomposition, inversion, and fusion [2, 54-57]. These stages are accomplished at different temperature thresholds and were defined in oxidizing burning conditions [2, 54-57]. The rate and degree of temperature induced changes depend on variables such as flesh coverage, heating and cooling rates and oxygen availability [54, 55]. Dehydration, or, the loss of water, occurs between 100 and 600˚C [2, 54, 56-58]. This wide temperature range likely accounts for the quicker loss of the loosely bound water between 25 and 250˚C and the eventual loss of the additional water more structurally bound to the mineral in temperatures above 100˚C [2, 31, 56, 57].

After initial dehydration, the second stage of bone combustion is organic decomposition, from 300 to 800˚C [2, 56, 57]. With collagen degradation starting at 112 - 260˚C, above 300˚C a large proportion of the organics is reduced to a char [58]. Between 300 and 500˚C most mass, 50 – 55 %, is lost, and above 500˚C any remaining char is removed by 700˚C [58]. The macroscopic transformation most noticeable with the decomposition stage is the striking changes in coloring, with bone becoming visibly blackened with the charring of organics (300˚C), corresponding to Stages 1-3 of the Stiner et al. [27] scale, and after the complete removal of organics (700˚C) transitioning to a grey and chalky white hue for Stiner et al. [27] Stages 4-6 [2, 27, 54, 56, 57]. Bone that is blackened is referred to as combusted or carbonized dependent on burning atmosphere, while grey and white bone with all organics removed can be referenced as calcined [27, 54, 55].

Simultaneous to the loss of organics is the alteration of the bioapatite mineral, or the inversion stage, between 500 and 1100˚C [2, 56, 57]. With the removal of the organic component at 300˚C, the larger, plate-like crystals can spontaneously grow at the expense of smaller crystals [2, 56-58]. Experiments with bone burnt while powdered and subsequently cleaned with acetone report mean crystallite size increasing to 10 - 30 nm, and crystallite thickness moving from 2 to 9 nm [58, 59]. Above 500˚C, additional growth has been observed, with reported crystallite sizes plateauing at 110 nm and with crystal thickness reaching 10 nm [58]. The crystals, transforming from platelet like to hexagonal, later become equiaxed at 900˚C, growing more spheroidal with overall dimensions reaching 300 - 550 nm [59].

The last stage of heat alteration to bioapatite, fusion, accounts for the microstructural changes noted with the inversion phase above 700˚C [2, 56, 57]. Bone porosity initially increases from the originally porous *in vivo* status with the loss and charring of organics (~300˚C), which also corresponds to a loss in bone density [32, 59]. Carbonized and charred bone is reported to be most porous right before temperatures of calcination (600˚C) [32]. Beginning at 700˚C there is a densification as the bioapatite crystal grains grow, and by 900˚C there is a total structural coalescence from the additional crystal growth, resulting in an interlocking structure and a marked decrease in porosity [2, 58, 59].

These changes are all products of burning in oxidizing conditions [55]. If a bone is brought to temperatures greater than 300˚C without access to oxygen, a different pattern of thermal alteration has been demonstrated in controlled experiments [55]. When heating occurs in reducing atmospheres, the organic char is not removed and instead becomes more ordered [55]. The crystallinity of the bioapatite does increase, however, although at a slower rate than indicated in oxidizing conditions [55]. New compounds, such as cyanamide, are also likely formed around 600˚-700˚C [55]. Bones burnt in reducing atmospheres above 600˚C do not lose the organic char component, and therefore remain black in coloring [55].

Burnt bone diagenesis

The rapid morphological and compositional changes to burnt bone tissue are similar to changes seen over prolonged periods of time in the diagenesis of unburnt bone. This includes the removal of organic components and incorporated water, as well as the recrystallization of the bioapatite crystals. The immediate and greater extent of these changes in bone burnt to both low and high temperatures, however, results in a markedly different biomaterial at time of burial than unburnt bone.

Burnt bone is more fragile than unburnt bone, with fragmentation a function of burning intensity [27]. The dehydration and eventual complete removal of collagen from bone tissue significantly changes the toughness and strength properties of bone, altering the density, the structural integrity, and the stress and strain relationship [27, 60-62]. This ultimately results in a greater likelihood of mechanical fracture correlated to the amount of collagen lost, leaving calcined bone the most mechanically vulnerable [27, 60]. Due to this extreme friability, recovered burnt bone fragments do not reflect initial size at deposition and processes such as burial and trampling can severely and easily fragment burnt bone [27, 63].

The fragility, likely presence of small fragment sizes, and elimination of organic components of bone burnt to lower temperatures provides greater surface area and easy access for diagenetic agents in the context of burial environments. Bone mineral does, however, undergo tremendous crystallite growth and reorganization with burning at higher temperatures, enabling calcined bone to be protected from contamination [54, 58, 64, 65]. Because of this, calcined bone is recognized to be the most reliable source of inorganic C14 for radiocarbon dating, as the elevated crystallinity that accompanies heat alteration at high temperatures protects the Type A and B carbonate substitutions and secondary carbonate incorporated from the burning atmosphere from further alteration, which subsequently can be used to date the burning event [64, 66].

Questions about the changing vulnerabilities of differentially burnt bone prompted our investigations into the characterization of structural changes of modern and archaeological bone burnt at different temperatures. Of specific interest to this study is the timing of the organic loss, and therefore loss of bioapatite protection, in reference to the increases in crystallinity and crystal sizes of bone mineral. Archaeological bone, both unburnt and burnt, is considered in this study as an actualistic reference to relate implications to commonly used zooarchaeological scales of burning intensity, and to monitor the extent of alterations related to the spontaneous postmortem recrystallization of bone mineral which occurs over time in burial environments.

Materials and methods

Modern bone sample collection and preparation

A controlled experimental reference collection was created with modern bone to investigate the timing and impact of thermal alteration on organic loss, recrystallization indices, and crystallite size growth. Cortical bone from three cow femurs and two horse metacarpals from five different individuals were selected for this study. Cow femurs were procured the day after butchery from a local butcher and were never frozen. Flesh was scraped manually to prepare for drilling. Horse metacarpals were obtained postmortem from completed forelimb tissue collections of horses humanely euthanized for purposes other than this study at the UC Davis School of Veterinary Medicine. Metacarpals were simmered in water with the addition of borax to assist with defleshing, although bones remained greasy.

A diamond drill coring bit was used to produce solid plugs of cortical bone 3mm x 3mm, with weights ranging from 53.2 to 58.1 mg. Coring was constrained to the cortical bone tissue from the mid-diaphysis of both cow and horse bones. Solid bone plugs were specifically utilized in lieu of bone powder to avoid the effects of powder heating, as powder has an increased surface area and would be more reactive to thermal alteration. To fit the dimensions of crucibles used for thermal analyses, plugs were filed with diamond files. Post-experimental heating, three samples were selected for imaging with Scanning Electron (SE) microscopy for visualization purposes. All bone samples were then powdered with an agate mortar and pestle and sieved with 234 μm mesh.

Modern bone thermal analysis

The controlled annealing of modern bone samples was performed with Setaram Labsys Evo thermal analyzer. Bone core samples were placed in a 100 µl Al_2O_3 crucible and air flow 40 ml/min was established. The samples were brought to desired temperatures from 100 to 1200°C in 100˚C increments, with heating rate 20˚C /min and held isothermally for 30 minutes. The weight change and heat flow traces were recorded continuously and corrected for the baseline. Additional samples were produced at 300 and 700˚C with ramp 50°C /min and one hour dwell time for comparison.

Archaeological case study sample collection and preparation

Archaeological unburnt and burnt bone samples were collected from the site of Tolbor-17, an open-air locale on a low altitude pass on the western flank of the Khangai Mountains of Northern Mongolia. The Ikh-Tolborin-Gol is part of the Selenga drainage system, the main river feeding Lake Baikal (Fig 1) [67]. This river valley preserves a wealth of Upper Paleolithic (UP) locales including Tolbor-4, Tolbor-15, Tolbor-16, and Tolbor-17 (T-17) [67-70]. Most of the sites document periodic human occupations starting with the Initial Upper Paleolithic, ca. 45 ka, until the Holocene. The latter has recently been dated with polymineral post-IR IRSL, Quartz OSL, and radiocarbon to 42.5-45.6 ka, establishing the timing for a movement of population between the Siberian Altai and Northwestern China, contemporaneous with the earliest *Homo sapiens* fossils in the region [67]. The following occupations in the valley are most likely associated with *Homo sapiens*, and are characterized as Upper Paleolithic (UP) in the broad sense. Although it is often assumed that fire is part of the modern human behavioral repertoire allowing expansion into cold climates, evidence of the use of fire in the UP Tolbor locales is rare and has been only briefly reported [71, 72].

Fig 1. Map of Mongolia with geographic position of Tolbor-17. Map modified after Geo-atlas.

Tolbor-17 provides a rare opportunity to investigate faunal remains, as organic material is usually poorly preserved in the region and burnt fauna has not yet been described in detail. Like most of the other locales, T-17 is an open-air environment with a fluctuating low energy run-off, constituting a fluctuating recharge water regime [24, 44]. Initially excavated as a series of two test pits with dimensions 2 m x 1 m, the excavators at T-17 piece plotted all finds > 2 cm, and the remaining sediment from each bucket volume of excavated material was dry sieved with 4 mm and 2 mm mesh screens, with all material subsequently sorted. The T-17 lithological Unit 3 is characterized by the presence of UP lithic artifacts and organic faunal preservation, despite sedimentary evidence for episodic sheet erosion, prolonged groundwater interaction, chemical weathering, and long surface exposure. Based on its geological setting, the material studied here belongs to the second half of the Marine Isotope Stage (MIS) 3, ca. 40 -30 ka cal. BP and is described as UP. Unburnt and burnt fauna have been successfully recovered from Unit 3; however, this assemblage is extremely fragmentary and traditional zooarchaeological analyses based on taxonomic identification and prey selection and processing are still in the preliminary stages.

Mapped (> 2 cm) and screened (< 2 cm-2 mm) faunal remains from the T-17 UP assemblage were cleaned, sorted following the Stiner et al. [27] seven stage visual scale of burning intensity, and weighed (Table 2). No burning was noted in bone > 2 cm except for a single fragment, but fauna < 2 cm- 2mm recovered in the screened material is found to span all stages of burning intensity within Unit 3 of the exposed excavation surface (Table 2). Of the burnt fauna, a large percentage is nearly or fully calcined, a notable observation due to the recognized mechanical fragility of calcined bone and the unprotected open-air environment of T-17. All excavated fauna was assigned burning stages following Stiner et al. [27] and 20 bones from the same test pit of the Unit 3 assemblage were sub-sampled. A minimum of one category representing bones from this sample were selected for subsequent spectroscopic analyses to confirm heat alteration and investigate organic composition, crystallinity, and crystallite size. Bones were cleaned with ionic water sonication, and two samples representing before and after calcination were selected for imaging with SE microscopy prior to all samples being powdered with a diamond file and an agate mortar and pestle. All archaeological bone powder samples were then sieved with 234 μm mesh. No permits were required for the described study, which complied with all relevant regulations.

Table 2: T17 Unit 3 fauna burning summary.

	Screened (< 2 cm)	Piece plotted (>2 cm)	Total
Burning Stage	Weight (g)	Weight (g)	Weight (g)
0	141.36	213.31	354.47
1	1.04	0	1.04
2	5.17	1.01	6.18
3	0.69	0	0.69
4	1.95	0	1.95
5	1.37	0	1.37
6	4.5	0	4.5

Burning stages following Stiner et al.[27].

Infrared spectroscopy data collection and analysis

FTIR spectroscopy is a semi-quantitative method which characterizes bond vibrations, absorbed at specific wavelengths of transmitted incident light from infrared radiation, to identify compositional and structural properties of materials [54, 73]. When applied to bone, FTIR spectroscopy can yield valuable information regarding the presence and quality of preserved organic components, as well as the relative degree of structural order, size, and strain of bioapatite crystals [74-78]. This is particularly useful for the detection of organic preservation in samples screened prior to radiocarbon and stable isotope studies, and for diagenetic studies evaluating the integrity of bone mineral [77-78].

FTIR spectroscopy has additionally had success identifying thermally altered bone, as changes to bone composition and bioapatite crystallinity can be monitored though several heat induced peak transformations which cannot be mistaken for macroscopic staining or bleaching [4, 33, 53-55, 79, 80]. The identification of FTIR spectral peaks associated with the thermal alteration of bone has been extensively documented, with major alterations monitored through: (1) the ratio of carbonate to phosphate present in the sample, the C/P ratio, (2) the depletion of the presence of amide I and II functional groups, representing the organic components of bone, and (3) the presence of heat specific peak splitting, such as the loss of the peak at 874 cm^{-1} correlated to CO_3^{2-} v2 at temperatures over 1000˚C, and the PHT shoulder peak at temperatures over 700˚C [54, 55, 57, 81-83]. Measures of the crystallinity of a sample can be inferred from the infrared splitting factor (IRSF), which extrapolates the changing size and order of bioapatite crystals through increase of splitting seen in the PO_4^{3-} v4 peaks [54, 57, 81].

Specific peaks relevant to this study and their inferred functional groups include the 1650 cm^{-1} and 1550 cm^{-1} peaks for the measurement of amide I and II, the 874 cm^{-1} and 1415 cm^{-1} peaks indicating presence of the v2 and v3 of carbonate, and the 900-1200 cm^{-1} and 50-600 cm^{-1} spectral regions related to the v3 and v4 phosphate components (Table 3). Additionally, the appearance of a 625cm^{-1} shoulder peak is attributed here to PO_4^{3-} v4 bending, known as the phosphate high temperature (PHT) [57].

Table 3: FTIR-ATR wavenumbers associated with likely functional groups relevant to this study and the thermal alteration of bone.

Wavenumber	Inferred peak assignment	Peak transformation relevant to this study
1630-1660 cm $^{-1}$	organic tissue and water, amide I + II	decrease and absence
1400-1550 cm $^{-1}$	CO_3^{2-} v3	1415 cm^{-1} peak a component of C/P ratio
1028-1100 cm^{-1}	PO_4^{3-} v3	1035 cm $^{-1}$ peak a component of the C/P ratio
874 cm^{-1}	CO_3^{2-} v2	peak loss
565 cm^{-1}, 605 cm^{-1}	PO_4^{3-} v4	growth of 565 cm^{-1} and 605 cm^{-1} and decrease of the 595 cm^{-1} trough utilized for the infrared splitting factor (IRSF); phosphate high temperature (PHT) shoulder growth at 625 cm^{-1}

A Nicolet 6700 Fourier transform infrared spectrometer with an ATR attachment and a deuterated triglycine sulfate (DTGS) detector and single bounce diamond crystal was used. The ATR method uses an attachment with a diamond or zinc crystal to produce spectra through the phenomenon of internal reflectance [84-86]. The application of ATR minimizes sample preparation, which in turn minimizes contamination [73, 82, 84]. Spectra were collected with 256 scans in the 4000 - 400 cm $^{-1}$ frequency region and with an 8 mm spectral range. Each archaeological and modern bone powder sample was retested for quality control.

Eight peak measurements were monitored for 168 scans representing 84 individual samples for this study, 62 modern and 22 archaeological. Each sample was tested twice, and measurements presented here represent the average values of both scans. FTIR-ATR spectra were processed with OMNIC software.

The IRSF measurements were procured for all samples following Weiner and Bar-Yosef [81].

$$\text{Infrared Splittng Factor:} \frac{(565\ \mathrm{cm}^{-1}\ peak\ ht + 605\ \mathrm{cm}^{-1}\ peak\ ht)}{595\ \mathrm{cm}^{-1}\ \ peak\ ht}$$

An additional measure of the carbonate to phosphate content, the C/P ratio, was also determined for all samples. The C/P ratio decreases with burning and utilizes the 1035 cm^{-1} phosphate peak unaffected by IRSF changes [73, 82].

$$\frac{\mathrm{C}}{\mathrm{P}}\ \text{ratio:} \frac{1415\ \mathrm{cm}^{-1}\ peak\ ht}{1035\ \mathrm{cm}^{-1}\ peak\ ht}$$

Other peaks observed for this analysis were noted as they are related to the loss of organics and specific heat-induced changes [54, 55, 57] (Table 3).

X-ray Diffraction

X-ray Diffraction (XRD) can be used to measure the relative sizes of bioapatite crystals [32, 54, 58, 59]. Powder XRD patterns here were obtained using Bruker D2 Phaser and Bruker D8 advance diffractometers using CuKα radiation. Bone powder samples taken from the solid bone plugs and archaeological fauna were spread with ethanol on a zero background silicon sample holder, and run from 10 to 90 °2θ with 0.02° step. Dwell time was chosen to obtain at least thousand counts on the most intense peaks. The average crystallite size of analyzed samples was obtained from diffraction peaks broadening using whole pattern fitting (Rietveld refinement) procedure as implemented in Jade MDI software [87]. Diffraction profile was modeled using hydroxyapatite $Ca_5(PO_4)_3OH$ structure (space group P63/m) and pseudo-Voigt profile shape function. The instrumental broadening was accounted for by calibration with NIST LaB_6 profile shape standard. The uncertainties in crystallite sizes are reported as obtained from least squares refinement.

Results

FTIR modern samples

The FTIR-ATR spectra were obtained for each sample, 25-1200˚C. All modern samples above 200˚C were found to exhibit spectra indicative of the thermal alteration of bone in oxygen atmospheres supported by previous research (Figs 2 and 3), including the decrease of C/P ratio, decrease of organic components by 300˚C with complete absence seen by 400˚C, the absence the 874 cm^{-1} peak above 1000˚C, and the presence of the PHT peak splitting above 700˚C (S1 Table, S2 Table). No differences were indicated in the reheated or increased rate samples taken to 300 and 700˚C from the single-heated or controlled rate counterparts.

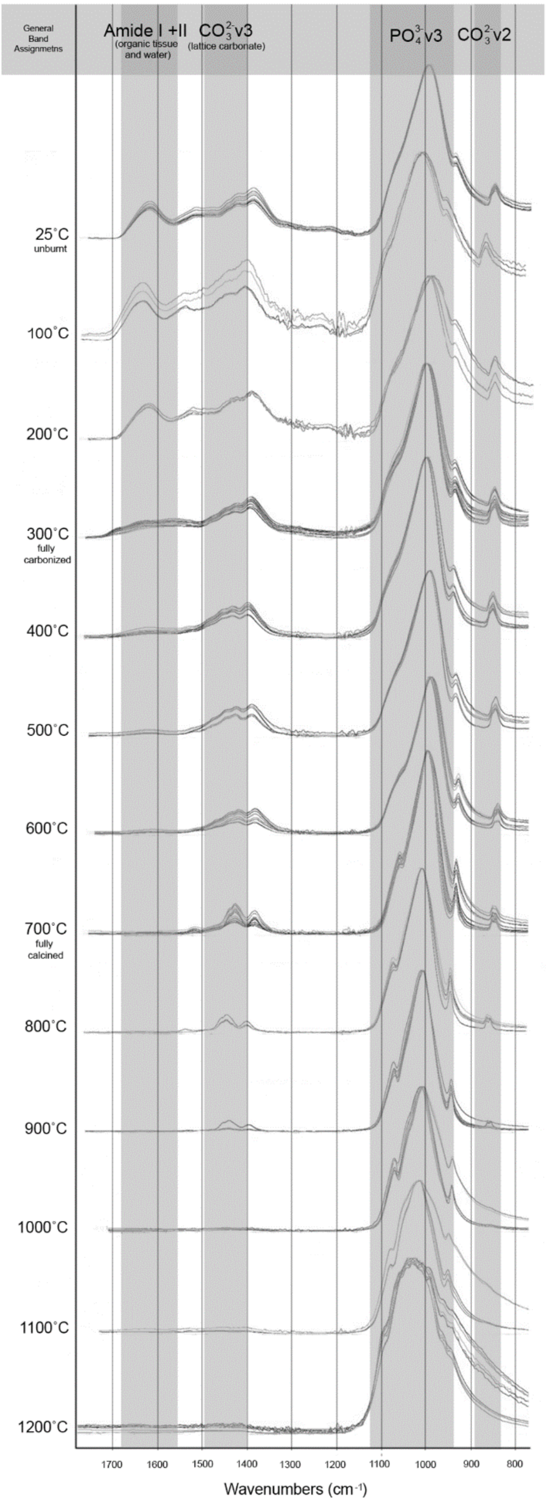

Fig 2. FTIR-ATR spectra of experimentally modern burnt samples grouped by with functional groups highlighted in the range of 1700-800 cm^{-1}.

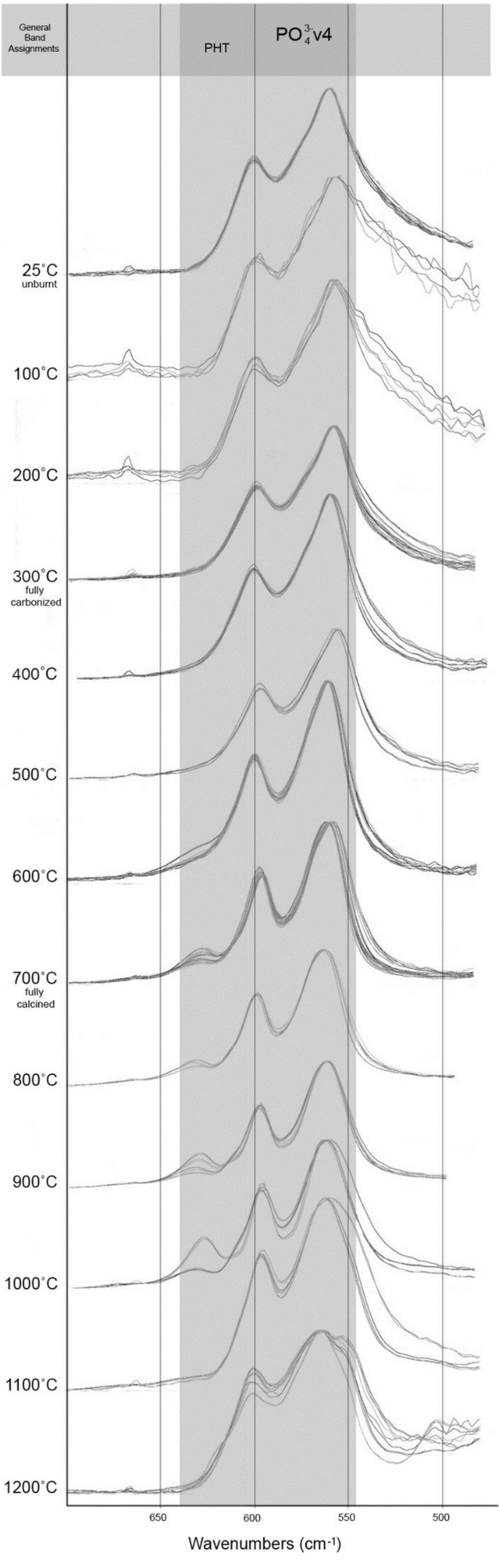
General Band Assignments
PHT
PO_4^{3-}v4
25°C unburnt
100°C
200°C
300°C fully carbonized
400°C
500°C
600°C
700°C fully calcined
800°C
900°C
1000°C
1100°C
1200°C
650
600
550
500
Wavenumbers (cm-1)

Fig 3. FTIR-ATR spectra of experimentally modern burnt samples with functional groups highlighted in the range of 700-500 cm^{-1}.

The IRSF of all modern samples also followed reported trends in bioapatite crystallinity, with order, size and strain increasing alongside intensifying temperatures and clearly demonstrated with the presence of calcination (Figs 2, 3, 4; Appendix A Tables 1 and 2) [54, 56]. This increase in crystallinity is seen until 1000˚C, after which there is a marked decrease in IRSF coinciding with the equiaxing of bioapatite crystals (Fig 4). Despite the acceptance of the IRSF metric and general consensus with previously described trends, the values of modern IRSF here do exhibit large variations [54, 56]. This is seen most dramatically in the range of IRSF values reported for all samples at 900˚C in this study (Fig 4; S2 Table). No changes in crystallinity were detected in samples which were reheated or heated with increased rates.

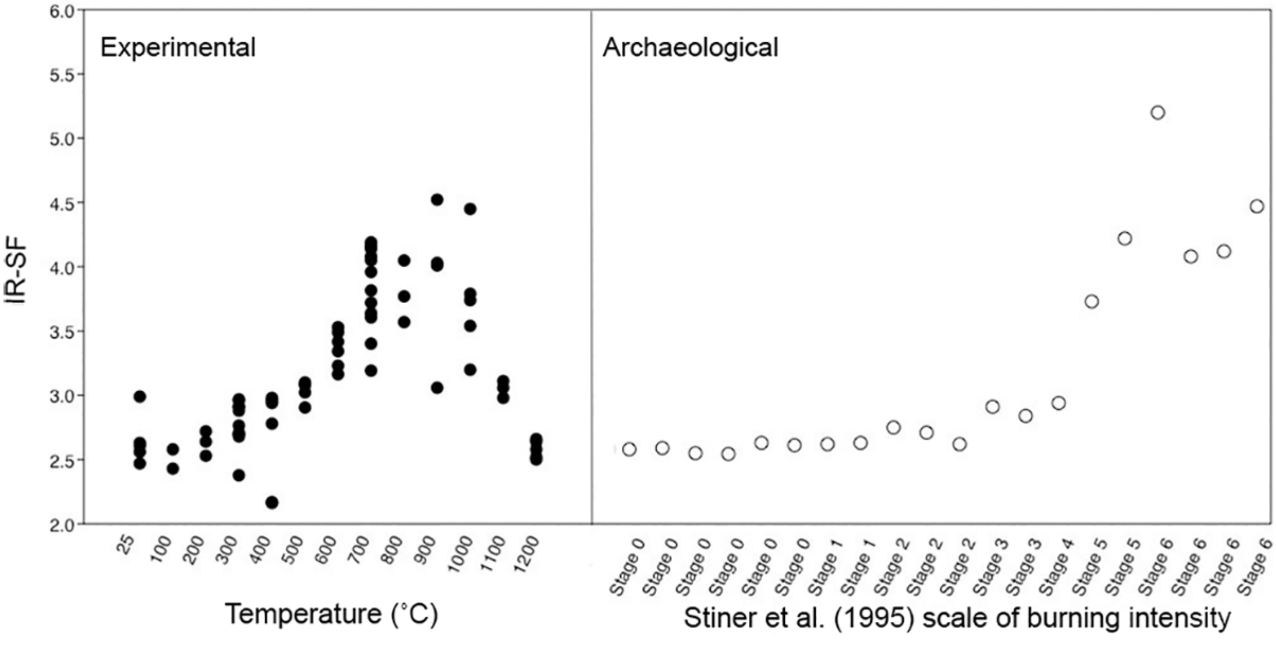

Fig 4. Infrared Splitting Factor (IRSF) of the experimental modern and archaeological collection measured from FTIR-ATR spectra following Weiner and Bar Yosef [81].

FTIR archaeological samples

The FTIR-ATR spectra produced from the T-17 archaeological collection is consistent with the Stiner et al. [27] stages of temperature intensity assignments based on color alteration. Unburnt bone is supported as non-heat altered and burnt bone does not indicate signs of intrusive staining or bleaching (Figs 5 and 6). Good agreement is seen with the relative decreases of C/P ratio and the loss of organic components by Stage 3 (fully carbonized) between the archaeological and modern samples (Figs 5 and 6; Appendix A tables 3 and 4). The appearance of the PHT with bones identified as Stage 5 supports the presence of temperatures above 700˚C at T-17, although the continued presence of CO_3^{2-} v2 inferred by the 874 cm^{-1} peak indicates temperatures likely did not reach above 1000˚C (Figs 5 and 6; S3 Table).

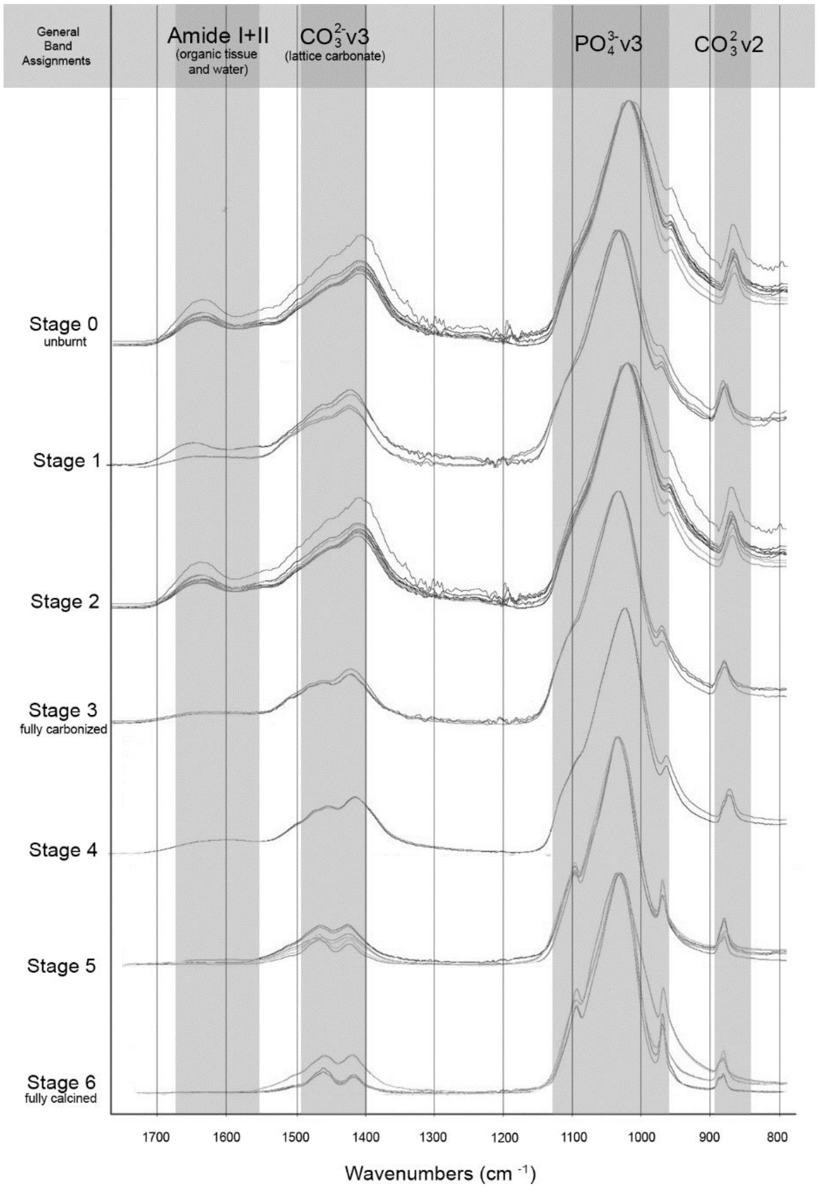

Fig 5. FTIR-ATR spectra of archaeological fauna from T-17 grouped by stage of burning intensity following Stiner et al. [27] with functional groups highlighted in the range of 1700-800 cm^{-1}.

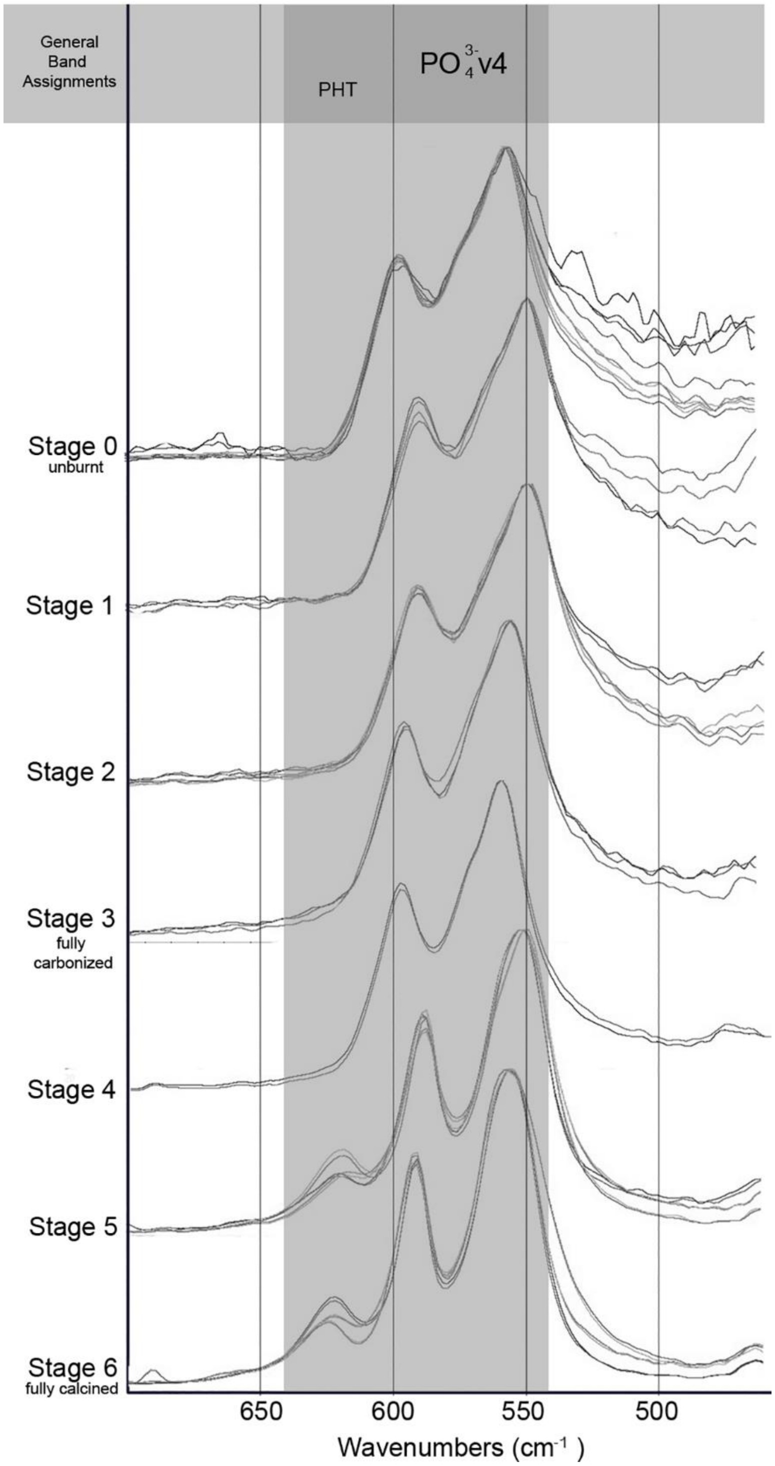

Fig 6. FTIR-ATR spectra of archaeological fauna from T-17 grouped by stage of burning intensity following Stiner et al. [27] with functional groups highlighted in the range of 700-500 cm^{-1}.

The IRSF of the T-17 samples also follows the trends of the experimental modern collection, with gradual increases seen through Stage 3 (fully carbonized) and demonstrably higher values reported with the presence of calcination at Stages 4, 5, and 6 (Fig 4; Appendix A tables 3 and 4). Elevated values are not seen within the Stage 0 unburnt samples of T-17 bone, demonstrating that the spontaneous recrystallization of bone mineral that accompanies diagenesis does not exceed here values of modern or archaeological samples which have been burnt at low or high temperatures. As expected, the IRSF values can distinguish between calcined and non-calcined samples but cannot distinguish between low temperature burning samples.

XRD modern samples

The results of the XRD analyses on the modern samples demonstrate the increasing crystallite size correlated to temperature, specifically above temperatures of calcination (700˚C) (Fig 7; Appendix A table 2). An average size threshold is clearly noted, with all samples unburnt through 600˚C averaging 9 nm, while all samples burnt at 700˚C jump to an average of 41 nm (Fig 7). An additional increase in crystallite size by approximately 30 nm is noted at 900˚C, coinciding with the fusion stage of thermal alteration of bone, with samples reaching an average of 72 nm (Fig 7). The XRD results also demonstrate that within fully calcined samples, corresponding to Stiner et al. [27] burning scale Stage 6, two temperature thresholds can be distinguished: the maximum crystal size of calcined bone >700˚C not exceeding 70 nm, and the maximum crystal size of calcined bone >900-1200˚ C exceeding 90 nm (Fig 7). This study therefore suggests average crystallite size as a metric to distinguish temperatures obtained within calcined bone classified as Stiner et al. Stage 6, > 700˚C and > 900˚C.

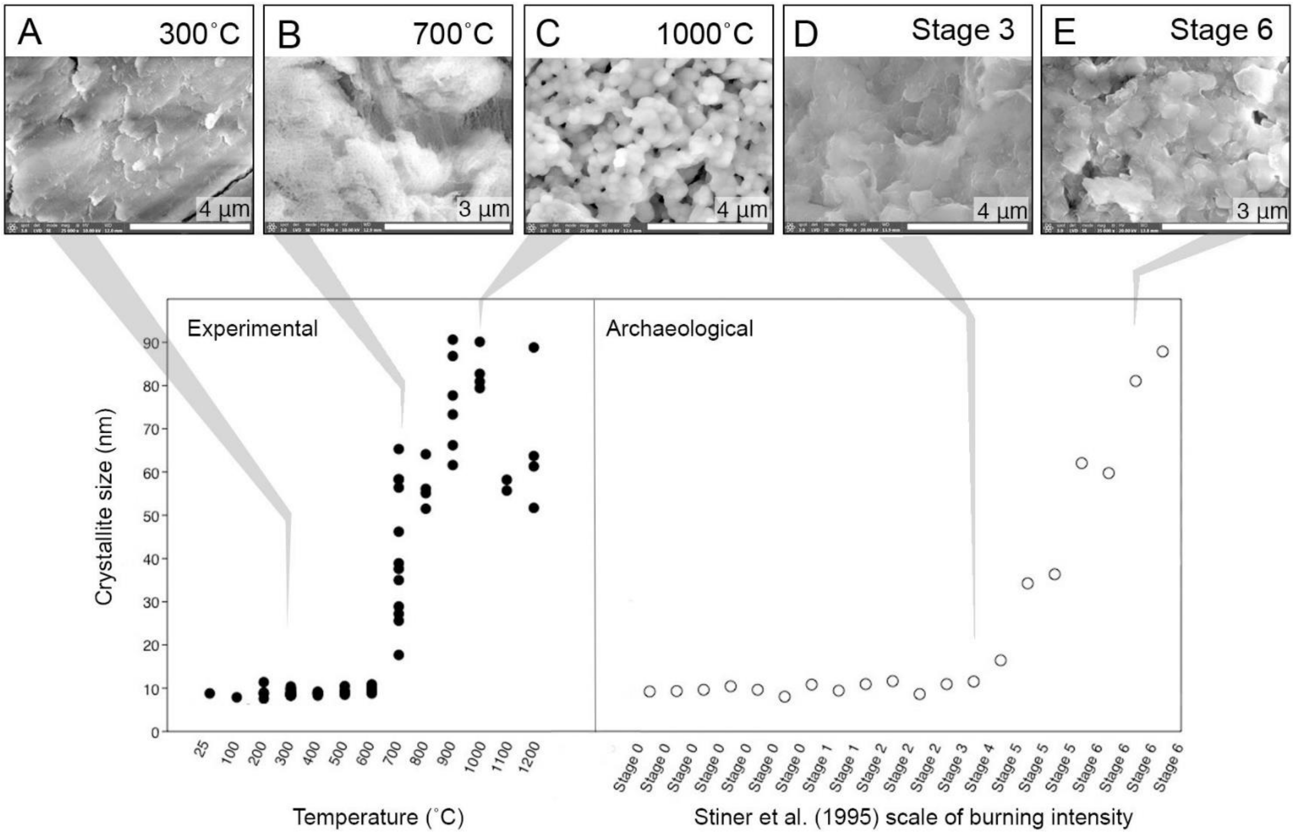

Fig 7. XRD results of averaged crystallite size (nm) alongside selected SE images of experimental modern (A-C) and archaeological (D-E) bone to visualize the changes to crystal shape with heat alteration. Images A and D highlight the small, platelike shape of bioapatite burned to at least 300˚C. Images B and C, both modern, demonstrate morphological range of bones burnt above 700˚C, both of which are fully calcined and are considered Stage 6 on the Stiner et al. [27] scale of burning intensity. The initial growth of hexagonal crystals ~700˚C (B) and eventual equaixing and further growth of crystals above 900˚C (C) are clearly seen in images B and C, and when compared to the archaeological sample of a fully calcined Stage 6 bone (E), the bioapatite crystal morphology corresponds to the size and shape of experimental bones burned above 900˚C. Magnification and instrument details described in S1 Appendix.

XRD archaeological samples

The average crystallite size measurements for the archaeological T-17 bioapatite samples confirm that the natural postmortem recrystallization of unburnt archaeological bone does not exceed crystal sizes of modern or archaeological bones burnt to low temperatures. The crystallite sizes do increase considerably with the presence of calcination at Stiner et al. [27] Stages 4, 5, and 6 and can be distinguished from lower temperature burning and unburnt bone (Fig 7; Appendix A table 4). Utilizing the metric of crystal size, we also suggest that for two of the archaeological samples of Stage 6 fully calcined bone there is evidence of burning > 900˚C - <1100˚C.

Discussion

The measurements presented here regarding the loss of organics, the degree of crystallinity, and the crystallite sizes are in consensus with trends reported by previous studies, with small variance likely introduced by the burning of solid bone versus powdered samples and different experimental sample preparation and burning regimes. Our results demonstrate that for bone burnt to lower temperatures before calcination, Stiner et al. [27] Stages 1-3, bioapatite retains the small reactive crystal sizes of unburnt bone but faces rapid organic loss. The depletion of the organic component is most complete just prior to temperatures of calcination (~700˚C). This disintegration of the collagen in charred or carbonized bone is recognized to produce a very open porosity, leaving bone mineral burnt highly exposed [58].

The increase in crystallinity and crystal size growth seen by 700˚C corresponding to calcination and Stiner et al., [27] Stages 4-6 immediately reduces the surface to mass ratio and active surface area of bone mineral. This lower surface area results in a product with a lower solubility potential than unburnt and charred or carbonized bone. For fully calcined Stage 6 bones which have also been exposed to temperatures above 900˚C in oxygen atmospheres, there is the additional benefit of reported compaction and closing of the porosity, further limiting the access of any destructive agents to the exposed crystallites [58]. The heat induced dimensional changes are also considerably larger than the small amounts of diagenetic recrystallization which assists with the prevention of contamination in fresh bone, as evidenced by the inclusion of unburnt archaeological samples

Diagenetic agents such as water dissolution are therefore inferred here to be a serious threat to bone burnt to temperatures under 700˚C, because partially and wholly carbonized and charred burnt bone has low levels of crystallinity and small crystals which preserve a reactive surface area similar to unburnt fresh bone at the time of deposition. The additional lack of organic protection, open porosity, and likely small fragment sizes due to the recognized friability of burnt bones calls attention to the further vulnerability of charred and carbonized fauna in Stiner et al. [27] Stages 1-3 due to bioapatite dissolution and disintegration. Correspondingly, the lack of organic presence in burnt bones, especially bones corresponding to Stiner et al. [27] Stages 3-6 is interpreted here to be a less attractive target for the diagenetic agent of microbial action than fresh and fleshed unburnt bone.

The results of this study propose a hypothesis of differential survivorship in bones burnt to different temperature thresholds in assemblages of archaeological fauna with fluctuating water movement. This study would further suggest that bones with low density and high porosity, such as trabecular and juvenile bone, are further susceptible to dissolution if charred or carbonized. This is due to the assumption that open porosities, likely small fragment sizes, and no organic protection exacerbates the access of diagenetic agents such as fluctuating water to their small and reactive crystals.

Bone which has been calcined, including trabecular and juvenile bone, potentially has a greater likelihood to resist dissolution due to the large crystal sizes and greater thermodynamic stability. These properties have been similarly recognized to contribute to the suitability of calcined bone for inorganic C14 dating analyses [64]. Calcined bone has been shown to be more mechanically fragile than both unburnt and charred or carbonized bone, however, and traumatic action including post-depositional movement and trampling can be highly destructive. Calcined bone therefore may be expected to preserve well in a variety of depositional environments, albeit in small fragment sizes recoverable only through screening.

Further work on the nature of burning and a full zooarchaeological profile of T-17 Unit 3 can test the hypothesis of differential survivorship, as the open-air site does have sedimentary evidence of active and fluctuating water movement. Preliminary faunal analyses indicate that there is a very low presence of bone in the Stiner et al. [27] 1-3 stages, but calcined bone identified as Stage 6 is recovered in comparatively considerable amounts (Table 2). Future work considering archaeological assemblages of burnt bone as proxies for natural and anthropogenic fire therefore should consider biases that may influence the differential survivorship of burnt bone, as properties of burnt bone vary widely between burning thresholds.

Conclusion

The spectroscopic measurements reported here encompass a large reference collection of burning in highly controlled conditions 100-1200˚C in fresh solid bone cores, extending previous modern and archaeological datasets that consider the structural and compositional changes to burnt bone. Especially of note is the average crystallite size difference between bone burnt above 700˚C, a metric which may be used to distinguish different burning temperatures within fully calcined archaeological bone, which are all considered as Stiner et al. [27] Stage 6.

Our results highlight the vulnerability of charred and carbonized bone to diagenetic agents and generate hypotheses regarding the differential survivorship of bone burnt to different temperatures. Here the nature of the hydrological environment is proposed to be a significant threat to bone burnt to low temperatures, as water fluctuation is a large factor in fresh bone bioapatite dissolution and charred and carbonized bone has similar bone mineral properties but has had organic protection already eliminated prior to burial.

This study reiterates the importance of small bone fragments in the study of ancient fire, observations also noted in previous studies [27,88]. Excluding the screened faunal material from T-17 would have obscured the presence of fire almost entirely, as all burnt bone except for a single fragment was recovered in the screened fraction likely due to the friability of burnt bone. The identification and recognition of further biases in addition to the mechanical fragility of burnt bone, and the variation within bones burnt to different temperatures, is emphasized here as burnt bone exhibits a range of structural and thermodynamic properties across zooarchaeological scales of visible burning intensity.

While burnt bone can provide valuable and detailed information on the properties of ancient fire relevant to behaviors of interest, the presence of fire which used fuel with low burning temperatures, such as grass, and from environments with fluctuating water interaction may not have surviving faunal evidence. Therefore, future studies should consider potential differential survivorship in archaeological assemblages of burnt bone, the impact of biased survivorship, and therefore the visibility of burnt fauna.

Acknowledgements

The authors would like to thank Dr. Teresa Steele for her continued feedback and illuminating discussions, and Cody Prang and Chris Gallo for their many helpful explanations. We additionally thank Drs. Eerkens, Darwent, and Parikh for their generosity and lab resources, as well as the patience, assistance, and expertise of the Peter A. Rock Thermochemistry Laboratory, NEAT research group, and the Parikh Environmental Soil Chemistry Group at the University California Davis. The authors also recognize the support given from the UC Davis Veterinary Medical Teaching Hospital, the UC Davis JD Wheat Veterinary Orthopedic Laboratory, the UC Davis AMCaT Laboratory, the UC Davis DHI Transdisciplinary Research Cluster “The Cluster for Archaeology and Soil Synergy”, the Prehistory department of Universit*é* Liège, and the Center for Experimental Archaeology at UC Davis (CEAD).

References

1. Mentzer, S. M., Romano, D. G., & Voyatzis, M. E. (2017). Micromorphological contributions to the study of ritual behavior at the ash altar to Zeus on Mt. Lykaion, Greece. *Archaeological and Anthropological Sciences*, *9*(6), 1017-1043.
2. Thompson T. Recent advances in the study of burned bone and their implications for forensic anthropology. Forensic Science International. 2004;146:S203–5.
3. Ubelaker DH. The forensic evaluation of burned skeletal remains: A synthesis. Forensic Science International. 2009 Jan;183(1–3):1–5.
4. Iriarte, E., García-Tojal, J., Santana, J., Jorge-Villar, S. E., Teira, L., Muñiz, J., & Ibañez, J. J. (2020). Geochemical and spectroscopic approach to the characterization of earliest cremated human bones from the Levant (PPNB of Kharaysin, Jordan). *Journal of Archaeological Science: Reports, 30*, 102211.
5. Costamagno S, Théry-Parisot I, Brugal J-P, Guibert R. Taphonomic consequences of the use of bones as fuel. Experimental data and archaeological applications. In: Biosphere to lithosphere: new studies in vertebrate taphonomy. Oxbow Books Oxford; 2005. p. 51–62.
6. Morin E. Taphonomic implications of the use of bone as fuel. Palethnologie. 2010;2:209-17.
7. Théry-Parisot I. Fuel management (bone and wood) during the Lower Aurignacian in the Pataud rock shelter (Lower Palaeolithic, Les Eyzies de Tayac, Dordogne, France). Contribution of experimentation. Journal of Archaeological Science. 2002;29(12):1415–21.
8. Schiegl S, Goldberg P, Pfretzschner H-U, Conard NJ. Paleolithic burnt bone horizons from the Swabian Jura: Distinguishing between in situ fireplaces and dumping areas. Geoarchaeology. 2003;18(5):541–65.
9. Costamagno S, Théry-Parisot I, Castel JC, Brugal JP. Combustible ou non? Analyse multifactorielle et modèles explicatifs sur des ossements brûlés paléolithiques. *Geston des combustibles au Paléolithique et au Mésolithique: nouveaux outils, nouvelles interpretations*. 2009:61
10. Speth J, Clark J. Hunting and overhunting in the Levantine Late Middle Palaeolithic. Before Farming. 2006 Jan;2006(3):1–42.

11. Barkai R, Rosell J, Blasco R, Gopher A. Fire for a reason: Barbecue at middle Pleistocene Qesem cave, Israel. Current Anthropology. 2017 Aug 1;58(S16):S314-28.
12. Turner-Walker G. The Chemical and Microbial Degradation of Bones and Teeth. In: Pinhasi R, Mays S, editors. Advances in Human Palaeopathology [Internet]. Chichester, UK: John Wiley & Sons, Ltd; 2007:3–29.
13. Binford LR, Bertram JB. Bone frequencies and attritional processes. In (LR Binford, Ed.) For Theory Building in Archaeology. 1977.
14. Lyman RL. Bone density and differential survivorship of fossil classes. Journal of Anthropological archaeology. 1984;3(4):259–99.
15. Grayson DK. Bone transport, bone destruction, and reverse utility curves. Journal of Archaeological Science. 1989 Nov 1;16(6):643–52.
16. Outram AK. A new approach to identifying bone marrow and grease exploitation: why the “indeterminate” fragments should not be ignored. Journal of archaeological science. 2001;28(4):401–10.

17. Munson PJ, Garniewicz RC. Age-mediated survivorship of ungulate mandibles and teeth in canid-ravaged faunal assemblages. Journal of Archaeological Science. 2003;30(4):405–16.
18. Robinson S, Nicholson RA, Pollard AM, O’Connor TP. An Evaluation of Nitrogen Porosimetry as a Technique for Predicting Taphonomic Durability in Animal Bone. Journal of Archaeological Science. 2003 Apr;30(4):391–403.
19. Von Endt DW, Ortner DJ. Experimental effects of bone size and temperature on bone diagenesis. Journal of Archaeological Science. 1984 May;11(3):247–53.
20. Lam YM, Chen X, Pearson OM. Intertaxonomic variability in patterns of bone density and the differential representation of bovid, cervid, and equid elements in the archaeological record. American Antiquity. 1999;64(2):343–62.
21. Lyman RL. Vertebrate taphonomy. Cambridge University Press; 1994.
22. Nielsen-Marsh CM, Hedges REM. Patterns of Diagenesis in Bone I: The Effects of Site Environments. Journal of Archaeological Science. 2000 Dec;27(12):1139–50.
23. Nielsen-Marsh CM, Smith CI, Jans MME, Nord A, Kars H, Collins MJ. Bone diagenesis in the European Holocene II: taphonomic and environmental considerations. Journal of Archaeological Science. 2007 Sep;34(9):1523–31.
24. Nielsen-Marsh C, Gernaey A, Turner-Walker G, Hedges R, Pike A, Collins M. The chemical degradation of bone. Human Osteology in archaeology and forensic science. 2000: 439-454.
25. Denys C. Taphonomy and experimentation. Archaeometry. 2002 Aug;44(3):469–84.
26. Maurer A-F, Person A, Tütken T, Amblard-Pison S, Ségalen L. Bone diagenesis in arid environments: An intra-skeletal approach. Palaeogeography, Palaeoclimatology, Palaeoecology. 2014 Dec;416:17–29.
27. Stiner MC, Kuhn SL, Weiner S, Bar-Yosef O. Differential Burning, Recrystallization, and Fragmentation of Archaeological Bone. Journal of Archaeological Science. 1995 Mar;22(2):223–37.
28. Martin RB, Burr DB, Sharkey NA, Fyhrie DP. Skeletal tissue mechanics. Second edition. New York: Springer; 2015. 762 p.
29. Stout SD, Cole ME, Agnew AM. Histomorphology. In: Ortner’s Identification of Pathological Conditions in Human Skeletal Remains [Internet]. Elsevier; 2019 [cited 2019 Oct 20]. p. 91–167.
30. Rollin-Martinet S, Navrotsky A, Champion E, Grossin D, Drouet C. Thermodynamic basis for evolution of apatite in calcified tissues. American Mineralogist. 2013 Nov 1;98(11–12):2037–45.
31. Drouet C, Aufray M, Rollin-Martinet S, Vandecandelaère N, Grossin D, Rossignol F, et al. Nanocrystalline apatites: The fundamental role of water. American Mineralogist. 2018 Apr 1;103(4):550–64.
32. Figueiredo M, Fernando A, Martins G, Freitas J, Judas F, Figueiredo H. Effect of the calcination temperature on the composition and microstructure of hydroxyapatite derived from human and animal bone. Ceramics International. 2010 Dec;36(8):2383–93
33. Greiner M, Rodríguez-Navarro A, Heinig MF, Mayer K, Kocsis B, Göhring A, et al. Bone incineration: An experimental study on mineral structure, colour and crystalline state. Journal of Archaeological Science: Reports. 2019;25:507–18.
34. Rey C, Combes C, Drouet C, Glimcher MJ. Bone mineral: update on chemical composition and structure. Osteoporos Int. 2009 Jun;20(6):1013–21.

35. Bala Y, Farlay D, Boivin G. Bone mineralization: from tissue to crystal in normal and pathological contexts. Osteoporos Int. 2013 Aug;24(8):2153–66.
36. Berna F, Matthews A, Weiner S. Solubilities of bone mineral from archaeological sites: the recrystallization window. Journal of archaeological Science. 2004 Jul 1;31(7):867-82.
37. Nyman JS, Ni Q, Nicolella DP, Wang X. Measurements of mobile and bound water by nuclear magnetic resonance correlate with mechanical properties of bone. Bone. 2008;42(1):193–9.
38. Trueman CN, Privat K, Field J. Why do crystallinity values fail to predict the extent of diagenetic alteration of bone mineral? Palaeogeography, Palaeoclimatology, Palaeoecology. 2008 Sep;266(3–4):160–7.
39. Koeppenkastrop D, Eric H. Sorption of rare-earth elements from seawater onto synthetic mineral particles: An experimental approach. Chemical geology. 1992;95(3–4):251–63.
40. Reynard B, Lécuyer C, Grandjean P. Crystal-chemical controls on rare-earth element concentrations in fossil biogenic apatites and implications for paleoenvironmental reconstructions. Chemical Geology. 1999;155(3–4):233–41.
41. Buikstra JE, Swegle M. Bone modification due to burning: experimental evidence. Bone modification. 1989;247–58.
42. Tripp JA, Squire ME, Hedges REM, Stevens RE. Use of micro-computed tomography imaging and porosity measurements as indicators of collagen preservation in archaeological bone. Palaeogeography, Palaeoclimatology, Palaeoecology. 2018 Dec;511:462–71.
43. Smith CI, Nielsen-Marsh CM, Jans MME, Collins MJ. Bone diagenesis in the European Holocene I: patterns and mechanisms. Journal of Archaeological Science. 2007;34(9):1485–93.
44. Hedges REM, Millard AR. Bones and Groundwater: Towards the Modelling of Diagenetic Processes. Journal of Archaeological Science. 1995 Mar;22(2):155–64.
45. Hedges REM. Bone diagenesis: an overview of processes. Archaeometry. 2002 Aug;44(3):319–28.
46. Wescott, D. J. (2019). Postmortem change in bone biomechanical properties: Loss of plasticity. *Forensic science international*, *300*, 164-169.
47. Trueman CN, Behrensmeyer AK, Potts R, Tuross N. High-resolution records of location and stratigraphic provenance from the rare earth element composition of fossil bones. Geochimica et Cosmochimica Acta. 2006 Sep;70(17):4343–55.
48. Baig AA. Influences of carbonate content and crystallinity on the solubility behavior of synthetic and biological apatites. Department of Pharmaceutics and Pharmaceutical Chemistry, University of Utah; 1997.
49. Baig AA, Fox JL, Wang Z, Higuchi WI, Miller SC, Barry AM, et al. Metastable Equilibrium Solubility Behavior of Bone Mineral. Calcified Tissue International. 1999 Apr 1;64(4):329–39.
50. Trueman, C. N., & Tuross, N. (2002). Trace elements in recent and fossil bone apatite. *Reviews in mineralogy and geochemistry*, *48*(1), 489-521.
51. Pfretzschner H-U. Fossilization of Haversian bone in aquatic environments. Comptes Rendus Palevol. 2004 Oct;3(6–7):605–16.
52. Shipman P, Foster G, Schoeninger M. Burnt bones and teeth: an experimental study of color, morphology, crystal structure and shrinkage. Journal of Archaeological Science. 1984 Jul;11(4):307–25.

53. Thompson T, Ulgium, P. Burned Human Remains. In Handbook of Forensic Anthropology and Archaeology. Routledge. 2016: 295-303.
54. Ellingham STD, Thompson TJU, Islam M, Taylor G. Estimating temperature exposure of burnt bone — A methodological review. Science & Justice. 2015 May;55(3):181–8.
55. Reidsma FH, van Hoesel A, van Os BJH, Megens L, Braadbaart F. Charred bone: Physical and chemical changes during laboratory simulated heating under reducing conditions and its relevance for the study of fire use in archaeology. Journal of Archaeological Science: Reports. 2016 Dec;10:282–92.
56. Thompson TJU. The Analysis of Heat-Induced Crystallinity Change in Bone. In: The Analysis of Burned Human Remains. Elsevier; 2015. p. 323–37.
57. Thompson TJU, Islam M, Bonniere M. A new statistical approach for determining the crystallinity of heat-altered bone mineral from FTIR spectra. Journal of Archaeological Science. 2013 Jan;40(1):416–22.
58. Etok SE, Valsami-Jones E, Wess TJ, Hiller JC, Maxwell CA, Rogers KD, et al. Structural and chemical changes of thermally treated bone apatite. J Mater Sci. 2007 Sep 21;42(23):9807–16.
59. Pramanik S, Hanif A, Pingguan-Murphy B, Abu Osman N. Morphological Change of Heat Treated Bovine Bone: A Comparative Study. Materials. 2013. Dec 21;6(1):65–75.
60. Waterhouse, K. (2013). The effect of weather conditions on burnt bone fragmentation. *Journal of forensic and legal medicine*, *20*(5), 489-495.
61. Herrmann, N. P., & Bennett, J. L. (1999). The differentiation of traumatic and heat-related fractures in burned bone. *Journal of Forensic Science*, *44*(3), 461-469.
62. Wang, X., Bank, R. A., TeKoppele, J. M., Hubbard, G. B., Althanasiou, K. A., & Agrawal, C. M. (2000). Effect of collagen denaturation on the toughness of bone. *Clinical Orthopaedics and Related Research®*, *371*, 228-239.
63. McKinley, J. I. (1994). Bone fragment size in British cremation burials and its implications for pyre technology and ritual. *Journal of Archaeological Science*, *21*(3), 339-342.
64. Lanting, J. N., Aerts-Bijma, A. T., & van der Plicht, J. (2001). Dating of cremated bones. *Radiocarbon*, *43*(2A), 249-254.
65. Major, I., Dani, J., Kiss, V., Melis, E., Patay, R., Szabó, G., ... & Jull, T. A. (2018). Adoption and evaluation of a sample pretreatment protocol for radiocarbon dating of cremated bones at HEKAL. *Radiocarbon*.
66. Zazzo, A., & Saliège, J. F. (2011). Radiocarbon dating of biological apatites: a review. *Palaeogeography, Palaeoclimatology, Palaeoecology*, *310*(1-2), 52-61.

67. Zwyns N, Paine CH, Tsedendorj B, Talamo S, Fitzsimmons KE, Gantumur A, et al. The Northern Route for Human dispersal in Central and Northeast Asia: New evidence from the site of Tolbor-16, Mongolia. Sci Rep. 2019 Dec;9(1):11759.
68. Zwyns N, Gladyshev SA, Gunchinsuren B, Bolorbat T, Flas D, Dogandžić T, et al. The open-air site of Tolbor 16 (Northern Mongolia): Preliminary results and perspectives. Quaternary International. 2014 Oct;347:53–65.
69. Gladyshev SA, Olsen JW, Tabarev AV, Jull AJT. The Upper Paleolithic of Mongolia: Recent finds and new perspectives. Quaternary International. 2012 Dec;281:36–46.
70. Tabarev A., Gunchinsuren .B, Gillam J., Gladyshev S., Dogandžić T., Zwyns N. Kompleks Pamiatnikov Kamennogo Veka v Doline r.Ikh Tulberiin-Gol, Severnaya Mongolia (razvedochnye raboty s ispolzovaniem GIS-Technnologii v. 2011 g) [The

Stone Age site complex in the Ikh-Tulberiin-Gol River Valley, North Mongolia (survey and research using GIS-technology in 2011)]. Studia Archaeologica Instituti Archaeologici Academiae Scientiarum Mongolicae. 2012;32:26–43

71. Gowlett JAJ. The early settlement of northern Europe: Fire history in the context of climate change and the social brain. Comptes Rendus Palevol. 2006 Jan;5(1–2):299–310.
72. Rybin EP, Khatsenovich AM, Gunchinsuren B, Olsen JW, Zwyns N. The impact of the LGM on the development of the Upper Paleolithic in Mongolia. Quaternary International. 2016 Dec;425:69–87.
73. Beasley MM, Bartelink EJ, Taylor L, Miller RM. Comparison of transmission FTIR, ATR, and DRIFT spectra: implications for assessment of bone bioapatite diagenesis. Journal of Archaeological Science. 2014 Jun;46:16–22.
74. Lebon, M., Zazzo, A., & Reiche, I. (2014). Screening in situ bone and teeth preservation by ATR-FTIR mapping. *Palaeogeography, Palaeoclimatology, Palaeoecology*, *416*, 110-119.
75. Lebon, M., Reiche, I., Gallet, X., Bellot-Gurlet, L., & Zazzo, A. (2016). Rapid quantification of bone collagen content by ATR-FTIR spectroscopy. *Radiocarbon*, *58*(1), 131.
76. Trueman, C. N., Behrensmeyer, A. K., Tuross, N., & Weiner, S. (2004). Mineralogical and compositional changes in bones exposed on soil surfaces in Amboseli National Park, Kenya: diagenetic mechanisms and the role of sediment pore fluids. *Journal of Archaeological Science*, *31*(6), 721-739.
77. Dal Sasso, G., Asscher, Y., Angelini, I., Nodari, L., & Artioli, G. (2018). A universal curve of apatite crystallinity for the assessment of bone integrity and preservation. *Scientific reports*, *8*(1), 1-13.
78. Gianfrate, G., D'Elia, M., Quarta, G., Giotta, L., Valli, L., & Calcagnile, L. (2007). Qualitative application based on IR spectroscopy for bone sample quality control in radiocarbon dating. *Nuclear Instruments and Methods in Physics Research Section B: Beam Interactions with Materials and Atoms*, *259*(1), 316-319.
79. Lebon, M., Reiche, I., Fröhlich, F., Bahain, J. J., & Falguères, C. (2008). Characterization of archaeological burnt bones: contribution of a new analytical protocol based on derivative FTIR spectroscopy and curve fitting of the ν 1 ν 3 PO 4 domain. *Analytical and Bioanalytical Chemistry*, *392*(7-8), 1479-1488.
80. Snoeck, C., Lee-Thorp, J. A., & Schulting, R. J. (2014). From bone to ash: Compositional and structural changes in burned modern and archaeological bone. *Palaeogeography, palaeoclimatology, palaeoecology*, *416*, 55-68.
81. Weiner S, Bar-Yosef O. States of preservation of bones from prehistoric sites in the Near East: A survey. Journal of Archaeological Science. 1990 Mar;17(2):187–96.
82. Thompson TJU, Gauthier M, Islam M. The application of a new method of Fourier Transform Infrared Spectroscopy to the analysis of burned bone. Journal of Archaeological Science. 2009 Mar;36(3):910–4.
83. Paschalis EP, DiCarlo E, Betts F, Sherman P, Mendelsohn R, Boskey AL. FTIR microspectroscopic analysis of human osteonal bone. Calcified tissue international. 1996 Dec 1;59(6):480-7.
84. Hollund HI, Ariese F, Fernandes R, Jans MME, Kars H. Testing an alternative high-throughput tool for investigating bone diagenesis: FTIR in attenuated total reflection

(ATR) mode: An alternative tool for investigating bone diagenesis. Archaeometry. 2013 Jun;55(3):507–32.

85. Nakamoto K. Infrared and Raman Spectra of Inorganic and Coordination Compounds (Part A: Theory and Applications in Inorganic Chemistry)(Volume 1A)(Part B: Applications in Coordination, Organometallic, and Bioinorganic Chemistry)(Volume 1B). NY, John Wiley & Sons, Incorporated; 1997
86. Bruno TJ. Sampling Accessories for Infrared Spectrometry. Applied Spectroscopy Reviews. 1999 Jul 20;34(1–2):91–120.
87. Rietveld H. A profile refinement method for nuclear and magnetic structures. Journal of applied Crystallography. 1969 Jun 2;2(2):65-71.
88. Villa P, Castel JC, Beauval C, Bourdillat V, Goldberg P. Human and carnivore sites in the European Middle and Upper Paleolithic: similarities and differences in bone modification and fragmentation. Revue de paléobiologie. 2004;23(2):705-30.

Chapter 3

Long durations and low temperatures: detection of prolonged heating in experimentally burnt bone exposed to air

Abstract

Pyrotechnology is an important lens into behaviors relevant for our understanding of ancient economic and social lifeways. Heating duration is one aspect of fire use and maintenance that is linked to combustion feature function but has low archaeological visibility. In this present study we test the utility of archaeological bone to recognize long duration thermal alteration. Fresh, modern bovid cortical bone cores were heated exposed to air at 300°, 550°, and 750°C in a sequence of experimental trials in a Nabertherm muffle furnace for periods of 10 minutes, 9 hours, and 48 hours, plus an extensive cooling period on heat retaining sediments (gravel or gravel compacted with fine quartz sand) to mirror the smoldering and extinguishing of anthropogenic and ethnographic fire events. After heating, bone cores were analyzed with a RM200 CAPSURE Color Matching tool, Fourier-Transform Infrared Spectroscopy (FTIR) with Attenuated Total Reflectance (ATR) attachment, and X-Ray Diffraction (XRD) to provide information on bioapatite crystallinity and the structural and compositional changes attributed to different temperature thresholds. Results indicate that bone can be an appropriate proxy to detect long durations and that coloration, a primary characteristic utilized by zooarchaeologists to record information about burning intensity, is not an exclusive indicator of moderate to high temperatures but may also result from long duration heating.

Introduction

Background

Ethnoarchaeological documentation of fire use in modern hunting and gathering societies has highlighted duration as a distinguishing factor between different functional roles of fire (Mallol et al. 2007; Mallol and Henry 2017). In observations of use of fire by living hunter gatherer populations, duration of a fire event was noted to be a central component of activities such as meat curing and hide smoking, as well as situation dependent activities such as hunting fires or long-lasting communally maintained cooking fires (Mallol et al. 2007; Mallol and Henry 2017).

Duration of fire activity is therefore a valuable characteristic for reconstructing ancient fire use practices such as the duration of stay, site function, and group size. This dimension of hominin fire use and maintenance has remained difficult to document, however, despite the applicability and intersection with recent research investigating hominin behaviors transmitted from archaeological combustion features. This includes the use of fuel and fuel economies (Albert et al. 2012; Henry 2017; Henry et al. 2018; Thery-Parisot 2002; Thery-Parisot and Henry 2012; Vidal-Matutano et al. 2017; Schiegl et al 2003), spatial and social organization (Alperson-Afil and Goren-Inbar 2010; Barkai et al. 2017; Blasco et al. 2016; Goldberg et al. 2012; Shahack-Gross et al. 2014; Vallverdu et al. 2012; Wadley et al., 2020), technological variability (Leierer et al. 2020; Mallol et al. 2013) and the specific properties of light and heat that may be used to modify tools, food, and the environment (Abdohlazadeh et al. 2022; Hoare 2020; Kozowyk et al. 2017; Revedin et al. 2020; Schmidt et al. 2019; for review, see Stahlschmidt et al. 2020).

In instances of determining and interpreting evidence for anthropogenic control of fire (hominin management of a local fire via fuel control), use of fire (hominin use of fire or fire altered materials naturally occurring in the landscape), or non-anthropogenic wildfire, knowledge of duration times can assist with identifying the burnt residues that are likely the result of natural causes (Buenger, 2003; Goldberg et al. 2017; Gowlett et al., 2017; Sandgathe 2017; Stahlschmidt et al., 2022). Natural wildfires are common and integral to many ecosystems and vary in intensity in relation to biome, climate, and vegetation (Scott 2009). Excluding peat fires, they are also documented to be ephemeral and fast-moving (Table 1; Bellomo 1993; David 1990; Gowlett et al., 2017; Payne et al., 1996; Santana et al. 2013; Scott 2000; Stinson and Wright, 1969; Whelan 1995). Therefore, detection of fire events with durations spatially constrained and exceeding 3 hours can indicate likely anthropogenic fire curation (Table 1).

This study uses bone tissue as a proxy for fire properties, as thermal alteration results in permanent changes to bone structure and chemistry which many be measured both in experimental and archaeological settings. Burnt archaeological fauna therefore are representative of conditions in past extinguished fire events and provide insight into hominin behaviors of interest. We performed a set of experimental trials in a laboratory setting heating bone at different durations (10 minutes, 9 hours, 48 hours) at controlled temperatures (300°, 550°, 750°C) to monitor changes to mammalian (bovid) cortical bone cores to take into consideration both time and temperature dependent changes. Macroscopic visible color was recorded with an RM200 CAPSURE Color Matching tool and spectroscopic instruments Fourier-Transform Infrared Spectroscopy (FTIR) with Attenuated Total Reflectance (ATR) attachment and X-Ray Diffraction (XRD) provided information on the micro- and nanoscopic properties. Results from these experimental trials suggest that bone is an appropriate tool to detect long duration archaeological fire through integrated visual and spectroscopic analyses and can be used by archaeologists to study burnt faunal assemblages to extrapolate new dimensions of fire using behaviors in the past.

Citation	**Environment/Biome**	**Burning substrate**	**Duration time**	**Temperature**
Bellomo 1993	Lowland forest, savanna (Virunga National Park, Zaire); Semi-desert (Sibiloi National Park, Kenya); Temperate grasslands and mixed forest (Illinois)	Grass fire of *Themeda triandra* or *Imperata cylindrica* (n=6) Stump fire *of Acacia cybouriora* (n=6)	2 minutes 2-3 hours	225°-100° C 250°-200° C
David, 1990	Australian bushfire	Grass	20-30 seconds of flaming combustion followed by minutes of smoldering	450-500°C
Gowlett et al. 2017	East and South African bushfires	Grass	< 30 minutes	Variable based on burned substrate and organic material, 200°-800° C
Pyne et al. 1996		Soil hummus and peat		300°- 600° C
Santana et al. 2013	Mediterranean Basin	Mediterranean hardwood surface fire (Heat-stimulated germination by obligate seeders *Ulex parviflorus, Cistus albidus, Rosmarinus officinalis*)	40-50 min from beginning until completely extinguished*	~80°-100° C at 1cm depth in sediment**

Scott 2000		Surface fire (shrubby, herbaceous plants, and litter of recently dead plats and decayed plant accumulations)	Not stated, implied to be ephemeral	< 350° C
		Peat fire (soil hummus, peat, decaying vegetations)	Hours- days	<350° C
Stinson and Wright 1969	Prairie	Prairie Grass	Duration of temps in excess of 65° c is between 1-10 min	700° C
		Tree stumps		200-250° C
Whelen 1995	Grassland, shrubland			200°-300° C (light to moderate fires); 500°-600° C (heavy fires)
Wright and Bailey 1982		Piled logs and slash	40 min	1430° c max, sustained 800 °C
**Personal communication with author* ***Authors note that they believe this is less severe in duration and temperature than natural conditions*				

Table 1: Reported details (biomes, temperatures, and duration) of observed and experimental natural wildfires

Burnt bone properties as a proxy for archaeological fire

Patterns in visible color changes of heated bone are widely recognized, with many scholars noting that a sequence of color gradients can be connected broadly to different intensities of burning and heating, i.e. carbonized/charred and calcined (Tables 3-5; Costamagno and Thery-Parisot, 2005; Costamagno et al., 2009; Ellingham et al. 2015; Shipman et al. 1984; Stiner et al. 1995). Observations of these macroscopic color changes have established widely used zooarchaeological scales of heating, such as the Stiner et al. (1995) scale which utilizes macroscopic cues of color and mechanical properties to indicate >/< 50% charred and >/< 50% calcined (Table 4). Studies which report and investigate heating through zooarchaeological methods often utilize these scales and similar schema to categorize the variability within an assemblage to provide information about fire using behaviors, such as Tellez et al. (2022)'s investigation into incidental burning of the Middle Paleolithic faunal assemblage Qa of Abric Romani (Spain) and Costamagno and Thery-Parisot's (2005) classifications for constructing a combustion index to discern bone burned as fuel.

Color code	Description
0	Not burned bone
1	Bone with unburned zones
2	Carbonized bone, mainly black
3	Bone mainly gray
4	Calcined bone, mainly white

Table 2: Modified Costamagno and Thery-Parisot (2005) heating scale with associated description.

Scale	Description	Reported associated coloration *
0	Not burnt	Yellow-white
1	Slightly burnt, < 50% carbonized	< 50 % dark brown/ dark grey/ reddish-brown
2	Majority burnt, > 50% carbonized	> 50% dark brown/ dark grey/ reddish-brown
3	Fully carbonized	Dark brown/ dark grey/ reddish-brown
4	Slightly highly burnt, < 50% calcined	< 50% grey/ grey-blue/ white
5	Majority highly burnt, > 50% calcined	> 50% grey/ grey-blue/ white
6	Fully calcined	White/ light grey/ grey-blue patches
**Snoeck et al. 2014*		

Table 3: Modified Stiner et al. (1995) burning scale with associated generalized coloration for recognition.

Scale	Temperature	Reported texture	Reported associated coloration
Stage I	20°- <185° C	Normal bone texture	Neutral white/ pale yellow/ yellow
Stage II	185°- <285° C	Bone surface more irregular, small granular asperities appear	Reddish brown/ very dark grey-brown/ neutral dark grey/ reddish yellow

Stage III	285°- <440° C	Bone surface becomes glassy, polygonal cracking pattern develops in subchondral bone. Plates are formed by cracks between vascular canals with their edges sharply demarcated.	Neutral black/ medium blue
Stage IV	440° - <800° C	Bone surface becomes highly particulate and turns frothy	Neutral white/ light blue-grey
Stage V	800°- <940° C	Particles melt and coalesce into larger structures	Neutral white/ medium grey/ reddish-yellow

Table 4: Modified Shipman et al. (1984) scale of burning and heating in bone tissue with associated generalized colorations reported for recognition.

Living bone itself is comprised of the inorganic mineral bioapatite, organic proteins primarily of collagen, and water (Martin et al. 2015; Stout et al. 2019). Bone is porous, to a large extent for facilitation of Haversian systems, with trabecular bone exhibiting a higher porosity due to a more open structure (Figueiredo et al. 2010; Lyman, 1994; Stout et al. 2019). Bioapatite crystallites *in vivo* are characterized by a hydrated, large surface area (above 200 m^{2}g) necessary for the regulation of homeostasis (Berna et al. 2004; Buikstra and Swegle 1989; Drouet et al. 2018; Koeppenkastrop 1992; Martin et al. 2015; Reynard et al. 1999; Rollin-Martinet et al. 2013; Trueman et al. 2008; Ubelaker, 2009), and small, plate-like morphologies (1-7 nm thick, 15-200 nm in length, 10-80 nm in width) which are cross-linked to the organic collagen fibrils (Bala et al. 2013; Berna et al. 2004; Gallo et al. 2021; Rey et al. 2009). Water is integrated into and around the organic and mineral components but also found in void spaces and in the extracellular matrix (Drouet et al. 2018; Nyman et al. 2008).

Bone is a sensitive proxy for analyzing natural and anthropogenic fire due to the irreversible changes that occur with thermal alteration. Macroscopic properties influenced by heat include changes to fragment size, friability, texture, and mass at different temperature thresholds (Buikstra and Swegle 1989; Ellingham et al. 2015; Stiner et al. 1995; Shipman et al. 1984; Thompson 2004; Zazzo et al. 2009). These transformations are intricately linked to the chemical and structural organization of the mineral, organic, and water content of bone. While these changes are similar to modifications which occur during normal bone diagenesis, heat induced transformations are often more exaggerated in the extent and amount of alterations (Gallo et al. 2021). The degree of alteration, material properties, and chemistry of burnt bone are also related to the specific conditions under which the bone was burnt, including maximum temperatures and burning atmosphere (Ellingham et al. 2015; Gallo et al. 2021; Reidsma et al. 2016; Snoeck et al., 2014; Snoeck et al., 2016; Van Hoesel et al. 2019).

Studies have documented these specific primary structural and chemical changes to bone heated at different temperatures, including the rate of organic loss, alterations in porosity, the presence of different compounds reflective of burning atmosphere, and mineral bioapatite recrystallization and crystallite size growth (Ellingham et al., 2015; Gallo et al., 2021; Reidsma et al. 2016; Van Hoesel et al. 2019). High resolution spectroscopic analyses such as FTIR-ATR and XRD can directly monitor these transformations to verify true burning, rather than staining, and elucidate maximum temperature thresholds and different burning atmospheric conditions (Ellingham et al. 2015; Piga et al. 2008; Shahack-Gross et al. 1997; Snoeck et al. 2016; Thompson, 2004).

Four major overlapping and interconnected stages of heating which broadly describe the transformations to the mineral, organic, and water components are well documented with macroscopic, microscopic, and spectroscopic studies for bone burnt and heated in oxygen atmospheres (Ellingham et al., 2015; Mayne Correia, 1997; Thompson 2004). Combustion (heating in the presence of oxygen) is here distinguished from charring (heating without the presence of oxygen), as bones undergoing thermal alteration in full reduction atmospheres experience different changes which do not overlap neatly with their oxygenated counterparts

(Reidsma et al., 2016; Van Hoesel et al. 2019). For bones burnt and heated with access to oxygen, stage 1, dehydration (100°-600°C), describes the evaporation of the water content of bone from within and between the organic and mineral components environments (Ellingham et al., 2015; Mayne Correia 1997; Thompson 2004). Stage 2, decomposition (300°-800°C) details the combusting and depletion of the organic portion (Ellingham et al., 2015; Mayne Correia, 1997; Thompson 2004). Bone at this stage of burning loses a great deal of mass and has the highest degree of porosity, as the organic and water components have been removed and the bioapatite minerals remain small and flat (Figueriedo et al. 2010; Gallo et al. 2021; Pramanik et al. 2012). Stage 3, inversion (500°-1100°C), describes the loss of structural carbonates and Stage 4, fusion (>700°, estimated to be closer to 900°-1000°C) accounts for the coalescing of the remaining inorganic component (Ellingham et al., 2015; Mamede et al., 2018; Mayne Correia 1997; Thompson 2005). Bone which has undergone the fusion stage experiences tremendous growth in shape and size of bioapatite minerals which additionally decreases porosity and produces a more crystalline structure (for review, see Ellingham et al. 2015; Gallo et al. 2021; Mamede et al., 2018).

Calcination applied to burnt bone is a categorization broadly identified by white or grey coloration, due to the removal of the combusted and charred organics, but further describes micro- and nanoscopic transformations to the bone material which occur alongside the stages of burning previously outlined. Many structural and chemical changes occur during this process, including replacement of carbonates with hydroxyl groups and, even before the large-scale coalescence of the fusion stage, bioapatite growth (Etok et al., 2007; Mamede et al., 2018; Piga et al., 2016). This crystallite growth is very similar to growth seen as a part of diagenetic processes (Ostwald's ripening) as crystallites reach more stable phases with a more ordered structure (i.e. become more crystalline) (Dal Sasso et al., 2018; Hedges, 2002). The growth that accompanies high temperatures can become intense than typical diagenetic alteration, however, as bioapatite grows to fill spaces left after both the removal of the water and organic phases and there are less distortions on the crystal lattice after the removal of structural carbonates (Dal Sasso et al., 2018; Gallo et al., 2021; Mamede et al., 2018). Calcined bone for the purpose of this study is therefore defined as the light coloration from the elimination of the combusted and charred organic components (Ellingham et al. 2015; Ramirez-Gutierrez et al. 2017) but also the rapid transformation of the mineral phase with high temperature exposure: loss of structural carbonates, shifting vibrational frequencies of the bone mineral reflecting differing chemical compositions, and a high order of crystallinity indicating more ordered crystals and a low lattice strain (Ellingham et al, 2015; Mamede et al., 2018; Marques et al., 2016).

The reported temperatures under which bones are calcined varies, likely due to different experimental variables including the initial status of bone sampled and method of measurement (Table 5; Ravaglioli et al., 1996; Snoeck et al. 2014).

Reported temperatures of calcination	Citation
600°C	Lanting et al., 2001; Naysmith et al. 2007
625°C	Person et al., 1996
650°C	Stiner et al., 1995
>700°C *	Ellingham et al. 2015; Thompson 1999, 2005
725°C	Van Strydonck et al., 2009
800°C *	Shipman et al. (1984)
**Discussed in terms of bioapatite coalescence or the start of fusion stages*	

Table 5: Sample of reported temperatures of bone calcination, modified from Snoeck et al. 2014

The connections between burning stages and visible color are most clearly seen in reference to the state of organic decomposition, as the dark coloration (dark brown or black) of burnt bone reflects the charred or carbonized organic content (Reidsma et al., 2016; Snoeck et al., 2014). Dark brown and black surface colorations can also be indicative of staining (e.g. mineral manganese, soil, or wood tannins) and not indicative of burning (Pollock et al., 2018; Shahack-Gross et al., 1997; Turner et al., 2018). Removal of organic components similar to calcination which also resulting in white bone can occur with prolonged exposure to UV radiation, known as sun bleaching (Dupras and Schultz, 2013). It is only with consideration of other heat related variables and characteristics measured with visible and spectroscopic methods, such as weight, surface texture, warping, and bioapatite crystal sizes, crystallinity, and other bone mineral transformations that burnt and heated bone can be securely distinguished.

Detection of duration prior studies

Previous studies addressing the thermal alteration of bone have not specifically evaluated the impact of duration. Prior experiments have indeed incorporated a range of duration times to highlight different questions of temperature intensity (Ellingham et al., 2016; Gallo et al. 2021; Reidsma et al. 2016; Shipman et al. 1984; Snoeck et al., 2014; Van Hoesel et al. 2019), burial environments (Bennett 1999, Herman and Bennett 1999; Stiner et al. 1995), carbon exchange (Snoeck and Schulting, 2013; Snoeck et al., 2014) and burning atmospheres (Reidsma et al. 2016; Van Hoesel et al. 2019; Table 6). Methodologies which incorporate different duration times all under three hours have reported that time length of heat exposure has little impact on the transformations to bone mineral at different temperatures (Ellingham et al., 2016; Gallo et al., 2021). These results are difficult to compare with experiments with duration times which exceed 3 hours at any temperature, as many of these studies have rarely included spectroscopic data to provide insight into micro- and nanoscale properties and alterations (Bennett, 1999). This pattern is likely due to the relatively recent advancements in spectroscopic analyses for archaeological application, and because of the difficulty of sustaining prolonged heating experiments at high temperatures (Table 6).

Discrepancies found between the different studies, such as the reports of calcination from underground burning experiments in Bennett (1999) but not Stiner et al. (1995), may be explained by considering the impact of length of the heat exposure and the initial status of the bone components (i.e., fresh or weathered, powdered or solid) at time of the experiment (Bennett, 1999; Ramirez-Gutierrez et al., 2017; Stiner et al., 1995). Variance in reported visible bone colors in prior experiments, therefore, are potentially a response to the depletion of organics achieved through duration of heating and unrelated specifically to the temperature induced chemical and structural changes. Additional factors which must be considered and vary between studies include fragment size and thickness, degree of flesh covering, and differences within and between species (Snoeck et al., 2014).

An advantage in utilizing FTIR-ATR is that spectra characterizing the vibrations of bonds within the sample reflecting heat and diagenesis induced changes can be produced with minimal sample preparation (Beasley et al. 2014; Dal Sasso et al. 2018; Ellingham et al. 2015, 2016; Gallo et al. 2021; Gianfrate et al. 2007; Lebon et al. 2014; Lebon et al. 2016). These spectra provide semi-quantitative measures of bone composition that reflect structural and chemical changes induced by heat, such as specific peaks representing new chemical compounds and peak changes that correspond to higher degrees of crystallinity due to increasing bioapatite mineral order, size, and strain (Ellingham et al., 2015; Gallo et al., 2021; Mamede et al., 2018; Snoeck et al., 2014; Weiner and Bar Yosef, 1990). XRD spectra can also provide complementary information on the relative sizes of the bioapatite crystallites which experience tremendous physiochemical transformation and growth at temperatures > 650°C, generating the higher degree of crystallinity (Ellingham et al. 2015; Etok et al. 2007; Figueiredo et al. 2010; Gallo et al. 2021; Pramanik et al. 2013; Ramirez-Gutierrez et al. 2017).

For this present study, macroscopic and spectroscopic data were collected to create a standardized comparative collection to better understand the dual impact of time and heat exposure on bones heated to different durations and temperature intensities. Our experimental design specifically aims to address the potential applicability of burnt fauna, here cortical tissue of mammalian bone, as a proxy for ancient fire using behaviors of long duration times. Many scales of analyses are considered here to reflect the practical methodologies utilized by zooarchaeologists when studying assemblages and to present practical discipline specific recommendations for spectroscopically sampling burnt fauna.

Citation	**Bone material**	**Temperature (°C)**	**Substrate/Instrument**	**Duration**	**Spectroscopic data reported**	**Atmosphere**
Bennett 1999	Modern weathered white tail deer; Middle Late Archaic archaeological white tail deer	Maximum Sand 408°C; Maximum clay 506°C	Buried in sediment (screened and compacted reddish-grey clayey-silt, fine grained sand) at 5, 10, 15, 20, 25 cm	48 hour with cooling period (84 hours monitored in total)	No	Oxygen
Ellingham et al., 2016	Modern sheep ribs (defleshed and one set retaining the abdominal wall with subcutaneous fat and skin)	100°-1100°C in 100° steps	Vectra electric muffle furnace	15, 45, 90 minutes	Yes	Oxygen
Gallo et al., 2021	Cortical bone of modern, fresh adult horse metapodials (mechanically defleshed and cleaned with simmering water and borax, air dried) and fresh adult bovid femurs (mechanically	100°-1200°C in 100° steps	Setram Labsys Evo Thermal Analyzer	30 min- 1 hr held at temperature in addition to cooling period	Yes	Oxygen

	defleshed, rinsed, air dried)					
Hermann and Bennett 1999	Fresh pig femurs	700-800° C	House	2 hour 30 minute	No	Oxygen
Reidsma et al., 2016	Cortical bone of fresh adult cow femur (mechanically defleshed, rinsed, air dried)	200°, 250°, 300°, 340,° 370°, 400°, 450°, 500°, 600°, 700°, 800°, 900°C	Carbolite tube oven	1 hour held at temperature; 24 hour cool period	Yes	Reduction
Shipman et al., 1984	Mandibles and astragali of goats and sheep	185°, 285°, 360°, 440°, 525°, 645°, 675°, 745°, 800°, 870°, 940°C	Norman test kiln	4 hours	No	Oxygen
Snoeck et al., 2014	Modern samples Cow tibia (muffle furnace) Joints of cow, pig, lamb, chicken (pyre)	Muffle furnace 500°-900°C, Pyre 600°-900°C	Muffle furnace Outdoor pyre	30 min to 24 hour	Yes	Oxygen
Stiner et al., 1999	Modern goat and cow (deceased > 3 months, still greasy) and archaeological material	900°-1000°C	Limestone surface, 6 kg local Mediterranean hardwood	Morning to evening, coals allowed to smolder overnight	Yes	Oxygen
Van Hoesel et al., 2019	Cortical bone of fresh adult bovid femur (mechanically defleshed, rinsed, air dried)	200°, 300°, 350°, 400°, 500°, 600°, 700°, 800°C	Gas powered muffle furnace	1 hour held at temperature in addition to cooling period	Yes	Oxygen

Table 6: Reported details for a selection faunal burning experiments

Materials and Methods

Sample Preparation and Experimental Trials

Cortical bone of cattle (*Bos taurus*) femurs, humeri, and radii were obtained from a local butcher (Fleischerei Engeln, Leipzig, Germany) to be utilized in this study. At time of purchase the bones segments were never frozen, and criteria for bone selection included the present bone availability and freshness. Bones were procured at several times so that samples for this study for a maximum of three days after purchase to preserve fresh cortical bone mechanical properties, and trial order was determined by this time limitation (Zhang et al. 2018). Bones were stored prior to experimental trials in saline solution at 5° C. Each bone prepared was given a unique identifying label (A-L, Appendix B table 1).

Domesticated cattle long bones were mechanically scraped of remaining flesh and periosteum and the diaphysis portions were cored utilizing a PROXXON Rotary Tool MICROMOT 60/EF drill with a Dremel 663 ¼ inch Diamond grit drill bit (Appendix B Fig 1; Appendix B table 1). Resulting solid cortical bone core diameters were approximately 4mm, and length measurements varied between 2 and 7mm, with an average of 3.92mm (n= 240; Fig 1). Bone cores of this dimension were selected to both be standardized and to be homogenously heated, as larger bone fragments potentially would exhibit differential heating signatures. Bone cores were stored wrapped in saline (NaCl .9%) soaked gauze to maintain a hydrated state following removal of the periosteum and refrigerated at temperatures around 4°C (Zhang et al. 2018). Bone segments for each trial were selected as to not be from the same element (e.g. both segments from the same left femur), but potentially could represent different elements of the same living animal (e.g. the left and right femur of the same animal).

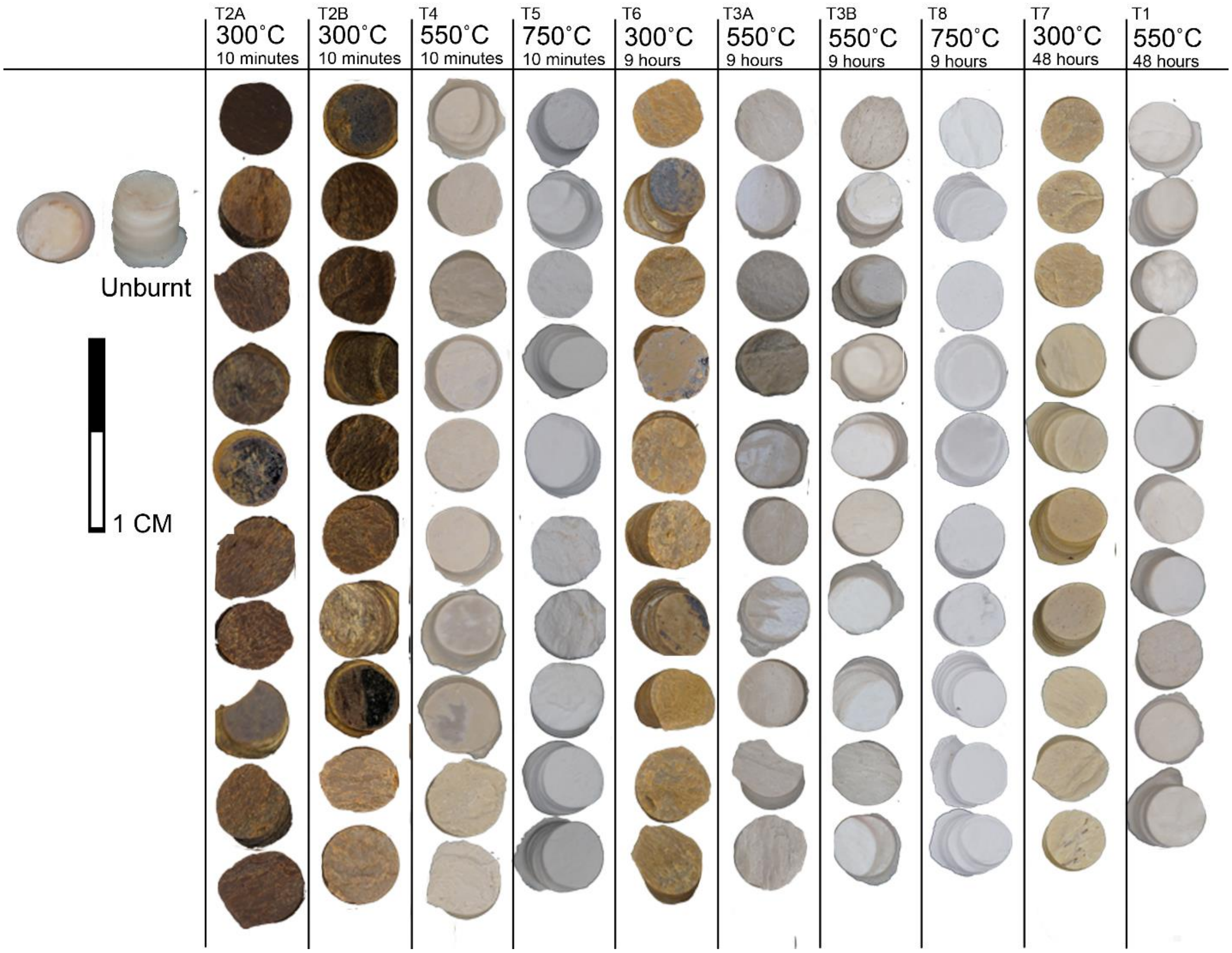

Fig 1: Sample of bone cores including unburnt (pre-heating) and all duration trials (T1-T8), organized by time length (10 minutes, 9 hours, and 48 hours). Note the stark color difference between the 10 minute duration period and bones heated at same temperatures but for 9 and 48 hours. Bones heated below the temperature of calcination (300° and 550°C) but for the elongated period show a striking color resemblance to those calcined at 750°C at any duration.

For each trial cores from three different bone segments (labeled A-L) were utilized in each crucible with the intention of randomizing variables related to the animal raw material outside of direct experimental control (Appendix B table 1). Each of the three bone cores were placed with approximately 1 cm distance from each other in consistent placements relative to labeling information on the crucible surface for later identification (Fig 2). For six of the trials a layer of bone samples were also buried -2 cm under the surface of the substrate (Table 7). Ceramic crucibles were 8 cm in maximum diameter and were filled either with substrates of loosely packed gravel (2-4 mm) or compacted gravel with fine quartz sand (1/8 – 1/4 mm) to emulate sediments with different heat retention properties (Fig 2; Table 7).

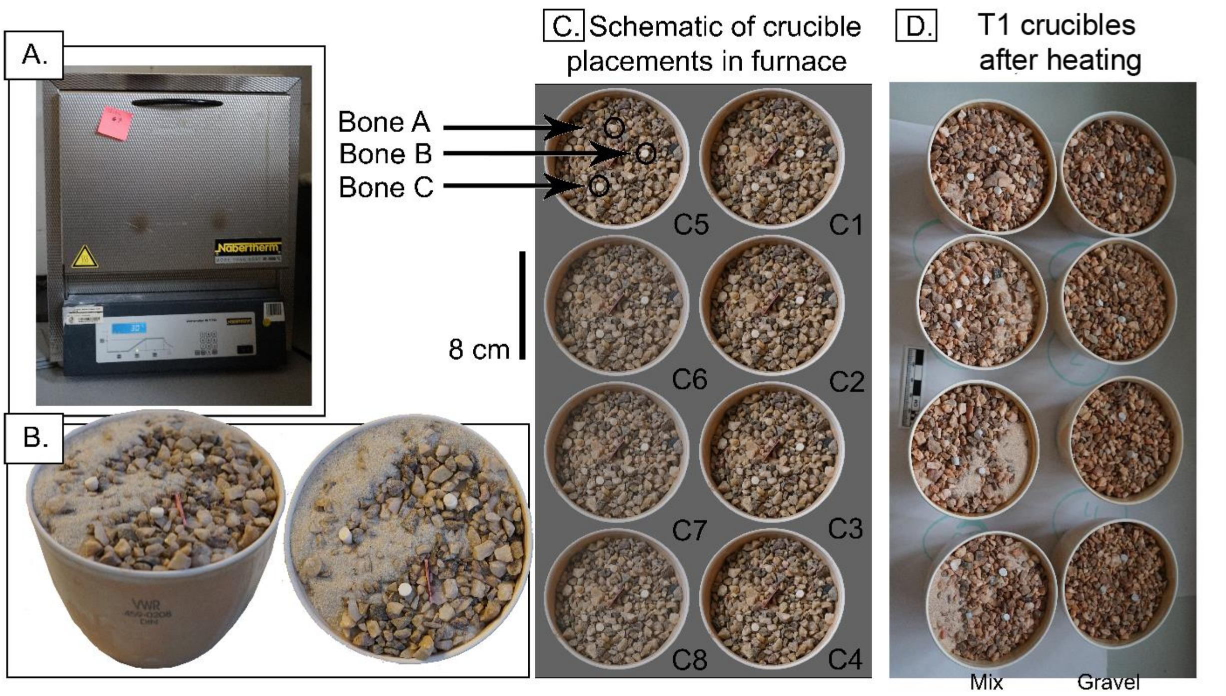

Fig 2. Muffle furnace and crucible set up: A) Nabertherm muffle furnace, B) crucible of gravel and fine quartz sand, crucible label visible which was used to orient samples, C) schematic of numbered crucible placements in muffle furnace. Crucibles 6, 7, and 8 only utilized for T1 (550°C, 48 hours). Bone cores (e.g. Bones A-C) arranged in sequential order in a triangle formation relative to visible crucible label. D) Crucibles from TI (550°C, 48 hours) in cooling period after removal from furnace and prior to excavation. Note rubified sediment composition and white bore cores in both gravel (crucibles 1-4) and mix gravel and quartz fine sand (crucibles 5-8).

Heating trials were designed to observe three temperature thresholds: 300°C, a moderate temperature well beneath published temperatures of calcination, 550°C, to test the brink of the calcination boundary, and 750°C, firmly within the range of calcination. Length of trials were selected to represent a quick heating event (10 minutes), a fire event of a longer length (48 hours), and a moderate value (9 hours). Trials were completed in a Nabertherm muffle furnace, programed to reach desired temperature at the fastest rate and to hold temperature for the length of the experiment. The muffle furnace was allowed to cool at a natural rate before samples were removed, mirroring the slow heat dissipation of an extinguished fire event.

Duration	Temperature (˚C)	Sediment composition Loose Gravel (G) or Compacted Gravel with Loose Sand (Mix)	N Crucibles	N Bone Cores	Trial reference number
10 minutes	300	G	5	0 cm = 15	T2A
				-2 cm = 15	
10 minutes	300	Mix	5	0 cm = 15	T2B
				-2 cm = 15	
10 minutes	550	G	4	0 cm = 12	T4
10 minutes	750	G	4	0 cm = 12	T5
				-2 cm = 12	
9 hours	300	G	4	0 cm = 12	T6
9 hours	550	G	5	0 cm = 15	T3A
				-2 cm = 15	
9 hours	550	Mix	5	0 cm = 15	T3B
				-2 cm = 15	
9 hours	750	G	4	0 cm = 12	T8
48 hours	300	G	4	0 cm = 12	T7
48 hours	550	G and Mix	8	0 cm = 24	T1
				-2 cm = 24	

Table 7: Trial parameters

Sample analyses

Bone color was documented with Munsell Soil Color codes using a Color Gun RM200 CAPSURE Color Matching tool on all bone cores post heating and prior to powdering with an agate mortar and pestle (Munsell color chart, 2010).

FTIR-ATR spectra (4000- 400 cm^{-1}) were produced with a Nicolet 6700 Fourier transform infrared spectrometer equipped with a deuterated triglycine (DTGS) detector and a single bounce diamond crystal. ATR was specifically utilized to minimize sample preparation, and contamination (Bruno 1999; Hollund et al. 2013; Thompson et al. 2009; Nakamoto et al. 1997). A total of 256 scans were collected with a sample gain of 8 and resolution of 4 cm^{-1}.

To assess organic content and calcination for this study eight peaks and peak transformations were collected for all samples in this study (n= 235), and all measurements and equations were standardized and processed with OMNIC software using OMNIC Macros Basic (Tables 8, 9). The CO/P ratio was monitored for the relative concentrations of organic components in bone, as this measurement assesses the functional group recognized as Amide I, a component of collagen proteins (Thompson et al., 2013; Mamede et al., 2018). Another measurement, the carbonate to phosphate (C/P) ratio, is utilized to understand the relative amount and loss of structural lattice carbonates within the sample (Thompson et al., 2013; Mamede et al., 2018). For reconstructing the degree of crystallinity (crystal order and lattice strain), a measure known as the Infrared Splitting Factor (IRSF or SF) captures the splitting of the PO_4^{3-} v4 peak in bone, a trough which lengthens with increasing crystallinity (Mamede et al., 2018; Weiner and Bar-Yosef, 1990). Finally, the appearance of two shoulders on different phosphate peaks indicate compositional changes within the chemical structure of the bone mineral which occur solely with high temperatures (~700-1100°C) including the growth of a shoulder at ~1090 cm^{-1} off the PO_4^{3-} v3 peak suggested to be the presence of francolite and a ratio measured from a shoulder at ~625cm^{-1} on the PO_4^{3-} v4 peak known as the Phosphate High Temperature (PHT) shoulder indicating an OH- librational mode associated with hydrogen bonding within the crystalline framework (Gallo et al., 2021; Mamede et al., 2013; Marques et al., 2015; Thompson et al., 2013)

Wavenumbers considered	**Infrared peak assignment**	**Peak transformation relevant to this study**
1630-1660cm^{-1}	Amide I	1650 cm^{-1} peak a component of the CO/P ratio
1400-1550 cm^{-1}	CO_3^{2-} v3	1415 cm^{-1} peak a component of C/P ratio
1090 cm^{-1}	Likely presence of francolite	Appearance as a shoulder on the 1035 cm^{-1} v4 phosphate peak corresponds to structural changes potentially linked to the presence of francolite
1028-1100 cm^{-1}	PO_4^{3-} v3	1035 cm^{-1} peak a component of C/P ratio

625 cm-1, 610 cm $^{-1}$	Phosphate High Temperature (PHT) PO_4^{3-} v4	Appearance of PHT shoulder splitting the PO43- v4 peak only relevant to high temperature (> ~650° C) transformation
565 cm-1, 595 cm^{-1}, 605 cm^{-1}	PO_4^{3-} v4	Growth of 565 cm^{-1} and 605 cm^{-1} and decrease of 595 cm^{-2} trough components of the infrared splitting factor (SF) equation

Table 8: FTIR-ATR wavenumbers associated with the likely functional groups relevant to this study and the thermal alteration of burnt bone (Ellingham et al., 2015; Gallo et al. 2021; Mamede et al., 2018; Reidsma et al. 2016; Thompson et al. 2013; Weiner and Bar-Yosef 1990).

Measurement	**Equation**	**Citations**
CO/P	1650 cm^{-1} *peak ht* / 1035 cm^{-1} *peak ht*	Ellingham et al., 2015 Thompson et al., 2013 Mamede et al., 2018
Carbonate to Phosphate ratio (C/P)	1415 cm^{-1} *peak ht* / 1035 cm^{-1} *peak ht*	Ellingham et al. 2015, Thompson et al. 2013, Mamede et al., 2018
Phosphate High Temperature (PHT)*	625 cm^{-1} *peak ht* / 610 cm^{-1} *peak ht*	Ellingham et al. 2015; Thompson et al. 2013; Mamede et al., 2018
Infrared Splitting Factor (IRSF or SF)	(565 cm^{-1} *peak ht* + 605cm^{-1} *peak ht*) / 595 cm^{-1} *peak ht*	Ellingham et al. 2015; Thompson et al. 2013; Mamede et al., 2018; Weiner and Bar-Yosef 1990
** Only available to be measured once peak appears*		

Table 9: Equations utilized for this study

To determine average crystallite size, diffraction peaks were obtained with a Bruker D2 Phaser and Bruker D8 advance diffractometers using CuKα radiation and run from 7 to 70° 2θ with 0.04° step and 0.02 θ increment. Divergent slits were set at 0.6 mm with a 1mm anti-scatter screen, and a max PSD opening of 4.8 degrees. Zero background silicon sample holders were used to hold the powdered bone and ethanol was used to spread the powder evenly. Average crystallite size and observations of bioapatite coarsening were measured with whole pattern fitting (Rietveld refinement) modeled using hydroxyapatite $Ca_5(PO_4)_3OH$ structure (space group P63/m) with pseudo-Voigt profile shape function with the GSAS-2 package (Rietveld, 1969).

Results and Discussion

Color

All colors are confirmed and represented through the Munsell values given by the Color Gun RM200 CAPSURE Color Matching tool. For the 10 minute duration trials, at 300°C (T2A, T2B) bones from all crucibles were shades of browns, ranging from pale to darker hues including grey-brown (Fig. 3). At 550°C for 10 minutes (T4), bones were categorized as darker greys, and at 750°C (T5) heat altered bones were shades of light greys and whites (Fig. 3).

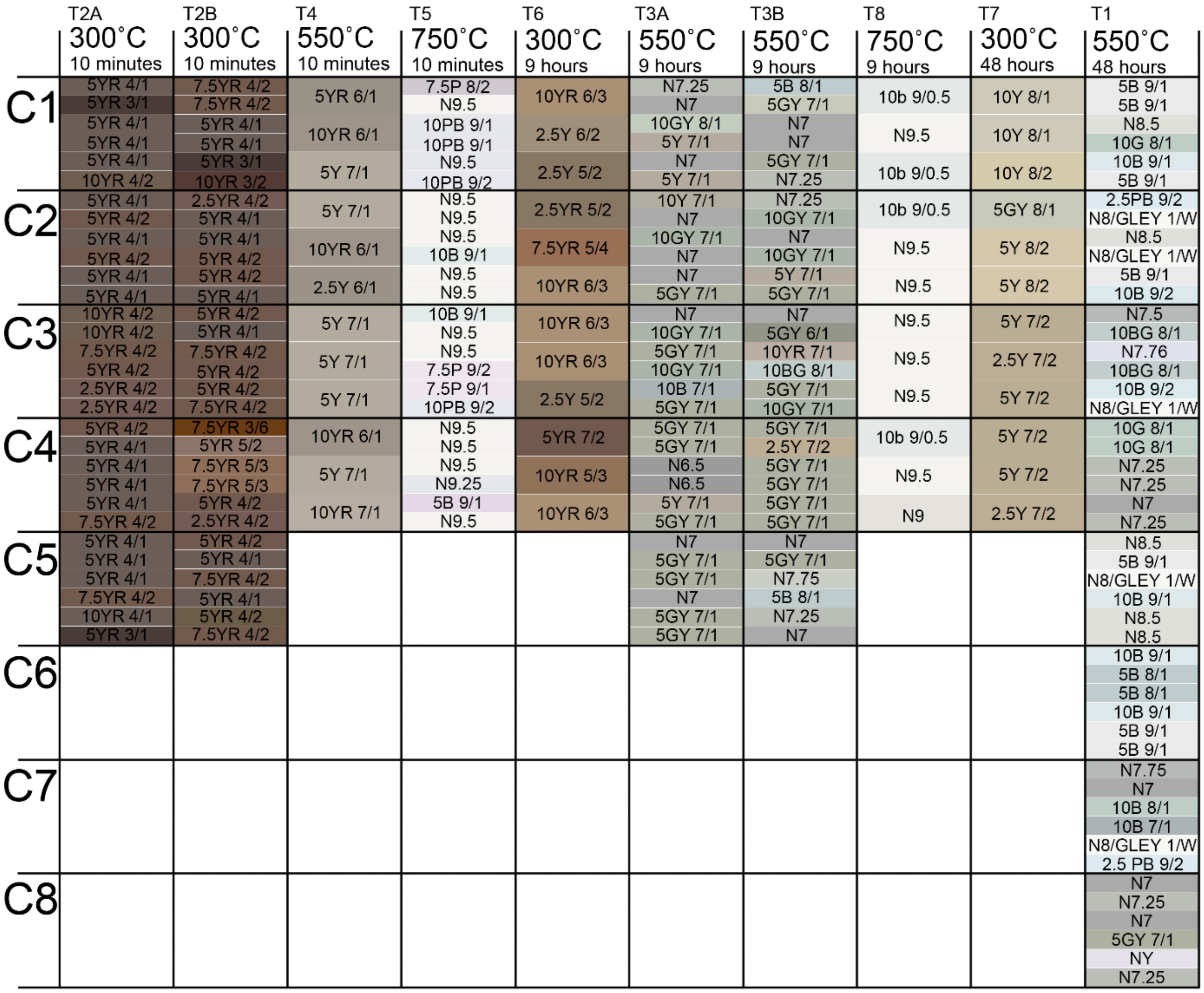

	T2A 300˚C 10 minutes	T2B 300˚C 10 minutes	T4 550˚C 10 minutes	T5 750˚C 10 minutes	T6 300˚C 9 hours	T3A 550˚C 9 hours	T3B 550˚C 9 hours	T8 750˚C 9 hours	T7 300˚C 48 hours	T1 550˚C 48 hours
C1	5YR 4/1	7.5YR 4/2	5YR 6/1	7.5P 8/2	10YR 6/3	N7.25	5B 8/1	10b 9/0.5	10Y 8/1	5B 9/1
	5YR 3/1	7.5YR 4/2		N9.5		N7	5GY 7/1			5B 9/1
	5YR 4/1	5YR 4/1	10YR 6/1	10PB 9/1	2.5Y 6/2	10GY 8/1	N7	N9.5	10Y 8/1	N8.5
	5YR 4/1	5YR 4/1		10PB 9/1		5Y 7/1	N7			10G 8/1
	5YR 4/1	5YR 3/1	5Y 7/1	N9.5	2.5Y 5/2	N7	5GY 7/1	10b 9/0.5	10Y 8/2	10B 9/1
	10YR 4/2	10YR 3/2		10PB 9/2		5Y 7/1	N7.25			5B 9/1
C2	5YR 4/1	2.5YR 4/2	5Y 7/1	N9.5	2.5YR 5/2	10Y 7/1	N7.25	10b 9/0.5	5GY 8/1	2.5PB 9/2
	5YR 4/2	5YR 4/1		N9.5		N7	10GY 7/1			N8/GLEY 1/W
	5YR 4/1	5YR 4/1	10YR 6/1	N9.5	7.5YR 5/4	10GY 7/1	N7	N9.5	5Y 8/2	N8.5
	5YR 4/2	5YR 4/2		10B 9/1		N7	10GY 7/1			N8/GLEY 1/W
	5YR 4/1	5YR 4/2	2.5Y 6/1	N9.5	10YR 6/3	N7	5Y 7/1	N9.5	5Y 8/2	5B 9/1
	5YR 4/1	5YR 4/1		N9.5		5GY 7/1	5GY 7/1			10B 9/2
C3	10YR 4/2	5YR 4/2	5Y 7/1	10B 9/1	10YR 6/3	N7	N7	N9.5	5Y 7/2	N7.5
	10YR 4/2	5YR 4/1		N9.5		10GY 7/1	5GY 6/1			10BG 8/1
	7.5YR 4/2	7.5YR 4/2	5Y 7/1	N9.5	10YR 6/3	5GY 7/1	10YR 7/1	N9.5	2.5Y 7/2	N7.76
	5YR 4/2	5YR 4/2		7.5P 9/2		10GY 7/1	10BG 8/1			10BG 8/1
	2.5YR 4/2	5YR 4/2	5Y 7/1	7.5P 9/1	2.5Y 5/2	10B 7/1	5GY 7/1	N9.5	5Y 7/2	10B 9/2
	2.5YR 4/2	7.5YR 4/2		10PB 9/2		5GY 7/1	10GY 7/1			N8/GLEY 1/W
C4	5YR 4/2	7.5YR 3/6	10YR 6/1	N9.5	5YR 7/2	5GY 7/1	5GY 7/1	10b 9/0.5	5Y 7/2	10G 8/1
	5YR 4/1	5YR 5/2		N9.5		5GY 7/1	2.5Y 7/2			10G 8/1
	5YR 4/1	7.5YR 5/3	5Y 7/1	N9.5	10YR 5/3	N6.5	5GY 7/1	N9.5	5Y 7/2	N7.25
	5YR 4/1	7.5YR 5/3		N9.25		N6.5	5GY 7/1			N7.25
	5YR 4/1	5YR 4/2	10YR 7/1	5B 9/1	10YR 6/3	5Y 7/1	5GY 7/1	N9	2.5Y 7/2	N7
	7.5YR 4/2	2.5YR 4/2		N9.5		5GY 7/1	5GY 7/1			N7.25
C5	5YR 4/1	5YR 4/2				N7	N7			N8.5
	5YR 4/1	5YR 4/1				5GY 7/1	5GY 7/1			5B 9/1
	5YR 4/1	7.5YR 4/2				5GY 7/1	N7.75			N8/GLEY 1/W
	7.5YR 4/2	5YR 4/1				N7	5B 8/1			10B 9/1
	10YR 4/1	5YR 4/2				5GY 7/1	N7.25			N8.5
	5YR 3/1	7.5YR 4/2				5GY 7/1	N7			N8.5
C6										10B 9/1
										5B 8/1
										5B 8/1
										10B 9/1
										5B 9/1
										5B 9/1
C7										N7.75
										N7
										10B 8/1
										10B 7/1
										N8/GLEY 1/W
										2.5 PB 9/2
C8										N7
										N7.25
										N7
										5GY 7/1
										NY
										N7.25

Fig 3: Munsell (Munsell color chart, 2010) color code results using a Color Gun RM200 CAPSURE Color Matching tool taken on bone cores post-heating for each heating trial. Note the color contrast between bones burnt at the same temperature but at different duration times.

For the 9 hour duration trials, bones heated at 300°C still were recognized as brown in color, although considerably lighter browns and less saturated hues than the 10 minute trials (Fig. 3). At 550°C for 9 hours (T3A, T3B), a range of greys including blueish-grey and brownish-greys were recognized (Fig. 3). These results are very light in coloration and are likely, given standard scales of zooarchaeological classification, to be considered heated at a higher temperature based on visual observation. At 750°C for 9 hours all heated samples were stark white and very desaturated greys as expected (Fig. 3).

Bones heated for 48 hours at 300°C (T7) were very pale, resembling light tans and pale greys (Fig. 3). This degree of depigmentation would additionally be difficult to classify given color classification schemes for burnt bone, and may be considered to have experienced high temperatures based solely on coloration. A similar scenario is also seen in the bones heated at 550°C for 48 hours (T1). All samples from this trial range from whites to light greys, with multiple samples determined as bluish-grey (Fig. 3)

All bones excluding 300° C for 9 hours (T6) and 300°C for 10 minutes (T2A, T2B) would be likely classified as Stiner et al. (1995) Stage 6 based on coloration (white, grey, and heavily muted pale tans).

FTIR results

10 minute trials

Four trials were conducted with duration times of 10 minutes: 300°C with dry, loose gravel (T2A), 300°C with dry compacted gravel and fine sand (T2B), 550°C in dry loose gravel

(T4), and 750°C in dry loose gravel (T5). At 300°C, bones exhibited strong presence of Amide I & II (1630-1660 cm^{-1}), relevant to their strong organic tissue and water content, and have CO_3^{2-} v3 peak heights similar to fresh, unburnt bone (1400-1550 cm^{-1}) typical of bones burnt to this temperature for brief durations (Gallo et al., 2021; Fig. 4). For both 300°C trials there are no indicators of high temperature alteration, primarily seen through the low SF ratio (565 and 605 cm^{-1} peaks and the 595cm^{-1} trough) and the absence of a PO_4^{3-} v3 shoulder or a Phosphate High Temperature (PHT) shoulder at 1090 cm^{-1} and 625 cm^{-1} respectively (Fig. 4).

At 550°C for 10 minutes much of the organic components and the lattice carbonates have been eliminated from the samples as seen in the 1630-1660 cm^{-1} and 1400-1550 cm^{-1} wavelength regions (Fig. 4). This is consistent with the described first release of carbonates (CO_2) from organic combustion, but not full structural carbonate loss (Etok et al., 2007; Mamede et al., 2018). Despite the dehydration and carbonate loss, the physical and chemical structure of the bioapatite here has not radically changed and there are no indications of high temperature alteration or calcination when referencing the SF, the 1090 cm^{-1} shoulder off the 1030 cm^{-1} peak, or the PHT shoulder (Fig. 4). This spectrum is typical of bone burned to this temperature threshold for brief durations (Gallo et al., 2021).

For the high temperature threshold, 750°C, major changes are seen when compared to the lower temperatures. At 750°C all organics and water are eliminated and for the CO_3^{2-} v3 functional group (the structural lattice carbonate within the bone), there is either a complete absence or a barely present small doublet absorption (Fig. 4). Off the PO_4^{3-} v3 peak at 1030 cm^{-1} there is a strong presence of a shoulder at 1090cm^{-1}, linked to high temperature alteration also seen in bones burnt for short durations between 700°C and 1100°C (Gallo et al., 2021; Thompson et al., 2013; Fig. 4). For the PO_4^{3-} v4 peak area there is both a strong presence of a

PHT shoulder as well as a much more deeply exaggerated trough at 595 cm^{-1} between the 565 and 605 cm^{-1} peaks which constitute a measurement of crystallinity through the SF ratio (Table 8; Fig. 4). These spectra are clearly calcined and exhibit a higher crystallinity than the samples burnt at 550°C and 300°C.

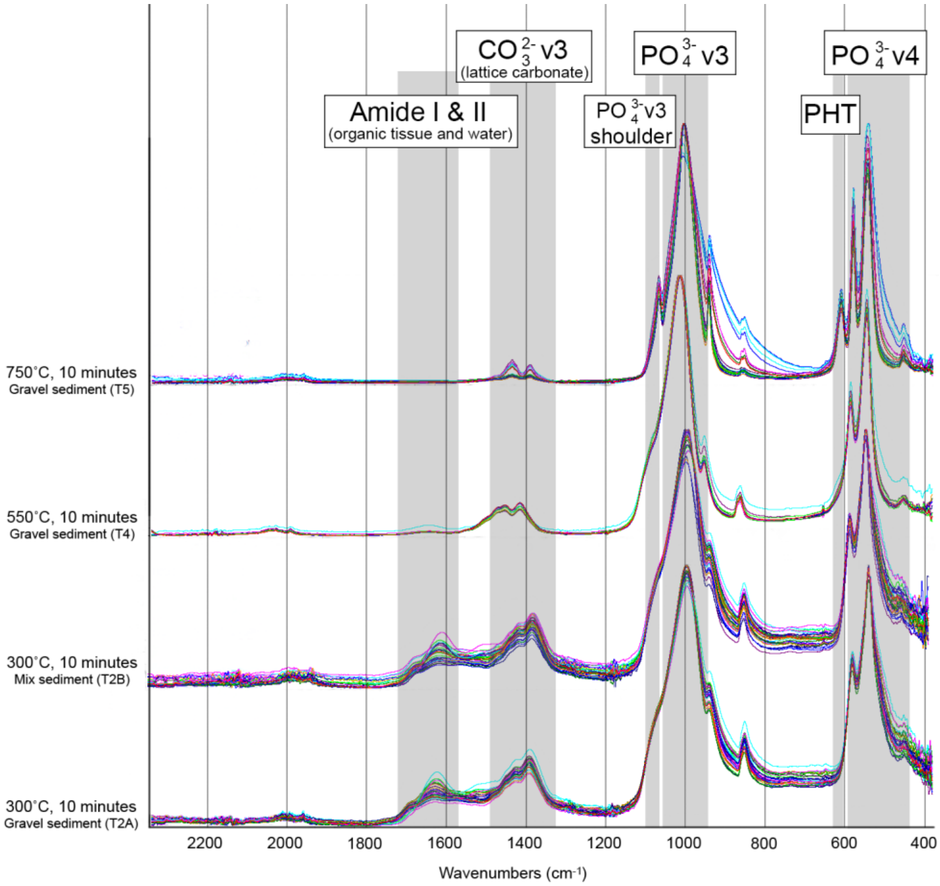

Fig 4. FTIR-ATR spectra for the shortest duration trial (10 minutes; T2A, T2B, T4, T5) at 300°, 550°, 750° C. Relevant peaks of interest representing different likely functional groups are highlighted, including the Amide I&II and the CO$_3^{2-}$ v3 peak areas which are visibly depleted with increases in temperature. Also highlighted are the 3rd and 4th vibration of PO$_4^{3-}$ functional groups which exhibit high temperature induced shoulder growths at ~1090 cm^{-1} and 625 cm^{-1} (the PHT) with structural and chemical calcination. Also visible is the deepening of the trough at 595 cm^{-1} on the PO$_4^{3-}$ v4 peak with greater temperatures, a correlate to increasing SF.

9 hour trials

Four additional trials were completed at 9 hours of sustained temperature duration: 300°C in dry loose gravel (T6), 550°C in both dry loose gravel (T3A) and dry compacted gravel and fine sand (T3B), and 750°C in dry loose gravel (T8). For the lowest temperature experiment, the primary difference seen between the 9 hour and 10 minute trials is the depletion of the organic content as monitored by the Amide I and II functional group areas (1630-1660 cm^{-1}; Fig. 5). This is similar to the degree of reduced organics seen in archaeological bone, where organics are depleted through normal diagenetic processes (Gallo et al., 2021). There remains a strong presence of the lattice carbonate, and there is no presence of a high temperature shoulder at 1090 cm^{-1} nor a PHT shoulder (Fig. 5). The infrared SF remains low and is not indicative of a highly crystalline sample nor calcination (Fig. 5).

Samples heat altered at 550°C show no influence from the different substrates and have a lower organic presence than both the 300°C at 9 hour trial (T6) and the 550° trial at 10 minutes duration (T4). Weakly present shoulder emergences are found for both the 1090 cm^{-1} area off of the 1030 cm^{-1} PO_4^{3-} v3 peak and the PHT shoulder off of the PO_4^{3-} v4 peak which are not found in the 550°C 10 minute trial (T4). There are also a deepened troughs seen at 595 cm^{-1} which results in a higher SF ratio, but these spectra do not indicate samples which have been fully calcined (Fig. 5).

For the 750°C trial, again we see clearly calcined bone with spectroscopic signatures of high temperature alteration through the very large splitting factor ratio on the PO_4^{3-} v4 peak, the PHT shoulder, and the PO_4^{3-} v3 1090 cm^{-1} shoulder (Fig. 5). There are also no remaining organics as seen through the predicted Amide I and II functional group area (1630-1660 cm^{-1}) and there is only a small remaining doublet regarding the CO_3^{2-} v3 area (Fig. 5).

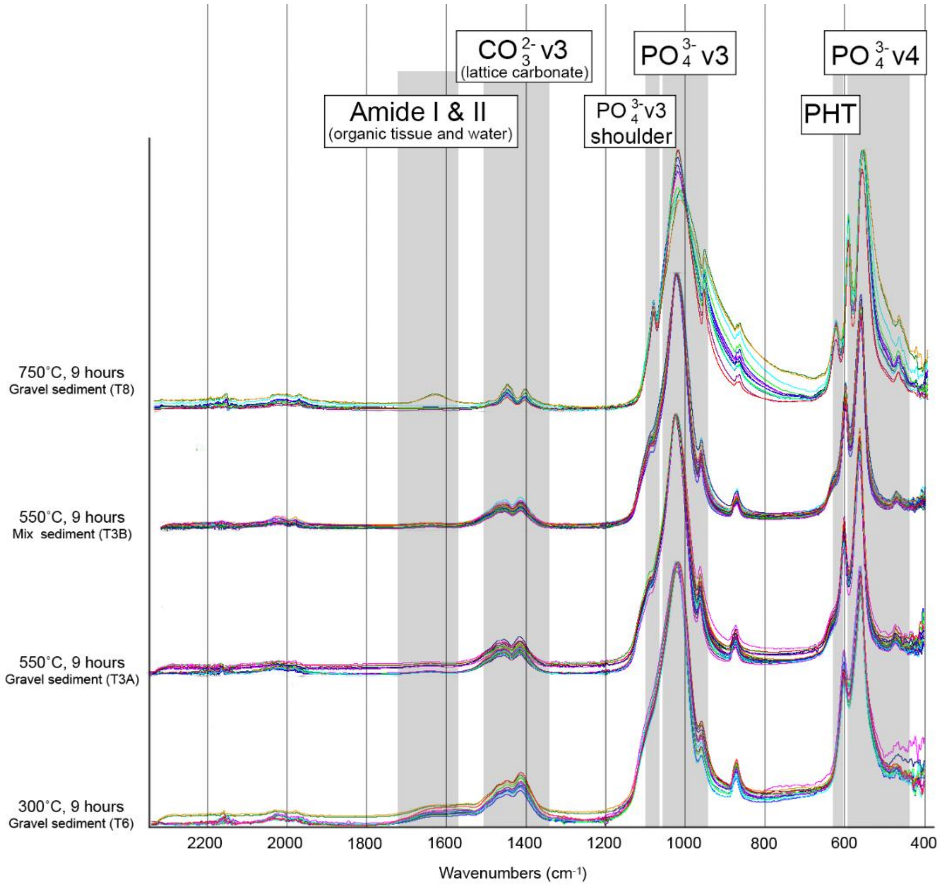

Fig 5. FTIR-ATR spectra for 9 hour duration trials (T3A, T3B, T6, T8) at 300°, 550°, and 750° C. Amide I&II peak areas are present in the 300°C trial but are weakly expressed compared to the 10 minute trials (T2A and T2B). The CO_3^{2-} v3 peak absorbance height remains similar to both shorter and longer durations at each respective temperature. The PO_4^{3-} v3 shoulder at 1090 cm^{-1} and PO_4^{3-} v4 625cm^{-1} (PHT) shoulder are distinguished at 750°C, as expected, but both can be seen weakly starting at 550°C. The SF also visibly increases both at 550° and at 750° C.

48 hour trials

Two trials, 300°C (T7) and 550°C (T1), were held at steady temperature for 48 hours. Elevated temperatures also continued past the 48 hour set experiment, as crucibles remained within the muffle furnace for the substantial cooling period (SI Fig. 1). For the 300°C trial (T7), crucibles were filled with dry, loose gravel, and for the 550°C trial (T1) four crucibles had a dry, loose gravel sediment base, and four had dry, compacted gravel with fine sand.

Bones heated at 300°C for 48 hours show reduced organics in the 1630-1660 cm^{-1} wavelength region when compared to their 10 minute counterparts (Fig. 6). There are not indications of calcination on any part of the spectra, however, neither in the PO_4^{3-} v3 peak area nor in the PO_4^{3-} v4 region through the splitting factor ratio or in the presence of a PHT shoulder (Fig. 6).

At 550°C for 48 hours (T1) two different signatures are seen within the same trial. This pattern of differential alteration is distributed by crucible placement within the furnace, as crucibles farthest from the furnace door (crucibles 1, 2, 5 and 6) exhibited the greatest amount of heat induced transformations with both the presence of the PHT shoulder, the PO_4^{3-} v3 shoulder at 1090 cm^{-1}, and elevated SF ratios (Fig. 6). These changes are not seen in the bones within crucibles near the door of the furnace, indicating temperatures varied within the same experimental trial and higher temperatures above 550°C were reached in a concentrated area at the back (SI Figs. 1-2). This observation validates the selection of 550°C as a temperature of interest, as it rests on a margin very close to temperatures capable of reaching structural and chemical calcination in samples. For all bones in this trial a small doublet peak representing the likely functional group of structural lattice carbonates, the CO_3^{2-} v3 peak area at 1400-1550 cm^{-1}, remains (Fig. 6). In an experimental reference collection utilizing the same FTIR-ATR instrument the full elimination of these carbonates was indeed not seen until greater temperatures are reached > 900°C (Gallo et al., 2021). This indicates that despite the presence of heat induced changes to the mineral portion of the bone seen in the 550C, 48 hour trial (T1), a small amount of lattice carbonates remained (Gallo et al., 2021).

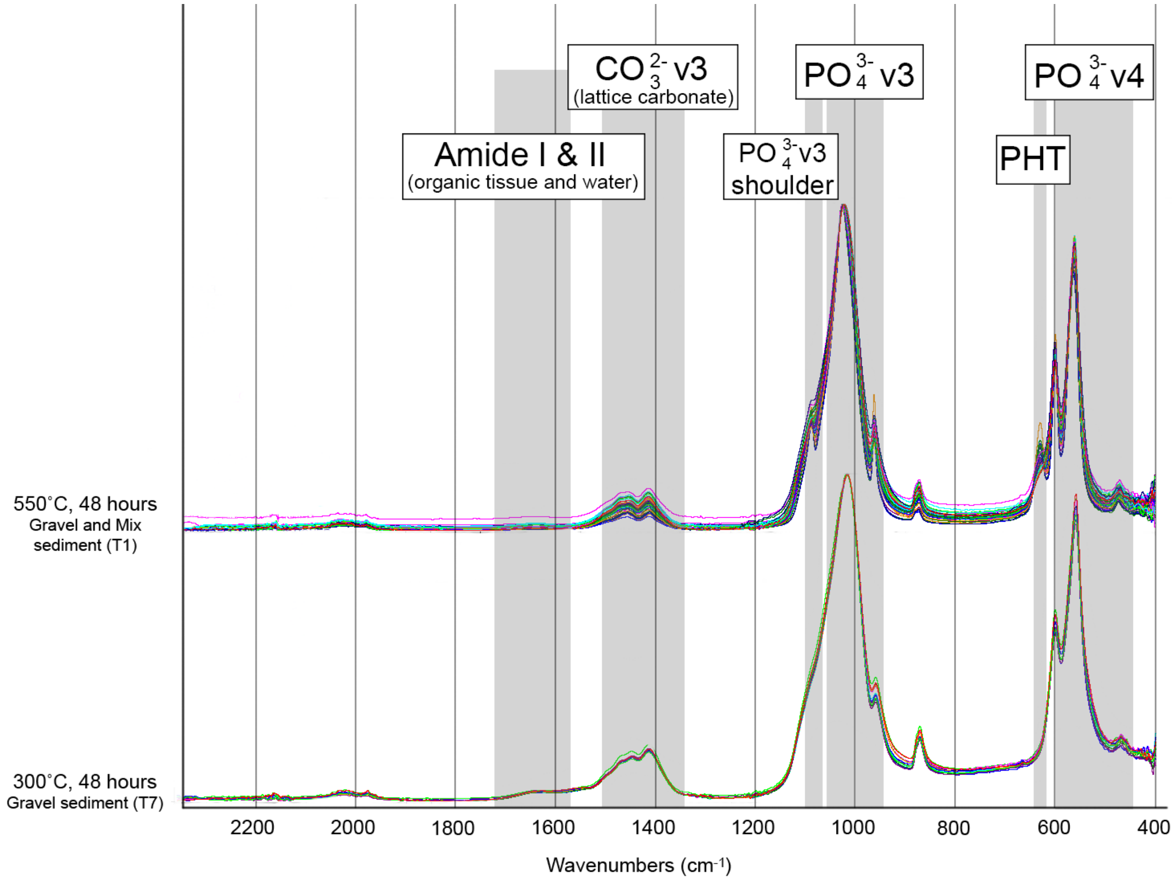

Fig 6. FTIR-ATR spectra for 48 hour duration trials (T1, T7) at 300° and 550° C. Both temperature trials retain the presence of the CO_3^{2-} v3 lattice carbonate functional group, similar to their corresponding temperatures at other duration periods. At 48 hours, bones burnt at 300°C clearly have only a weak absorption of Amide I&II functional group presence (~1630-1660 cm^{-1}), a striking difference from bones burnt to the same temperature but sustained at 10 minutes. There are no indications of structural or chemical calcination for the 300°C samples on either the PO_4^{3-} v3 and v4 peaks and the SF is not elevated, represented here by a shallow dip between the 605 and 565cm^{-1} peaks. At 550°C two patterns are noted which map clearly with the crucible distribution within the muffle furnace. Half of the bone samples, located at the front of the muffle furnace close to the door, remain uncalcined with moderate changes to the SF values and no presence of a 1090cm^{-1} or 625cm^{-1} (PHT) shoulder off of the PO_4^{3-} v3 or v4 peaks (SI Figs 2, 3). The remaining samples from crucibles 1,2, 5 and 6 were located in the back of the furnace and likely experienced slightly elevated temperatures due to this placement. These samples do have heat induced changes to shoulders off the PO_4^{3-} v3 and v4 peaks (SI Figs 2, 3).

In sum, the results of the FTIR-ATR spectra follow expectations for bones burnt at the desired temperature threshold with one discrepancy. Most samples exhibited progressively higher SF ratios representing degree of crystallinity and two stages of C/P loss representing the carbonate loss with organic removal and, at higher temperatures, the elimination of most of the lattice carbonate (Figs. 7-10). The presence of a PHT peak is also primarily seen in the 750°C trials (T5, T8) and is not noted in the 300°C trials (T2A, T2B, T6, T7) at any duration despite changes in coloration (Figs. 4-6, 11). The highest CO/P ratio is noted in the 10 minute 300°C trial, notably also the only trial with dark brown coloration of bone cores (Figs. 2, 4, 9; Table 7). Negligible differences of all measurements were seen between samples buried at different depths, although a small pattern is seen between samples of gravel and gravel with quartz fine sand, presumably due to slight differences in matrix heat retention.

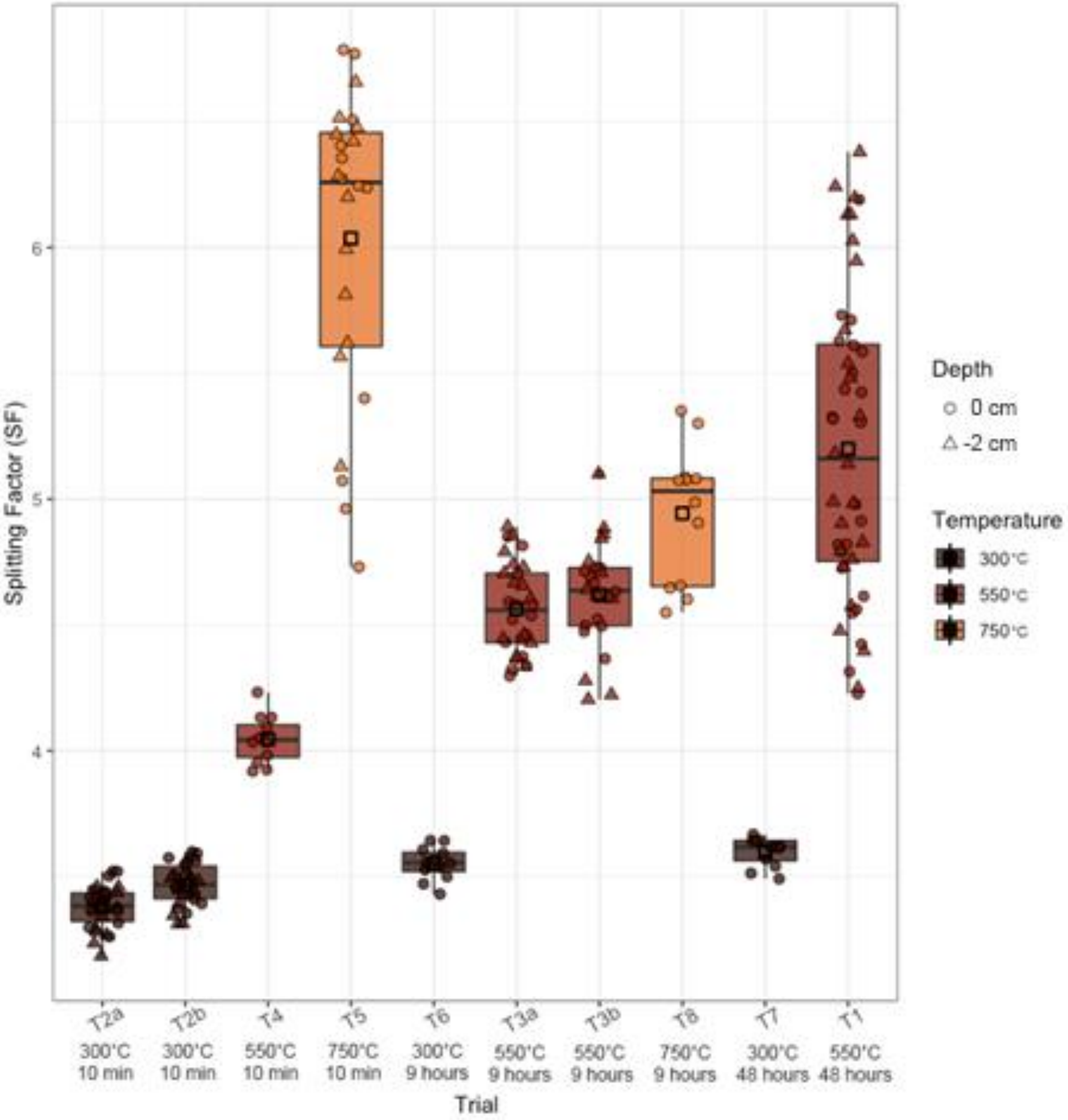

Fig 7. Splitting Factor (SF) organized by trial. Temperature and bone core depth represented by color and shape, respectively. For the 10 minute duration trials (T2A, T2B), bones burned to 300°C have low infrared SF, as expected. At 10 minutes 550°C (T4) has a moderate value and 750C (T5) has a range of elevated values, all above the highest value of 550°C. For the 9 hour trials, the SF of bones burnt at 300°C (T6) remains consistent with the 10 minute experiment, and the 550°C (T3A, T3B) values now fall within range of the 750°C (T8) heated bones. This is likely due to the tremendous crystallite growth seen in this trial, and with coalesencse and sintering of the crystallites the relationship the SF is measuring changes, a pattern noted by many studies which report falling SF values above 700°-800°C (Ellingham et al., 2016; Snoeck et al. 2014; Thompson et al., 2013; Lebon et al., 2010; Mamede et al., 2018). At 48 hours the 300°C trial (T7) heated bones again retains low crystallinity, whereas the 550°C (T1) samples have bone cores with small crystallites with low crystallinity, and samples which experienced more heat and have larger crystallite growth and therefore are more crystalline with a higher SF value.

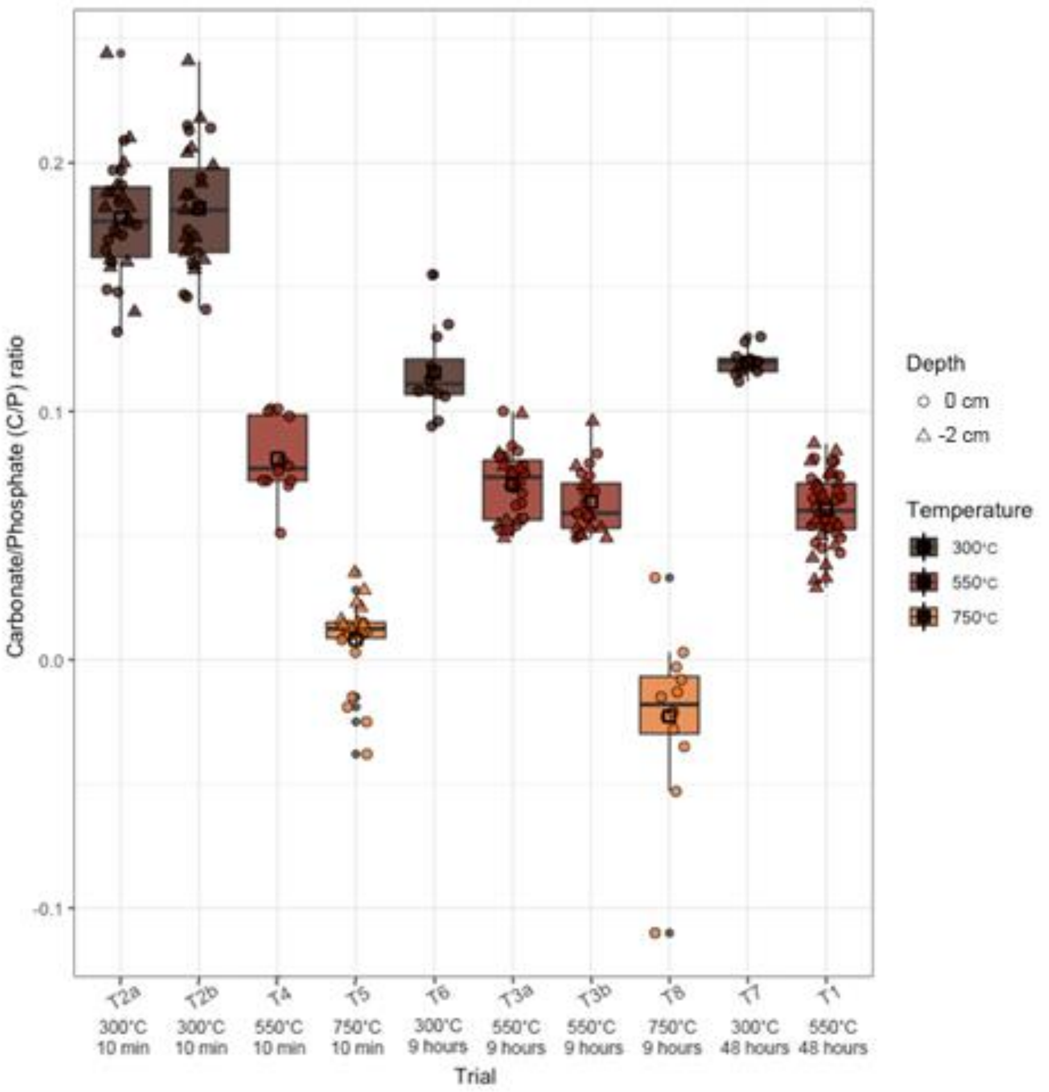

Fig 8. Carbonate/Phosphate (CP) ratio organized by duration and trial. Temperature and depth represented by color and shape, respectively. For the 10 minute trials, 300°C (T2A, T2B) have the highest value, representing the presence of structural carbonates. Heated bone at 550°C (T4) for 10 minutes still has detectable amounts of carbonate, whereas the 750°C (T5) samples are completely depleted. When heating is extended for 9 hours, bones heated at 300°C were measured at much lower C/P values than the 10 minute counterparts, representing the decreasing lattice carbonate content solely through duration. For the 550°C, 9 hour (T3A/ T3B) trials a moderate decrease is seen from 10 minute trials, and the 750°C 9 hour (T8) samples exhibit the lowest values, as expected. Duration times of 48 hours demonstrate that the 300C trial (T7) values are closely aligned with the decreased presence of carbonates in the 300°C 9 hour (T6) experiment, while the 550°C heated bones are either at similar values to the 550°C 9 hour (T3A, T3B) trial or lower values, representing the crucibles which experienced elevated temperatures.

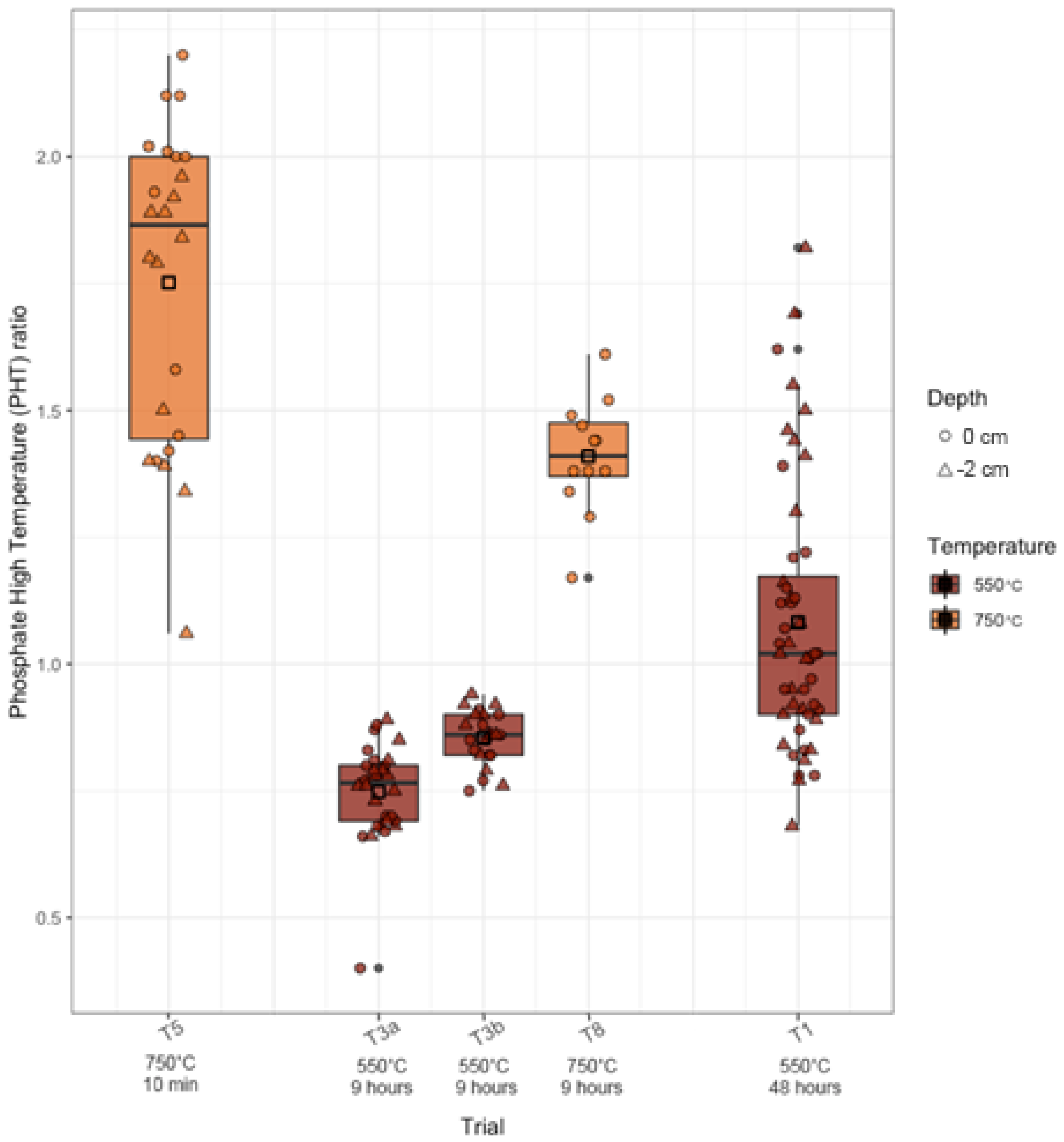

Fig 9. Phosphate high temperature (PHT) ratio, organized by duration and trial. Temperature and depth represented by color and shape, respectively. Only trials with PHT shoulder presence represented: 10 minutes at 750°C (T5), 9 hours at 550°C in gravel sediment (T3A), 9 hours at 550°C in compacted mixed sediment (T3B), 9 hours at 750°C (T8), 48 hours at 550°C in both gravel and compacted mixed sediment (T1).

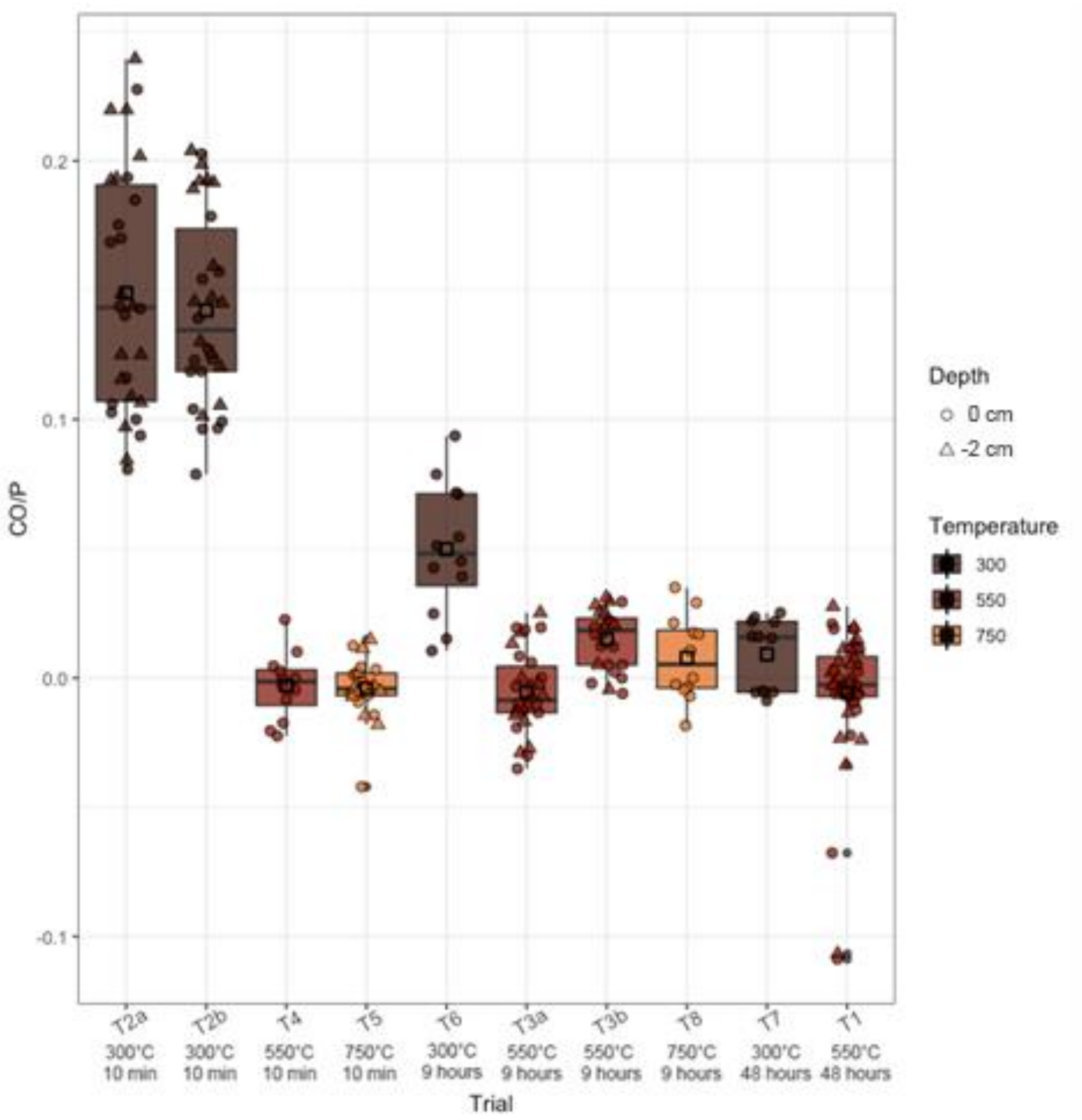

Fig 10. CO/P ratio, organized by duration and trial. Temperature and depth represented by color and shape, respectively. The 300°C, 10 minute trials (T2A, T2B) have bones with the highest values, representing the strong presence of Amide I (collagen) within the sample, indicating the existence of organics. This signal is also visually observable through the strong brown color values from these samples (Figs 1, 3). Bones heated at 300C for 9 hours have moderate values, while bones heated at 300°C for 48 hours fall within similar ranges to the bones heated to 550° and 750°C, transformations also visually recognized by the increasingly pale colors (Figs. 1, 3).

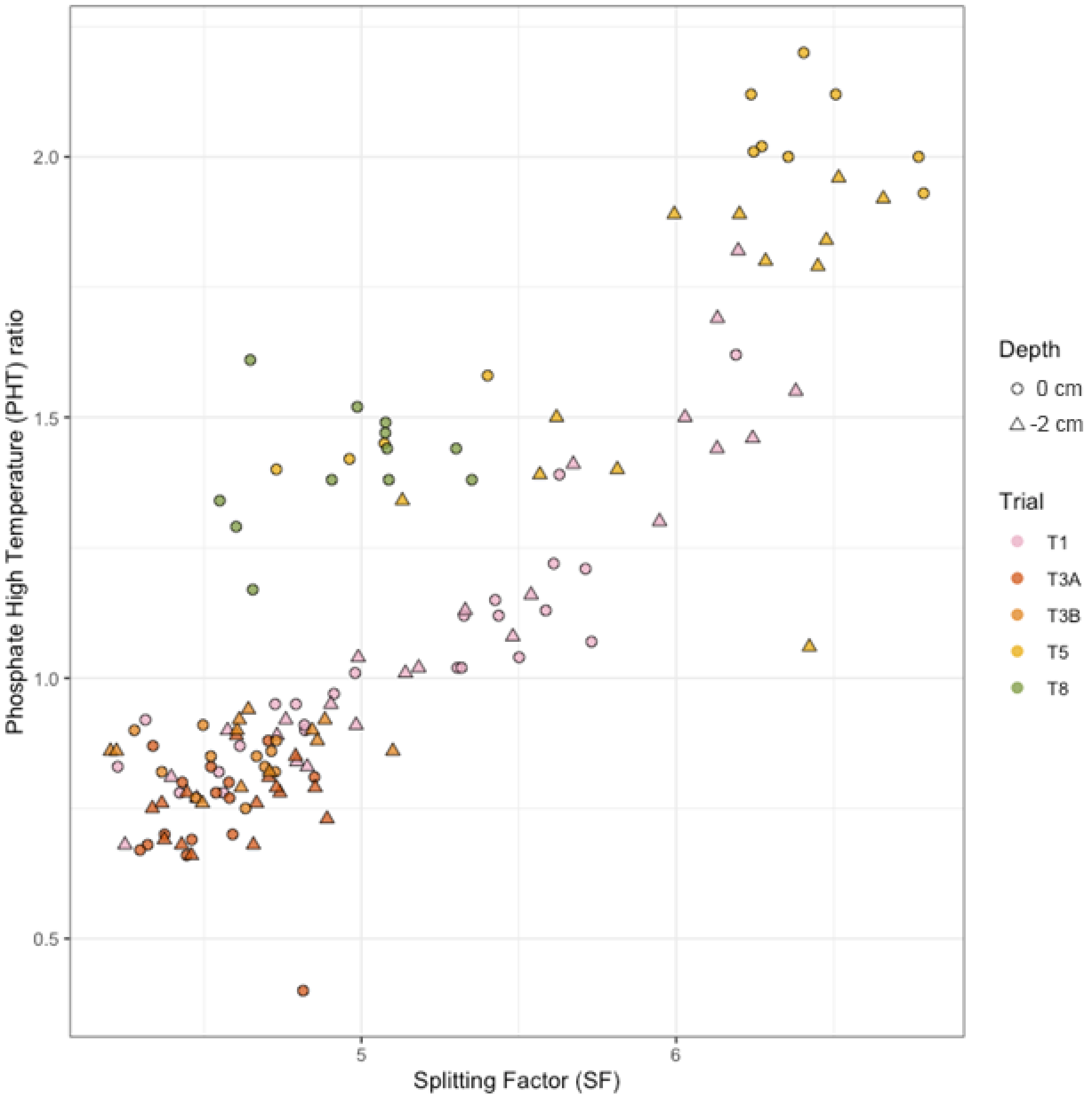

Fig 11. PHT and SF ratios for all trials with 625 cm^{-1} shoulder present in FTIR-ATR spectra (T1, T3A, T3B, T5, T8). The largest SF values align with the largest PHT peak ratio, as expected with high temperatures. Note the large PHT ratio seen in the 750°C 9 hour trial (T8), where the infrared SF value is decreased due to fusion stage thermal alteration but the PHT remains clearly expressed.

The C/P ratio is noted to be the lowest in the 750°C trials (T5, T8) and highest in the 300°C trials (T2A, T2B, T6, T7; Fig. 8; Table 7). C/P values similar to each other are also seen for all duration times at 550°C (T1, T3A, T3B, T4), and the 9 and 48 hour 300°C trails in comparison are only slightly elevated (Fig. 9; Table 7). Additionally, the presence of the heat-induced shoulder on the PO_4^{3-} v3 peak at 1090 cm^{-1} is also seen in both 750°C trials as well as with a weak expression in all 550°C / 9 hour trials (T3A and T3B). For the 48 hours for 550°C trial (T1), this peak at 1090 cm^{-1} is seen fully present in the crucibles located at the back of the furnace (crucibles 1,2,5 and 6), with weak expression in the front crucibles near the furnace door (crucibles 3,4,7 and 8; Fig. 4-6; Appendix B Figs. 2-3), which shows that experimental temperatures within the furnace were not completely homogenous.

Combining information from both the visual observations and the spectroscopic data indicates that bones from both the 750°C trials (T5 and T8) at all durations are colored stark white and greys, as expected. At 10 minutes duration the bones from the 300°C trials (T2A, T2B) were additionally colored in typical hues of brown for that stage of bone decomposition, also with elevated CO/P ratios demonstrating the clear presence of organics (Fig. 9). Unexpectedly, bones heated at 550°C for all duration trials (T1, T3A, T3B, T4) were light in color despite many not being truly calcined (Figs. 1, 3). This is also reflected in the CO/P measurements where bones burnt at 550°C have similar values to the 750°C samples in all trials (Fig. 9). There additionally was not a coloration difference between the bones within the 550°C 48 hour trial (T1) in which half of the bone samples were truly calcined and half did not experience the structural changes which come with calcination. The 300°C, 48 hour trial (T7) also resulted in bone heavily depigmented with colors of heavily muted tans and greys whose range of CO/P values fell well within the distribution of bones burnt to 550° and 750°C, a stark contrast to bones burnt at the same temperature for only 10 minutes (Fig. 9).

XRD results

The average crystallite sizes as measured by XRD provide an independent calculation of bioapatite growth, and therefore, heat induced transformation. Results align closely with inferences taken from the FTIR-ATR spectroscopic data, with samples heated for a duration of 9 hours at both 300° and 550°C not having crystal size indicative of calcination (Fig. 12).

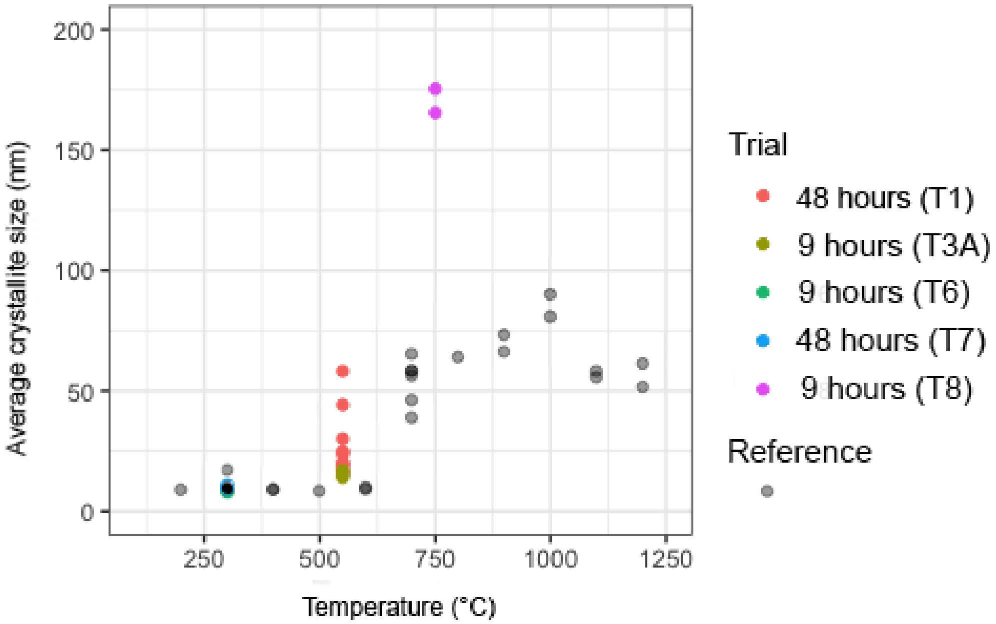

Fig 12:. XRD results of averaged crystallite size (nm) for sampled bone samples both from duration trials and from an experimental reference collection 200°-1200°C (Gallo et al. 2021). Reference collection duration times were primarily 30 minutes, with two 300° and 700°C samples cooled and reheated an additional 30 minutes for no greater than 1 hour and 30 minutes of heating time in total. Average crystallite sizes of bone which has been chemically and structurally calcined can be inferred from this dataset to be of an average size > 30 nm, with sizes >80 nm representing heated bone which has undergone the fusion stages of bioapatite sintering

Samples burned at 9 hours at 750°C (T8) have tremendous average crystallite size, clearly separating from bones burnt at lower temperatures both at the same duration and longer durations (Fig. 12). Bone cores burnt under these conditions demonstrate average crystallite sizes larger than twice the size of referential samples burned at 700°C and even 1000°C (Gallo et al., 2021). The exhibition of such exaggerated growth, but without the full elimination of the lattice carbonate functional group as seen from the FTIR-ATR spectra, may indicate long duration heating at temperatures above calcination but below the temperatures associated with the fusion stage (likely 900°-1000°C). This tested in archaeological contexts can address subtle transformations related to combustion feature properties within bone considered at the end stages of burning based on macroscopic, visual observations.

All bones burnt at 300°C for 48 hours (T7) and 300°C at 9 hour trial (T6) do not have large average crystallite sizes (Fig. 12). Several of the samples from the 550°C 9 hour trial (T3A), despite being white and grey, additionally have not experienced bioapatite growth associated calcination. These average crystallite sizes do support the inference that half of the bones white and grey in color which would be identified as Stiner et al. (1995) Stage 6 from the 300°C 48 hour trial (T7) do not have the large crystallite sizes indicative of structural and chemical calcination (Fig 12). Of the 11 sampled cores from each crucible of this trial, only cores from crucibles 1 and 5 exhibit the large, averaged crystallite growth >30 nm. These samples overlap in size with reference samples burned in air for 30 minutes or 1 hour 30 minutes at 700°C (Fig 14; Gallo et al., 2021). Crucibles 1 and 5 from this trial were placed in the far end of the muffle furnace and experienced a higher temperature intensity from the remaining crucibles, an inference which is supported from the FTIR-ATR data.

Discussion

The duration of a fire is deeply relevant and interconnected to fire function, construction, and maintenance. Additionally, as wildfires are predominately rapid events, the length of a heating event is relevant to distinguishing between natural or likely anthropogenic fire traces (Buenger, 2003; Gowlett et al., 2017). Addressing duration can in this way provide a crucial lens for interpreting and understanding ancient fire use and maintenance. This study explicitly includes duration as an experimental variable to test if duration times can impact the results of heating on bone material. Using the combined methods of macroscopic color evaluation and spectroscopic testing with FTIR-ATR we demonstrate that the relative length of the duration of a combustion event can be inferred. Duration of a fire event is relevant to several fire using behaviors and fire functions and potentially distinguishing natural and anthropogenic fires, therefore providing a new lens by which to interpret archaeological burnt bone.

Primarily, prolonged exposure to heat in oxygen environments depletes the combusted organic content of bone and therefore changes the visible color to resemble bone that are heated to higher temperatures. This is as the organic components in bones burnt to high temperatures in oxygen atmospheres are eliminated quickly and completely. This is demonstrated in this experiment by bones heated for 9 and 48 hours at 300°C and 550°C which are light greys and white in color, but are not calcined. These samples at 300° and 550°C are depigmented due to organic deletion from prolonged heat duration, demonstrated by the CO/P ratio, and their structural and chemical compositions have limited changes to the bioapatite crystal sizes and crystallinity which do not constitute the calcination. The recognition of archaeological or experimental bones which are muted white, grey, and tan in color as represented from the Munsell color schema therefore are not always directly representative of high temperatures but can be verified with spectroscopic testing to recognize structural and chemical changes that constitute calcination.

This study also demonstrates that temperatures slightly above 550°C are likely reaching the necessary conditions for bones to calcine. Otherwise, it is only with high temperatures consistent with the reported thresholds for bioapatite recrystallization, here represented by the 750°C trials, that the bioapatite crystals consistently and spontaneously grow. Future work can be designed to address when duration periods begin to impact bone material, the differences under reduction atmospheres, as well as compare measures of friability and surface warping on these depigmented but not calcined samples to clarify the relationship between time length, temperature, and material properties of bone heated under different conditions.

As bones in this study which were exposed to lower temperatures (here 300°C and, generally, 550°C) over long durations do not experience fusion and inversion stages of thermal alteration, but still show macroscopic discoloration resembling those of calcination, specimens which have been burned for long time periods at low temperatures should be recognizable in archaeological contexts to provide a signal of duration. The massive average crystallite size (here measured with XRD) for samples burned at 750°C for 9 hours also indicate a possible avenue for testing duration in archaeological samples which would all previously be considered highly burnt or heat altered, i.e. a Stiner et al. (1995) Stage 6 bone fragment. Bones heated at temperatures of 750 C for a duration of 9 hours (in additional to an extended cooling period) show crystal growth that exceeded referential crystallite sizes when compared to those of bones burned at high temperatures at durations between 30 minutes and 1 hour 30 minutes (Gallo et al., 2021). To screen for duration in a zooarchaeological study of archaeological fire proxies, data from this experiment recommend conducting spectroscopic testing primarily with FTIR-ATR on samples which would be classified based on macroscopic color evaluations as calcined and testing for true signals of structural and chemical calcination (the presence of high temperature dependent peaks, high calculated infrared SF, little to no organic content). Subsequent to FTIR-ATR testing, we suggest further XRD analyses to calculate average crystallite sizes for samples that are demonstrated to be calcined to infer the extent of the bioapatite transformations. Spectroscopic sampling strategies will likely fluctuate considering the different parameters and conditions of the archaeological assemblage, but large sampling procedures are made reasonable by the relatively low cost, minimal sample material, and minimal preparation needed for these analyses.

Adding the variable of duration to parameters which can investigate archaeological fire traces will provide opportunities to better distinguish fire function and the social and economic role of fire for hominins. Especially for sites with excellent preservation in which distinct features can be identified, researchers can address variability within features and look to ethnoarchaeological correlates to understand the connections between duration and function, i.e. relatively long duration, low temperature, smoking fires for drying animal remains (Mallol and Henry, 2017). The dimension of duration can address questions central to the behaviors surrounding fire use and maintenance to support studies considering fire as an artifact, a product of human technology.

This present study impacts both the use of bone used to investigate properties of anthropogenic fire and the greater zooarchaeological recognition of calcination, as calcined bone is a reliable source of inorganic C14 for radiocarbon dating as the large bioapatite crystals of true calcined bone provide protections from diagenetic substitutions of carbon (Lanting et al. 2001; Zazzo and Saliege 2011). Primarily, rather than viewing the potentially deceiving coloration of bone as a weakness, it can be a strength for the recognition of long duration times when macroscopic observations are considered alongside spectroscopic analyses. This multiscale approach can combine the ease of analysis of traditional zooarchaeological methodologies which classify burnt bone on macroscopic observations alongside a sampling strategy to use spectroscopic methods for verification of burning temperature, atmosphere, and now indicators of duration to address outstanding questions of fire use and behavior in the past.

Conclusions

Duration times of anthropogenic fire are integrally related to the social, economic, and technological behaviors most important to understanding fire use and control, such as fire function, maintenance, and fuel procurement. Contextualizing and detecting prolonged heating environments provides an extremely valuable and previously unaddressed dimension of ancient fires which can be combined with other observations of temperature and burning atmosphere to assist with determining likelihoods of behavioral possibilities. The identification of long duration fires in archaeological setting can also help researchers more confidently distinguish between primarily quick-moving and ephemeral wildfires and anthropogenic intentional combustion features.

Bone is a powerful proxy for ancient fire because it can provide complementary data to other studies of heat alteration utilizing lithic, charcoal, and geochemical studies. Bone is also more likely to preserve compared to charcoal and as it can provide specific information on heating properties that burned lithics cannot address. Zooarchaeological studies incorporating heated and burnt bone to interpret primary burning locations, combustion feature temperatures and burning atmospheres, and fuel strategies therefore must consider the variance in burnt bone appearance and chemistry, as macroscopic visual observations alone may not accurately describe burning conditions.

Bone which is muted in color and can be recognized as heated or burnt burnt through other visible cues (e.g. surface texture, weight) but without the chemical or structural signatures of high heat alteration and calcination can therefore be explored further as examples of prolonged heating. Methodological recommendations resulting from this study for the incorporation and interpretation of burnt bone are to systematically use different scales of analyses to sample faunal assemblages, including the standard visual cues alongside spectroscopic analyses, to best categorize and describe ancient fire conditions. This study shows duration can be estimated with archaeological samples.

Alongside this robust reference collection, future research must also consider the starting condition of bone (i.e. fresh or weathered), different diagenetic conditions, and different types of bone tissue and species to fully understand the material properties of burnt bone and extrapolate highly compelling behaviors of fire using hominins.

Ethics and disclosure paragraph re use of animal bones

All animal remains utilized in this study were obtained through a local butchery where animals prepared for consumption were euthanized humanely (stunned before exsanguination) following German government standards through the Federal Ministry of Food, Agriculture, and Forestry. These guidelines were established to ensure the welfare of animals within the German state.

References

Abdolahzadeh, A., McPherron, S. P., Sandgathe, D. M., Schurr, T. G., Olszewski, D. I., & Dibble, H. L. (2022). Investigating variability in the frequency of fire use in the archaeological record of Late Pleistocene Europe. *Archaeological and Anthropological Sciences*, *14*(4), 1-26.

Albert, R. M., Berna, F., & Goldberg, P. (2012). Insights on Neanderthal fire use at Kebara Cave (Israel) through high resolution study of prehistoric combustion features: Evidence from phytoliths and thin sections. *Quaternary International*, *247*, 278-293.

Alperson-Afil, N., & Goren-Inbar, N. (2010). *The Acheulian site of Gesher Benot Ya'aqov volume II: Ancient flames and controlled use of fire*. Springer Science & Business Media.

Bala, Y., Farlay, D., & Boivin, G. (2013). Bone mineralization: from tissue to crystal in normal and pathological contexts. *Osteoporosis international*, *24*(8), 2153-2166.

Barkai, R., Rosell, J., Blasco, R., & Gopher, A. (2017). Fire for a reason: Barbecue at middle Pleistocene Qesem cave, Israel. *Current Anthropology*, *58*(S16), S314-S328.

Beasley, M. M., Bartelink, E. J., Taylor, L., & Miller, R. M. (2014). Comparison of transmission FTIR, ATR, and DRIFT spectra: implications for assessment of bone bioapatite diagenesis. *Journal of Archaeological Science*, *46*, 16-22.

Bellomo, R. V. (1993). A methodological approach for identifying archaeological evidence of fire resulting from human activities. *Journal of Archaeological Science*, *20*(5), 525-553.

Bennett, J. L. (1999). Thermal alteration of buried bone. *Journal of Archaeological Science*, *26*(1), 1-8.

Berna, F., Matthews, A., & Weiner, S. (2004). Solubilities of bone mineral from archaeological sites: the recrystallization window. *Journal of archaeological Science*, *31*(7), 867-882.

Blasco, R., Rosell, J., Sanudo, P., Gopher, A., & Barkai, R. (2016). What happens around a fire: faunal processing sequences and spatial distribution at Qesem Cave (300 ka), Israel. *Quaternary International*, *398*, 190-209.

Bruno, T. J. (1999). Sampling accessories for infrared spectrometry. *Applied Spectroscopy Reviews*, *34*(1-2), 91-120.

Buenger, B. A. (2003). *The impact of wildland and prescribed fire on archaeological resources*. University of Kansas.

Buikstra, J. E., & Swegle, M. (1989). Bone modification due to burning: experimental evidence. *Bone modification*, 247-258.

Costamagno, S., Thery-Parisot, I., Brugal, J. P., & Guibert, R. (2005). Taphonomic consequences of the use of bones as fuel. Experimental data and archaeological applications. *Biosphere to lithosphere: new studies in vertebrate taphonomy*, 51-62.

Costamagno, S., Théry-Parisot, I., Castel, J. C., & Brugal, J. P. (2009). Combustible ou non? Analyse multifactorielle et modèles explicatifs sur des ossements brûlés paléolithiques. *GESTION DES COMBUSTIBLES AU PALÉOLITHIQUE ET AU MÉSOLITHIQUE NOUVEAUX OUTILS, NOUVELLES INTERPRÉTATIONS FUEL MANAGEMENT DURING THE PALAEOLITHIC AND MESOLITHIC PERIOD*, 61.

Dal Sasso, G., Asscher, Y., Angelini, I., Nodari, L., & Artioli, G. (2018). A universal curve of apatite crystallinity for the assessment of bone integrity and preservation. *Scientific reports*, *8*(1), 1-13.

David, B. (1990). How was this bone burnt. *Problem Solving in Taphonomy: Archaeological and Paleontological Studies from Europe, Africa and Oceania*, *2*, 65-79.

Drouet, C., Aufray, M., Rollin-Martinet, S., Vandecandelaère, N., Grossin, D., Rossignol, F., ... & Rey, C. (2018). Nanocrystalline apatites: The fundamental role of water. *American Mineralogist: Journal of Earth and Planetary Materials*, *103*(4), 550-564.

Dupras, T. L., & Schultz, J. J. (2013). Taphonomic bone staining and color changes in forensic contexts. *Manual of forensic taphonomy*, 315-340.

Ellingham, S. T., Thompson, T. J., Islam, M., & Taylor, G. (2015). Estimating temperature exposure of burnt bone—A methodological review. *Science & Justice*, *55*(3), 181-188.

Ellingham, S. T., Thompson, T. J., & Islam, M. (2016). The effect of soft tissue on temperature estimation from burnt bone using Fourier transform infrared spectroscopy. *Journal of forensic sciences*, *61*(1), 153-159.

Etok, S. E., Valsami-Jones, E., Wess, T. J., Hiller, J. C., Maxwell, C. A., Rogers, K. D., ... & Woodgate, S. L. (2007). Structural and chemical changes of thermally treated bone apatite. *Journal of Materials Science*, *42*(23), 9807-9816.

Figueiredo, M. J. D. F. M. D., Fernando, A., Martins, G., Freitas, J., Judas, F., & Figueiredo, H. (2010). Effect of the calcination temperature on the composition and microstructure of hydroxyapatite derived from human and animal bone. *Ceramics international*, *36*(8), 2383-2393.

Gallo, G., Fyhrie, M., Paine, C., Ushakov, S. V., Izuho, M., Gunchinsuren, B., ... & Navrotsky, A. (2021). Characterization of structural changes in modern and archaeological burnt bone: Implications for differential preservation bias. *PloS one*, *16*(7), e0254529.

Gianfrate, G., D'Elia, M., Quarta, G., Giotta, L., Valli, L., & Calcagnile, L. (2007). Qualitative application based on IR spectroscopy for bone sample quality control in radiocarbon dating. *Nuclear Instruments and Methods in Physics Research Section B: Beam Interactions with Materials and Atoms*, *259*(1), 316-319.

Gifford-Gonzalez, D. (1989). Ethnographic analogues for interpreting modified bones: some cases from East Africa. *Bone modification*, 179-246.

Goldberg, P., Dibble, H., Berna, F., Sandgathe, D., McPherron, S. J., & Turq, A. (2012). New evidence on Neandertal use of fire: examples from Roc de Marsal and Pech de l'Azé IV. *Quaternary International*, *247*, 325-340.

Goldberg, P., Miller, C. E., & Mentzer, S. M. (2017). Recognizing fire in the Paleolithic archaeological record. *Current Anthropology*, *58*(S16), S175-S190.

Gowlett, J. A. J., Brink, J. S., Caris, A., Hoare, S., & Rucina, S. M. (2017). Evidence of burning from bushfires in southern and east Africa and its relevance to hominin evolution. *Current Anthropology*, *58*(S16), S206-S216.

Hedges, R. E. (2002). Bone diagenesis: an overview of processes. *Archaeometry*, *44*(3), 319-328.

Henry, A. G. (2017). Neanderthal cooking and the costs of fire. *Current Anthropology*, *58*(S16), S329-S336.

Henry, A. G., Büdel, T., & Bazin, P. L. (2018). Towards an understanding of the costs of fire. *Quaternary International*, *493*, 96-105.

Herrmann, N. P., & Bennett, J. L. (1999). The differentiation of traumatic and heat-related fractures in burned bone. *Journal of Forensic Science*, *44*(3), 461-469.

Hoare, S. (2020). Assessing the function of palaeolithic hearths: experiments on intensity of luminosity and radiative heat outputs from different fuel sources. *Journal of Paleolithic Archaeology*, *3*(4), 537-565.

Hollund, H. I., Ariese, F., Fernandes, R., Jans, M. M. E., & Kars, H. (2013). Testing an alternative high-throughput tool for investigating bone diagenesis: FTIR in attenuated total reflection (ATR) mode. *Archaeometry*, *55*(3), 507-532.

Koeppenkastrop, D., & Eric, H. (1992). Sorption of rare-earth elements from seawater onto synthetic mineral particles: An experimental approach. *Chemical geology*, *95*(3-4), 251-263.

Kozowyk, P. R., Soressi, M., Pomstra, D., & Langejans, G. H. (2017). Experimental methods for the Palaeolithic dry distillation of birch bark: implications for the origin and development of Neandertal adhesive technology. *Scientific reports*, *7*(1), 1-9.

Lebon, M., Zazzo, A., & Reiche, I. (2014). Screening in situ bone and teeth preservation by ATR-FTIR mapping. *Palaeogeography, Palaeoclimatology, Palaeoecology*, *416*, 110-119.

Lebon, M., Reiche, I., Gallet, X., Bellot-Gurlet, L., & Zazzo, A. (2016). Rapid quantification of bone collagen content by ATR-FTIR spectroscopy. *Radiocarbon*, *58*(1), 131-145.

Leierer, L., Alonso, Á. C., Pérez, L., Lagunilla, Á. H., Herrera-Herrera, A. V., Connolly, R., ... & Mallol, C. (2020). It's getting hot in here–Microcontextual study of a potential pit hearth at the Middle Paleolithic site of El Salt, Spain. *Journal of Archaeological Science*, *123*, 105237.

Lyman, R. L., & Lyman, C. (1994). *Vertebrate taphonomy*. Cambridge University Press.

Mallol, C., Hernández, C. M., Cabanes, D., Machado, J., Sistiaga, A., Pérez, L., & Galván, B. (2013). Human actions performed on simple combustion structures: an experimental approach to the study of Middle Palaeolithic fire. *Quaternary International*, *315*, 3-15.

Mallol, C., Marlowe, F. W., Wood, B. M., & Porter, C. C. (2007). Earth, wind, and fire: ethnoarchaeological signals of Hadza fires. *Journal of Archaeological Science*, *34*(12), 2035-2052.

Mallol, C., & Henry, A. (2017). Ethnoarchaeology of Paleolithic fire: methodological considerations. *Current Anthropology*, *58*(S16), S217-S229.

Mamede, A. P., Gonçalves, D., Marques, M. P. M., & Batista de Carvalho, L. A. (2018). Burned bones tell their own stories: A review of methodological approaches to assess heat-induced diagenesis. *Applied Spectroscopy Reviews*, *53*(8), 603-635.

Martin, R. B., Burr, D. B., Sharkey, N. A., & Fyhrie, D. P. (2015). *Skeletal Tissue Mechanics*. Springer.

Marques, M. P. M., Mamede, A. P., Vassalo, A. R., Makhoul, C., Cunha, E., Gonçalves, D., ... & Batista de Carvalho, L. A. E. (2018). Heat-induced bone diagenesis probed by vibrational spectroscopy. *Scientific reports*, *8*(1), 1-13.

Mayne Correia, P. (1997). Fire modification of bone: a review of the literature. *Forensic taphonomy: the postmortem fate of human remains*, 275-293.

Munsell Color (Firm). (2010). Munsell soil color charts : with genuine Munsell color chips. Grand Rapids, MI :Munsell Color.

Nakamoto, K. (2009). *Infrared and Raman spectra of inorganic and coordination compounds, part B: applications in coordination, organometallic, and bioinorganic chemistry*. John Wiley & Sons.

Nyman, J. S., Ni, Q., Nicolella, D. P., & Wang, X. (2008). Measurements of mobile and bound water by nuclear magnetic resonance correlate with mechanical properties of bone. *Bone*, *42*(1), 193-199.

Piga, G., Malgosa, A., Thompson, T. J. U., & Enzo, S. (2008). A new calibration of the XRD technique for the study of archaeological burned human remains. *Journal of Archaeological Science*, *35*(8), 2171-2178.

Piga, G., Gonçalves, D., Thompson, T., Brunetti, A., Malgosa, A., & Enzo, S. (2016). Understanding the crystallinity indices behavior of burned bones and teeth by ATR-IR and XRD in the presence of bioapatite mixed with other phosphate and carbonate phases. *International Journal of Spectroscopy*.

Pollock, C. R., Pokines, J. T., & Bethard, J. D. (2018). Organic staining on bone from exposure to wood and other plant materials. *Forensic Science International*, *283*, 200-210.

Pramanik, S., Hanif, A. S. M., Pingguan-Murphy, B., & Abu Osman, N. A. (2012). Morphological change of heat treated bovine bone: a comparative study. *Materials*, *6*(1), 65-75.

Pyne, S. J., Andrews, P. L., & Laven, R. D. (1996). Introduction to wildland fire, revised 2nd edn.

Ramirez-Gutierrez, C. F., Londoño-Restrepo, S. M., Del Real, A., Mondragón, M. A., & Rodriguez-García, M. E. (2017). Effect of the temperature and sintering time on the thermal, structural, morphological, and vibrational properties of hydroxyapatite derived from pig bone. *Ceramics International*, *43*(10), 7552-7559.

Ravaglioli, A., Krajewski, A., Celotti, G. C., Piancastelli, A., Bacchini, B., Montanari, L., ... & Piombi, L. (1996). Mineral evolution of bone. *Biomaterials*, *17*(6), 617-622.

Reidsma, F. H., van Hoesel, A., van Os, B. J., Megens, L., & Braadbaart, F. (2016). Charred bone: Physical and chemical changes during laboratory simulated heating under reducing conditions and its relevance for the study of fire use in archaeology. *Journal of Archaeological Science: Reports*, *10*, 282-292.

Revedin, A., Grimaldi, S., Florindi, S., Santaniello, F., & Aranguren, B. (2020). Experimenting the use of fire in the operational chain of prehistoric wooden tools: the Digging Sticks of Poggetti Vecchi (Italy). *Journal of Paleolithic Archaeology*, *3*(4), 525-536.

Rey, C., Combes, C., Drouet, C., & Glimcher, M. J. (2009). Bone mineral: update on chemical composition and structure. *Osteoporosis international*, *20*(6), 1013-1021.

Reynard, B., Lécuyer, C., & Grandjean, P. (1999). Crystal-chemical controls on rare-earth element concentrations in fossil biogenic apatites and implications for paleoenvironmental reconstructions. *Chemical Geology*, *155*(3-4), 233-241.

Rietveld, H. M. (1969). A profile refinement method for nuclear and magnetic structures. *Journal of applied Crystallography*, *2*(2), 65-71.

Rollin-Martinet, S., Navrotsky, A., Champion, E., Grossin, D., & Drouet, C. (2013). Thermodynamic basis for evolution of apatite in calcified tissues. *American Mineralogist*, *98*(11-12), 2037-2045.

Sandgathe, D. M., & Berna, F. (2017). Fire and the genus Homo: An introduction to supplement 16. *Current Anthropology*, *58*(S16), S165-S174.

Santana, V. M., Baeza, M. J., & Blanes, M. C. (2013). Clarifying the role of fire heat and daily temperature fluctuations as germination cues for Mediterranean Basin obligate seeders. *Annals of botany*, *111*(1), 127-134.

Schiegl, S., Goldberg, P., Pfretzschner, H. U., & Conard, N. J. (2003). Paleolithic burnt bone horizons from the Swabian Jura: distinguishing between in situ fireplaces and dumping areas. *Geoarchaeology: an international journal*, *18*(5), 541-565.

Schmidt, P., Blessing, M., Rageot, M., Iovita, R., Pfleging, J., Nickel, K. G., ... & Tennie, C. (2019). Birch tar production does not prove Neanderthal behavioral complexity. *Proceedings of the National Academy of Sciences*, *116*(36), 17707-17711.

Scott, A. C. (2000). The Pre-Quaternary history of fire. *Palaeogeography, palaeoclimatology, palaeoecology*, *164*(1-4), 281-329.

Scott, A. C. (2009). Forest fire in the fossil record. In *Fire effects on soils and restoration strategies* (pp. 17-54). CRC Press.’’

Shahack-Gross, R., Berna, F., Karkanas, P., Lemorini, C., Gopher, A., & Barkai, R. (2014). Evidence for the repeated use of a central hearth at Middle Pleistocene (300 ky ago) Qesem Cave, Israel. *Journal of archaeological science*, *44*, 12-21.

Shipman, P., Foster, G., & Schoeninger, M. (1984). Burnt bones and teeth: an experimental study of color, morphology, crystal structure and shrinkage. *Journal of archaeological science*, *11*(4), 307-325.

Snoeck, C., Brock, F., & Schulting, R. J. (2014). Carbon exchanges between bone apatite and fuels during cremation: impact on radiocarbon dates. *Radiocarbon*, *56*(2), 591-602.

Snoeck, C., & Schulting, R. J. (2013). Fire and Bone: An experimental study of cremation. *Exarc Journal*, (EXARC Journal Issue 2013/2).

Snoeck, C., Schulting, R. J., Lee-Thorp, J. A., Lebon, M., & Zazzo, A. (2016). Impact of heating conditions on the carbon and oxygen isotope composition of calcined bone. *Journal of Archaeological Science*, *65*, 32-43.

Stahlschmidt, M. C., Mallol, C., & Miller, C. E. (2020). Fire as an artifact—advances in paleolithic combustion structure studies: Introduction to the special issue. *Journal of Paleolithic Archaeology*, *3*(4), 503-508.

Stahlschmidt et al., TORTOISE PAPER? CAN/ SHOULD I MENTION IT?

Stiner, M. C., Kuhn, S. L., Weiner, S., & Bar-Yosef, O. (1995). Differential burning, recrystallization, and fragmentation of archaeological bone. *Journal of archaeological science*, *22*(2), 223-237.

Stinson, K.J., Wright, H.A.(1969). Temperatures of Headfires in the Southern Mixed Prairie of Texas. Journal of Range Management, *22*, 169-177.

Stout, S. D., Cole, M. E., & Agnew, A. M. (2019). Histomorphology: Deciphering the metabolic record. In *Ortner's identification of pathological conditions in human skeletal remains* (pp. 91-167). Academic Press.

Téllez, E., Saladié, P., Pineda, A., Marín, J., Vallverdú, J., Chacón, M. G., & Carbonell, E. (2022). Incidental burning on bones by Neanderthals: the role of fire in the Qa level of Abric Romaní rock-shelter (Spain). *Archaeological and Anthropological Sciences*, *14*(6), 1-20.

Théry-Parisot, I. (2002). Fuel management (bone and wood) during the Lower Aurignacian in the Pataud rock shelter (Lower Palaeolithic, Les Eyzies de Tayac, Dordogne, France). Contribution of experimentation. *Journal of Archaeological Science*, *29*(12), 1415-1421.

Théry-Parisot, I., & Henry, A. (2012). Seasoned or green? Radial cracks analysis as a method for identifying the use of green wood as fuel in archaeological charcoal. *Journal of Archaeological Science*, *39*(2), 381-388.

Thompson, T. (2004). Recent advances in the study of burned bone and their implications for forensic anthropology. *Forensic science international*, *146*, S203-S205.

Thompson, T. (2005). Heat-induced dimensional changes in bone and their consequences for forensic anthropology. *Journal of Forensic Science*, *50*(5), JFS2004297-8.

Thompson, T. J. U., Islam, M., & Bonniere, M. (2013). A new statistical approach for determining the crystallinity of heat-altered bone mineral from FTIR spectra. *Journal of Archaeological Science*, *40*(1), 416-422.

Trueman, C. N., Privat, K., & Field, J. (2008). Why do crystallinity values fail to predict the extent of diagenetic alteration of bone mineral?. *Palaeogeography, Palaeoclimatology, Palaeoecology*, *266*(3-4), 160-167.

Turner, E., Hutson, J., Villaluenga, A., García Moreno, A., & Gaudzinski-Windheuser, S. (2018). Bone staining in waterlogged deposits: a preliminary contribution to the interpretation of near-shore find accumulation at the Schöningen 13II-4 'Spear-Horizon'site, Lower Saxony, Germany. *Historical Biology*, *30*(6), 767-773.

Ubelaker, D. H. (2009). The forensic evaluation of burned skeletal remains: a synthesis. *Forensic science international*, *183*(1-3), 1-5.

Vallverdú, J., Alonso, S., Bargalló, A., Bartrolí, R., Campeny, G., Carrancho, Á., ... & Carbonell, E. (2012). Combustion structures of archaeological level O and mousterian activity areas with use of fire at the Abric Romaní rockshelter (NE Iberian Peninsula). *Quaternary International*, *247*, 313-324.

van Hoesel, A., Reidsma, F. H., van Os, B. J., Megens, L., & Braadbaart, F. (2019). Combusted bone: Physical and chemical changes of bone during laboratory simulated heating under oxidising conditions and their relevance for the study of ancient fire use. *Journal of Archaeological Science: Reports*, *28*, 102033.

Vidal-Matutano, P. (2017). Firewood and hearths: Middle Palaeolithic woody taxa distribution from El Salt, stratigraphic unit Xb (Eastern Iberia). *Quaternary International*, *457*, 74-84

Wadley, L., Esteban, I., De La Peña, P., Wojcieszak, M., Stratford, D., Lennox, S., ... & Sievers, C. (2020). Fire and grass-bedding construction 200 thousand years ago at Border Cave, South Africa. *Science*, *369*(6505), 863-866.

Weiner, S., & Bar-Yosef, O. (1990). States of preservation of bones from prehistoric sites in the Near East: a survey. *Journal of Archaeological Science*, *17*(2), 187-196.

Whelan, R. J. (1995). *The ecology of fire*. Cambridge university press.

Wright, H. A., & Bailey, A. W. (1982). *Fire ecology: United states and southern canada*. John Wiley & Sons.

Zazzo, A., Saliege, J. F., Person, A., & Boucher, H. (2009). Radiocarbon dating of calcined bones: Where does the carbon come from?. *Radiocarbon*, *51*(2), 601-611.

Zhang, G., Deng, X., Guan, F., Bai, Z., Cao, L., & Mao, H. (2018). The effect of storage time in saline solution on the material properties of cortical bone tissue. *Clinical biomechanics*, *57*, 56-66.

Chapter 4

Summary of faunal evidence for Neanderthal fire use at Roc de Marsal (SW France), layer 9.

Abstract

Fire presence within many Middle Paleolithic Neanderthal sites is well established, but far less is known regarding the burning conditions and fire using behaviors represented by these combustion features. Fire evidence here is considered within the faunal assemblage of layer 9 of Roc de Marsal (SW France) to describe fire feature temperatures, contents, and fuel strategies utilizing traditional methodologies at several scales of analysis (piece plotted and screened material) alongside infrared spectroscopy (FTIR-ATR, mFTIR), micromorphological observations, and spatial analyses. The majority of the zooarchaeological evidence for fire is identified here in the coarse fraction (< 2.5 cm), demonstrating the importance of screened materials for the identification and study of archaeological fire. Spatial and temperature intensity patterning are noted within the entire faunal assemblage corresponding to locations of identified combustion features, representing differences in Neanderthal fire use and maintenance, potentially related to different fire functions. Overall, fauna remains are established as an appropriate tool for describing combustion features, and they provide complementary information to lithic, paleobotanical, and geological analyses of fire proxies.

Introduction

The manipulation of fire is a uniquely human trait that provides warmth, light, and the ability to modify food and other raw materials. Hearths are also noted to be catalysts for social interaction in modern human populations, as fires extend visibility and lengthen the day (Wiessner, 2014). The timing of habitual fire use for hominins is highly debated, with the archaeological visibility of fire seen at increasing frequencies after 400 ka (Roebroeks and Villa, 2011). This transition is hypothesized to be supported by cultural transmission and diffusion processes and not repeated independent invention of fire technology, despite fire presence still only sporadically recognized even at 200 ka (Chazan, 2017; MacDonald et al., 2021; Stahlschmidt et al., 2015).

Evidence for anthropogenic *Homo sapiens* fire use within the African Middle Stone Age (MSA), ~350-35 ka, documents use of fire technology for site maintenance, such as clearing bedding material, and for the heat treating of silcrete (Blackwell et al., 2018; Brown et al., 2009; MacDonald et al., 2021; Schmidt et al., 2016; Schmidt et al., 2020; Wadley et al., 2020). In western Europe, observational similarities in anatomically modern humans (AMH) fire features are found at several Upper Paleolithic (UP) sites in the early Aurignacian of SW France (~33-32 ka) and these patterns of fire technology have been argued to demonstrate standardized systems of fire management (White et al., 2017). White et al. (2017) suggest that the qualitative patterns between fire features at these sites are evidence of consistent maintenance strategies and an adaptation to glacial conditions. Fire strategies documented within a broad range of UP European sites ~48-13 ka are also found to increase in complexity, intensity, and in types of combustion feature forms (Murphee and Aldeias, 2022). Murphee and Aldeias (2022) describe a shift in pyrotechnology coinciding with the Gravettian culture (32-28 cal Before Present, BP) related to increased intensive use, and a diversity in complexity of fire features that include fire for the creation of symbolic material culture. These sophisticated technologies and use of fire support inferences about the role of fire in the everyday life of UP European AMH in the face of increasingly cold conditions prior to the glacial maximum.

Fire use is noted to be common in western European Middle Paleolithic (MP) contexts associated with Neanderthals, but it has been suggested that potentially while some of these Neanderthal groups (who were contemporaneous to the African MSA modern humans) exhibited the ability to use fire, some populations may not have been obligate fire users (Allue et al., 2022; Dibble et al., 2017; Roebroeks and Villa, 2011; Sandgathe et al., 2011). This is because fire is not always found in every Neanderthal MP layer of every site, most notably absent in layers occurring in colder periods in Southwestern France, and the frequency of detected fire presence does not fully address if Neanderthals habitually used and were dependent on pyrotechnology.

Differences between Neanderthal and subsequent AMH fire use in western Europe may be influenced by differential preservation impacting older assemblages, changing patterns in Neanderthal mobility strategies affecting where fires were utilized and therefore detected, and different standards of assessing behaviors between these hominins. Historical biases in the interpretation of Neanderthal behavior may potentially be highlighting and emphasizing the perceived absence of fire, whereas the same questions have not been asked in AMH European contexts due to the presumption of *Homo sapiens* fire mastery in the UP. Investigating Neanderthal fire absence has, however, prompted researchers to explore the many caloric energy costs to maintaining fires and the potential ways hominins can survive northern latitudes without dependent fire usage (Dibble et al., 2017; Henry, 2017; Henry et al., 2018). These observations are relevant to both Neanderthal and modern humas, and there is much to be learned in regards to fire technologies and the roles of fire for both groups of hominins.

Questions of Neanderthal fire knowledge and the roles of fire for Neanderthal communities therefore address behavioral signatures both within the western European MP but also between contemporaneous African MSA and later European UP AMH. Fully documenting and comparing Neanderthal and African MSA fire technology also can contribute to greater understanding of fire use for the last common ancestor of these populations. Every Neanderthal MP fire event provides an opportunity to better contextualize the role of fire within Neanderthal lifeways and observe decisions that groups made relative to their energetic needs. This includes both the benefits gained from fire use (i.e. cooking to increase the efficiency of mastication) and the costs, including the caloric burden of fuel procurement (Henry, 2017; Henry et al., 2018; Van Casteren et al., 2022).

Simple, open, and flat combustion features that are characteristically found in the European MP are still the product of several interactions and decisions between the past hominins and their environment, even if not as diverse as in later stages of pyrotechnological systems described for AMH UP (Allue et al., 2022; Murphee and Aldeias, 2022). These technological choices tied to fire use and maintenance are relevant and embedded in social and economic lifeways even in non-constructed features, as fire use is linked to the modification of food, tools, and environment through the production of heat and light. Technological sequences relevant to pyrotechnology include fuel preparation and gathering, the ignition of the fire, fire use, fire maintenance and event duration, and extinguishing (trampling, sweeping, ash dumping, etc.). Evidence to address each of these stages provides insight into aspects of Neanderthal behavior such as: resource availability and mobility ranges, the structure and use of space, site maintenance, specific functions such as cooking and the production of tar, and duration of fire event necessitating continual curation and potentially communal functions.

Documenting the Neanderthals’ fire strategies, and further, the degree of variation seen within MP pyrotechnology, has not yet been attempted at a large scale, nor in a comparative framework. This is likely due to the lack of standardization in methodological approaches and site-specific biases which may impact comparisons. The aim of this study is to present a methodological framework for a zooarchaeological perspective of fire technology to contribute to a multiscale effort approaching fire as an artifact, the product of hominin action and use (Allue et al., 2022; Goldberg et al., 2017; Stahlschmidt et al., 2020). This framework includes interdisciplinary perspectives and the utilization of microcontext to investigate fire function and reconstruct patterns and processes of distinct fire using behaviors amongst Pleistocene hominins (Goldberg et al., 2017; Stahlschmidt et al., 2020).

The MP site of Roc de Marsal (RDM) provides an opportunity to research and compare zooarchaeological characteristics of Neanderthal fire technology, as layer 9 exhibits multiple combustion features from Marine Isotope Stage (MIS) 5 which are well documented from lithic, geoarchaeological, and traditional zooarchaeological perspectives (Aldeias et al., 2012; Dibble et al., 2018; Goldberg et al., 2012; Sandgathe et al., 2011). RDM is suitable for these analyses as layer 9 exhibits excellent preservation, little post depositional movement, and was excavated with modern excavation methodologies (Aldeias et al., 2012; Goldberg et al., 2012). Several in-situ combustion features have also been previously identified (Aldeias et al., 2012; Goldberg et al., 2012). This study utilizes burnt faunal remains to identify combustion feature locales and to investigate aspects of pyrotechnology related to maximum and dominant temperature thresholds, reduction conditions, fire duration, bone as fuel, and behaviors which resulted in bone being thermally altered (i.e. disposal and site maintenance).

Documented aspects of European MP Neanderthal fire use currently includes the presence of stacked hearths (Aldeias et al., 2012; Goldberg et al., 2012; Goldberg and Berna, 2010), trampling and ash dumping (Aldeias et al., 2012; Goldberg et al., 2012; Goldberg and Berna, 2010), burnt lithics (Abdolahzadeh et al., 2022; Vaquero et al., 2015), habitual use as inferred from frequency of burnt lithics (Shimelmitz et al., 2014) and from geochemical signatures (Brittingham et al., 2019), structuring activity areas (Clark, 2016; Spagnolo et al., 2018; Vallverdu et al., 2010; 2012), ephemeral fire potentially linked to high mobility patterns (Leierer et al., 2019), depressed pit hearths (Leierer et al., 2020); the production of birch tar (Boeda et al., 2008; Koller et al., 2001; Mazza et al., 2006), different wood and bone fuels (Costamagno et al., 2005; 2009; Vidal-Matutano et al., 2017; 2018), and use of fire in deep cave settings (Jaubert et al., 2016; for summary see Allue et al., 2022).

Despite the abundant positive evidence for Neanderthal European MP anthropogenic fires, the striking absences of fire visibility which cannot be explained by preservation or excavation biases has prompted researchers to propose that not all Neanderthals may have been obligate fire users (Dibble et al., 2018; Sandgathe et al., 2011). This pattern in fire absence challenges assumptions that humans necessarily depend on fire use and presents (not exclusive) scenarios such as Neanderthal groups losing the knowledge of fire technology, populations dependent on natural occurrences to utilize fire, or, fire economies potentially changing in response to different environmental factors and mobility patterns. All questions regarding Neanderthal’s relationship with fire can be addressed and explored by studying contexts in which MP fire is present, specifically considering the types and variation of fire technology exhibited to better extrapolate to periods in which fire is not seen in great frequencies.

Zooarchaeological approaches to the study of fire technology

Previous research utilizing burnt bone as a proxy for fire properties has resulted in a better understanding of behaviors related to cooking, waste disposal, cremation, fuel use, and the recognition of ancient natural fire (Clark and Ligouis, 2010; Costamagno et al., 2005; Gifford-

Gonzalez, 1989; Reidsma et al., 2016; Speth and Clark, 2006; Stiner et al., 1995; Thery-Parisot et al., 2005). Transformations which accompany the thermal alteration of bone are well documented, with early studies focusing on the macroscopic changes to bone color and texture, and more recent developments documenting the primary nano- and microscopic changes to bone mineral using approaches such as infrared spectroscopy (Chapters 2, 3; Buikstra and Swegle., 1989; Ellingham et al., 2015; Mamede et al., 2018; Shipman et al., 1989; Snoeck et al., 2014; Stiner et al., 1995; Thompson, 2004). Codifying burnt assemblages using traditional observational zooarchaeological scales of burning intensity alongside high-resolution spectroscopic analyses has the potential to directly address aspects of fire technology such as: the likely use of bone as fuel, the mean and maximum temperature thresholds reached in a given firing event, and the atmospheric burning conditions (i.e. reduction or oxidizing conditions), duration of fire event, and pre-burning bone status (Barkai et al., 2017; Chadefaux et al., 2009; Costamagno et al., 2005; 2009; Ellingham et al., 2015; Mamede et al., 2018; Thompson et al., 2013; Reidsma et al., 2016; Snoeck et al., 2014).

The thermal alteration of bone results in permanent changes to bone structure and chemistry which are still measurable after normal diagenetic processes (Chapter 2). Bone is a poorly crystalline hierarchal composite material composed of three major categories: water, organics (collagen), and mineral bioapatite (Martin et al., 2015; Stout et al., 2019). Bioapatite has a non -stoichiometric, carbonate-substituted hydroxyapatite composition: $Ca_{10-x}(PO_4)_{6-x}(HPO_4, CO_3)x(OH,1/2CO_3)_{2-x}$ with $0<x<2$ (Drouet et al., 2018; Mamede et al., 2018; Rey et al., 2009). Two types of substitutions which are commonly found within in vivo bone and are related to measures of thermal alteration include Type B, the more common, carbonate (CO_3^{2-}) substitution for phosphate groups (PO_4^{3-}) within the crystalline matrix, or carbonate (CO_3^{2-}) substitution for the hydroxyl groups (OH-) (LeGeros et al., 1969; Rey et al., 1989; for summary see Mamede et al., 2018).

Stages of thermal alteration are described in detail in this manuscript (Chapters 2 and 3) and can be summarized as first the loss of water and water organic content, then the structural carbonates are lost alongside final organic removal, and, at higher temperatures with structural reorganization, and the size and relative order of the mineral bioapatite crystals change dramatically. At extreme temperatures (> 1000 °C), bone ultimately transforms into β-tricalcium phosphate (β-TCP) (Piga et al., 2018). The use of Fourier-Transform Infrared Spectrometry (FTIR) and X-Ray Diffraction (XRD) can monitor these transformations, verifying burning and elucidating maximum temperature thresholds and burning conditions that cannot be mistaken for macroscopic staining or bleaching (Ellingham et al., 2015; Mamede et al., 2018; Piga et al., 2008; Shahack-Gross et al., 1997; Snoeck et al., 2014; Thompson, 2004).

Roc de Marsal (RDM)

RDM is a cave in the southwest of France, approximately 5 km south of Les Eyzies in a tributary river valley of the Vézère (Fig.1; Aldeias et al., 2012; Sandgathe et al., 2011). RDM has been extensively excavated since 1953, first under the direction of Jean Lafille, and later with excavations from 2004-2010 (Aldeias et al., 2012; Goldberg et al., 2012). The RDM stratigraphic sequence is currently divided into thirteen archaeological layers defined by sedimentological changes, comprising 2 meters spanning Marine Isotope Stages (MIS) 5-3 (Goldberg et al., 2012; Sandgathe et al., 2011). The dating of RDM is ongoing, with current thermoluminescence (TL) and single grain optical luminescence (OSL) data indicating that layers 9-7 correspond to MIS 4 (Guerin et al., 2012). The TL samples from layer 9 resulted in three dates spanning from 77.4

+/- 4.8 ka to 86.7 +/- 5.2 ka, although they have poor agreement with the OSL dates which suggest a younger occupation between 70-65 ka (Sandgathe et al., 2011; Guérin et al., 2012). Paleobotanical data indicates that layer 9 is likely from a warmer, wetter climate, which is also supported by the prevalence in this layer of temperate fauna such as red deer (*Cervus elpahus*); supporting a milder climate than the generally colder and arid MIS 4 as suggested by the luminescence results (Hodgkin et al., 2016; Wroth et al., 2019).

Layers 9-7 at the base of RDM have prevalent evidence for fire, and visible high frequencies of burnt bone, heat altered lithics, charcoal, ash units, and rubified sediments (Aldeias et al., 2012; Goldberg et al., 2012). The absence of visible fire proxies in the overlaying layers at RDM dating to Marine Isotope Stages 4 and 3 and associated with a reindeer-dominated faunal assemblage has opened many questions for researchers surrounding Neanderthal fire use because researchers assume that fire is beneficial in continental climates (Goldberg et al., 2012; Guerin et al., 2012; Sandgathe et al., 2011).

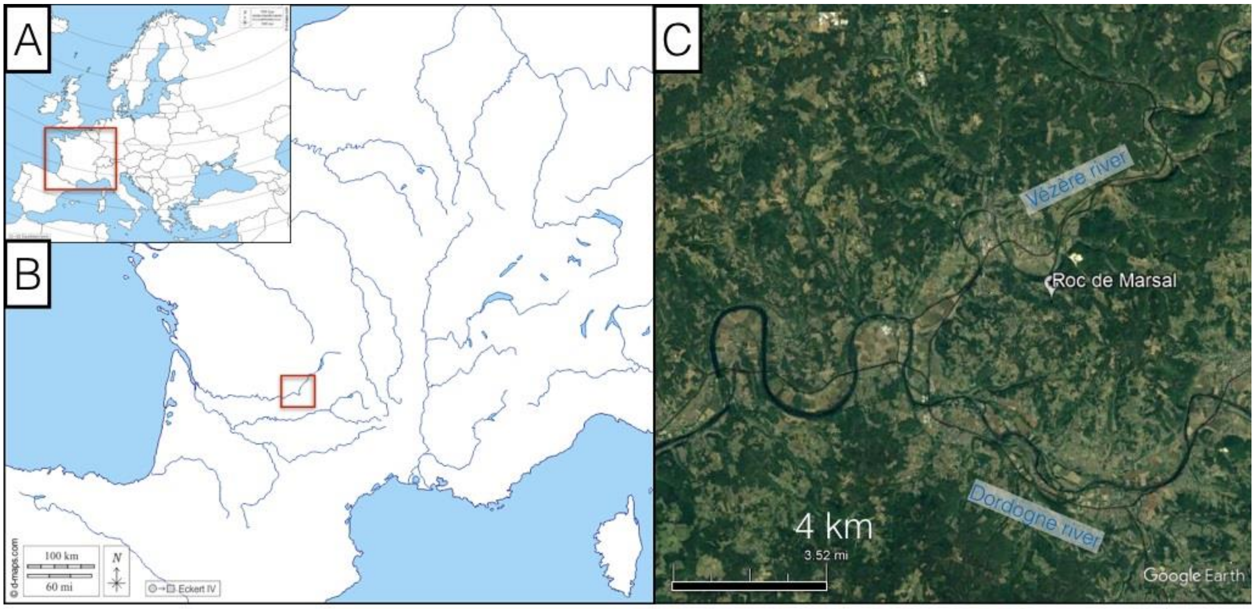

Fig 1: Map of France (A) with site Roc de Marsal situated in the southwest (B) along the Vézère river (C).

Fire properties at RDM have previously been approached through the study of spatial analyses of lithic discard and through geoarchaeological analyses with a particular focus on the organization of burnt and unburnt lithic artifacts, the spatial distributions of fire features, and sedimentary composition (Aldeias et al., 2012; Goldberg et al., 2012; Reeves et al., 2019; Sandgathe et al., 2011). Burned lithics ≥ 2.5 cm were visualized with Kernel density estimations, although no patterning was distinguishable horizontally or vertically (Aldeias et al., 2012). Reeves et al. (2019) also investigated repetitive behaviors, specifically in reference to lithic discard, with the use of Neighborhood analyses with Local Moran's I statistics. Reeves et al. (2019) found that combustion features did influence the structuring of space within RDM layers 9 and 7, and that scrapers, cores, and elevated levels of lithic breakage on flakes near burned areas were evidence of high activity areas. A discrepancy noted between the burned flake areas and the visible traces of fire from field observations, however, demonstrates the need for additional research to identify and study primary fire locations (Reeves et al., 2019).

Phytolith analyses from combustion feature and non-combustion feature areas of RDM layers 9 and 7 provide additional information regarding the nature of anthropogenic burning (Wroth et al., 2019). Phytolith densities are noted to be much greater at the bottom of the sequence, and variability is seen both between layers 9 and 7 and within the limits of combustion features and non-combustion areas of each fire-bearing layer (Wroth et al., 2019). Specifically, combustion feature areas of layers 9 and 7 have the highest concentration and variety of phytoliths when compared to other areas and layers of RDM, attesting to the important role plant material played in fire activities (Wroth et al., 2019). For layer 9 wood and bark dicotyledonous phytoliths constituted 30-50% of sampled material, indicating that wood fuel was used (Wroth et al., 2019). Grass phytoliths were also found in large quantities, potentially related to fire starting materials, ground cover surrounding the features, or the result of a combination of activities such as bedding or food resources (Wroth et al., 2019). Differences between layers 9 and 7 show relative increased percentages of melted phytoliths in layer 9 combustion features (2-5% of identified specimens) indicating high temperatures and/or longer durations of firing events when compared to combustion features form layer 7 (Wroth et al., 2019).

Geologically, layer 9 is described as a 5-10 cm thick substrate composed of clayey-silt with high concentrations of burnt materials, including lithics, charcoal, and fauna (Aldeias et al., 2012; Goldberg et al., 2012). Layer 9 has the most abundant evidence of burned accumulations within the sequence, with a minimum of 15 combustion features identified in excavation and subsequent laboratory analyses (Aldeias et al., 2012; Goldberg et al., 2012). The general morphology of these features was measured when observable, with an average length of 81.66 cm and an average thickness of 2.05 cm reported (Aldeias et al., 2012; Goldberg et al., 2012). In terms of their preservation, soil micromorphological analyses point to the presence of well-preserved and intact combustion features (as determined by intact lenses of ash superimposed on charcoal rich deposits which can, in turn, be overlaying heat-altered substrates), as well as features which have varied orientations of contents, inferred to be disturbed or displaced from their original position (Aldeias et al., 2012).

The internal components of these features vary, with some features dominated by ash lenses and others noted to be primarily composed of small, burned fauna (Goldberg et al., 2012). These differences are inferred to be the result of different burning behaviors and utilized fuels (Goldberg et al., 2012). Despite the excellent preservation and in-situ features, effects of trampling are still described as well as evidence of localized diagenetic alteration in the form of thin phosphatized ashes (Goldberg et al., 2012).

Prior zooarchaeological studies on RDM layer 9 and 7 demonstrate that high frequencies of red and roe deer are present in both layers, and sampled microfauna include the field vole, the garden door mouse, and the European pine vole, consistent with temperate climates (Castel et al., 2017; Hodgkins et al., 2016). Evidence for heavy carcass processing is also present, with abundant percussion and cut marks (Hodgkins et al., 2016).

A zooarchaeological perspective of burning has not yet been considered for the fauna of RDM layer 9, although burnt fauna from layer 4 has been studied and included in analyses utilizing combustion indices to discern between behaviors that result in bone being burnt (Castel et al., 2017; Costamagno et al., 2005. 2009). RDM layer 4 notably has a low signature of burnt bone presence, only 1.2% of screened and piece plotted fauna from 5 fully analyzed meter squares distributed throughout the site show heat alteration (Castel et al., 2017). This signature corresponds to a low frequency of more ephemeral fire residue such as charcoal and ash (Castel et al., 2017; Sandgathe et al, 2011). However, in one study, a sample of burnt fauna from layer 4 clusters with other assemblages attributed to purposeful burning due to the relative abundance of burnt spongey bone (Costamagno et al., 2009). A Principle Components Analyses considering metrics of burning could not distinguish, however, the intentional burning of spongey fragments which would support a bone fuel or maintenance strategy (Costamagno et al., 2009). Fauna with indications of burning are recovered in much larger amounts in layers 9 and 7 (Sandgathe et al., 2011). This study aims to provide a systematic study of the thermally altered fauna from RDM layer 9 to consider aspects of hearth functionality and fuel use, including the application of combustion indices following Costamagno et al., (2009), and will contribute complementary data to previous RDM investigations to address variability in MP pyrotechnology (Table 1).

Table 1: Faunal assemblage considered for this study and relation to prior work

Sample Category	**Previous studies**	**This study**
2.5 cm-6mm (coarse fraction of screened bone)	1922 fragments from randomized units of layer 9 considered in a study of taxonomic assessment, taxon abundance, and transport strategies (Hodgkins et al., 2016)	All coarse screened fragments from layer 9 are weighted, counted, and assigned burning scales following Stiner et al. (1995) and amount of cancellous or cortical bone composition is recorded.
≥ 2.5 cm (primarily piece plotted bone)	3658 piece plotted bones from layer 9 were selected from different curation trays and examined for a study of taxonomic assessment, taxon abundance, and transport strategies (Hodgkins et al., 2016). 3,655 faunal remains recorded from a sampling of five meter squares from layer 9 (Castel et al, 2017)	All piece plotted bone from layer 9 are weighted, counted, and assigned burning scales following Stiner et al. (1995) and amount of cancellous or cortical bone composition is recorded.
Micromorphological slides	Sedimentary subunits and compositions described in detail, general details of bone and relevant temperatures mentioned (Aldeias et al., 2012; Goldberg et al., 2012)	Bone from thin sections of micromorphological samples from each identified combustion feature are systematically categorized and tested with mFTIR to investigate the microstratigraphic behavior of burnt bone and the relation bone in thin section has to the bone studied from the screened and piece plotted material. Thin sections: RDM 506a, RDM-211ash, RDM 501

This study uses bone to specifically address questions regarding the location of features, describe the faunal variability within features, identify the distribution of temperatures within features, and monitor for presence of reduction conditions or long duration fires to describe pyrotechnological variability within the assemblage.

Burnt bone from all three scales of analysis, (piece plotted, coarse screened fraction, and bones within the micromorphological slides) can speak to regimes of heat intensity and the role of bone as a component of fire technology. Utilizing fragments from screened remains to address questions of burning allows the capture of greater signatures of thermal alteration, as burnt bone is significantly more friable and fragile than unburnt bone and is easily fragmented (Stiner et al., 1995). However, given the micro-stratigraphical complexity of fire features, where, for instance, an ash lens can be only from a few mm, or thinner, and directly overlaying another older feature, it is crucial to integrate data from burned bone fragments within their specific micro-context. Here, the identification of bone within micromorphological slides builds a methodological bridge between the microcontextual analyses captured within the slides to the greater faunal component recovered in larger units through excavation. This integration allows for a better grasp of how bone is related to microstratigraphic subunits (such as ash layers, etc.) within a given fire feature, or, on the contrary, related to events impacted post-depositionally heated by fires lit on top of prior features. Recorded fauna from the entire recorded assemblage of layer 9 additionally provides the benefit of representing the entire scope of variability and spatial distribution of the burning surfaces and their contents.

This study also proposes using spectroscopic methods across these categories, both bone in the micromorphological thin sections and found in the coarse screens, to address qualities of structural and chemical composition which cannot be answered with traditional zooarchaeological studies and macroscopic observations. Burnt fauna in this way can add a complementary perspective on fire use and properties, ideally to be integrated within a larger framework of various fire proxies both within site and between different sites for comparative analyses of fire technology. Here, I first consider bone as an independent line of evidence contributing to the discussion on fire presence within layer 9 of RDM. Then, I will integrate the results into the existing zooarchaeological dataset to include alongside prior work conducted on the exhibited layer 9 fire technology (Table 2).

Table 2: Previously documented fire proxies for RDM layer 9.

Fire proxy	Pyrotechnology evidence	Citation
Lithics	- Highest frequency of heated lithics within RDM sequence (n = 3150 burned lithics of 8132 total lithics within 868 liters of sediment) - Higher percentage of unburnt lithics associated with combustion sediments, except for combustion feature 10 and 18a which exhibit higher than 50% burned lithics, potentially related to deposition after fire event ended - Higher concentration of burnt lithics located inside the cave using Kernel Density analyses - Highest proportions of burned flakes form a significant cluster on the terrace using Neighborhood analyses with a Local Moran's I test applied to the results ; hotspots of heated lithics exhibit weak correlation to visible combustion features - Burned flakes do not correspond to any single combustion feature	Aldeias et al.,2012; Reeves et al., 2019; Sandgathe et al., 2011
Paleobotanical (phytoliths)	- Evidence for wood fuel through significant portion of wood/bark dicotyledonous phytoliths (30-50% of samples) with distinct differences between combustion feature areas and	Wroth et al., 2019

	non-combustion feature areas- likely due to greater incorporation of wood/bark elements in combustion features - High proportion of grass phytoliths (potentially related to fire-starting materials or other behaviors) - More overall concentrations of phytoliths compared to other layers - Higher amount of melted phytolithis, on average between 2-5% of identifiable specimens (melting point at 1000 °C for silica, but also can be achieved through durations and the presence of mineral salts); evidence for high temperatures/ long duration fires - Evidence for the fire features in layer 9 being created on a cleaner surface, due to cleaner separation between distinct combustion feature and non-combustion feature areas	
Geoarchaeological	- Identification of visible combustion features in the field composed of localized lenses of burned material, including ash and charcoal rich lenses. Recovery of abundant identifiable burnt bone associated with the combustion feature sediments. - Observations on dimensions when possible (length, width, thickness, color, shape of the feature, components) of identified combustion features. - Higher proportion of piece plotted lithics to faunal remains in sediments associated with combustion features 1, 10, and 18a - Trampling behaviors likely due to in situ crushed and broken bones (attributed with additional mixing of unburned lithics with association of fire events) - Distribution of fire events not patterned, except for localized concentrations and stacking of features (fires constructed on top of previously abandoned features) concentrated along the current dripline of RDM and likely would have been placed	Aldeias et al., 2012; Goldberg et al., 2012

	just beyond the ancient dripline - Combustion feature structural integrity intact, many likely not redistributed and raked hearths - Micromorphological identification for Combustion feature 10 of weathered subunits replacing calcareous ashes with apatite (ashy layer exposed for a significant time and was diagenetically altered while exposed) - Locally exhibit a notable degree of diagenetic alteration present in the micromorphological spectroscopic analyses	

Materials and Methods

Archaeological data collection and sample preparation

The counts and weights (g) of all piece plotted (≥ 2.5 cm) and coarse fraction (< 2.5 – 6 mm) bone from RDM layer 9 were recorded along with their burning stage modified from Stiner et al., (1995), along with the degree of adhering concretions and percentage cancellous or cortical bone tissue present (Fig. 1; Table 3). Some bones (n= 111) were recorded as indeterminant in burning stage when coloration could not be confidently assessed.

Portion of bone tissue and amount of burnt bone within the total assemblage are included following Costamagno et al. (2005; 2009) to calculate indices for differentiating categories of burned assemblages (fuel, non-fuel, and fuel/maintenance). Weight estimations were only calculated from specimens with less than 50% adhering concretions, and spongiosa fragments were only considered if cancellous bone accounted for more than 50% of the fragment

For bone larger than 2.5, maximum length and width were also collected. This includes both piece plotted bones with unique recorded coordinates as well as bones ≥ 2.5 cm found within the screened material. Identifications were made when possible within the burnt assemblage and observations were recorded on anthropogenic modifications including scraped and cut-marked fragments within the coarse screened fraction. Identifications provided by prior studies were only included if independently verified. Deposits from the cave interior and exterior were included in this study, totaling to approximately 19 square meters of material (Fig. 2).

Table 3: Modified scale of burning following Stiner et al., (1995)

Burning Scale	Description
0	Not burnt
1	Slightly burnt, < 50% carbonized
2	Majority burnt, > 50% carbonized
3	Fully carbonized
4	Slightly highly burnt, < 50% calcined
5*	Majority highly burnt, > 50% calcined
6**	Fully calcined

** Stage 5b indicates burning scale 5 bone with presence of blue coloration*
*** Stage 6b indicates burning scale 6 bone with presence of blue coloration*

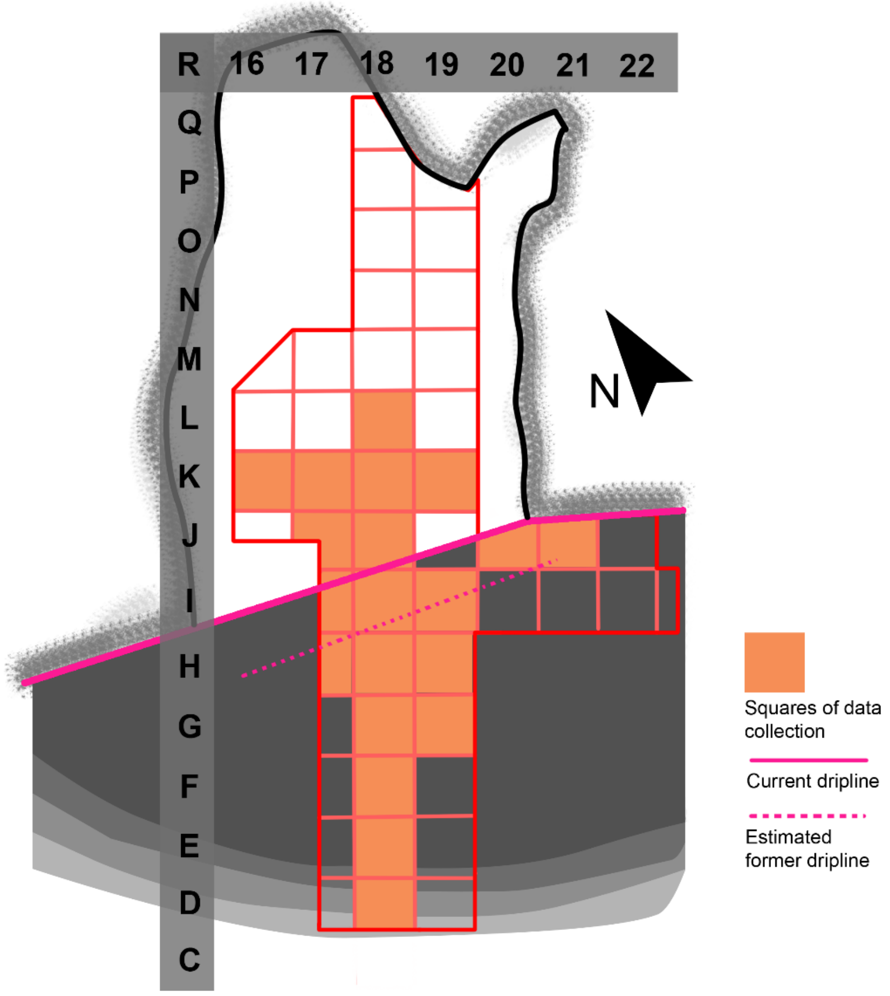

Fig 2: Site plan of Roc de Marsal with meter squares investigated for this study within layer 9 highlighted (modified from Goldberg et al., 2012).

Spectroscopy

FTIR-ATR

Infrared spectroscopy provides a qualitative assessment of the structural and chemical components of bone (see Chapters 2, 3, this volume; Ellingham et al., 2015; Gallo et al., 2021; Mamede et al., 2018). Several signals of diagenetic and thermal alteration can be monitored through peaks and peak transformations in the spectral range, providing means by which to verify thermal alteration and temperature thresholds when visible observations alone may not be sufficient to distinguish between heating, staining, and sun-bleaching (Ellingham et al., 2015; Piga et al., 2008; Pollock et al., 2018; Shahack-Gross et al., 1997; Turner et al., 2018). FTIR-ATR has the additional benefit of being minimally destructive, as only very small amounts of powdered bone are required which may be recovered and reused.

All archaeological material selected for spectroscopic analyses were from the coarse screens of 8 squares of layer 9 and were classified by the Stiner et al., (1995) scale of burning that was assigned during data collection (Appendix C table 1). Selection protocol was primarily informed by fragment size, to ensure enough material for powdering, and with the aim to include a selection of burning variability within the screened material. Fauna subsequently was cleaned with ionic water in an ultrasonic bath, and small portions of each bone were powdered in an agate mortar and pestle and sieved with 234 um mesh.

A Nicolet 6700 Fourier transform infrared spectrometer was utilized for this study with 256 scans collected in wavelength range of 4000-400 cm^{-1}(4 cm^{-1} resolution) for each specimen. The instrument was equipped with a deuterated triglycine (DTGS) detector, a single bounce diamond crystal, and an attenuated total reflectance attachment (ATR) to minimize contamination introduced from sample preparation (Bruno 1999; Hollund et al. 2013; Thompson et al. 2009; Nakamoto et al. 1997). Nineteen FTIR-ATR spectra peak locations and 12 ratios from the coarse fraction bones were investigated for this study using OMNIC software processing tools (Tables 4 and 5).

Table 4: FTIR absorbance inferred functional groups relevant to diagenetic processes and thermal alteration (Ellingham et al., 2014; Mamede et al., 2018; Thompson et al., 2013; Toffolo et al., 2015; Weiner and Bar-Yosef, 1990).

Wavenumber	**Inferred peak functional group assignment**	**Appearance or Transformation Significance**
2010 cm^{-1}	Cyanamide (CN)	May indicate burning in the presence of ammonia or organics, noted in studies related to burning in reduction conditions. Often seen alongside peak at 712 cm^{-1}.
1660 cm^{-1}	Amide I (Collagen)	Found in fresh bone, decreases both with diagenesis and with thermal alteration.
1650 cm^{-1}	Water (HOH)	
1540 cm^{-1}	Amide II (Collagen)	Organic content decreases both with diagenesis and thermal alteration; linked to Type A carbonates which increases alongside decrease of type B carbonates until temperatures of calcination.
1450 cm^{-1}	Type A and B carbonates (CO_3^{2-} v3)	Carbonates are reorganized and depleted with high temperature alteration (as organics and their carbonyl groups are eliminated). Elevated carbonate presence may also be linked to the diagenetic incorporation of exogenous calcite.
1415 cm^{-1}	Type B carbonates (CO_3^{2-} v3)	
1090 cm^{-1}	Likely presence of francolite	Appearance as a shoulder on the 1035 cm^{-1} v4 phosphate peak corresponds to structural changes potentially linked to the presence of francolite
1035 cm^{-1}	Phosphate (PO_4^{3-} v1)	
900 cm^{-1} - 878 cm^{-1}	Type A carbonates (CO_3^{2-} v2)	Peak transformations relevant to changing ratios of carbonate and phosphate presence.
875 cm^{-1}	Precipitating calcite (CaCO3 v2)	Indicates exogenous calcite from the environment which is incorporated during diagenesis.
872 cm^{-1}	Type B carbonates (CO_3^{2-} v2)	Peak transformations relevant to changing ratios of carbonate and phosphate presence.
797 cm^{-1}	Quartz	Incorporation of quartz from the diagenetic environment.

779 cm^{-1}	Quartz	
712 cm^{-1}	Precipitating calcite ($CaCO_3$ v4)	Indicates exogenous calcite from the environment which is incorporated during diagenesis.
630 cm^{-1}- 625 cm^{-1}	Libration of Hydroxyl group (OH-)	Presence is linked to changes in the structural and chemical components of bone which have been altered by high temperatures. OH- group librational mode associated with hydrogen bonding within the crystalline framework
605 cm^{-1} 595 cm^{-1} 565 cm^{-1}	Phosphate (PO_4^{3-} v4)	Deepening trough at 595 cm^{-1} between the peaks at 605 cm^{-1} and 565 cm^{-1} indicate a higher order of crystallinity which is both a product of diagenesis but grows more significantly with temperature alteration.

Table 5: Ratios and measurements utilized for this study taken for FTIR-ATR analyses

Infrared indices	Formula	Measurement	Reference
IRSF (SF)	$\frac{(565\ cm-1\ peak\ ht + 605\ cm-1\ peak\ ht)}{595cm-1\ peak\ ht}$	Degree of crystallinity	Beasley et al., (2014); Mamede et al., (2018); Thompson et al., (2013); Weiner and Bar Yosef (1990)
C/P	$\frac{1415\ cm-1\ peak\ ht}{1035\ cm-1\ peak\ ht}$	Carbonate content	Beasley et al., (2014); Thompson et al., (2013); Mamede et al., (2018)
C/C	$\frac{1450\ cm-1\ peak\ ht}{1415\ cm-1\ peak\ ht}$	Carbonate A+B content to carbonate B	Mamede et al., (2018); Snoeck et al., (2014); Thompson et al., (2009)
CO/P	$\frac{1650\ cm-1\ peak\ ht}{1035\ cm-1\ peak\ ht}$	Relative content of Amide I and II (organic presence)	Thompson et al., (2013); Mamede et al., (2018)
CO/CO3	$\frac{1650\ cm-1\ peak\ ht}{1415\ cm-1\ peak\ ht}$	Relative content of Amide I and II (organic presence)	Mamede et al., (2018); Thompson et al., (2013)
CO3/P		Carbonate to phosophate ratio	Mamede et al., (2018);

	$\frac{878\ cm - 1\ peak\ ht}{1035\ cm - 1\ peak\ ht}$ $\frac{900\ cm - 1\ peak\ ht}{1035\ cm - 1\ peak\ ht}$		Thompson et al., (2013)
CN/P*	$\frac{2010\ cm - 1\ peak\ ht}{605\ cm - 1\ peak\ ht}$ $\frac{2010\ cm - 1\ peak\ ht}{1035\ cm - 1\ peak\ ht}$	Relative content of Cynamide	Mamede et al., (2018); Thompson et al., (2013)
PHT	$\frac{625\ cm - 1\ peak\ ht}{610\ cm - 1\ peak\ ht}$	Shoulder on the POv4 which is related to the libration of OH	Thompson et al., (2013)
OH/P	$\frac{630\ cm - 1\ peak\ ht}{605\ cm - 1\ peak\ ht}$	Amount of OH groups	Snoeck et al., (2014)
Cal/PO4	$\frac{712\ cm - 1\ peak\ ht}{1035\ cm - 1\ peak\ ht}$	Degree of secondary calcite precipitation	Dal Sasso et al., (2016)
API	$\frac{1540\ cm - 1\ peak\ ht}{605\ cm - 1\ peak\ ht}$	Amount of type A carbonate	Mamede et al., (2018); Snoeck et al., (2014) Sponheimer and Lee Thorp (1999)
BPI	$\frac{1415\ cm - 1\ peak\ ht}{605\ cm - 1\ peak\ ht}$	Amount of type B carbonate	LeGeros and LeGeros (1983); Mamede et al., (2018); Snoeck et al., (2014)

Micro FTIR-ATR

Considering burning evidence on the scale of the microcontext provides valuable opportunities to evaluate the internal structure and organization of combustion features (Aldeias et al., 2012; Goldberg et al., 2012, 2017; Goldberg and Berna, 2010). Bone within thin sections from RDM layer 9 are utilized in this study to contextualize the presence of burnt bone within different microstratigraphic levels, as well as test the applicability of established FTIR-ATR ratios on the in-situ fragments to inform future studies. This study uses three micromorphological thin sections (RDM-211ash, RDM-501, and RDM-506a) representing three different types of microstratigraphic layers, and specifically two different burning events within the sample RDM-501 (Table 1; Aldeias et al., 2012).

Microscopic FTIR (mFTIR) allows IR spectra to be directly collected from bones preserved in the petrographic thin sections (30 um thick) and provide contextual data as these samples maintain the original geometric integrity of the archaeological deposits (Goldberg et al., 2012; Goldberg and Berna, 2010). No sample preparation further than procedures to produce the thin sections are necessary, as spectra are obtained directly from the uncovered slides. The instrument must manually be positioned over faunal fragments of interest, however, necessitating location of bone within the sequence to be identified prior to sampling. Spectra (65 scans) were obtained for each sampled area with a ThermoScientific Nicolet iN10 mFTIR equipped with ATR and Germanium crystal with a spectral range of 4000-600 cm^{-1}. As this instrument could not capture the 600-400 cm^{-1} range, ratios utilizing measures under 600 cm^{-1} were excluded from analyses. Sixteen functional group areas and 11 ratios remained suitable for collection to evaluate the extent of diagenesis and degree of thermal alteration (Tables 4 and 5). Analyses were conducted by splitting .map files produced by OMNIC PICTA for further processing with OMNIC software.

Spatial Analyses

Visualizing the density and distribution of burnt fauna can provide a useful measure of the relationship between identified archaeological combustion features and faunal remains likely burned in those fires. Spatial analyses in this study are used as an exploratory tool to investigate if accumulations of burning are found within the faunal assemblage, as burnt bone is specifically hypothesized to be indicative of primary combustion feature location (Moreau et al., 2021). This study utilizes Kernel Density Estimation (KDE) as a modeling approach to visualize significant concentrations of burnt fauna, following established methodologies utilizing KDE analyses (Aldeias et al., 2012; Alperson-Afil et al., 2009; Clark, 2016; Moreau et al., 2021; Spagnolo et al., 2018).

Quantum GIS software (version 2.13.1) was utilized to produce KDEs of burnt fauna following Stiner et al. (1995) burning stages 0-6b for RDM layer 9. KDE spatial analyses calculate histograms in 2D geographic space of smoothed bivariate frequencies via kernel type function for each cell of a defined grid (Moreau et al., 2021). For these analyses, research radius size is emphasized to have a significant role in the results, as search radius parameters are set by individual users and the larger the radius the greater likelihood of less (and larger) concentrations of materials (Moreau et al., 2021). For the purposes of this study, the full extent of layer 9 from the 2000-2003 excavations (Fig. 2) were utilized as study parameters, and the coordinates utilized to plot fauna included both the exact provenance location for the piece plotted materials as well as the coordinates recorded for excavated materials of the screens, which represents a generalized area surrounding the reported coordinate.

The search radius size, or the distribution area within which density is calculated, was defined as 75 centimeters, for a total diameter of 150 cm surrounding each coordinate point. Selection of this search radius was informed by the excavation area coarse screened faunal materials in this study could cover (~ 50 cm^2 in all horizontal plans), and the average size of combustion features reported (81.66 cm). The quartic (spherical) kernel density functions were also utilized here, and the metric of bone weight (g) for each datapoint was used to weight the equation. This decision gives observations of mass greater influence than count data, which may be biased due to the extreme friability of burnt bone.

Results

Zooarchaeological assemblage

84,140 bone fragments were considered for this study, the majority from the coarse fraction (< 2.5 cm- 6mm) of the assemblage (Fig. 3; Tables 6 and 7). Layer 9 in total is composed of a significant amount of burnt faunal remains, with 42% of the total counted assemblage, and 30.16% by weight (g)- exhibiting visual indications of burning including color changes, surface warping, and cracking (Fig. 4; Table 6; Shipman et al., 1989; Stiner et al., 1995). 97% of this burning is found within the coarse fraction, in line with expectations regarding the fragility and friability of burnt bone (Fig. 5; Table 6; Stiner et al., 1995). Within the burnt assemblage, there are near equal percentages of presence of charred/carbonized bone and calcined bone: 55% and 44% respectively by count and 57.29% and 42.26% by weight (g), a considerable amount given that calcined bone is lighter than archaeological unburned and charred/carbonized bone (Fig. 6; Table 6).

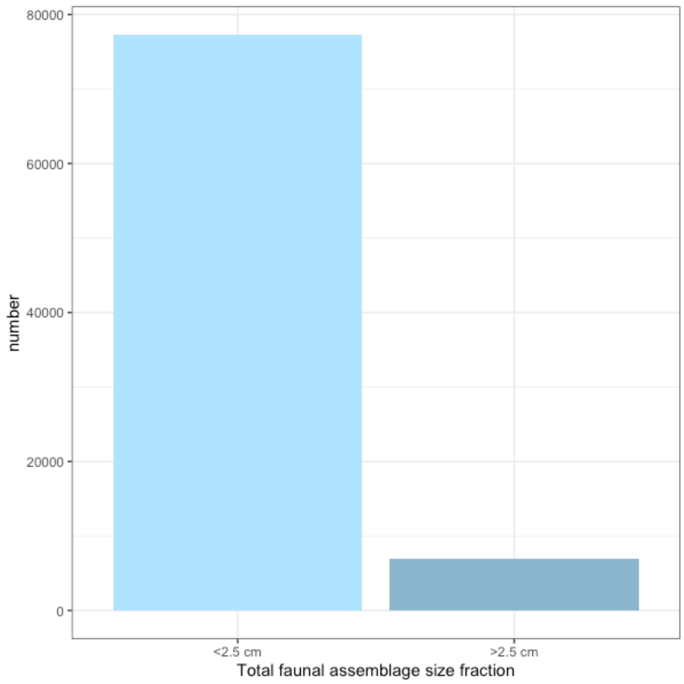

Fig 3: Visualization of the total RDM layer 9 studied faunal assemblage organized by size fractions which predominantly correspond to the coarse screened (< 2.5 cm- 6mm) and piece plotted (≥ 2.5 cm) fauna.

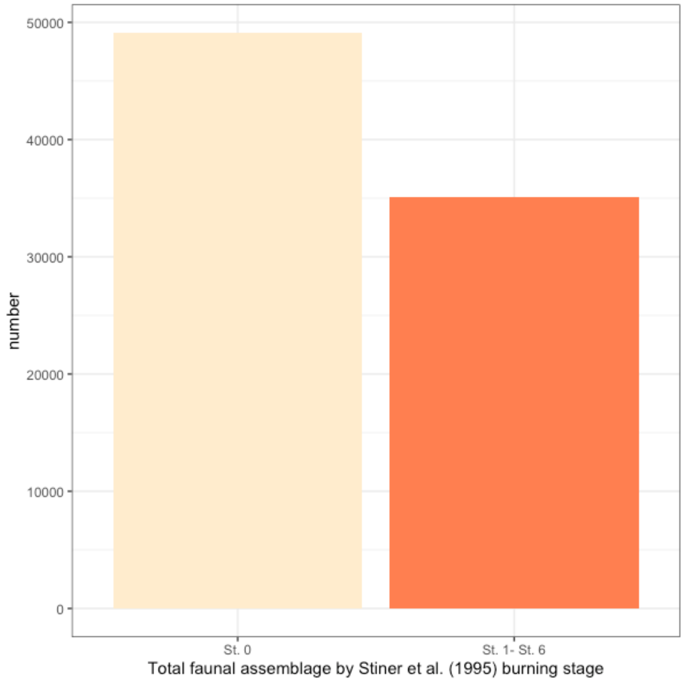

Fig 4: Total studied RDM RDM layer 9 faunal assemblage, following Stiner et al., (1995) burning stages. Stage 0 indicates unburnt bone, while stages 1-6 represent partial charring and carbonization through total calcination.

Table 6: Summary of faunal assemblage from piece plotted and coarse screens. Bone larger than 2.5 cm located in the coarse fraction were measured separately and added to the ≥ 2.5 bone total.

Category	**N**	**% of total assemblage**	**% of total burnt assemblage**	**Weight (g)****	**% of total assemblage**	**% of total burnt assemblage**
bone > 2.5 cm	6,910	*9%*		23,297.78	*44%*	
bone < 2.5 cm	77,230	*92%*		30,174.38	*56%*	
total bone	84,140			53,472.16		
total bone, burned (Stages 1-6)	35,061	*42%*		16,131.96	*30%*	
total bone, burned (Stages 1-6), ≥ 2.5 cm	1,102		*3%*	2,870.01		*18%*
total bone, burned (Stages 1-6), < 2.5 cm	33,959		*97%*	13,261.95		*82%*
total presence of carbonization or charring (Stages 1-3)	19,419	*23%*	*55%*	9,243.55	*17%*	*57%*
total presence of calcination (Stages 4-6)	15,530	*19%*	*44%*	6,818.82	*13%*	*42%*

**Costamagno et al., 2005, 2009*

*** no specimen with > 50% concretion included in weight estimations*

Table 7: Summary of faunal assemblage by Stiner et al. (1995) burning stage, number and weight (g). Stages added to the Stiner et al. (1995) schema include stages 5b and 6b, “b” representing here the presence of a blue hue.

	Stage	**N**	**Weight (g)***
all ≥ 2.5 cm		6,910	23,297.78
all ≥ 2.5 cm	Stage 0	5,808	20,452.55
all ≥ 2.5 cm	Stage 1	88	249.34
all ≥ 2.5 cm	Stage 2	227	607.04
all ≥ 2.5 cm	Stage 3	450	1,053.71
all ≥ 2.5 cm	Stage 4	80	379.08
all ≥ 2.5 cm	Stage 5	63	176.45
all ≥ 2.5 cm	Stage 5b	2	3.7
all ≥ 2.5 cm	Stage 6	178	26.07
all ≥ 2.5 cm	Stage 6b	14	349.84
all < 2.5 cm		77,230	30,174.38
all < 2.5 cm	Stage 0	43,463	16,957.23
all < 2.5 cm	Stage 1	1,384	719.39
all < 2.5 cm	Stage 2	2,778	1,442.61
all < 2.5 cm	Stage 3	14,412	5,171.46
all < 2.5 cm	Stage 4	2,831	1,112.36
all < 2.5 cm	Stage 5	2,183	994.45
all < 2.5 cm	Stage 5b	53	24.79
all < 2.5 cm	Stage 6	9,184	3,392.55
all < 2.5 cm	Stage 6b	942	359.535

**no specimen with > 50% concretion included in weight estimations*

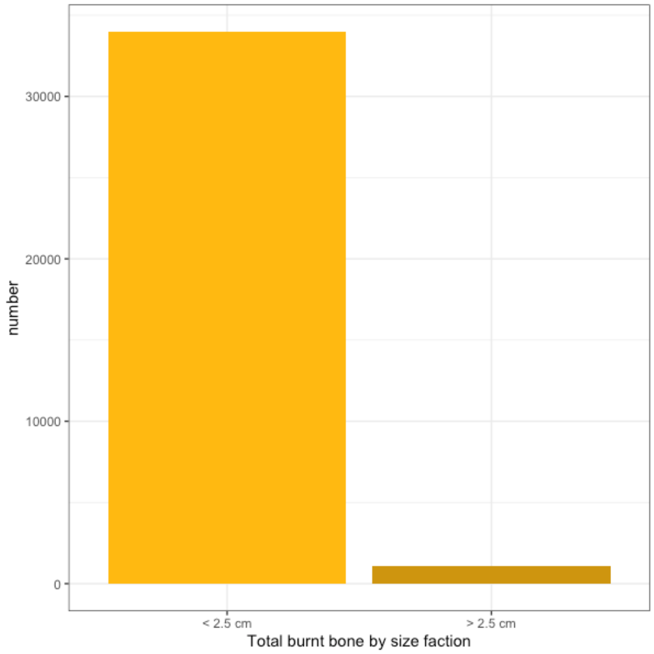

Fig 5: Total burnt bone assemblage classified by size faction. Bone < 2.5 cm is primarily found in the coarse screen fractions, while bone ≥ 2.5 cm is a majority of piece plotted fragments.

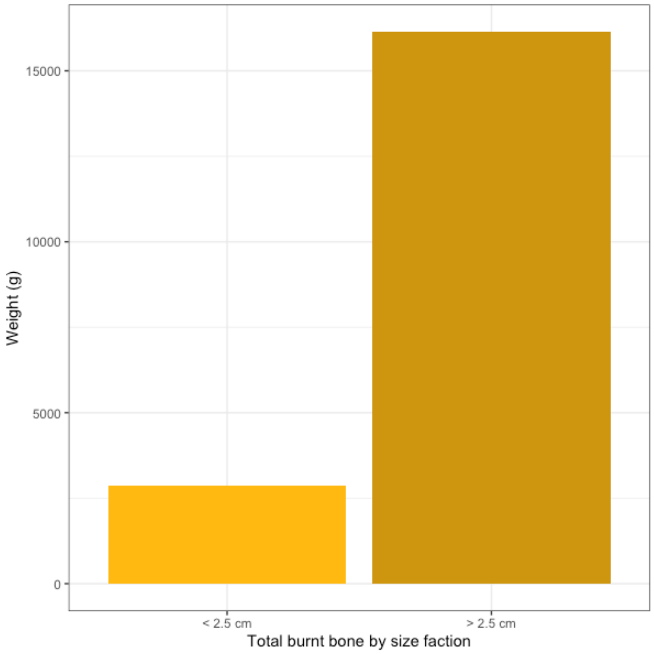

Fig 6: Total burnt bone assemblage by weight (g) classified by size faction. Less than 2.5 cm constitutes a majority of screened finds, while sizes ≥ 2.5 cm are often piece plotted remains.

Layer 9 fauna can be categorized as displaying low surface readability, with a large percentage of the assemblage both unburnt and burnt dominated by adhering concretions (Figs. 7-12). Many concretions are of calcite or calcium carbonate and are likely related to the fire activity and calcareous ash deposits, noted in geological descriptions to have a large presence within the layer (Figs. 9-12).

Fig 7: Humerus likely of red deer (*Cervus elaphus*) which is not burnt (stage 0) and is exhibiting typical surface texture and cracking.

Fig 8: Unburnt bone, non-identifiable long bone shaft which is not burned (stage 0), with cracked surface texture and large amount of adhering concretions with bone and lithic debitage in the matrix.

Fig 9: Long bone unburnt (stage 0) unidentified fragment with typical surface texture, adhering concretion, and staining.

Fig 10: Partially charred or carbonized (stage 2) fragment with adhering calcite concretion, back and front view.

Fig 11: Partially calcined (stage 4) fragment with more than 50% adhering calcite concretions, back, front, and side view.

Fig 12: Partially calcined (stage 5) refitted fragment exhibiting cracked and stained surface and adhering calcite concretions < 50%.

Identifications

Despite the heavily fragmented nature of the assemblage, several identifications were made within the coarse screened material, building on prior work (Figs. 13-21; Castel et al., 2017, 2018; Hodgkins et al., 2016). Burning and low readability contributed to challenges in assigning identifications, with diagnostic features such as foramen and muscle attachments often obscured or warped with high temperature alteration (Figs. 22, 23). Prior identifications from previous studies were only utilized when they could be independently verified. Identifications which were possible did align closely with previous studies of the assemblage, with red deer (*Cervus elaphus*) and roe deer (*Capreolus capreolus)* dominating (Figs. 13-21). Notable within the burnt identifiable assemblage includes three fragments of calcined lumbar vertebral elements of wild boar (*Sus scrofa*) within the same screened material, as well as several groups of burned cervid sesamoids within the coarse fraction (Figs. 19, 21; Table 8).

Table 8: Broad categorization of burnt percentages within identified faunal elements. Burning stages following Stiner et al., (1995).

Element		**Total N**		**N Burnt stage 1-3**	**% Burnt stage 1-3**	**N Burnt stage 4-6**	**%Burnt stage 4-6**
antler		6					
crania		3					
petrous		13		1	*8%*		
mandible		16		4	*25.00%*	1	*6%*
vertebrae		16				3	*19%*
rib		15				1	*7%*
sternebrae		1					
scapula		5					
long bones		99		4	*4%*	2	*2%*
	humerus		17	1	*6%*		
	radioulna		17				
	femur		15				
	tibia		27	2	*7%*	2	*7%*
	fibula		1				
sacrum		1					
ischium		1					
metapodial		207		39	*19%*	28	*14%*
	metacarpal		19				
	metatarsal		49	3	*6%*	12	*24%*
phalange			37	2	*5%*	5	*14%*
	1st phalanx		6				
	2nd phalanx		2				
	3rd phalanx		8			1	*13%*
	vestigial phalanx		3			2	*67%*
carpals or tarsals		6					
calcaneus		1					
sesamoids		31		5	*16%*	8	*26%*
microfauna		3		1	*33%*		

Fig 13: Front and back of roe deer (*Capreolus capreolus*) partially charred/carbonized (stage 2) tibia shaft fragment with adhering concretion.

Fig 14: Carbonized/charred (stage 3) fragment of a red deer (*Cervus elaphus*) posterior metapodial shaft with characteristic breakage, warping, and low surface readability for the assemblage.

Fig 15: Anterior portion of carbonized/charred (stage 3) metapodial shaft surface (with presence of anterior groove preserved) of red deer (*Cervus elaphus*).

Fig 16: Partially carbonized/charred (stage 2) red deer (*Cervus elaphus*) mandibular fragment, outer and inner surface pictured.

Fig 17: Partially calcined but predominately carbonized/charred (stage 4) proximal warped phalange with adhering concretions. Front, side, and internal view pictured.

Fig 18: Top and side views of two distal metapodial condyles of roe deer (*Capreolus capreolus*), fully calcined (stage 6). Both fragments are from the same screened coarse fraction materials.

Fig 19: Set of fully calcined (stage 6) sesamoids (all side view) found within a single excavated coarse screen. All sesamoids here are likely roe deer (*Capreolus capreolus*).

Fig 20: Roe deer (*Capreolus capreolus*) calcined (stage 6b) metapodial anterior shaft fragment still identifiable despite typical cracking and warping. Blue hue tinges also are present on metapodial ridges.

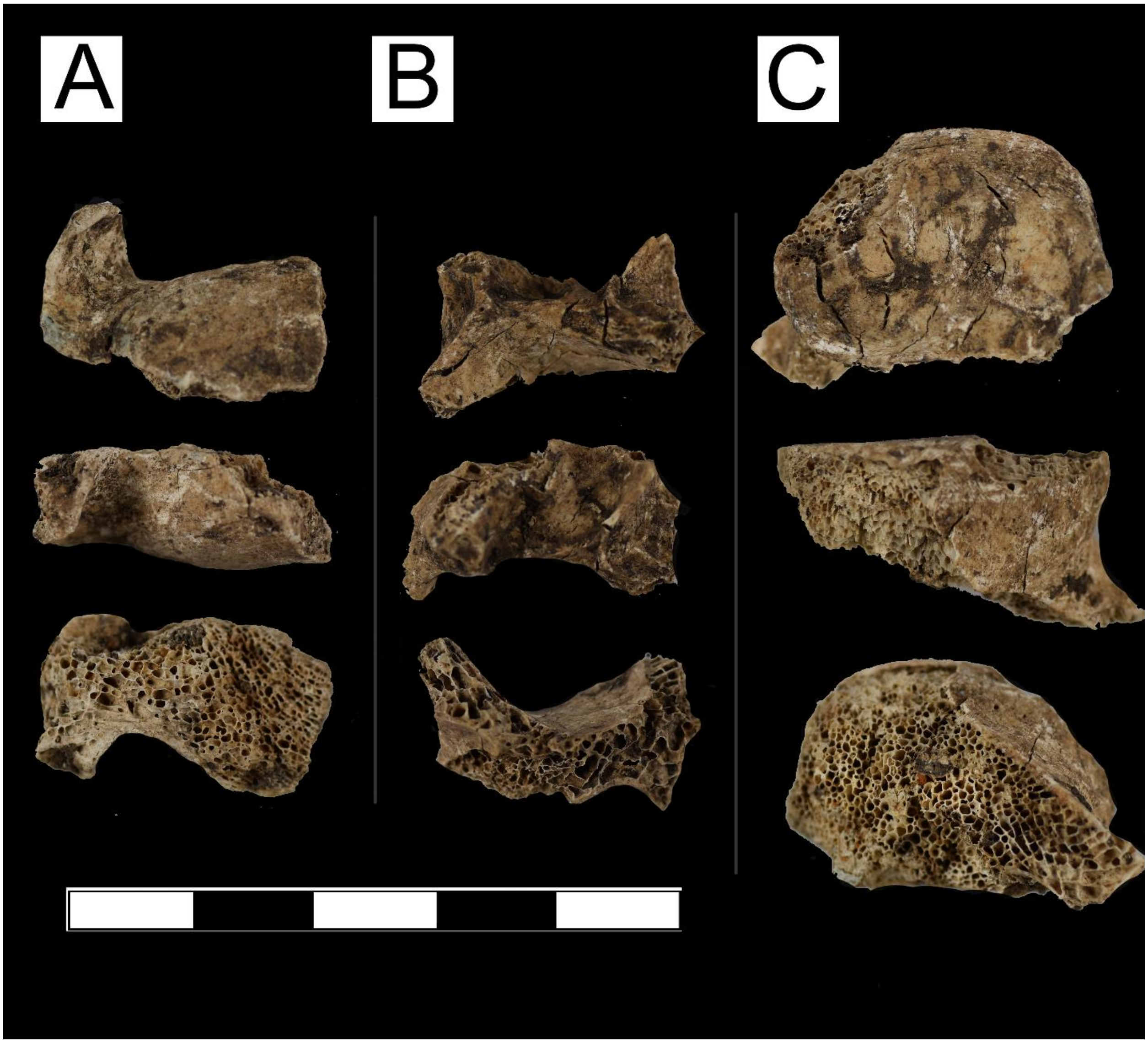

Fig 21: Three non-articulating fully calcined (stage 6) lumbar vertebrae fragments of wild boar (*Sus scrofa*). Fragments do not refit and represent different numbers of vertebrae. Each fragment has front, side, and internal views pictured.

Fig 22: Unidentified calcined (stage 6b) long bone fragment (front and back) with low surface readability.

Fig 23: Unidentified long bone fragment fully calcined (stage 6) exhibiting cracking and low surface readability.

Comparisons between bone density values between the unburned and burned assemblage indicates that low density burned bone fragments are present in layer 9, including vertebrae, epiphyses of metapodials, and phalanges (Fig. 15; Table 9). Identified burned bones are primarily of high-density fragments, however (Fig. 15; Table 9). Values are calculated following Lam et al., (1999) for *Rangifer tarandus*, as bovid, cervid, and equid species were found to have similar patterns of relative bone density.

Table 9. Bone density values (*Rangifer tarandus* following Lam et al., 1999) for unburnt and burnt assemblage. Fragile burned elements, including vertebrae, are present, despite overall pattern of burned dense element portions such as metapodials and long bone diaphyses.

Element		Unburnt	BMD*	Burnt	BMD*
petrous		12	*1.29*	1	*1.29*
mandible		12	*1.06*	4	*1.06*
vertebrae		13	*0.146*		
	lumbar vertebrae body			2	*0.45*
	lumbar vertebrae spine			1	*0.48*
rib		14	*0.95*	1	*0.95*
scapula		5	*1.02*		
long bones					
	humerus				
	proximal shaft	1	*0.44*		
	diaphysis	13	*1.12*	1	*1.12*
	distal shaft	2	*1.08*		
	radioulna				
	diaphysis	12	*1.08*		
	distal shaft	2	*1.09*		
	femur				
	diaphysis	3	*1.15*		
	distal shaft	12	*0.61*		
	tibia				
	diaphysis	22	*1.13*	4	*1.13*
	fibula				
	distal shaft	1	*0.68*		
sacrum		1	*0.4*		
ischium		1	*0.94*		
metapodial					
proximal shaft		1	*0.109*	1	*0.109*
diaphysis		124	*1.09*	46	*1.09*
distal shaft		2	*0.445*		
distal epiphysis		4	*0.43*	2	*0.43*
	metacarpal				
	proximal epiphysis	1	*0.92*		
	proximal shaft	3	*1.08*		
	diaphysis	15	*1.1*		
	metatarsal				
	proximal epiphysis	1	*0.9*	5	*0.9*
	proximal shaft			1	*1.1*
	diaphysis	27	*1.08*	7	*1.08*

	distal epiphysis	1	*0.11*	2	*0.11*
phalange					
	phalange	11	*0.75*	7	*0.75*
	1st phalanx	6	*0.92*		
	2nd phalanx	2	*0.92*		
	3rd phalanx	7	*0.72*	1	*0.72*
carpals or tarsals		6	*0.69*		
calcaneus		1	*0.94*		

**BMD2 data and using BMD1 when not available following Lam et al., 1999*

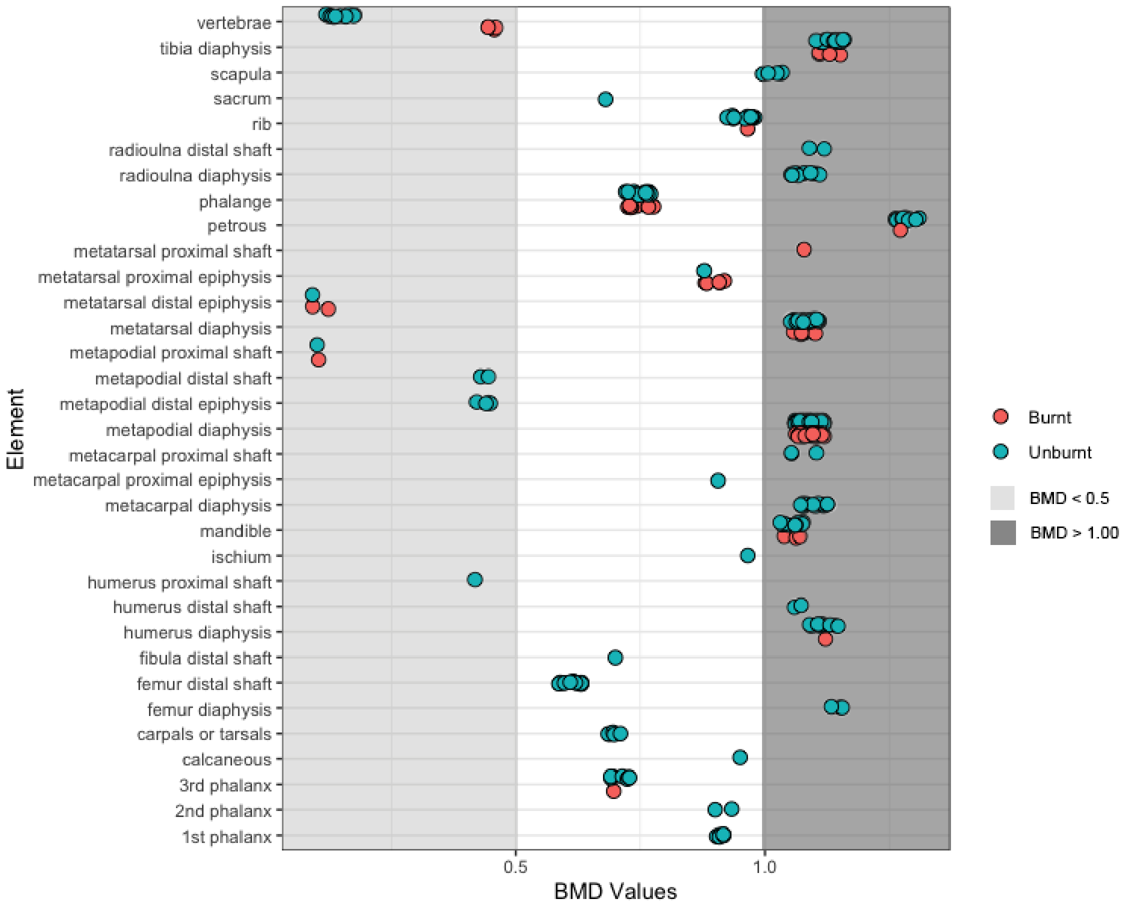

Fig 24: Distribution of unburned and burned identified fragment BMD. Values following Lam et al., 1999 for *Rangifer tarandus*. Light shading indicates relatively low BMD values, darker shading represents here relatively high BMD values.

Anthropogenic modification

Surface modifications were observed on a small percentage of bones despite low surface readability and were confirmed with low-powered magnification and incident lighting (Figs. 24, 25; Table 10). Bones with clear cut marks, scrape marks, retouch, and percussion marks which were also burnt indicate that defleshing, butchering, and periosteum scraping occurred prior to burning (Binford, 1978). Anthropogenic modifications were most commonly recognized on carbonized and charred bone (maximum stage 3), because calcination significantly transforms surfaces, eliminating visible markings (Fig. 22, 23).

Table 10: Summary of anthropogenic modification for layer 9, burning stages following Stiner et al., (1995).

Modification	Total N	N Burnt stage 1-3	% Burnt stage 1-3	N Burnt stage 4-6	%Burnt stage 4-6
cut marks	14	7	50%		
retouch	1	1	*100%*		
scrape marks	21	15	*71%*	1	*5%*
percussion marks	7	1	*14%*		

Fig 24: Two fragments ≥ 2.5 cm with observable longitudinal scrape marks, likely from the removal of periosteum from the fleshed sample. Both fragments are fully carbonized or charred (stage 3).

Fig 25: Dinolite images of anthropogenic marks on burnt bone from layer 9 of RDM at 24x magnification. The presence of scraping and cut marks indicate bone was on these occasions scraped and cut prior to burning. Samples J17-7881a and K18-2668 are featured in Fig. 24 as A and B, respectively.

Indices of bone burning

Distinguishing by what means bones were burnt within an archaeological assemblage is a valuable factor to investigating fire use and maintenance behaviors of hominins. Costamagno et al. (2005, 2009) established indices informed by experimental research which can be used to characterize faunal assemblages into three groupings: use of bone as fuel, bone not as fuel, and bone burnt as a component of a fuel or maintenance strategy (Thery-Parisot et al., 2005). Criteria utilized for this evaluation include the percentage of cancellous bone burned (ratio of burned spongosia to total burnt bone in the assemblage), percentage of bone burnt under 2.5 cm (ratio of total bone burnt under 2.5 cm to all burnt bone within the assemblage), percentage of bone at least carbonized within the assemblage (ratio of bone burnt Stiner et al. 1995 stages 2-6 to all burnt bone), and percentage of bone burnt overall within the assemblage (ratio of burnt bone to unburnt bone; Table 11). Indices which contribute to the inference of bone not used as fuel are low degrees of fragmentation and low overall burning intensity (Costamagno et al., 2009).

Faunal data collected for this study was converted from the Stiner et al., (1996) burning stages to the Costamagno et al. (2005; 2009) burning schema for the purpose of the calculations (Appendix C tables 2, 3). Through these indices burned assemblages can also be compared between sites and layers to provide insight into larger scale behavioral questions (for published data see Costamagno et al., 2009).

The results of layer 9 indicate that bone burned here was a product of either fuel or site maintenance as classified by a Principle Components Analysis (PCA) with values consistent with those obtained from other Paleolithic fires (Figs. 26, 27; Appendix C tables 4-6). Fuel or maintenance strategies were also identified for the faunal assemblage of RDM layer 4 (Castel et al., 2017, 2018; Costamagno et al., 2009).

Table 11: Indices proposed by Costamagno et al. (2005, 2009) including the combustion index.

Indices	Formula		%
% of cancellous bone burned*	(Spongiosa† Stage 2-6)/ (Total burned bone Stages 2-6) x 100		3.39
% of bone burnt under 2.5 cm*	(Total burned < 2.5 cm) / (Total burned) x 100		96.88
% of bone burnt at least carbonized*	(Total Stages 2-6)/ (Total burned) x 100		95.85
Combustion index*	Total ((X_a x 0) (X_b x 1) (X_c x 2) (X_d x 3) (X_e x 4))	91,203	0.27
	Total (X_a + X_b + X_c + X_d + X_e) x 4	336,560	

† > 50% spongiosa
**Converted from Stiner et al. (1995)*

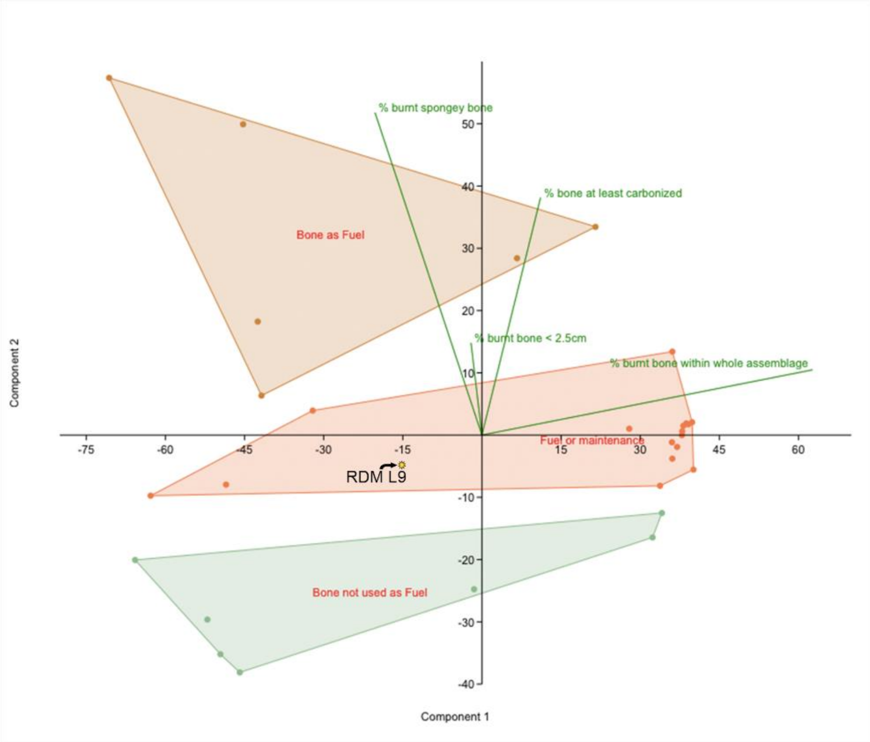

Fig 26: Principle Components Analysis (PCA) 1 vs PCA 2 of RDM layer 9 (yellow star) amongst other published indices following Costamagno et al. (2009). The designation of bone as fuel (gold polygon) indicates likely purposeful bone fuel use, bone not used as fuel (green polygon) recognizes no signature of purposeful bone burning as a fuel source, and fuel or maintenance (orange polygon) indicates a strategy which can not be distinguished but supports bone burnt purposefully for either service. The close vectors indicate variables which are positively correlated.

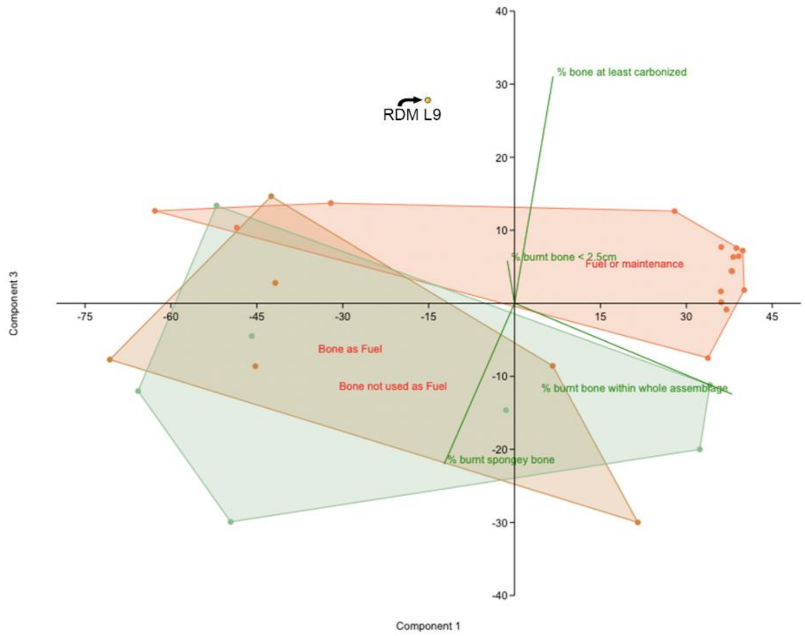

Fig 27: PCA 1 and 3 following Costamagno et al., (2009). RDM is represented by a yellow star. The obtuse biplot angles indicate variables which are negatively correlated.

Blue bone

Bone tinged with blue was found on fauna exhibiting the presence of calcination, both Stiner et al., (1995) stages 5 and 6, > 50% calcined and fully calcined (Figs. 28, 29; Table 7). The appearance of blue coloration on bones which are not fully calcined and retain portions which are charred/carbonized (i.e. stage 5 bones) indicates that blue coloration is not only the product of high temperature alteration. Yet, blue is only found cooccurring with calcination and is not seen on bone of any other stages, therefore likely linked with processes of high temperature alteration (Buikstra and Swegle, 1989; Shipman et al., 1984).

Blue hues primarily are found as ephemeral patches only on cortical surface, similar to staining patterns, but blue coloration fully penetrating bone interior and exposed on broken surfaces were also observed. Light blue coloration has been previously described in experimental studies to be found on calcined bones, specifically heated to > 940 °C (Buikstra and Swegle, 1989; Shipman et al., 1984), but recent documentation of experimental reference collections found no occurrence of any blue hue at temperatures up to 1200 °C (Chapter 1 of this volume; Gallo et al., 2021). Blue coloration therefore cannot only be indicative of high temperature alteration alone.

Circumstances surrounding burning, such as status of the bone as fleshed or fresh when heated, have been hypothesized for blue coloration (Scott et al., 2010). Buikstra and Swegle (1989) report blue coloration on fresh bone burned in the presence of flesh, but remains only one of many experimental studies burning fleshed elements to do so. Bone burnt in the presence of guano (concentrated excrement of birds and bats composed of nitrogen, phosphate, and potassium) deposits have been proposed as an alternative hypothesis but with little explanatory supplemental information (Robles et al., 2002).

Blue staining on fossil ivory (Odontolite), used for decorative purposes in the Middle Ages, is documented to be the result of precipitating manganese from the diagenetic environment which is incorporated during the fossilization process (Chadefaux et al., 2009; Reiche et al., 2000, 2001, 2002). Ivory apatite here has tetrahedral and anionic MnO_4^{3-} substituting for phosphate, PO_4^{3-}, within the mineral matrix (Chadefaux et al., 2009; Reiche et al., 2000, 2001, 2002). The presence of manganese (MN2+) within the matrix is due to diagenetic or fossilization processes, as MN2+ can be incorporated at the divalent M11 metal positions of apatite, noted to be found at the M(I) site on a C3 axis, in the Ca (I) position of the floride apatite, and in the tetrahedral position in the (+V) oxidation state (Mayer et al., 2003).

Mn substitution within hydroxyapatite (chemical equivalent of biological bioapatite) does not change any lattice constants with hydroxyapatite samples without Mn presence (Mayer et al., 2003). When Mn containing samples were heated, hydroxyapatite with low carbonate content undergoes a structural transformation starting at 400 °C (and fully transformed at 800 °C) to β-TCP, a transformation which is also described to occur in bone burnt at temperatures greater than 1000 °C (Piga et al., 2018). When the hydroxyapatite samples are heated to similar temperatures but with larger amounts of carbonate (> 4%), the process of chemical modification was seen to be prevented, however, as carbonate substitution stabilized the crystal lattice (Mayer et al., 2003). The high carbonate Mn containing samples were also seen to have color changes to blue above 600 °C, with the oxidation of MN2+ producing MNO_4^{2-}, likely substituting for CO_3^{2-} (+OH-) in the lattice structure (Chadefaux et al., 2009; Mayer et al., 2003).

Research demonstrating the origin of blue color within non-biological hydroxyapatite indicates that bone must have incorporated manganese and carbonates prior to burning to result in blue coloration with temperatures of calcination. This is the most likely explanation for the blue hues on calcined fragments within layer 9 of RDM. This inference is supported by the pattern of color distribution on bones, as the outer exposed surface of bone fragments most often exhibited the coloration, and it is these surfaces which would be first to have precipitated carbonates and manganese from the depositional environment, similar to sub-superficial manganese staining on buried bone (Arroyo et al., 2008). This hypothesis is directly opposed to discussions of bone which have blue coloration after being burnt fleshed or ‘fresh’, as reported in the literature (Buikstra and Swegle, 1989; Scott et al., 2010). Future research must investigate the modes of manganese and carbonate incorporation and the initial status of bone in prior burning experiments to clarify the mechanisms responsible for blue coloration on fleshed remains.

This study proposes that the presence of blue bone within layer 9 of RDM represents bone which incorporated both exogenous carbonates > 4% and manganese from the burial environment prior to burning and was subsequently chemically and structurally calcined through exposure to high temperatures in oxidizing conditions. Circumstances of the initial status of bone prior to burning which would allow for carbonates and manganese to precipitate include bone which was defleshed and left on the burial environment prior to heating. Hypotheses for such a scenario include the potential incidental burning of accumulated bone in the surrounding area, or, the intentional gathering and burning of older bone fragments with periosteum removed from prior butchering activities for the purpose of adding to a fire event.

Fig 28. Examples of calcined Stiner et al. (1995) stage 6 bone with presence of blue coloration from the RDM coarse screen fraction.

Fig 29. Examples of calcined Stiner et al. (1995) stage 6 bone with presence of blue coloration from the RDM coarse screen fraction partially embedded in calcareous concretions.

Spectroscopic analyses

FTIR-ATR

Results of the FTIR-ATR analyses verify thermal alteration within the faunal assemblage, as opposed to scenarios such as staining or sun-bleaching (Pollock et al., 2018; Shahack-Gross et al., 1997; Turner et al., 2018). This assemblage exhibits poor organic preservation even in unburnt bones (classified here as Stiner et al. 1995 stage 0), observable within the weak presence of elevated peaks within the 1660-1540 cm^{-1} spectral range (Figs. 30, 31; Table 3). Elevated splitting factor ratios (SF), indicative of the order of crystallinity, are also heightened within the stage 0 unburnt bone when compared to unburned modern referential samples (Figs 30, 31; Table 3; Gallo et al., 2021). This is an expected consequence of diagenetic alteration in burial environments and the normal process of Ostwald ripening, in which larger crystals grow at the expense of smaller crystals to reach a more stable form with less soluble bioapatite crystals (Dal Sasso et al., 2018; Gallo et al., 2021; Hedges, 2002). Extreme diagenetic alteration is not present, as very few samples exhibit indications of calcite presence from the depositional environment (observable through the 1540-1415 cm^{-1} and 875 cm^{-1} elevated peak areas), and no samples are permeated with quartz (Figs 30; Table 4).

Two well documented phases of carbonate loss can be monitored within the assemblage, first seen with the combustion of organics in stages 1-3 and further elimination along with the structural and chemical reorganization accompanying calcination in stages 4-6 (Chapter 3; Figs 30, 32-34). This can be observed by the decreasing peak area at 1415cm^{-1} (Table 4). All calcined samples retain presence of structural lattice carbonates, indicating that they were burned under temperatures of 1000 °C, where in experimental reference collections structural carbonates were seen to be completely removed related to the transformation to β-TCP) (Figs. 24, 25; Gallo et al., 2021; Piga et al., 2018).

The appearance of two peak shoulders specific to high temperature exposure and calcination, the 1090 cm^{-1} peak shoulder off of the PO_4^{3-} v3 peak at 1035cm^{-1} and the 630-625 cm^{-1} peak shoulder emerging from the PO_4^{3-} v4 peak (the PHT) at 605cm^{-1}, are seen emerging alongside the presence of calcination in stage 4 bones (Figs 30, 33, 34; Table 4). These peaks indicate the changing chemical organization of bone and are only possible with high temperatures (Table 4; Chapter 2).

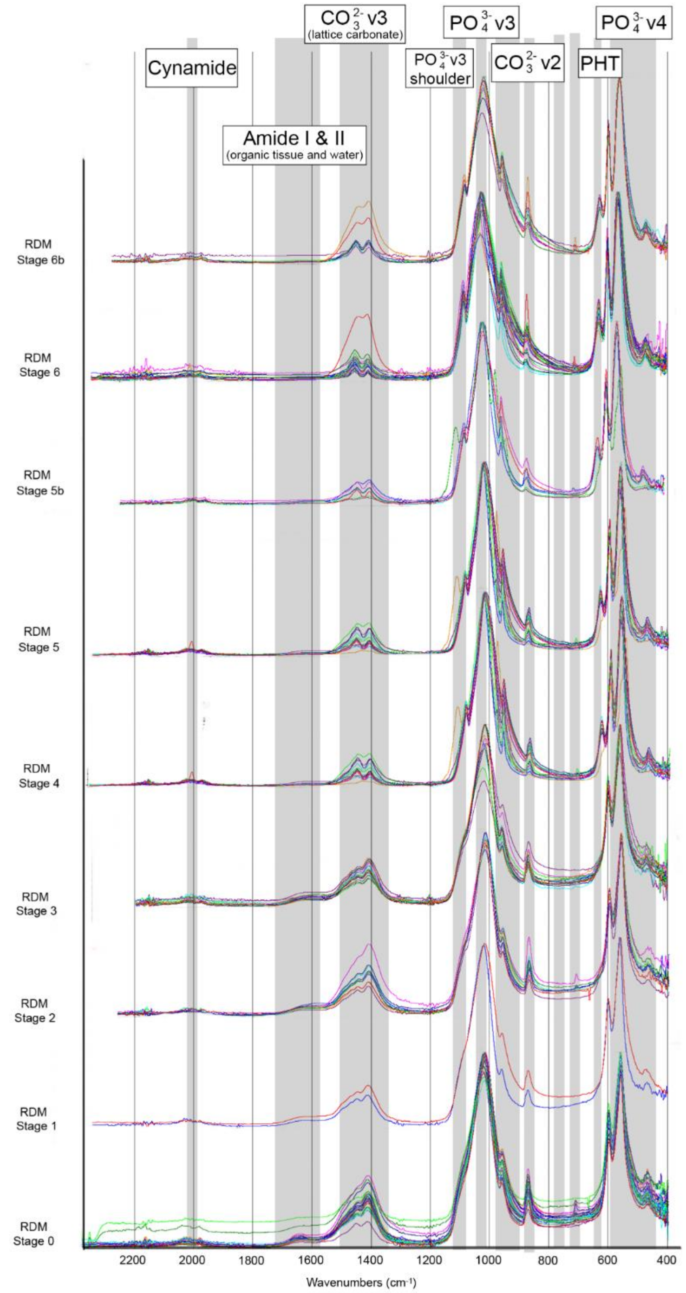

Fig 30: Full FTIR-ATR absorbance spectra of all RDM layer 9 bone samples, classified by burning stage following Stiner et al., (1995) with the addition of distinguishing blue tinged bone within stage 5 as stage 5b, and within stage 6 as stage 6b. Peak areas of interest to this study are highlighted. Stages 5b and 6b primarily have spectra very similar to their expected counterparts (stages 5 and 6 respectively), with the notable exception of significant elevated carbonate levels within several samples of the 6b samples and one stage 6 sample, seen at 1415 cm^{-1} in the CO32- v3 peak area, the 878 cm^{-1} CO$_3^{2-}$ v2 peak area, and the 712 cm^{-1} peak, all indicative of calcite precipitation within the sample.

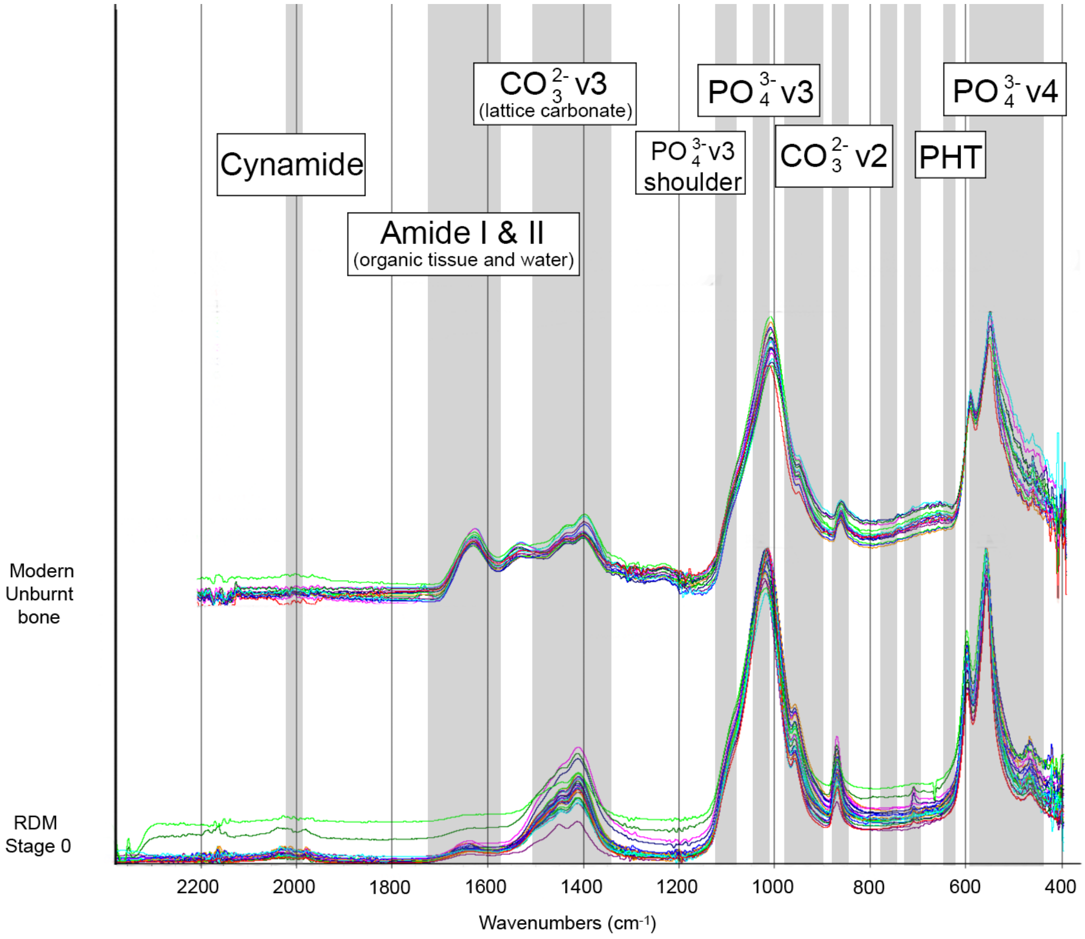

Fig 31: FTIR-ATR absorbance spectra of RDM unburnt (stage 0 bone following Stiner et al., 1995) compared to modern unburnt bone collected on same instrument for the creation of a referential database (Gallo et al., 2021). Peak areas relevant to study parameters are highlighted, with the low degree of preserved organics observable by the low peak height area ~1650 cm^{-1}. The elevated SF ratio, as measured by the peaks and trough at 605, 595, and 565 cm^{-1} is also apparent and elevated within the archaeological specimens due to diagenetic alteration.

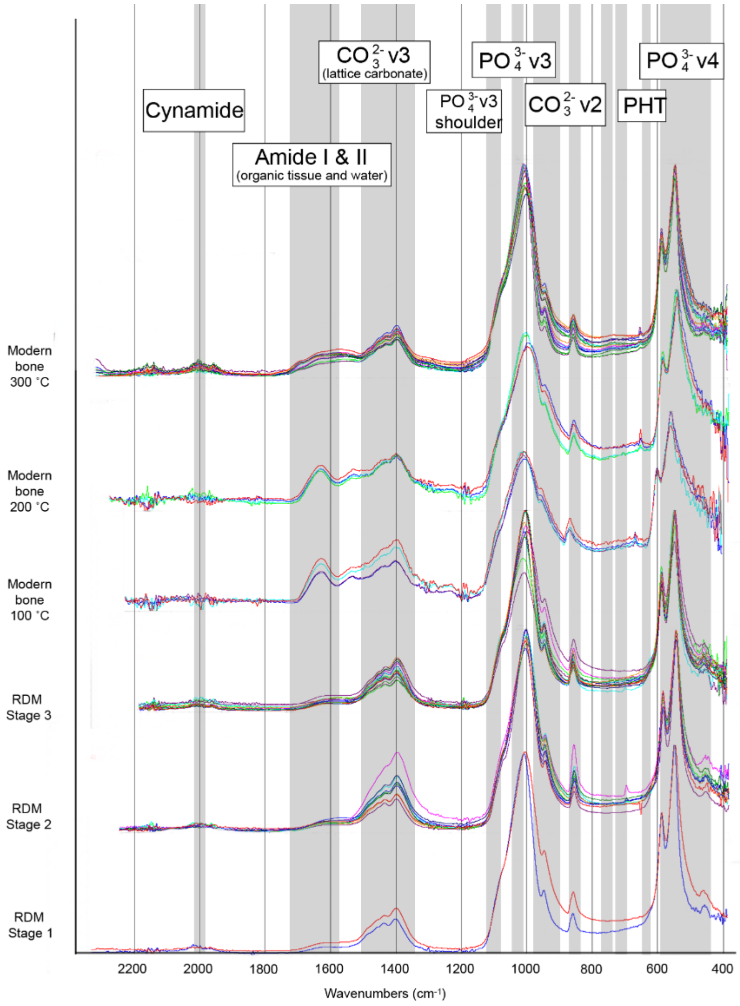

Fig 32: FTIR-ATR absorbance spectra of archaeological samples from RDM layer 9 exhibiting presence of carbonization and charring, identified by Stiner et al. (1995) stages 1-3, are compared to modern experimental reference collection spectra burned in air at temperatures of 100-300 °C. Archaeological samples have very low organic preservation, transforming the peak height area for the functional group of Amide I&II (from collagen presence) when compared to the 100 and 200 °C modern samples. Archaeological samples particularly from stage 2 also have clear presence of exogenous carbonates (likely calcite) which results in elevated peak areas at 1415cm^{-1} and 875 cm^{-1}.

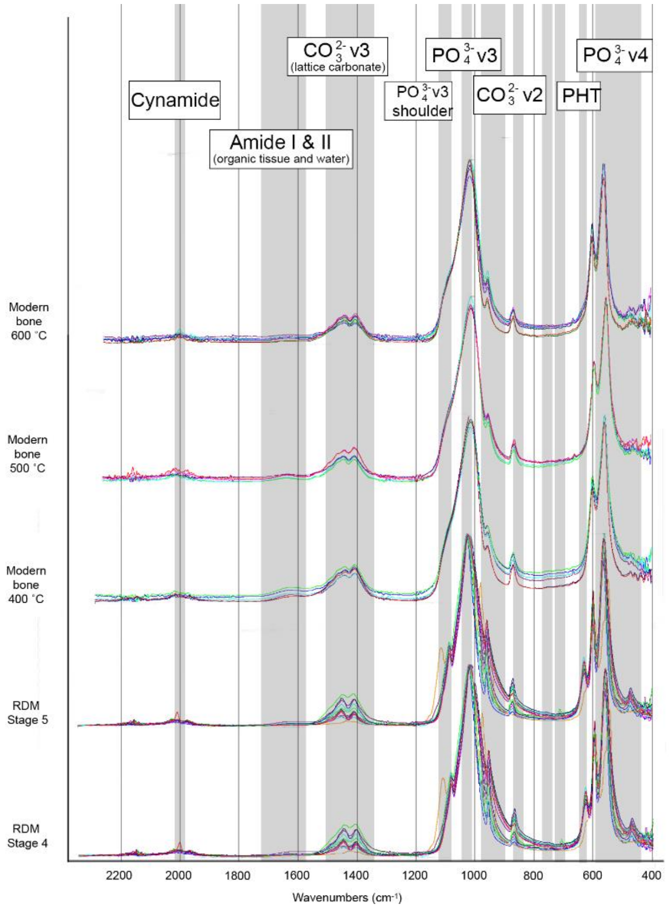

Fig 33: FTIR-ATR absorbance spectra of archaeological samples with < (stage 4) and > (stage 5) 50% calcination following Stiner et al., (1995) to modern bones burnt for 30 minutes in air at 400, 500, and 600 °C. Archaeological samples already exhibit peak shoulders at 1090 cm^{-1} and 630-625 cm^{-1} (PHT) which is expected, as they are classified due to their presence of visible calcination. Variation is most notable in the presence and amount of lattice carbonates in the CO_2^{3-}v3 peak area ~1415cm^{-1}, likely related to the temperature the calcined portion of the fragment reached and the amount of charred organics remaining in the samples.

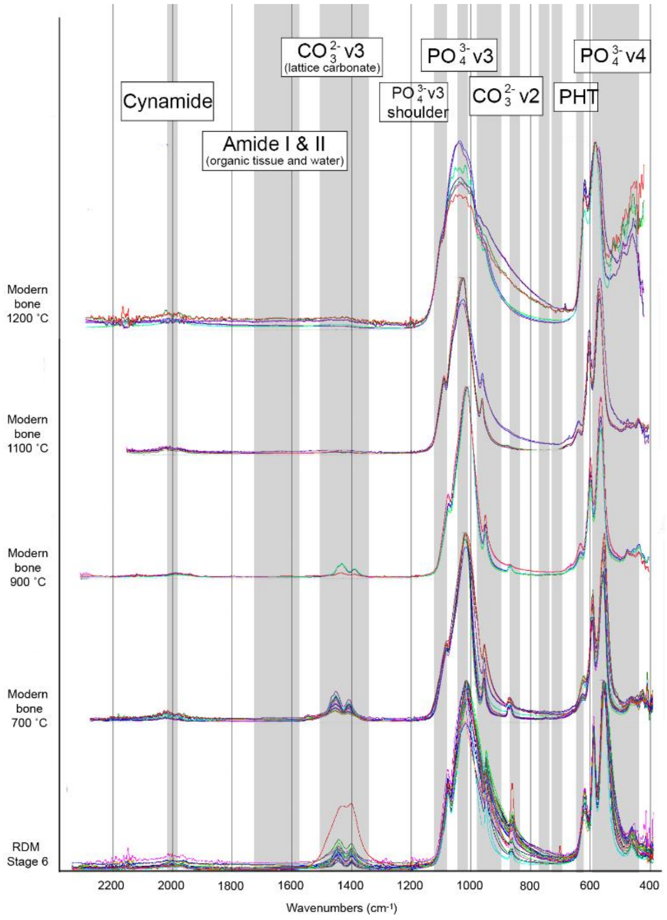

Fig 34: RDM layer 9 fully calcined samples (Stiner et al. 1995 stage 6 bone) compared to modern experimental samples burned in air for 30 minutes at 700, 900, 1100, and 1200 °C. Archaeological samples exhibit significantly elevated peak shoulders at 1090 cm-1 and 625-630 cm^{-1} (PHT), likely due to the combined processes of thermal alteration and diagenetic transformation and stabilization. One stage 6 RDM archaeological sample has a large amount of exogenous carbonate incorporation, noted in the elevated 1540-1415 cm^{-1} peak area and 875 cm^{-1} peak area.

Reduction atmosphere

Bone burnt without access to oxygen in reduction conditions has been demonstrated in laboratory settings to exhibit a different pattern of burning both in macroscopic observable characteristics as well as in chemical and structural transformations (Reidsma et al., 2016). This process, defined as charring with the total exclusion of combustion, notably results in bones remaining dark in coloration (dark browns and blacks) even after temperatures which should induce calcination with white and grey coloring (600-900 °C; Reidsma et al., 2016). Heat exposure without oxidation in this scenario does not fully eliminate the organic char residue, and while crystallinity does increase (as measured by the SF) it is not to the degree seen in samples heated at the sample temperature exposed to air (Chapter 3; Gallo et al., 2021; Reidsma et al., 2016). Changes to the FTIR-ATR spectra indicative of other attributes of charred bone chemical organization also include the presence of peaks at 2010 cm^{-1} and 712 cm^{-1} attributed to cynamide, likely produced from compounds which are created due to a reaction between the calcium content of bone mineral and the residual carbon and nitrogen from the remaining organics (Dowker and Elliott, 1979; Reidsma et al., 2016). No libration of the hydroxyl groups (the PHT peak at 625-630 cm^{-1}) are seen as well at 600-900 °C, although a weakly emerging shoulder at 1090 cm^{-1} is present at 900 °C (Reidsma et al., 2016).

Detecting fauna heated under reduction conditions is a valuable line of evidence, as it is hypothesized that reduction conditions can be met by the thermal alteration of buried bone, bone heated in the inner cavity of unbroken elements, bones buried underneath fire features, or in fires large enough that remains within the feature are completely shielded from air (Gallello et al., 2013; Reidsma et al. 2016). To screen for reduction atmospheres within this sampled assemblage, FTIR-ATR spectra from bones which exhibited > 50% black in color (Stiner et al., 1995 stages 2 and 3) were considered, as no white coloration was noted in laboratory studies (Reidsma et al., 2016). Special attention was paid within these samples to the crystallinity order (SF), as well as the 2010, 1090, and 712 cm^{-1} peak areas.

No evidence of reduction atmospheres was detected within the RDM layer 9 faunal assemblages. Future experimental work discerning the conditions under which bone may be burnt in reduction conditions extreme enough to elicit laboratory responses will allow for better contextualization of burning scenarios which may have other geological signals, informing FTIR-ATR sampling procedures.

Duration

Length of a fire event is intrinsically linked to function of the combustion features (Mallol et al. 2007; Mallol and Henry 2017). Under significant time lengths, here defined loosely as ~ 9 hours, burned bone experiences diagnostic transformations which may be utilized to identify long durations within archaeological assemblages (Chapter 3; Gallo et al., in prep). Bone burned at temperatures under the threshold of calcination (~700 °C) do not experience structural and chemical alteration characteristic of calcination as expected but do become depigmented and are observed to be hues of whites, greys, and light tans (Chapter 3; Gallo et al., in prep). These visual cues traditionally have been inferred to be of calcination, however, and therefore the discrepancy presents an opportunity to be detected by spectroscopic methods such as FTIR-ATR (Chapter 3; Snoeck et al., 2014; Stiner et al., 1995).

Within the sampled coarse screen fraction of RDM layer 9, some samples were noted to be "indeterminant"; four of these samples, some exhibiting partial carbonization (Fig 35), were selected for FTIR-ATR. All of these indeterminant fragments had presence of light coloration which was dissimilar to unburnt bone within the assemblage, exhibiting hues of tans and greys (Fig 35). These samples are potentially linked to longer duration fire events at low temperatures, as they all have not had color transformation from structural or chemical calcination as observed by their FTIR-ATR spectra (Fig 35). From the FTIR-ATR data, besides the absence of heat related peaks at 1090 cm^{-1} and the PHT shoulder on the PO_4^{3-} v4 peak, organics are at very low quantity, but similar to other bone due to poor organic preservation with the assemblage. The trough at 595 cm^{-1} between the 605 and 565 cm^{-1} peaks is extended, indicating a higher order of crystallinity than bones only partially burnt for short durations, making misidentification of stage 2 bone unlikely (Fig 35).

These samples are kept separate for the calculation of the FTIR-ATR indices, and it is recommended that future research more extensively sample bone fragments within these coarse screens to provide a larger dataset on any fire which may have occurred in the vicinity to confirm long duration burning. Micromorphological slides should also be consulted to gain information regarding fire lenses in proximity to these excavated materials.

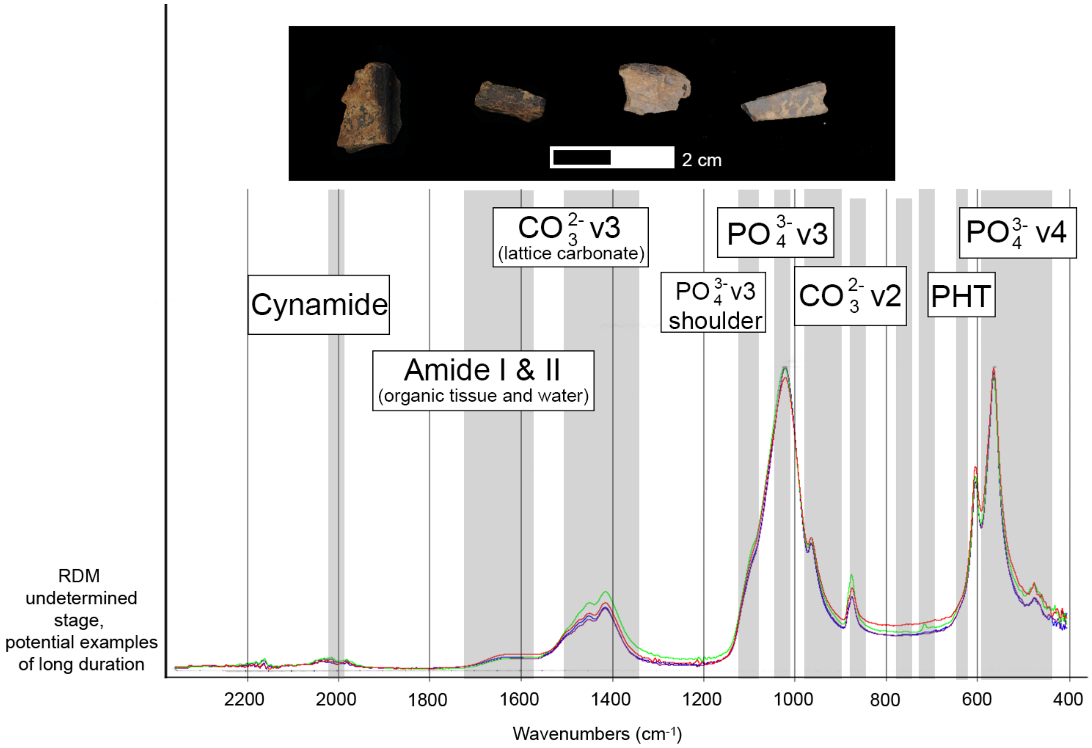

Fig 35: FTIR-ATR absorbance spectra of bones flagged as potentially representing samples which have undergone low temperature heating at long temperatures. This includes a mixed signal of depigmented, light coloration, no spectral indications of calcination (observable through the not present 1090 cm^{-1} and 635-630 cm^{-1} PHT shoulders), and an elevated degree of crystallinity as measured by the SF ratio which is higher than bones observed to be burnt to lower temperatures within the same assemblage.

FTIR-ATR indices

Twelve indices were calculated to quantify the relationships between different chemical and structural components of the burnt faunal assemblage of RDM layer 9 (Table 5). It is expected that the C/P, CO/CO3, CO/P, API, and BPI will show decreasing trends along with burning, while the SF, C/C, OH/P, and PHT will increase with increasing temperature intensity. Special attention in this study is given to the carbonate content of bones assigned to stages 5b and 6b, as it is hypothesized that blue coloration is indicative of bone burnt with high carbonate content along with manganese from post-mortem incorporations. Samples which may represent low temperature and long duration fires are additionally expected to not show any spectral indications of calcination but have low organic content, presumably removed without high temperature exposure (Chapter 3). Variation within samples fully calcined, stage 6, are also highlighted here as if stage 6 bone experienced different degrees of high temperatures (>700 °C) differing signals within the measurements should be detected and not observed visually as all bone heated > 700 °C in air is white in coloration.

Infrared splitting factor (SF)

The calculated SF from the PO_4^{3-}v4 peak area of the archaeological samples demonstrates strong alignment with expectations of increasing orders of crystallinity from unburnt bone (stage 0), bone burnt to lower temperatures experiencing organic decomposition (stages 1-3), large values subsequent to calcination presence starting with stage 4, and, finally, decreasing values within stage 6 likely indicative of temperatures reached above 800 °C (Fig. 35). Indeed, great variation is seen within the stage 6 category, including high values which represent temperatures reaching 800 °C, and the lower values (here under SF 5), demonstrating the well described crystallinity decrease of bone burnt above 800 °C . This decrease is related to the chemical and structural changes with the fusion stage of bone transformation, as bioapatite crystals melt and sinter at extreme temperatures (Fig. 36; Ellingham et al. 2015; Gallo et al. 2021; Mamede et al., 2018; Piga et al., 2018). This example clearly demonstrates the internal variability within the broad range of bones all categorized as Stiner et al. (1995) stage 6.

Unburnt bone (Stiner et al., 1995, stage 0) here has the lowest values, despite being relatively elevated by diagenetic crystal ripening compared to modern samples (Fig. 36). Samples flagged as potential representatives of long duration fire events (due to discrepancies between visible coloration and internal chemistry) have SF values higher than bones burnt to low temperatures and partially to fully carbonized and charred, supporting inferences of an alternative burning scenario outside of the typical burning stages (Fig. 35).

Stage 4 bone, bone with < 50% calcination, has the largest variation in SF values, bridging the carbonized/charred segments of the sample with calcined portions with higher order of crystalline structure within the same fragment (Fig. 36). Bones with presence of blue and carbonized/charred segments, stage 5b, exhibits SF values within the range of both stage 5 and stage 6 bone, while bone which is fully blue or blue alongside full calcination, stage 6b, has a striking pattern of low values, grouping with the stage 6 bone which is likely burned to over 800 °C (Fig. 36). This observation fits well with the understanding of manganese incorporation in the crystal lattice of bone alongside high carbonates, which are fully transformed above 800 °C (Chadefaux et al., 2009; Mayer et al., 2003).

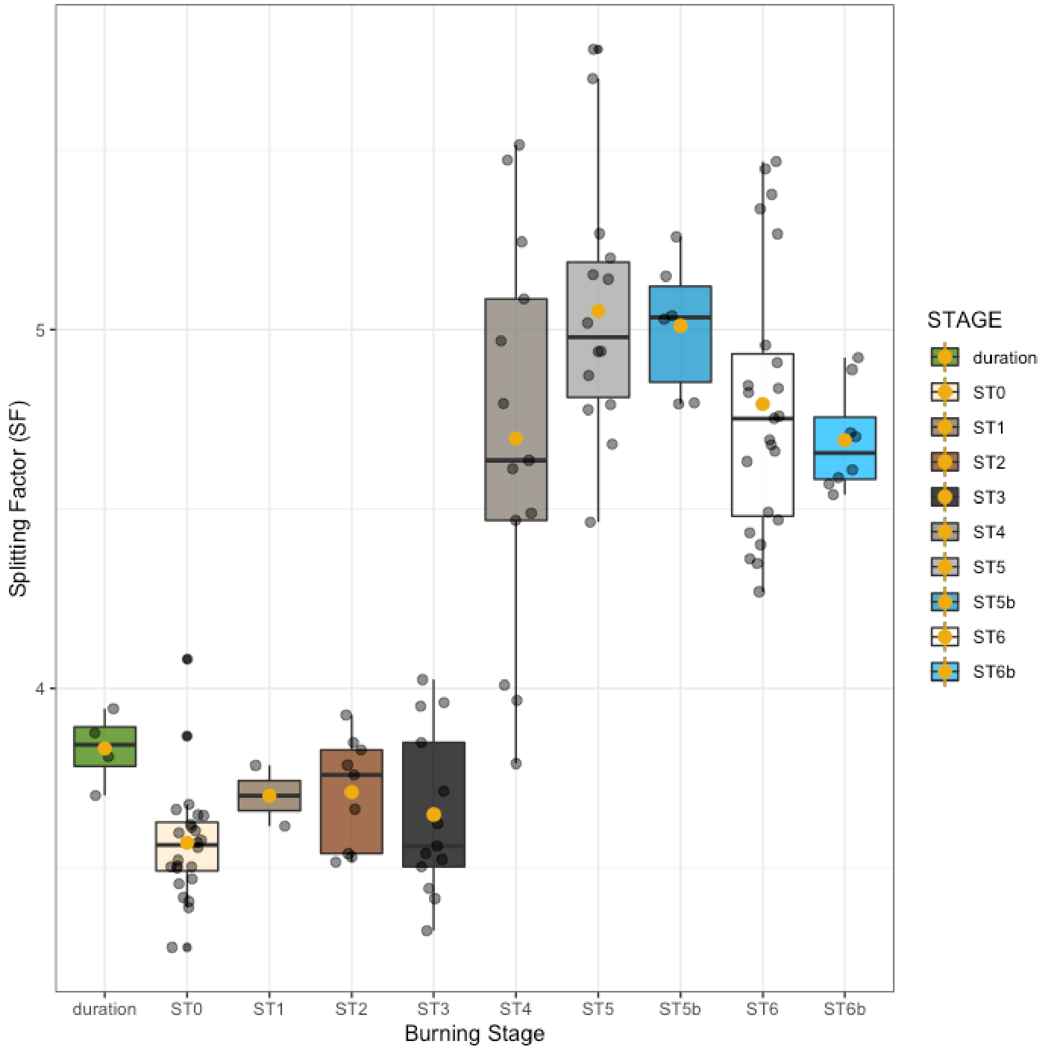

Fig 36: The splitting factor (SF) for archaeological samples from the coarse screen fractions of RDM layer 9 classified by Stiner et al. (1995) burning stages with the addition of blue bone within stages 5 and 6, stages 5b and 6b respectively. Values demonstrate increased crystallinity after unburnt bone (stage 0), which themselves have elevated values due to diagenetic processes. Samples noted to potentially represent long duration fires at low temperatures (under calcination thresholds) have higher values than counterparts within stages 1-3 which are partially to fully charred and carbonized. Stage 4 bones have the first indications of calcination and experience a growth in values, followed by even more ordered degrees of crystallinity measured for the stage 5 and 5b bones. Stage 6 bones experience a great deal of variation likely to the fusion stage of bone burning which takes place ~ 800 °C. Stage 6b bones have values similar to the lower stage 6 bones, indicative of the internal chemistry and impact of substitutions within the crystal lattice after calcination.

Carbonate to Phosphate ratio (C/P)

The C/P ratio captures the loss of lattice carbonate within bones, carbonate which is lost in two stages as organics are eliminated (~300 °C) and, further, as structural carbonate is lost when bone chemistry is reorganized by calcination (~680 °C). Bones which are unburnt and burned to low temperatures (stages 1-3), including the bones potentially representing duration signals, have median ratios and no large distinguishing values as expected (Fig. 37). After carbonization and charring, bone is seen to have much lower ratios in stage 4, with further losses accounted for in bone that is > 50% and fully calcined (stages 5, 5b, 6; Fig 36). Extremely high C/P values are noted in one stage 2 sample and several stage 6 and 6b samples, indicative of the incorporation of exogenous carbonates from the diagenetic environment (Fig. 37). This information supports inferences that bones with the presence of blue, primarily stage 6b, are bones burnt with high amounts diagenetic carbonate inclusion (Fig. 37).

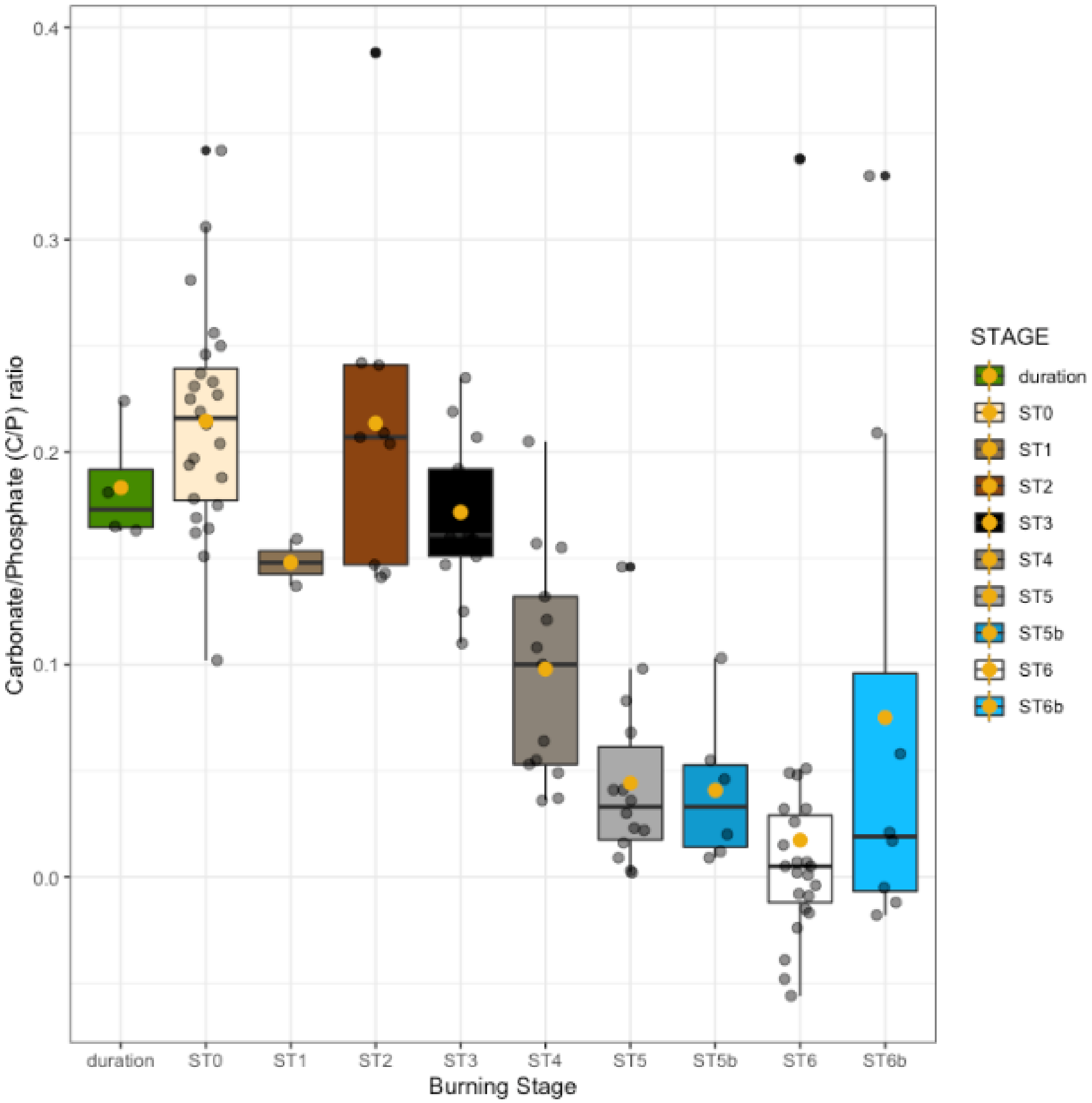

Fig 37: Carbonate to Phosphate (C/P) values for archaeological samples classified by the Stiner et al. (1995) scale of burning intensity. Two losses in carbonate are seen clearly here, after the combustion of organics in stage 3 and further with > 50% calcination in stages 5 and 6. Exogenous carbonates are detected here with large values, supporting hypotheses especially that stage 6b bone has blue coloration due to the structure and chemistry of bone prior to burning.

C/C

The C/C ratio describes the ratio of carbonates A and B to carbonate B (Mamede et al., 2018; Snoeck et al., 2014). This ratio is described to be higher when bones are burnt above 600 °C but under 900 °C, as type B carbonates transfer to A sites for an increased value at the A site (Holcomb and Young, 1980; Mamede et al., 2018; Snoeck et al., 2014). The same effect can also be reached by other depletions of B type structural carbonate, which is lost both after organic combustion and with reorganization after calcination (Mamede et al., 2018). With the RDM layer 9 samples an increased C/C ratio is indeed seen within the stage 5 and 6 bones (Fig. 38). Large variation within stage 6 bones may be explained by diagenetic incorporation of carbonates, which would also explain the lower values within stage 5b and 6b bones (Fig. 38).

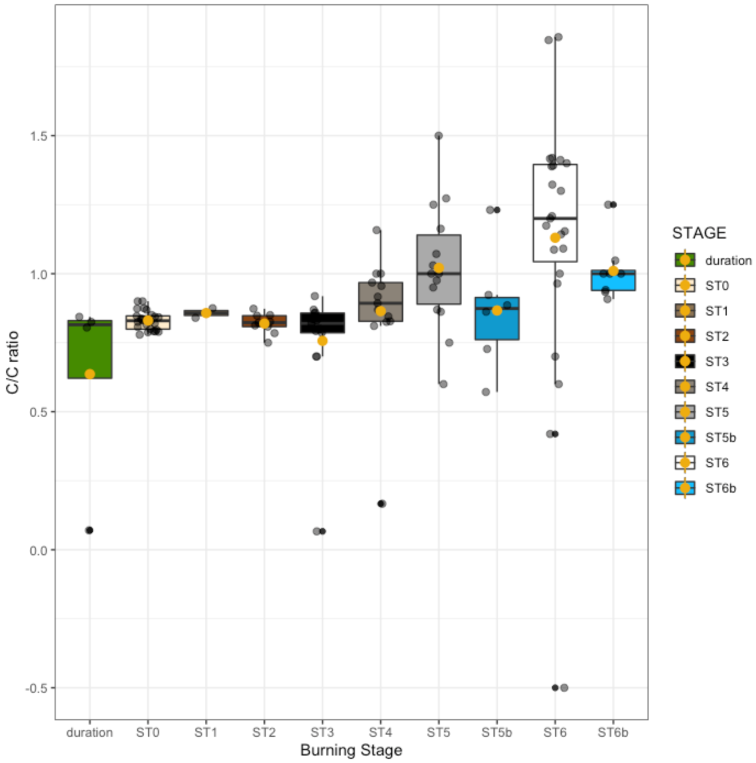

Fig 38: C/C ratio of archaeological coarse screened bone samples from RDM layer 9, organized by Stiner et al. (1995) stage of burning intensity. Higher values are noted with calcination following expectations.

CO/P

The CO/P ratio represents another measure of carbonate to phosphate content of bone, here utilizing a different carbonate peak area which is elevated also in the presence of organic content (Amide I and II from collagen). This ratio is suggested to investigate differences between burning at lower temperatures, but as the organic preservation within layer 9 is sparse, this ratio does not demonstrate statistical differences between bones thermally altered under the threshold of calcination (Fig. 38; Mamede et al., 2018; Thompson et al., 2013). Unburnt stage 0 bone is recognized, however, to have many values above the mean burnt data, indicating that some organic material remains within these few samples (Fig 39).

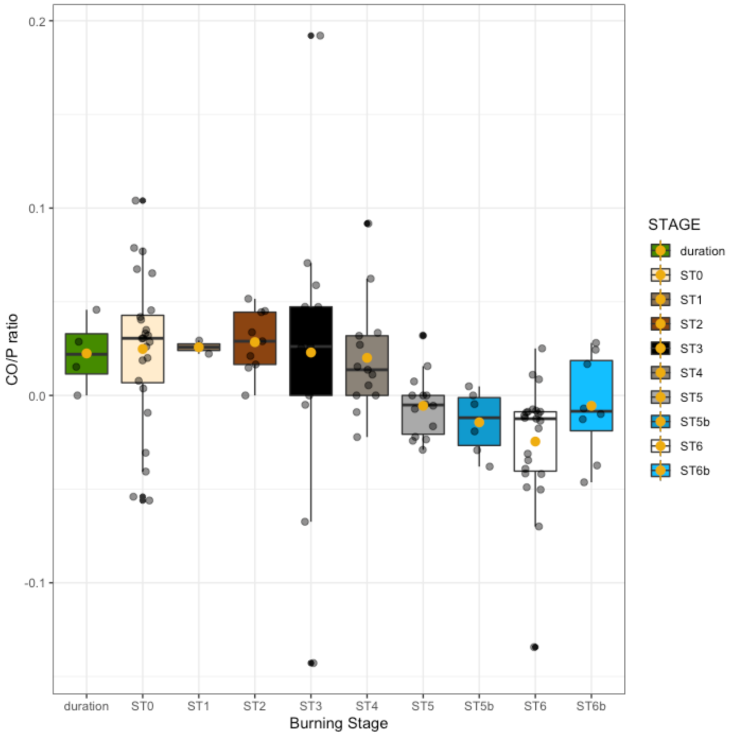

Fig 39: The CO/P ratio of archaeological samples organized by Stiner et al. (1995) burning stage. Major distinguishing values are not seen within unburnt bone (stage 0) and bone burnt to low temperatures (stages 1-3) due to the low organic content within the assemblage due to poor preservation.

CO/CO3

The CO/CO3 ratio provides a measure of organics relative to a carbonate peak (1415 cm^{-1}). Similar to the CO/P ratio, the poor preservation of organics (primarily collagen) yields samples as nearly indistinguishable and therefore is not a useful measure to differential burning at lower temperatures within this assemblage (Fig. 40). Large variance seen in stage 6 bone again is potentially skewed due to exogenous carbonate content measured at 1415 cm^{-1}.

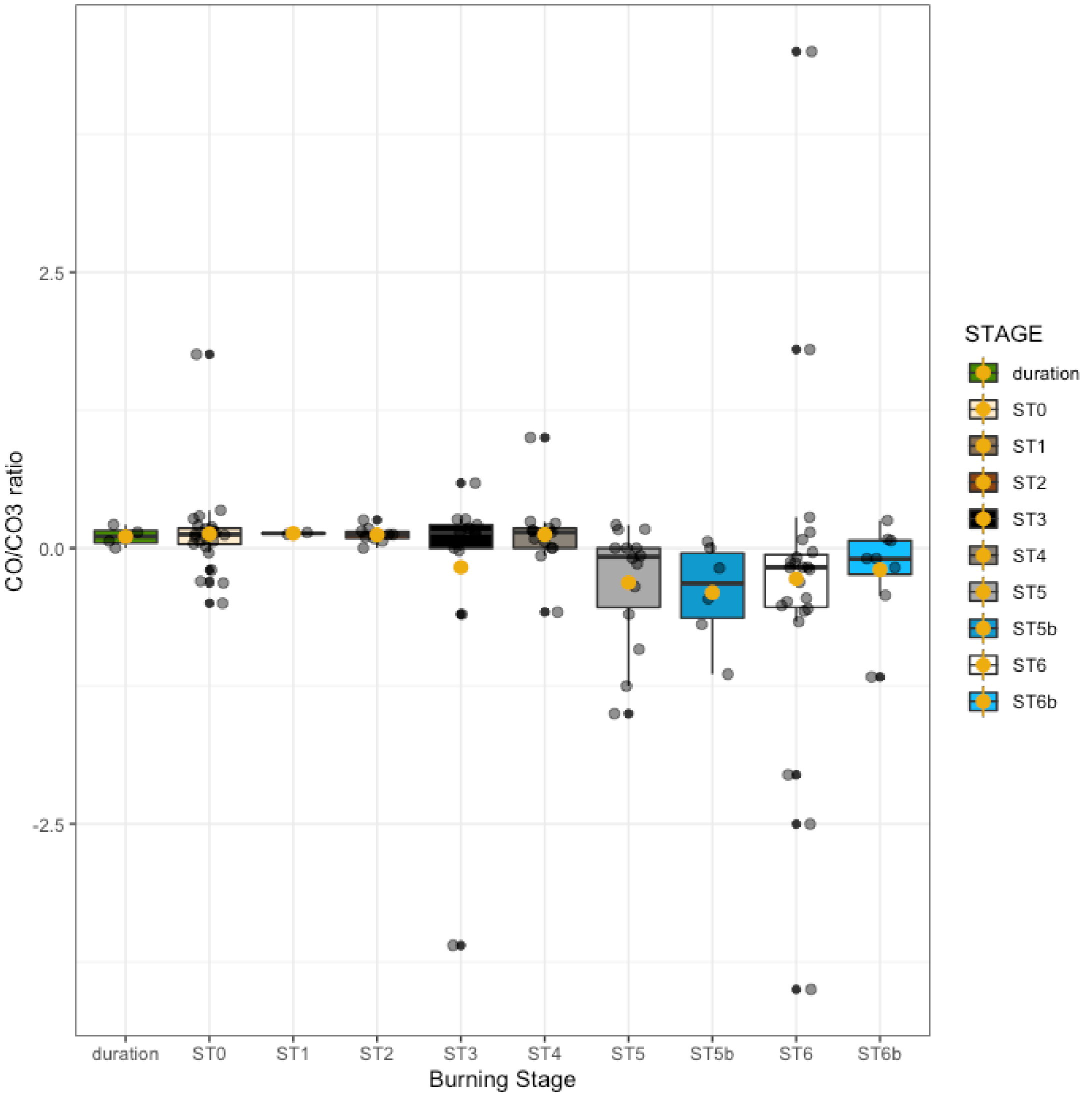

Fig 40. CO/CO3 ratio with samples classified by Stiner et al., (1995) burning stage. Differences between samples burnt to lower temperatures here are not visible, as organic preservation is poor within the assemblage**.**

API

The API ratio monitors the type A carbonate content within bone samples, utilizing the 1540 cm^{-1} carbonate type A peak and the 605 cm^{-1} phosphate peak (PO_3^{4-} v4). API values are reported to be not be applicable at lower temperatures, as the Amide II band overlaps with the carbonate peak before the organics are removed (Mamede et al., 2018; Snoeck et al., 2014). As the samples within the RDM layer 9 assemblage do not have organic content present, 1540 cm-1 values are here indicating the carbonate content present (Fig. 41). While Snoeck et al. (2014) describes increasing API values, as type A substitutions are thought to increase at the expense of type B carbonates until 800 °C, that pattern is not seen here (Fig. 41). This pattern does follow inferences and expectations of carbonate loss with both decomposition and structural and chemical calcination, however.

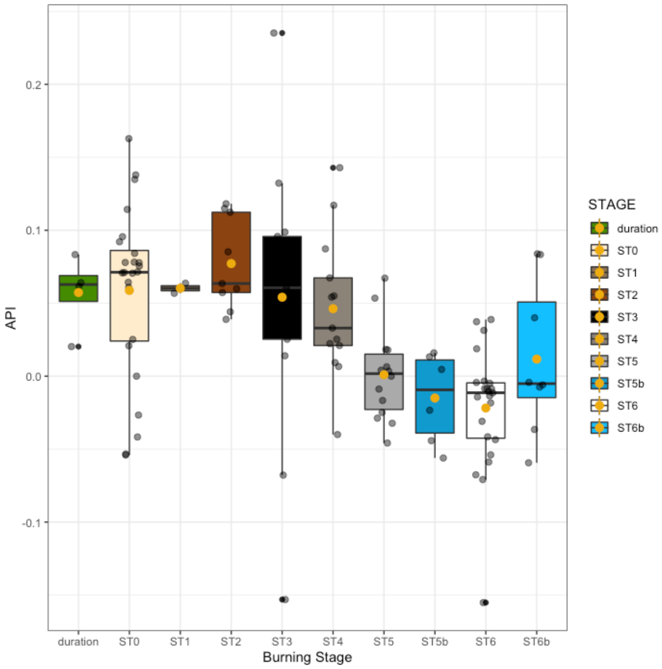

Fig 41. API ratio of type A carbonate presence relative to phosphate content classified by Stiner et al., (1995) burning stage. Values are seen to decrease with increasing temperature, likely capturing the elimination of all carbonates with heat intensity.

BPI

The BPI index represents relative amounts of type B carbonates which are predicted to be eliminated, noted to be CO_2 by Mamede et al. (2018), with high temperatures. Type B carbonates are described to be lost first substituting with type A carbonates and then lost with calcination at higher temperatures (Snoeck et al., 2014). Values presented here do follow expectations, with increasingly lower values with significant separation between bones burnt to lower temperatures and bones which have experienced partial or complete calcination (Fig. 42). High ratios are noted within the stage 6 and stage 6b samples, likely influenced again by exogenous carbonates (Fig. 42).

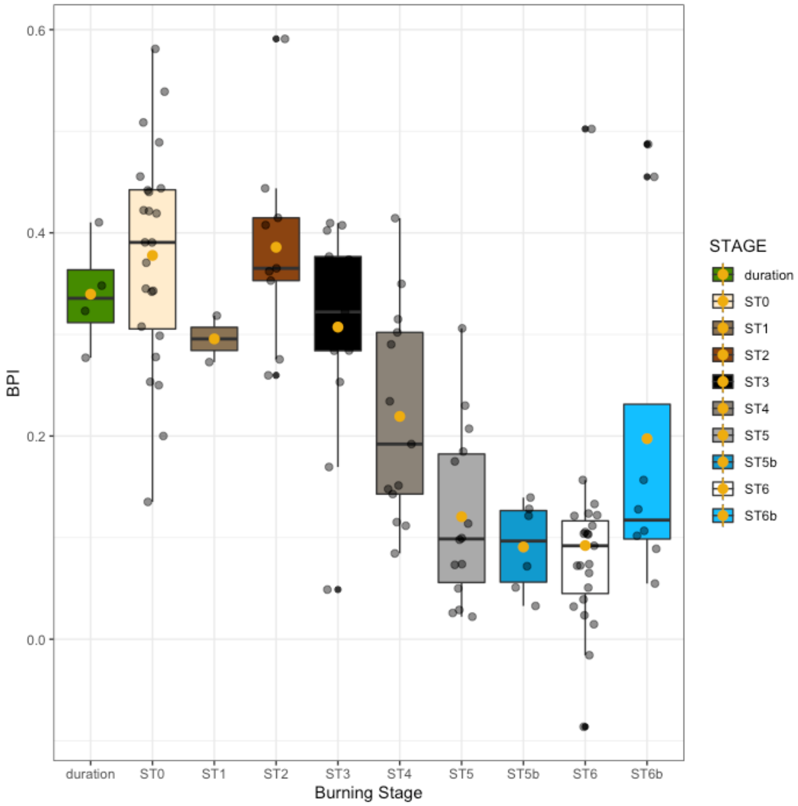

Fig 42: BPI ratio of archaeological bone organized by Stiner et al., (1995) burning stage. Decreasing values are seen alongside increases in temperature intensity, with the lowest value indicating the near loss of all type B carbonates after structural and chemical calcination.

CO3/P

The CO3/P here ratio is determined here with two measures, the 878 cm^{-1} peak height and the 900 cm^{-1} peak height (Thompson et al., 2013). This is as the CO3 band is assigned to the 878 cm^{-1} peak height, potentially shifted for the description of the index by Thompson et al. (2013) due to shifts in the spectral range assigned to different carbonate environments (Mamede et al., 2018). Both measures result in similar patterns of decreasing values in bones reaching stages of full combustion and partial calcination (stages 3-5), followed by sharply increasing values with full calcination, stage 6, and calcined samples with blue coloration, stage 6b (Fig. 43). The decrease in ratio values indicates decreasing carbonate loss, as expected (Fig. 43). The high ratio seen with calcined samples indicates two relevant shifts in bone structure and chemistry, including the decrease of carbonates at 878 cm^{-1} with increasing temperature (Fig. 43). Shifts in the broadening of the PO_4^{3-} v1 peak, broadening at 960 cm^{-1} resulting in a generally raised area, is additionally responsible for the shift in ratio values (Mamede et al., 2018).

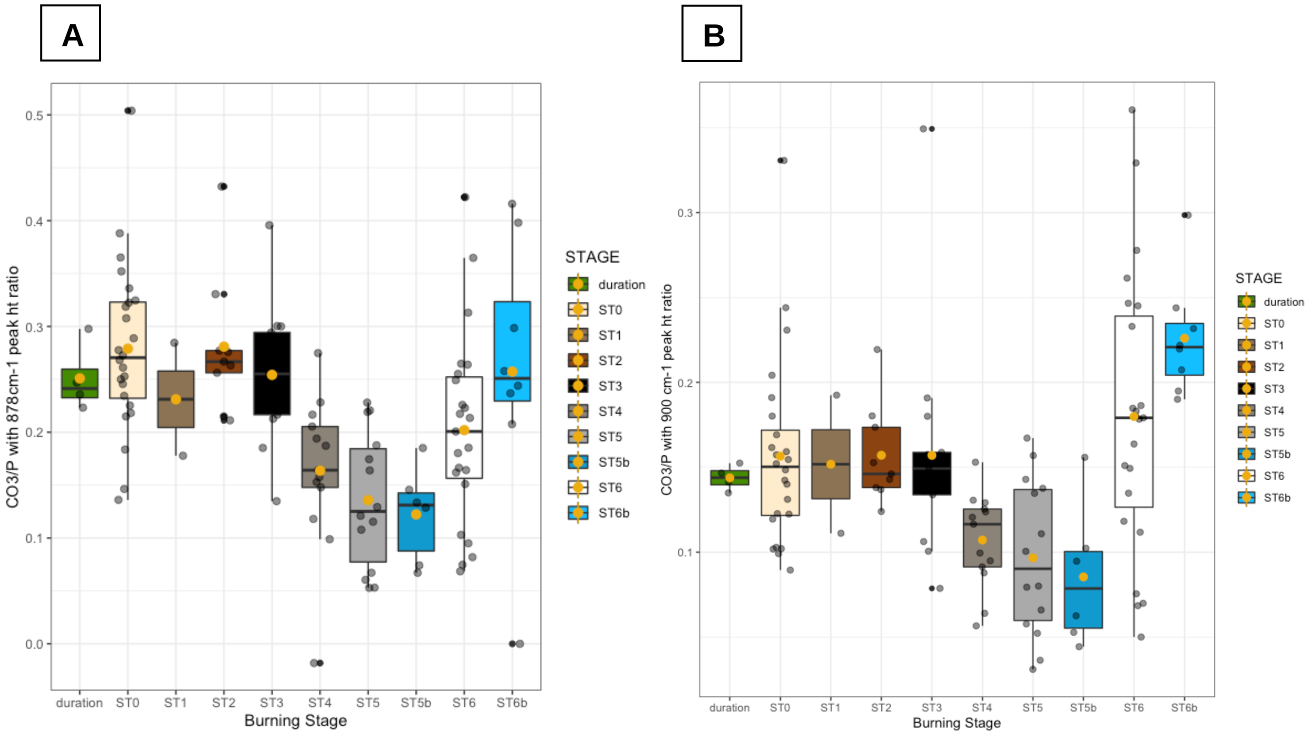

Fig 43: CO3/P ratio calculated both with 878 cm^{-1} (A), the assigned peak area for CO$_3^{2-}$v3, and 900 cm^{-1}(B), the measurement described by Thompson et al., (2013). Patterns are similar between the ratios, both with increasing values alongside temperature exposure seen until full calcination, seen in the stage 6 and 6b samples. Increasing PO$_4^{3-}$ v1 peak area broadening, due to structural reorganization coinciding with high temperatures, changes the relationship between peak heights used in this index, resulting in a large range of values within the stage 6 category with the higher ratio values within this category representing samples burnt to higher temperatures.

CN/P

Measures of cynamide within samples are argued to be indicative of burning conditions, such as burning in the presence of ammonia, potentially from burning of fleshed elements (Mamede et al., 2018). Interestingly, cynamide is also seen burning at high temperatures (reported at 900 °C) in laboratory reduction conditions (Reidsma et al., 2016). This observation potentially indicates that burning fleshed bone works as reduction conditions.

CN/P ratios for the RDM assemblage do not indicate cynamide presence at any stage of burning utilizing both ratios suggested in the literature (Fig. 44). Ratio are differentiated by different measures of phosphate, both the PO_4^{3-} v3 and v4 peak heights (Fig 44; Mamede et al., 2018).

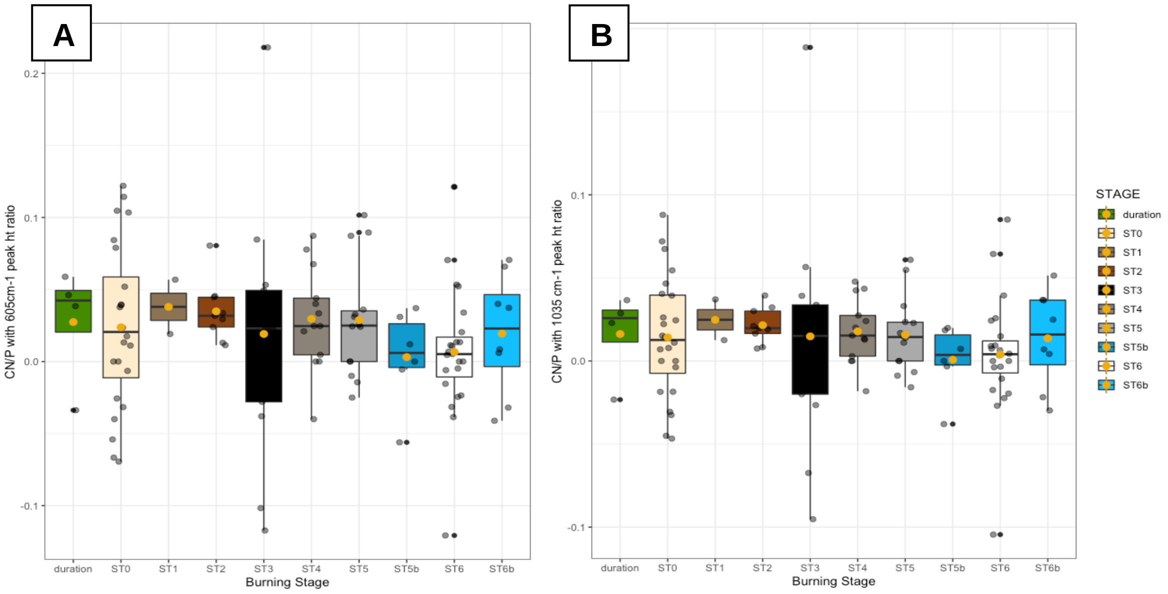

Fig 44: CN/P ratios utilizing both the 605 cm^{-1} (A) and 1035 cm^{-1} (B) phosphate peaks (PO_4^{3-} v4 and v3, respectively).

OH/P

The OH/P ratio represents the emergence of a peak from the PO_4^{3-} v4 shoulder, indicating the libration of OH- (hydroxyl group). This peak shoulder is only apparent with high temperature alteration, as it is necessary for the restructuring of bone's chemical order that changes the vibrational mode of the hydroxyl incorporation (Grunenwald et al., 2014; Mamede et al., 2018). This measure is nearly identical to the PHT ratio, as both monitor the same shoulder appearance and height.

Archaeological samples from RDM layer 9 follow expectations for the behavior of this index. Ratios are seen to increase significantly alongside calcination, first noted in stage 4 bone (Fig. 45). These values are still seen to breach averages similar to bone burnt to lower temperatures, fitting with stage 4 bone's composition of both carbonized/charred material (Fig. 44). A similar scenario can explain low values for stages 5 and 5b (Fig. 45). Large increases in OH/P with greater degrees of calcination provide a clear indication of high temperature alteration that fits well with burning classifications (Fig. 45). Samples which potentially represent long durations at low temperatures have ratios similar to unburnt bone and bone burnt to low temperatures, they are not structurally or chemically calcined (Fig. 45).

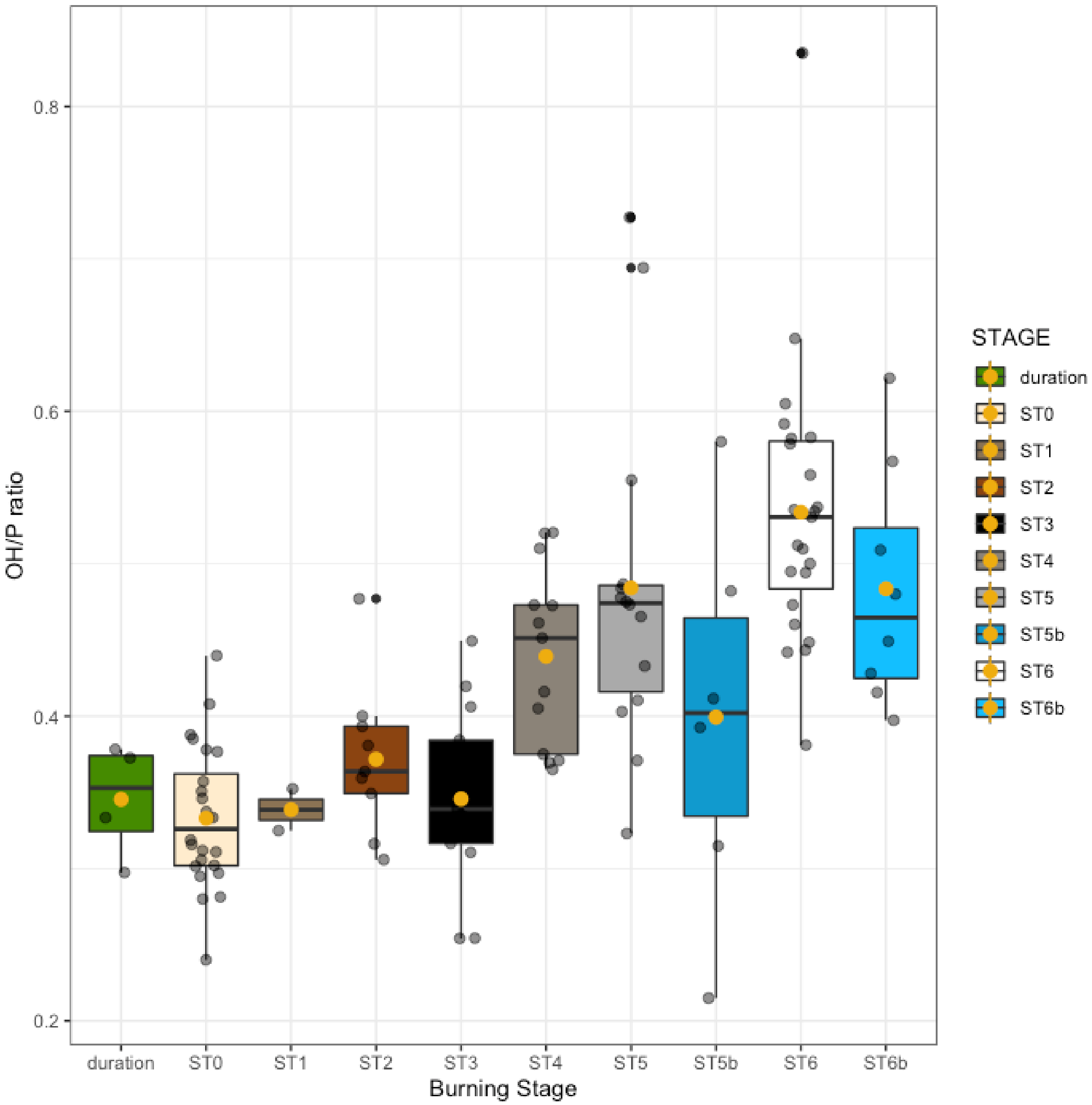

Fig 45: OH/P ratio for RDM layer 9 bone by Stiner et al., (1995) burning stage. Values are seen to increase with presence of calcination, indicative of the emergence of the shoulder on the PO_4^{3-} v4 peak and structural and chemical calcination at high temperatures.

Cal/PO4

The Cal/PO4 index has been suggested as a measure to estimate the amount and degree of secondary calcite precipitation within archaeological samples (Dal Sasso et al,, 2016). Ratios calculated for the RDM layer 9 bone do highlight several samples with large ratios, monitored through the 712 cm^{-1} peak height (Fig. 46). These samples are also samples exhibiting exogenous carbonate measured at other points in the spectra (primarily 1415 cm^{-1} and 878 cm^{-1}), indicating samples which have undergone more extensive diagenetic alteration in addition to thermal alteration.

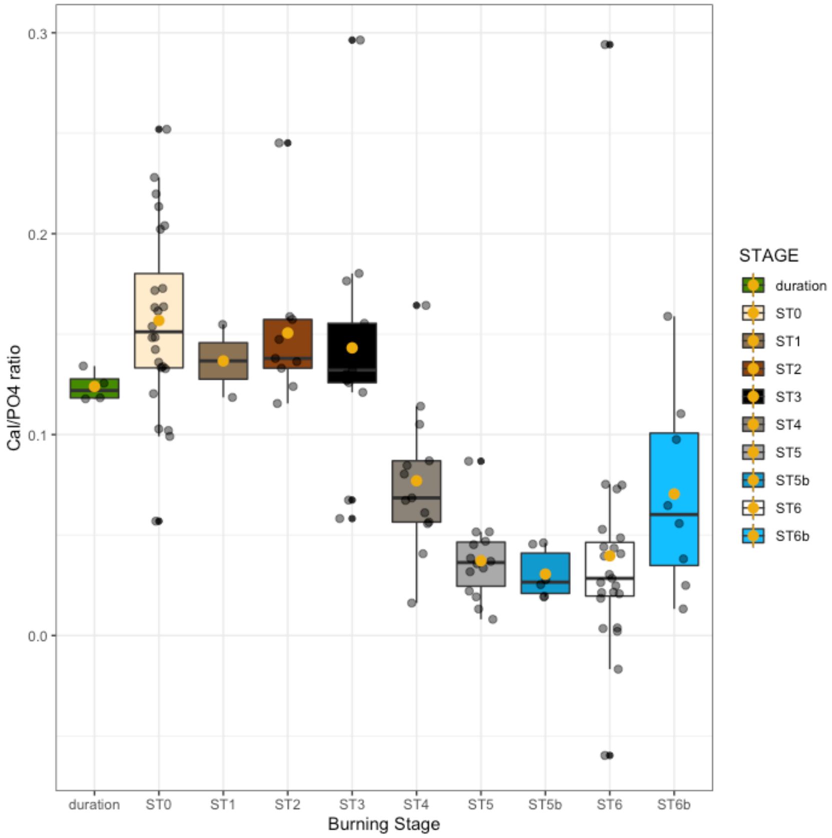

Fig 46: Cal/PO4 ratio, an index for determining the degree of secondary calcite precipitation, classified by Stiner et al., (1995) stages of burning intensity. Values follow a pattern of decreasing ratio alongside increasing temperature, but several extremely high values within stage 0, stage 2, stage 3, and stage 6 likely represent diagenetically altered bone material. Fortunately, the exogenous incorporation of calcite from the environment overall does not impact measures relevant to evaluating high temperature alteration.

High temperature exposure

Several spectral indicators, such as the large range of SF values within fully calcined bone, provide indications that a range of temperatures are reached within bone classified as Stiner et al., (1995) stage 6. This includes ranges of values within stage 6 for the CO3/P and SF indices, as bone burnt to higher temperatures in each scenario change the behavior of the ratio (Figs. 36, 43). As bone becomes white with the full elimination of organic char, typically seen with other structural and chemical changes that constitute calcination, stage 6 bone can be expected to represent minimally temperatures of ~680 °C. As full carbonates are eliminated over 1000 °C along with other changes to the spectra, signals not seen in any archaeological sample tested here, maximum boundaries can additionally be established for this assemblage at < 1000 °C. Data from the study of blue bone predicts that full blue expression is seen at temperatures of 800 °C, providing a temperature estimate for the stage 6b burned bone (Mayer et al., 2003). Finally, Snoeck et al. (2014) reported a strong relationship between elevated C/C ratios and lower SF values. This is as for temperatures above 800 °C, the SF index lowers for calcined bone due to structural reorganization with fusion stages of bone thermal alteration (Piga et al., 2008), but high C/C values still represent bone burnt to high temperatures. When ratios of C/C and SF are compared for all samples with indications of calcination within the RDM layer 9 assemblage, two groups of bone assigned to stage 6 are observable (Fig. 47). The first cluster, grouped around the lower SF values between 4 and 5, likely represent bone burnt above temperatures of 800 °C, with one sample from square J18 potentially indicating even higher temperatures (Fig. 47; Snoeck et al., 2014). Stage 4 bone also clusters with the stage 6 bone with low SF values, but this is due to the presence of low orders of crystallinity within the charred and carbonized portion of the bone mineral and represents temperatures only barely reaching calcination (~680 °C). Bone with high SF values and median C/C ratios are estimated here to represent temperatures reached around 700 °C (Snoeck et al., 2014).

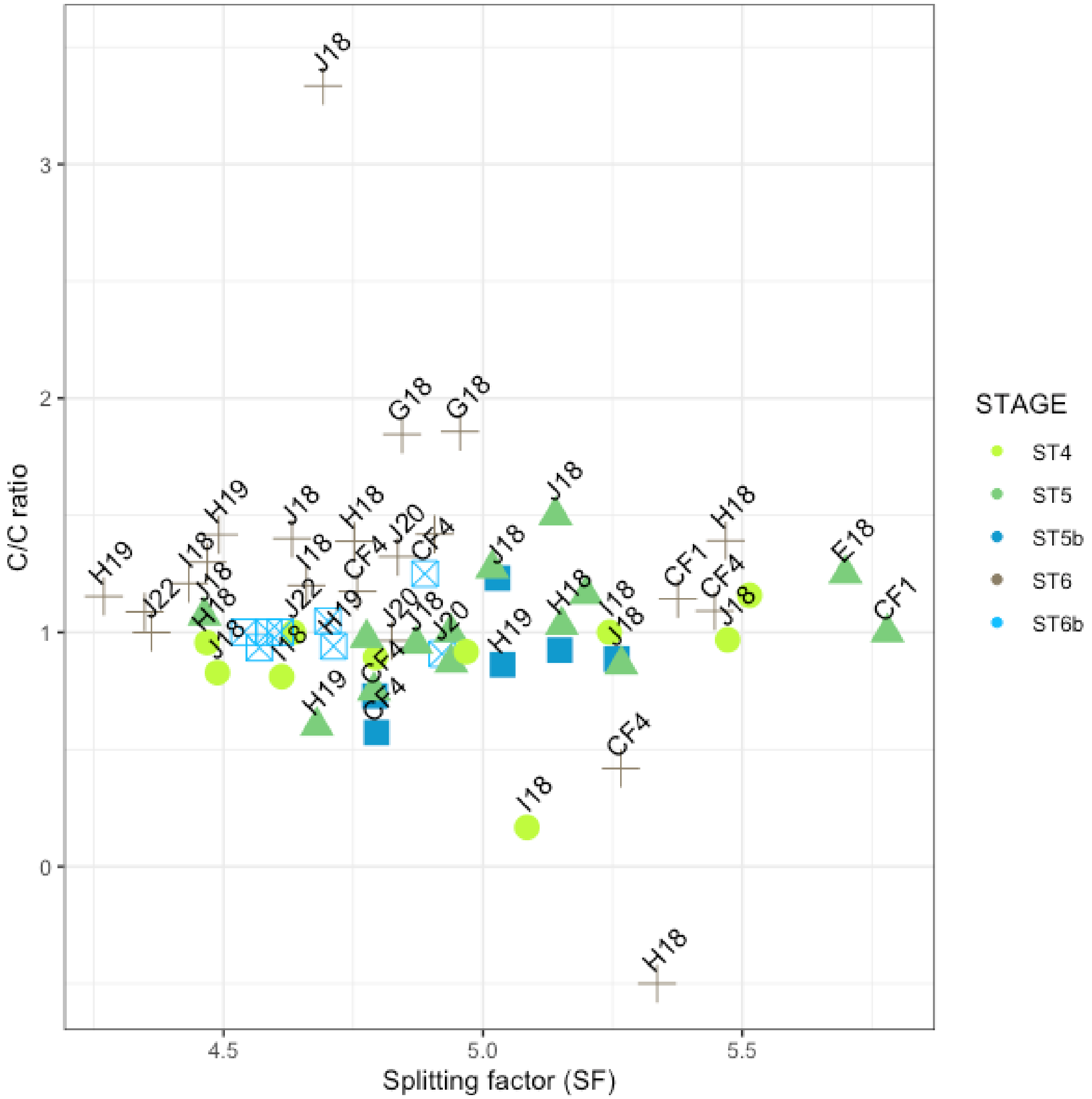

Fig 47: C/C and SF ratios compared for bones with partial to complete calcination, Stiner et al., (1995) stages 4-6, with distribution of bone specifically within stage 6 highlighted here to be representative of temperatures reached likely at and above 800 °C for C/C values of 1 and above alongside SF values lower than 5. Color schema has been adjusted for clearer distinguishing between samples at different Stiner et al. (1995) stages.

Micro- FTIR

The ability to observe combustion features at RDM layer 9 within micromorphological thin sections provides an opportunity to evaluate the sequence of burning, preservation (in primary or secondary location of fire residues) and nature of contents within features while preserving depositional fidelity. Further, the use of mFTIR directly on bone captured within micromorphological samples allows researchers to precisely record infrared spectra representing the chemical and structural composition of bone simultaneous to documenting the undisturbed relationships between the sampled faunal fragments and their burial environment. This is a significant tool for establishing details of specific fire events which are blurred and time-averaged at the scale of both types of excavated fauna: coarse fraction from the screens and piece plotted remains (Goldberg et al., 2017). Understanding details of burning in relation to the depositional microcontext additionally can explain and explore patterns in diagenetic alteration relevant to burning, such as the incorporation of exogenous carbonates and manganese potentially resulting in deposits of blue calcined bone.

Three micromorphological slides, RDM-211ash, RDM-501, and RDM-506a, from RDM layer 9 are considered here to test the applicability of standard infrared indices related to thermal alteration on bones within thin sections, as well as to discuss patterns of burning represented in-situ faunal fragments. As the mFTIR instrument utilized for this study has a spectral range of 4000-600 cm^{-1}, indices which utilize measurements lower than 600 cm^{-1} are excluded from analyses, including the SF. Due to these limitations, bone here can be categorized as calcined (heated above temperatures of 700 °C) or not calcined (represented bone both unburned and burned to lower temperatures), and 11 indices were calculated for each thin section considered.

Sample RDM-211ash

Sample RDM-211ash features two ashy localities processed together but not stacked in situ, with an upper and lower unit which are separated clearly in resin indicating their perimeters (Fig. 47). Four bone fragments were found large enough to be tested within the 211-ash thin section, providing two samples within each unit (Fig. 48). Bones within these two domains of Sample RDM-211ash are less common and are primarily composed of calcium carbonate. No indications of calcination were found for these samples. Significant peak heights are observed at 1540, 1415, 878, and 712 cm^{-1}, areas relevant to the incorporation of environmental carbonates and calcite (Fig. 48). Despite being embedded in ash deposits, the analyzed bones were not subjected to temperatures high enough for calcination.

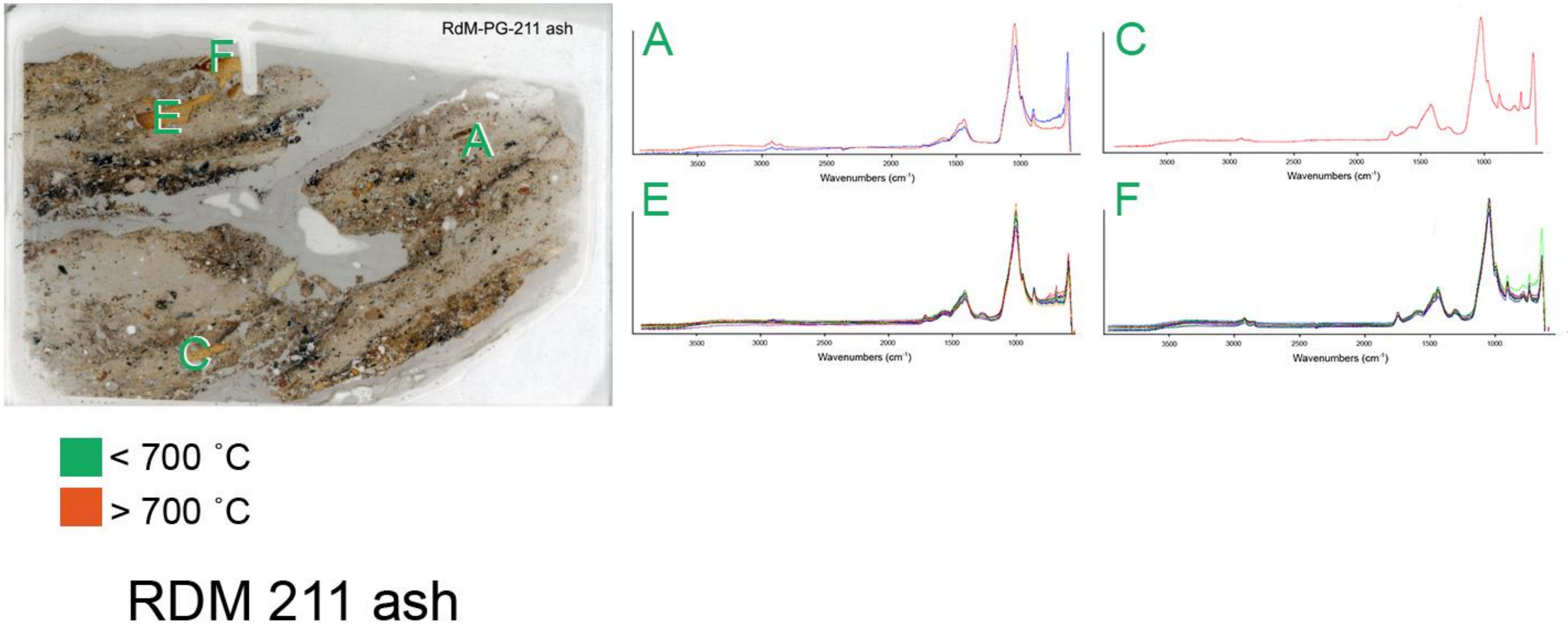

Fig 48: Micromorphological thin section of RDM-211ash with bone identified labeled corresponding to extracted FTIR spectra. No calcination was documented for these bones imbedded in ash deposits of calcium carbonate.

Sample RDM-501

Sample RDM-501 is extensively described in Aldeias et al. (2012) from a micromorphological perspective and represents two intact superimposed features (Fig. 49). The first feature at the base of the sample (Unit II) is very thin, 1 cm thick, bioturbated lens with both calcined (> 700 °C) and not calcined (< 700 °C) bone fragments (Fig. 49; Aldeias et al., 2012). The top feature (Unit I) is described as containing charcoal and black plant fragments, as well as rubified aggregates of silty clay (Aldeias et al., 2012). All bone of sufficient size to be tested with mFTIR within this upper unit demonstrate spectral signals of calcination, while at the base of Unit I bone primarily is not calcined and is within an organic-rich matrix (Fig. 49). Despite the lower feature being post-depositionally disturbed, mFTIR evidence provides here indicates likely evidence of different temperature distributions within these features- Unit II represents a high temperature event with high quantities of bone burnt, while Unit I reached lower temperatures and bone had a less prevalent role (Fig. 49). Many spectra of tested bone have indications of exogenous calcite and carbonate precipitation, as noted from the 1415 cm^{-1}, 878 cm^{-1}, and 712 cm^{-1} peak heights (Fig. 49).

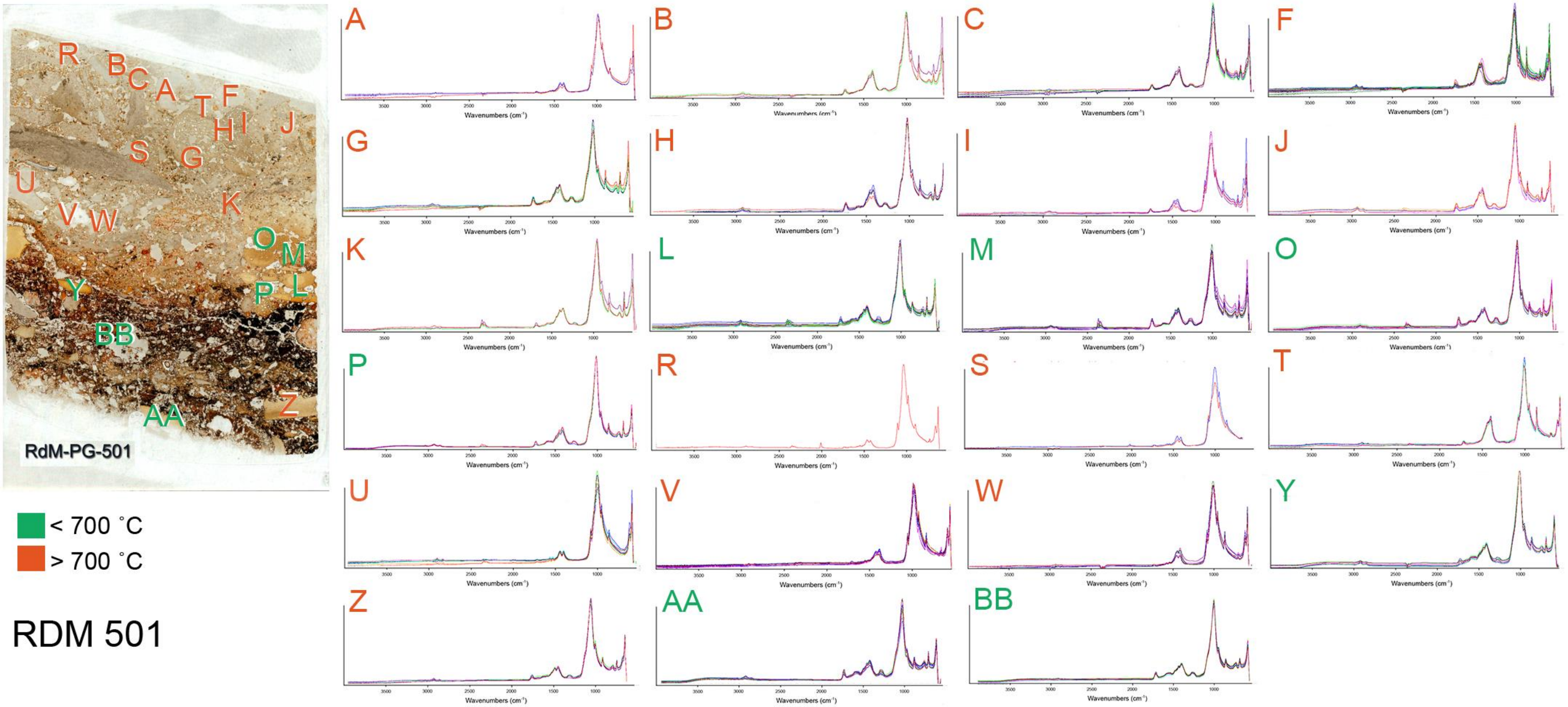

Fig 49: Micromorphological thin section of RDM 501, capturing two in-situ fire events. 23 bones were sampled within this slide, with temperatures primarily above 700 °C in the upper Unit 1 feature, and a mix of temperatures below 700 °C present in the lower Unit II.

Sample RDM-506a

Sample RDM-506a is characterized by large lithic artifacts dominating the central portion of the micromorphological slide. Bone is primarily organized above and around the lithic artifacts with several in-situ breakages present (see Fig. 50 samples L and K, P and Q, I and J). Different levels of preservation of bone are also observable, with highly degraded bone occupying the upper left hand corner of the slide, and bone with preserved cancellous portions visible (Fig. 50 sample M). Bone is primarily not calcined (< 700 °C). The observable spectral indications of diagenetic alteration are seen ubiquitously throughout sampled bone at peaks relevant for the incorporation of carbonates and calcite from the burial environment including 1415, 1540, 878, and 712 cm^{-1} (Fig. 50; Table 4).

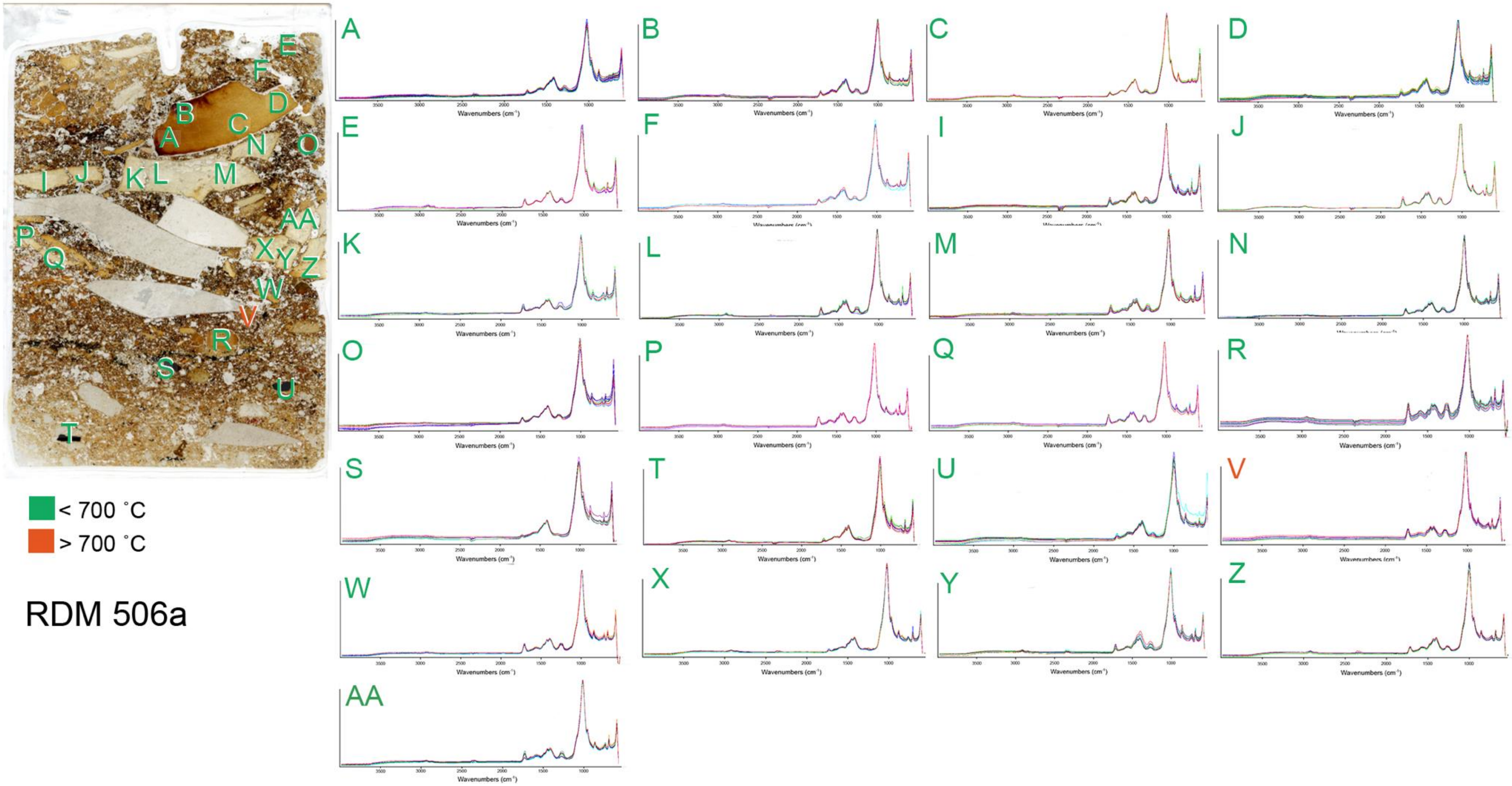

Fig 50: Sample 506a with 26 sampled bones documented. Only one bone of (V) shows indications of calcination and high temperature alteration.

C/P, C/C, CO/P, and CO/CO3

The extent of diagenetic carbonates incorporated and detected within the thin section bones have heavily altered and biased the C/P and C/C measurements (Fig. 51 A and B). Low initial amounts of organic preservation, here monitored with the CO/P and CO/CO3 ratio, also render these ratios without significant meaning (Fig. 51, C and D). This pattern of poor organic preservation within samples which are not calcined indicates that these measurements are not useful for interpreting the burnt assemblage, similar to the low organic content found within the coarse screened assemblage (Figs. 39, 40, 51 C and D).

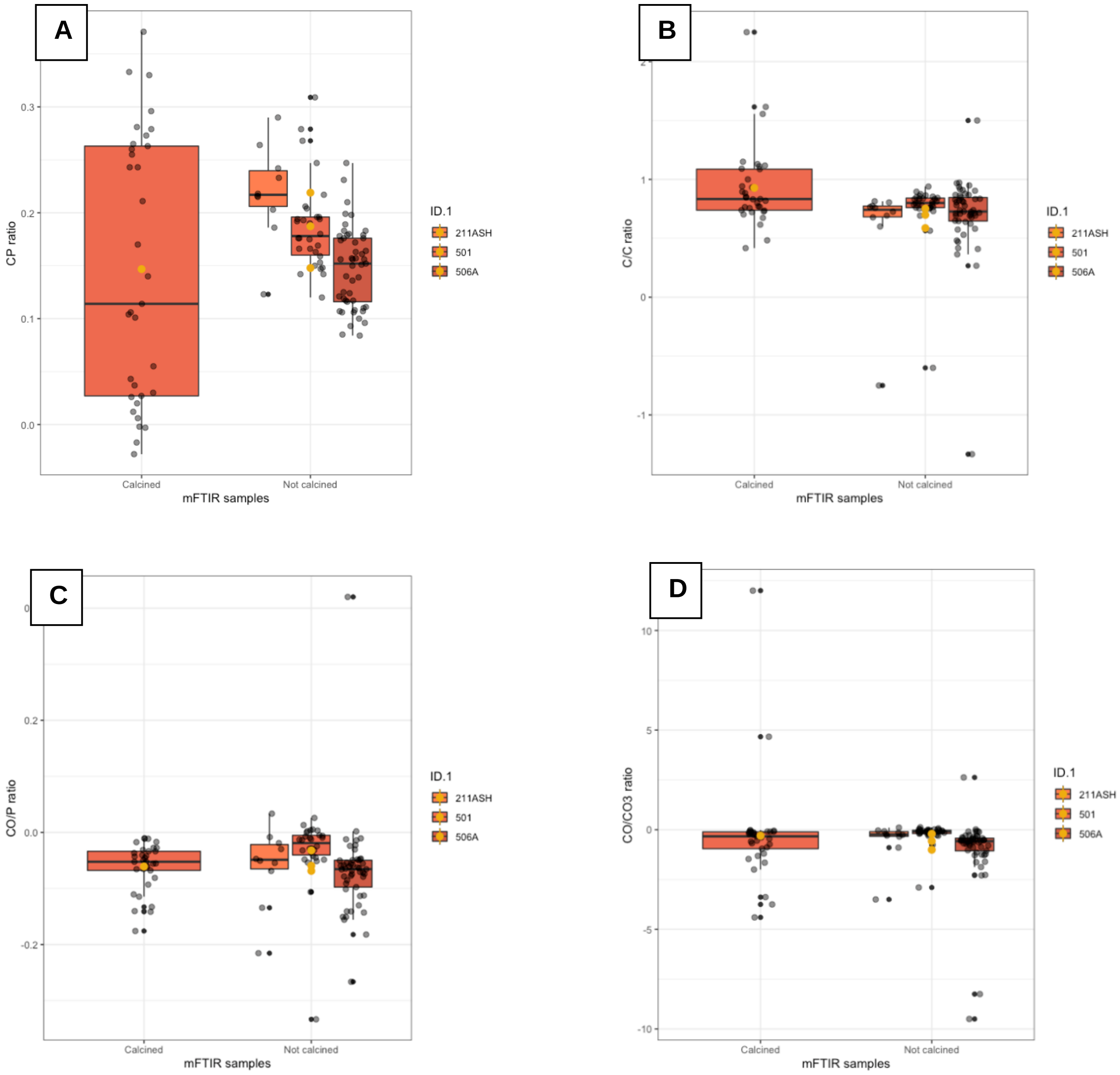

Fig 51: mFTIR results for bones within thin sections RDM-211ash, RDM-501, and RDM-506a organized by calcined or not calcined representing temperatures reached above and below < 700 °C. A) Carbonate to Phosphate (C/P) ratio of bones showing significant variation not distinguishable between burning thresholds. B) C/C ratios, with little variation in values. Such obscuring of differences, especially between bones burnt above and below 700 °C, a threshold which encompasses massive structural and chemical changes, indicates that the diagenetic alteration of samples and exogenous carbonate incorporation is preventing utilization of these indices. C) CO/P ratios low and uniform due to the near elimination of organic content in both calcined and not calcined bone. D) CO/CO3 index also does not provide differentiating signals from calculated values between burning categories, as expected. This is also directly influenced by the poor degree of organic preservation within all samples.

API, BPI, CO3/P

No patterns of decreasing API or BPI were seen within the micromorphological samples, despite expectations of low values within the calcined assemblage due to removal of carbonates (Fig. 52, A and B). This pattern can be explained by the high degree of exogenous carbonates found at 1540 and 1415cm^{-1} in both type A and B sites (Figs. 48-50). The CO3/P ratio calculated with the 900 cm^{-1} peak height following Thompson et al. (2013) shows highly constrained values between calcined and non calcined bones, all of which are slightly elevated (Fig. 52 C). There is no decrease in value in calcined samples as expected with carbonate elimination at high temperatures. Opposite circumstances are seen when the CO3/P ratio is calculated with the 878 cm-1 peak height, with calcined samples instead exhibiting the higher ratio (Fig. 52 D). This can be explained by the high degree of exogenous carbonates here at the 878 cm^{-1} site, obscuring the meaning of the measurement.

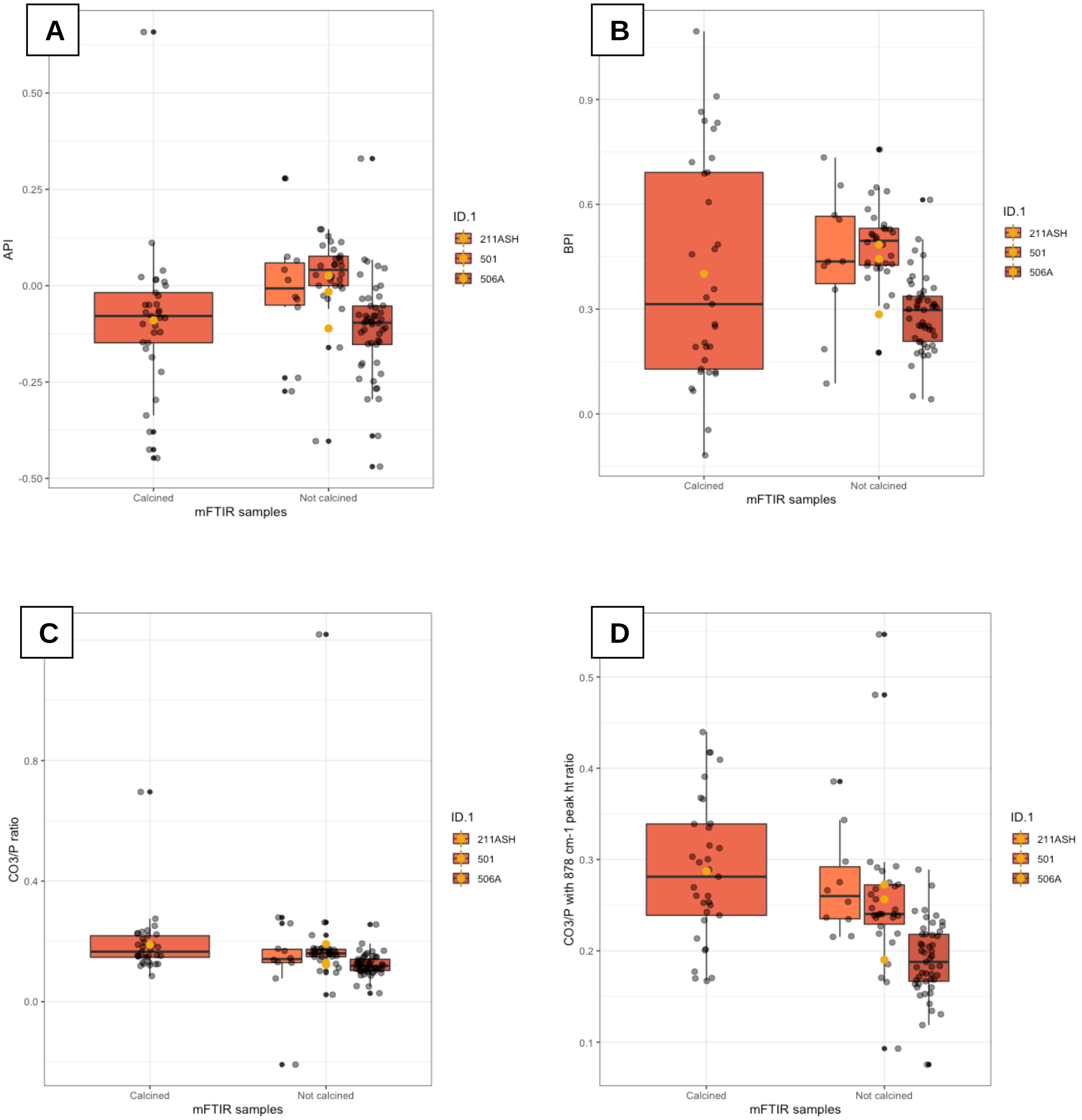

Fig 52. mFTIR results for micromorphological thin sections RDM-211ash, RDM-501, and RDM-506a, organized by calcined or not calcined representing temperatures reached above and below < 700 °C. A) API ratio, demonstrating very similar values across samples both calcined and not calcined. B) BPI ratio, with large variation in calculated indices within calcined samples, despite the average grouping with not calcined fragments. C) Highly constrained CO3/P values across samples calculated with 900 cm^{-1} value following Thompson et al. (2013). D) CO3/P ratio calculated with the 878 cm^{-1} peak. Sample 506a is seen to have the lowest values within the not calcined fragments, and with calcined fragments demonstrating higher ratios which represent the degree of carbonate presence, the opposite of expected values given carbonates are eliminated with increasing temperatures. All indices here are also influenced and biased by exogenous carbonate content.

CN/P, OH/P, and Cal/PO4

Within the micromorphological samples, little amounts of cyanide were present, indicating that burning conditions which potentially could have incorporate ammonia or have full reduction conditions were not present following Snoeck et al. (2014)'s recommended threshold of 0.25 (Fig. 53 A and B). Two phosphate peaks were utilized to construct the ratio, PO_4^{3-} v4 (605 cm^{-1}) and v3 (1035 cm^{-1}), and no differences were seen between the ratios (Fig. 53 A and B). The OH/P ratio, measuring the peak shoulder which emerges from the PO_4^{3-} v4 peak is present and elevated within the calcined samples, showing clear separation from the non calcined bone (Fig. 53 C). This index confirms true burning above 700 °C and is not obstructed by diagenetic carbonate. Measures of calcite within samples do indicate that calcite is present within most of the micromorphological bone tested at higher concentrations compared to the coarse screened faunal bone (Fig. 53 D).

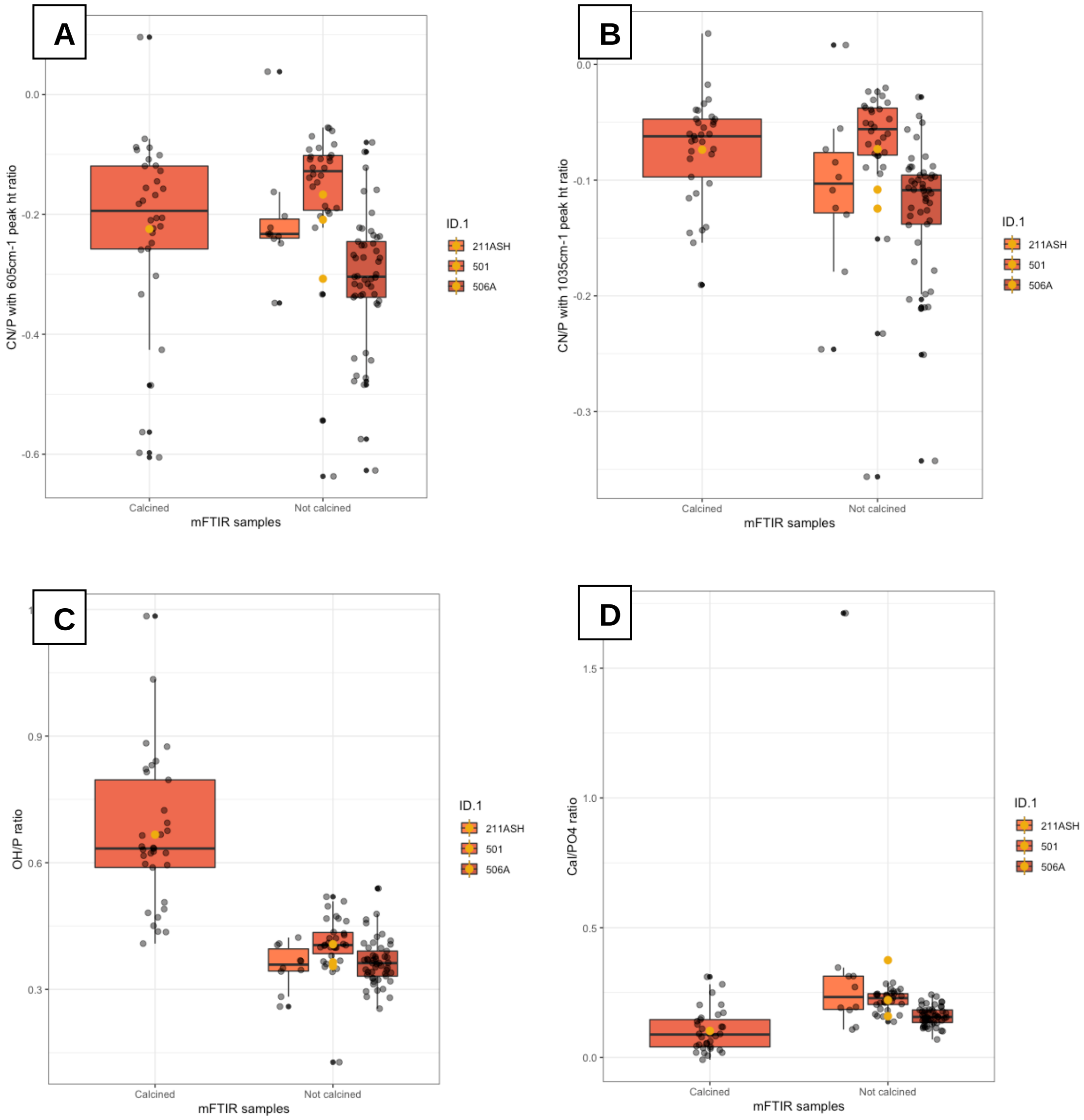

Fig 53: mFTIR results for micromorphological thin sections RDM-211ash, RDM-501, and RDM-506a, organized by calcined or not calcined representing temperatures reached above or below < 700 °C. A) Cynamide presence calculated with the CN/P ratio with 605 cm^{-1} phosphate peak values exhibits a large range of variation, but values do not exceed 0.25 indicating a non-measurable amount of cynamide present following Snoeck et al., (2014). B) CN/P ratios calculated with the 1035 cm-1 peak values demonstrate a pattern similar to that of the 605 cm^{-1} calculation (A), and values are also below 0.25. C) OH/P ratio presents a measurement not impacted by diagenetic presence of carbonates and clearly distinguishes the calcined samples from samples not heated to temperatures above 700° C. D) The Cal/PO4 index does indicate that calcite was measured within nearly all micromorphological samples with values higher than the values produced by FTIR testing of the archaeological bone from the coarse screened fraction. Of all samples, calcined specimens exhibit the lowest degree of precipitating calcite.

PHT

As represented by the OH/P ratio, the libration vibration of hydroxyl groups in bone which has undergone chemical and structural calcination through high temperature alteration is measurable within the micromorphological samples (Fig. 54). PHT values align well with partially to fully calcined bones found within the coarse screened fractions, and likely demonstrate a wide range of values due to encompassing these different stages of burning themselves, as Stiner et al. (1995) stages cannot be distinguished for bone imbedded in thin sections (Fig. 54). Despite the significant presence of exogenous carbonates and to a lesser extent precipitating calcite, the measure of the shoulder appearing at 625-630 cm^{-1} still indicates thermal alteration above temperatures of 700 °C.

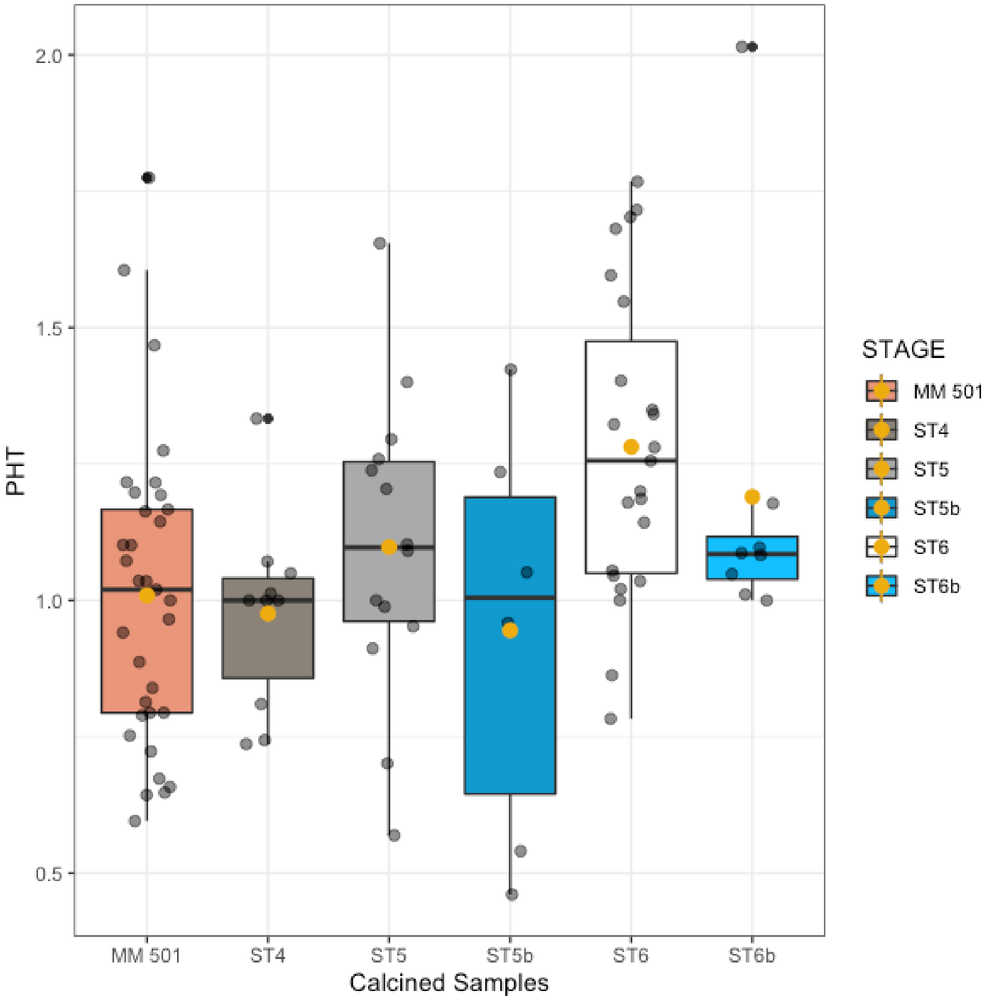

Fig 54: Calculated PHT ratios for calcined bone within the micromorphological slide 501 compared to calcined samples ranging from Stiner et al. (1995) stage 4-6 as well as stages 5b and 6b from the screened coarse remains. Ratios from the micromorphogical thin section 501 fall well within ranges seen in calcined coarse fraction bone demonstrating true presence of calcination detected in the bone within the thin section. The wide range of values seen for sample 501 are representative of all stages (4-6) likely captured here, unable to be distinguished based on color classification.

In sum, mapping the burning signatures of fauna across micromorphological thin sections is a promising methodology for characterizing the degree of burning within the depositional environment where the sample was taken. Even measures broadly defined as calcined samples, experiencing temperatures above 700 °C, and not calcined samples can contribute to contextualizing temperatures reached within identified and often discrete fire lenses

– some of which are too small to be recognized in the field- and monitor the content of different combustion features, for example the low degree of both bone and the presence of burning within ash localities present in sample RDM-211ash.

As small fragments are more susceptible to diagenetic alteration as a function of increased surface area and low mass, micromorphological bone potentially carries larger signals of diagenetic alteration within an assemblage compared to larger fragments recovered from coarse screened remains or piece plotted bones. This diagenetic signature may leave established ratios ineffective, but does yield valuable information regarding the burial environment. RDM layer 9 has been described previously as characterized by localized diagenetic alteration, specifically noting the dissolution or transformation of calcite into dahllite (Goldberg et al., 2012). These signatures are detected within the infrared spectroscopy of bone fragments identified for this study, and future work may build towards potentially deconvoluting peaks of interest to better access information related to low temperature burning within altered samples. Other solutions for exogenous carbonate, such as acetic acid pretreatments, are not possible here as bones are fully impregnated within the resin (Snoeck et al., 2014).

Spatial Analyses

Stage 0 bone

KDE results visualizing the density and distribution of unburnt bone within RDM layer 9 depict heavy concentrations of unburnt, stage 0 fauna both inside and outside the ancient dripline (Fig. 55). Stage 0 unburnt bone accounts for the majority of the faunal assemblage and is well represented in both screened and piece plotted remains (Fig. 4). Superimposed on the KDE heatmap are circles representative of each point of recorded faunal data, piece plotted and screened, with the sizes of the circle relational to the amount of bone recovered (increasing in diameter 0.25pt steps for every 10g of bone).

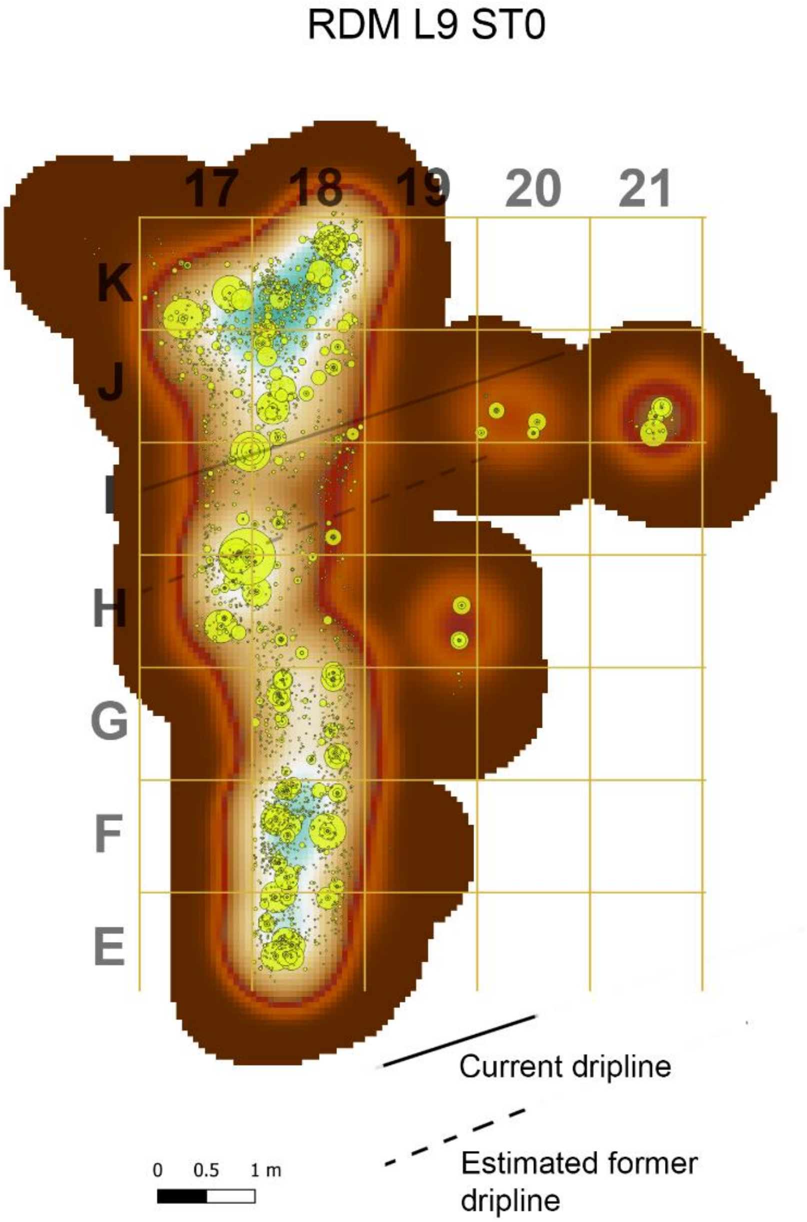

Fig 55: KDE of Stiner et al., (1995) stage 0 unburnt fauna within layer 9 or RDM. Circles represent individual datapoints, with circle diameters proportional to the weight (g) of recorded fauna.

Stage 1-3

Visual heatmaps constructed for burnt bone are depicted at 1/4x the scale of the density of unburnt bone, due to the differences in sheer quantity between burning categories. For partially to completely carbonized and charred bone, Stiner et al., (1995) stages 1-3, KD estimations depict very low densities of stage 1 bone which increases as bones become more fully carbonized and charred with stage 3 representing the greatest mass (Fig. 56). Points indicate here relative mass of fauna (g), with diameters increasing 0.25pt for every 10g of measured fauna. For stage 3 bone, three concentrations are distinguished: inside the cave interior, at the estimated ancient dripline, and directly in front of the cave opening (Fig. 56). This signature is distinguished primarily from the KDE of unburnt bone, as greater accumulations of stage 0 bone located within the cave are in square K18, whereas stage 3 bone clusters are shifted towards J18. In the cave exterior, stage 0 bones are also estimated to be further from the dripline (F18) while stage 3 exterior concentrations are seen in H and G18 (Fig. 56).

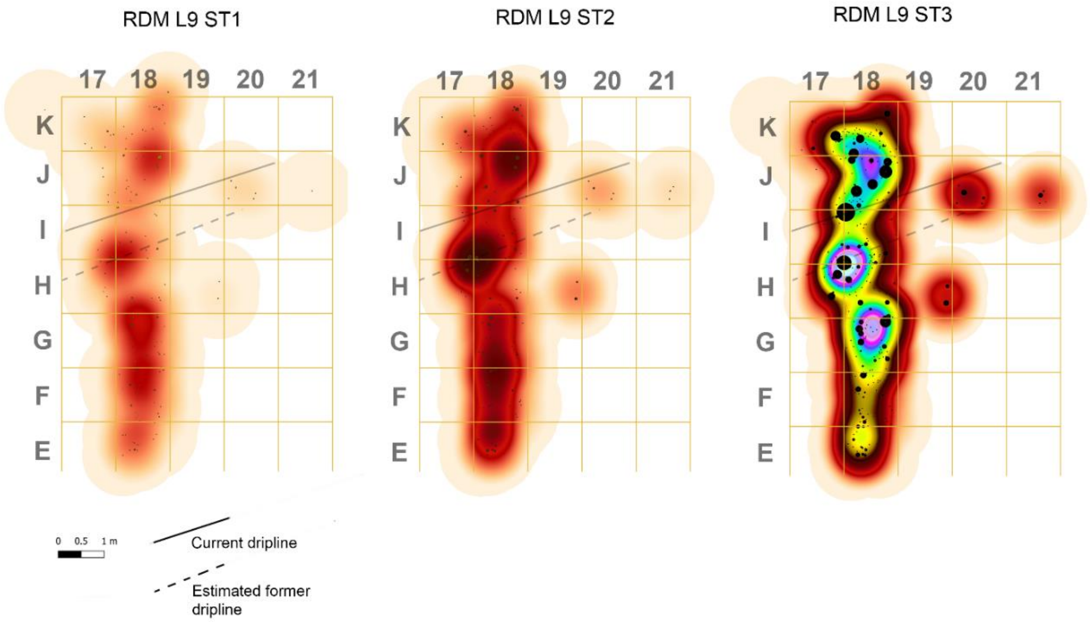

Fig 56: KDE heatmaps with superimposed data points, size scaled to bone weight (g), for Stiner et al. (1995) stages of burning 1-3 representing partially to fully carbonized and charred samples.

Stages 4-6

Stiner et al. (1995) stages 4 and 5 of RDM layer 9 fauna are distributed in two groups in the KDE analysis, inside and outside of the ancient dripline (Fig. 57). This signature is altered in KDE of fully calcined stage 6 bone, which observes two clusters within the cave interior (despite the second concentration in squares I and H 17 and 18 now past the modern dripline), and a less intense third group located in the cave exterior (Fig. 57). These identified accumulations of calcined bone additionally are in shifted positions compared to KDE visualizations of stage 3 bone (observed in squares G-E; Figs 56, 57). These results demonstrate that the greatest accumulation of stage 6 bone, potentially indicating that bone was burned at high temperatures to induce calcination, is concentrated within combustion features just within the cave (Fig. 57). As calcined bone is thermodynamically stable when compared to unburnt bone and, further, charred and carbonized bone, this signature is likely not the result of differential preservation and elimination of stage 6 calcined fragments from depositional processes impacting the cave exterior (Chapter 2; Gallo et al., 2021). The inference of high temperature fire events within the cave interior seen in the KDE are additionally supported by the J18 stage 6 calcined sample which indicated temperatures > 800 °C from observations of the C/C and SF ratio (Fig. 47).

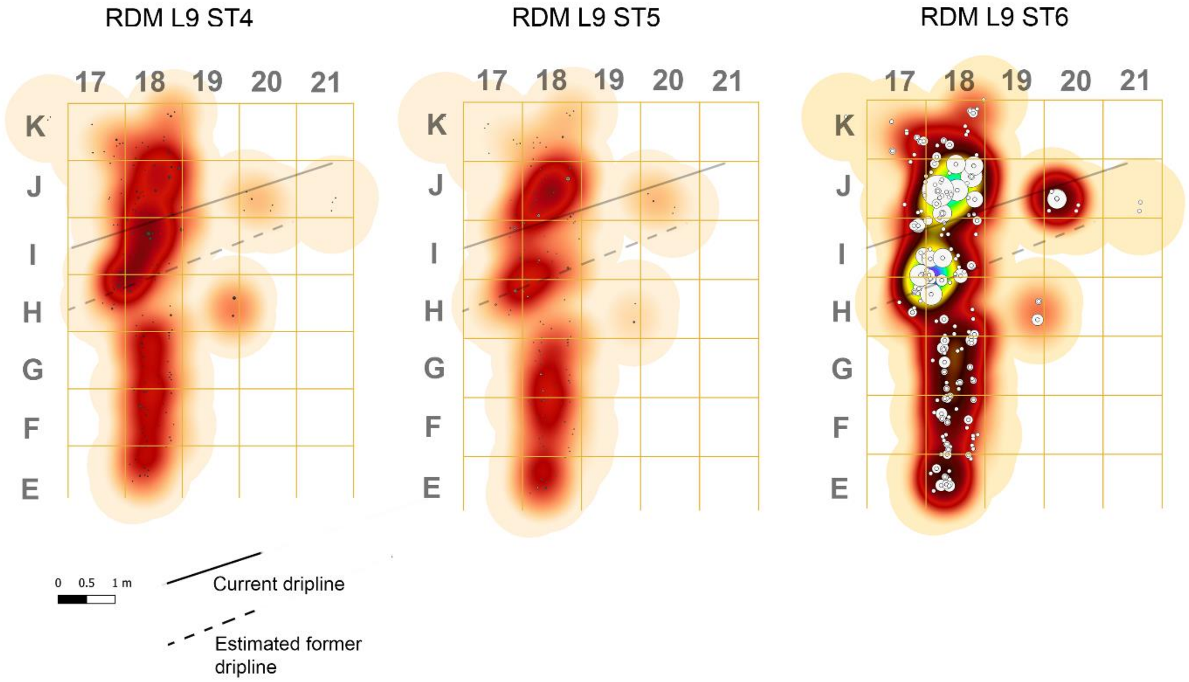

Fig 57: KDE visualizations for Stiner et al. (1995) stages 4, 5 , and 6 within the RDM layer 9 assemblage. Increasing heatmap intensity is representative of bone weight (g), and superimposed circles represent data points, with diameter of points associated with degree of burnt bone mass (g).

Stages 5b and 6b

Heatmaps produced using KD estimations for stages 5b and 6b within RDM layer 9 initially show no pattern of deposition for bones partially calcined with presence of blue coloration (Fig. 57). Fully calcined samples with blue coloration, however, exhibit an extreme concentration in square J18, also an accumulation center of stage 6 burnt material and a location of stacked hearths within layer 9 (Goldberg et al., 2012; Figs. 57; 58). This relationship provides supplementary information on the nature of temperatures reached in J18 fire events (> 800 °C), as well as scenarios in which stage 6b bones received their distinctive coloration. One scenario responsible for this signature may be that a concentration of older, defleshed bones remaining on the substrate where faunal remains were burned purposefully for fuel or as a part of cleaning maintenance behaviors, potentially impacted by the construction of features on top of previously extinguished events. Ultimately, this exploration of distribution of stage 6b bone supports similar inferences from the stage 6 calcined bone, and indicates that a larger amount of bone was burnt to high temperatures within the RDM cave entrance and ancient dripline.

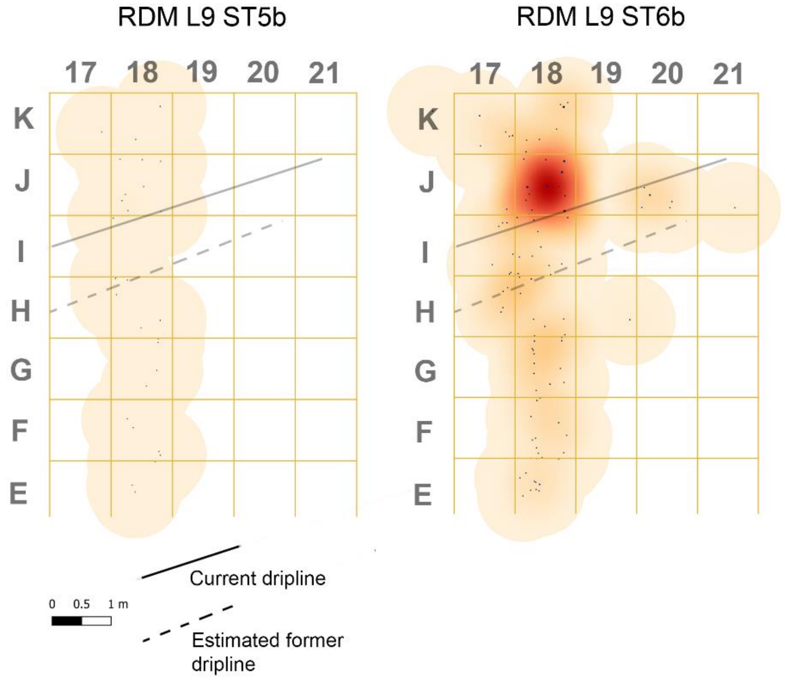

Fig 58: KDE heatmapsfor bone exhibiting blue presence by weight (g). Small amounts of stage 5b bone are distributed evenly with no discernable pattern of concentration. Stage 6b bone estimations, however, clearly indicate a very tight accumulation within one meter square (J18), with a low dispersed presence of stage 6 blue bone within the rest of layer 9.

Distribution of activities

The locations of bones potentially burnt for long durations at low temperatures align closely with the location of combustion feature (CF) 1, but also CF 10 (H and I 18; Fig 60). CF 10 is noted to be well organized, small (55 cm length) and composed of a minimum of two features, consisting of both heavily burnt lenses but also exposed ash layers (Aldeias et al., 2012; Goldberg et al., 2012). It is unclear which burning event may have been sustained at low temperatures for long periods, but potentially more sampling within this unit can provide supplementary information to detect these conditions in further detail.

Other distributions relevant to Neanderthal fire use within layer 9 include the location of burnt cervid sesamoids within the assemblage, as sesamoids are dense tiny bones embedded in tendons and likely not burned separate from the lower limb segments. Clusters of burnt sesamoids then potentially are indicative of burning entire low utility distal limb portions (Fig. 60). Sesamoids are found to be associated and overlapping with several CF locations (CF 1, 5, 9/11, 14, 18, 19). Calcined fragments of wild boar (*Sus scrofa*) lumbar vertebrae are also found aligned spatially with CF 1 (Fig. 62). Mapping the locations of burnt bone with evidence of anthropogenic modification relevant to butchery activities such as scraping and cutting, and percussive activities such as retouching is seen well dispersed across layer 9 of RDM (Fig. 63). Locations of these bones, burned after defleshing, are associated spatially with CF 13, 9/11, and 1 (Fig. 63). In sum, these bones provide positive evidence that segments of bones may have been placed still articulating together in fire features (i.e. sesamoid clusters), included both axial and long bone fragments, and bone was burnt after butchery and tool modification activities (Figs. 61- 63; Table 8). This is supported by indices following Costamagno et al. (2009) which designate a fuel and maintenance strategy to the layer 9 burnt faunal assemblage (Fig. 26; Table 11).

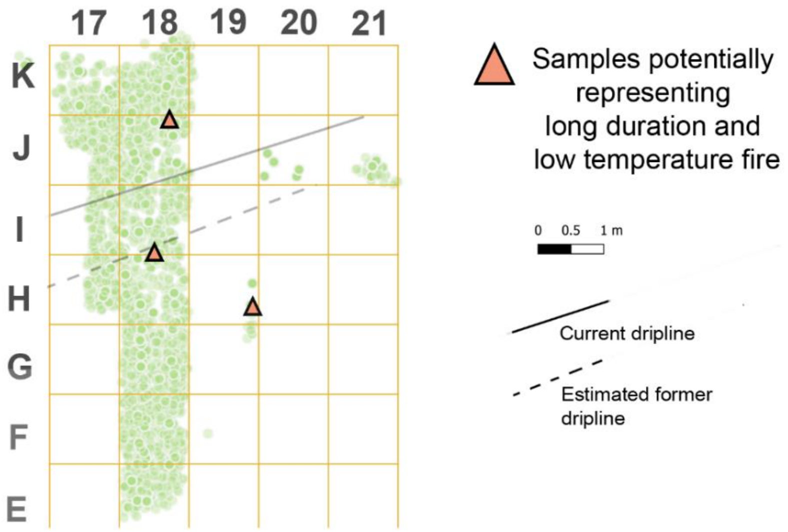

Fig 60: Distribution of faunal remains detected as potentially indicative of long duration at low temperature fire events. Green circles represent the complete faunal assemblage of RDM layer 9.

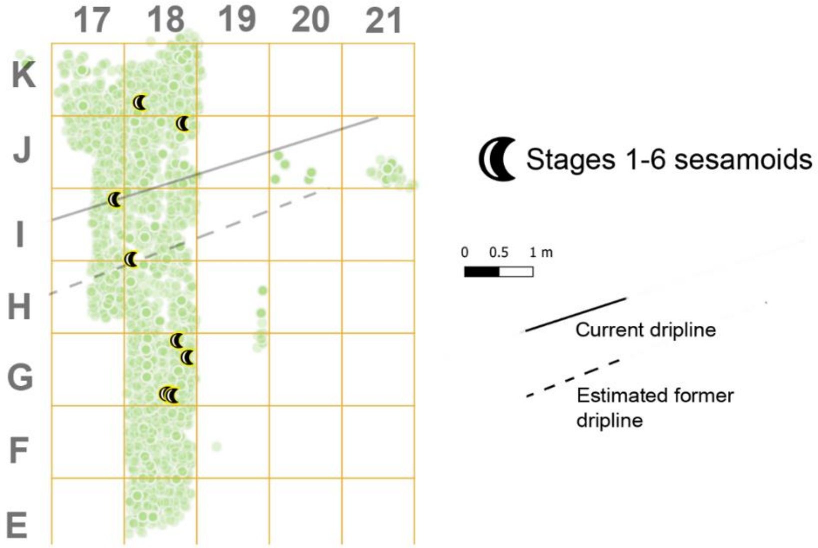

Fig 61: Distribution of burnt identified sesamoids within the layer 9 assemblage. Green circles represent the complete faunal assemblage of RDM layer 9.

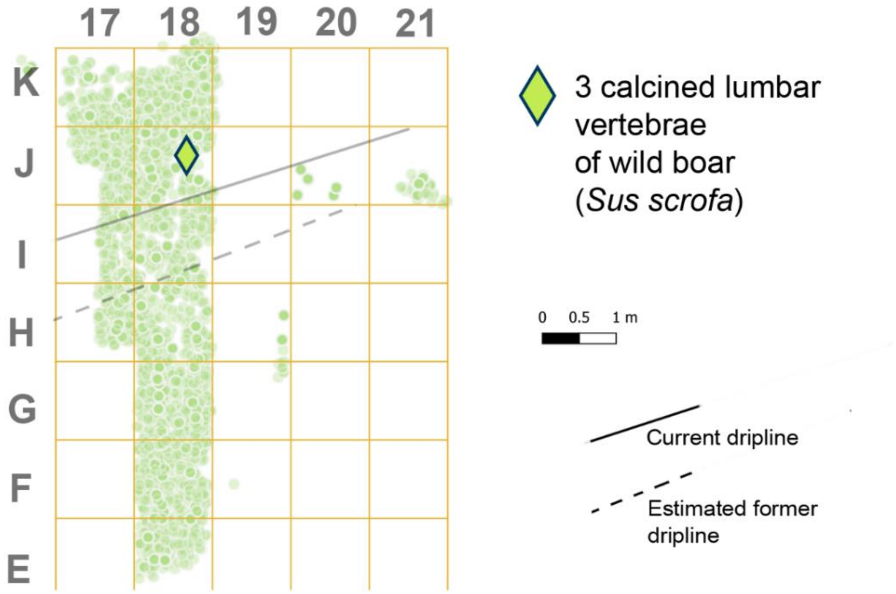

Fig 62: Location of the three lumbar vertebrae elements of wild boar (*Sus scrofa*), aligned with CF 1 of RDM layer 9. Green circles represent the complete faunal assemblage of RDM layer 9.

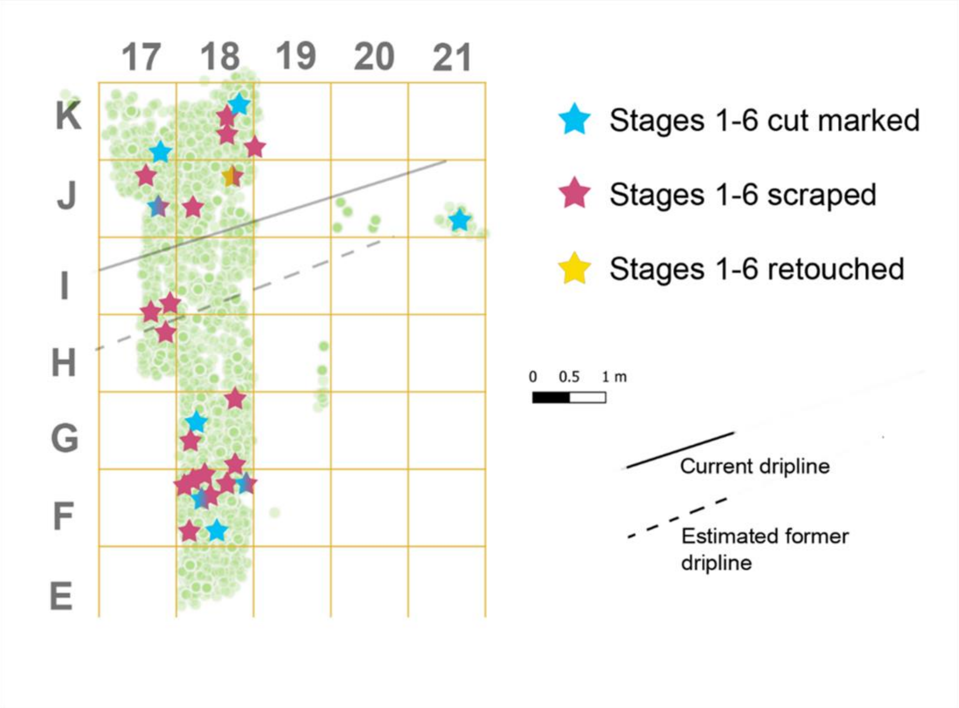

Fig 63: Locations of burnt bones with evidence of anthropogenic modification within layer 9 of RDM. Stars with two colors indicate fragments with more than one type of anthropogenic modification. Green circles represent the complete faunal assemblage of RDM layer 9.

Discussion

RDM layer 9

Layer 9 of RDM is described as having several superimposed combustion features, and fire events viewed on the micromorphological scale further have identified several fire lenses related to distinct fire events (Aldeias et al., 2012; Goldberg et al., 2012; Sandgathe et al., 2011). Piece plotted and coarse screened faunal data collected for this study therefore primarily represents time averaged episodes of behavior (Reeves et al., 2019). This scale of analysis allows insights into large scale patterns of hominin activities, here explored in terms of fire properties and contents.

KDE visualizations for burning density of faunal assemblage by weight (g) classified into Stiner et al., (1995) burning stages show different detected patterns in burnt faunal density by temperature threshold (Figs. 55-57). Compared to burnt lithic spatial analyses for layer 9 presented in Aldeias et al., (2012) burnt fauna does not overlap with clusters seen for densities of burnt lithics. Comparison with the spatial distribution of burned flakes in relation to all flakes at RDM layer 9 presented in Reeves et al., (2019), overlap is noted in high density areas of burning specifically in the clusters of burnt material around the dripline (Figs. 55-57).

Referencing published data regarding the size and placement of layer 9 combustion features, the KDE analyses of burnt bone produced for this study show high alignment between different combustion feature locations, with different patterns noted between the combustion areas dominated with either carbonized/charred or calcined clusters (Fig. 58; Goldberg et al., 2012). Lower temperature fauna clusters, discerned as spatial accumulations which are dominated by fauna burnt to temperatures likely 300-500 °C classified as Stiner et al. (1995) stages 1-3, match locations of combustion features (CF) 1, 5, 14, 18, and 19. Excluding CF 1 and

18, these combustion features are all located outside of the cave dripline (Fig 88; Goldberg et al., 2012). Small amounts of stages 4-6 bone are still found in these detected areas related to the identified combustion features but are not found in great quantities and likely represent minority portions of fire events that reach temperatures of calcination, or palimpsests of fire events with the majority having low temperatures and some exhibiting higher temperatures. Finally, two combustion features noted in field observations at RDM layer 9, CF 13 and 14, were not observed in the visualizations of burnt fauna (Goldberg et al., 2012). This signature may be due to bone not being a major component of these features, rendering them invisible from a faunal perspective.

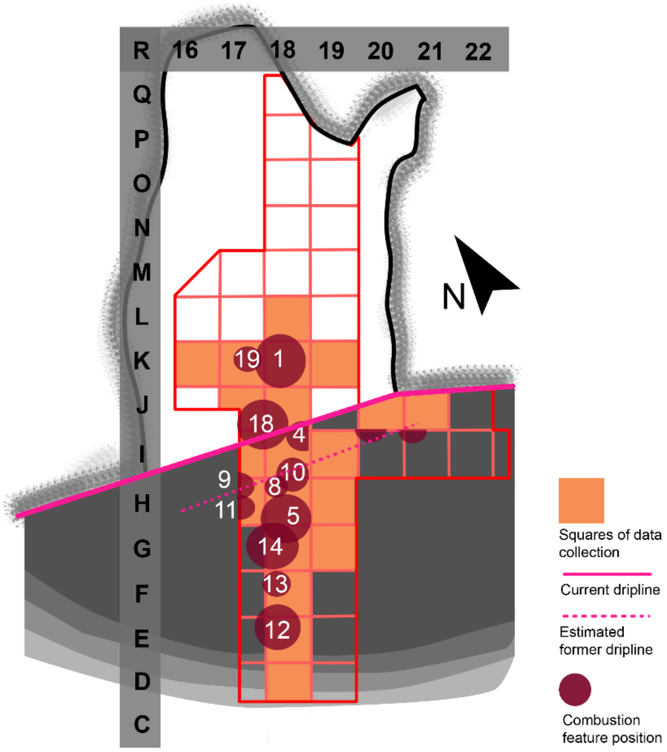

Fig 58: Position of measured and observed combustion feature location within RDM layer 9, map modified from Goldberg et al., 2012.

Calcined bone dominated accumulations, inferred by the degree and density of calcined fragments concentrations indicating a large presence of bone burnt to temperatures at or above 700 °C, demonstrates a different spatial signature than stage 3 carbonized bone heated to 300-500 °C. KD estimation concentrations are only seen here to overlap neatly with the location of CF 18, as well as slightly shifted from the published location of CF 1 (Goldberg et al., 2012). Indeed it is possible that high stage 6 bone densities recorded within J18 belongs to both extents of CF 18 and CF 1 but are altered in placement, as CF 1 is described as being massive, not structured, and likely including several superimposed fire events (Goldberg et al., 2012). CF 1 is also noted as being rich in burnt bone as monitored by micromorphological samples (Goldberg et al., 2012). These accumulations are dominated by bone burnt to temperatures at or above 700 °C, in fact likely reaching 900 °C based on spectroscopic data (Fig. 46).

Faunal remains are utilized here to document both high (> 700 °C) and low (< 700 °C) temperature fires within RDM layer 9, with bone likely incorporated into combustion features consistently as discard strategies subsequent to butchery activities, not as a primary fuel source. High intensity fire is seen to be located within the cave interior, while lower intensity fires occupy the cave exterior. Concentrations of burnt bone are also not always aligned with the identification of combustion features in the field, indicating that bone was not always incorporated into fire events.

Within the micromorphological samples utilized for this study, clear diagenetic alteration is seen, specifically for the uptake and incorporation of exogenous carbonates which biases results from several published indices considering different aspects of thermal alteration of bone. Bone can still be confidently distinguished as calcined (> 700 °C) and not calcined (< 700 °C) however, providing crucial information for contextualizing the behavior of bone within features.

Research building on this dataset can now investigate further the specific faunal content differences between features. Future work can use these finer scales of analyses to provide more detailed information regarding the different decisions made by Neanderthals, such as spatial analyses that incorporate the depth of excavated materials to better utilize screened materials within models, as well as greater incorporation of micromorphological documentation and the behavior of bone within in-situ samples. This study recommends extensive sampling of calcined, or visually identified as calcined, fragments within assemblages to monitor maximum temperatures as well as signals of long durations. Sampling strategies also must test bone identified as Stiner et al., (1995) stage 3 to screen for reduction combustion conditions, and further research is necessary to clarify the types of burning environments which constitute reduction conditions in actualistic settings.

Further analyses will investigate the chemical structure of the recovered blue bones through the use electron paramagnetic resonance (EPR) spectroscopy to confirm presence and location of the manganese substitutions for the blue bone located in layer 9 of RDM. Experimental research may also investigate the timing and degree of carbonate and manganese incorporation under different burial conditions to estimate the necessary duration between defleshing and burning for blue tinged bone.

Neanderthal fire using behaviors at RDM

Within the burnt faunal assemblage of RDM layer 9, differences in combustion feature properties are seen in relation to the low and high temperature threshold fires, defined here as the proportion of highest temperature reached as inferred from contents primarily of either carbonized or calcined fragments by weight (g). Excavation observations and geoarchaeological studies identified some combustion features that were not apparent in this study because bone was not a major component (CF 13 and 14). Differences between these features present a few possibilities for behavioral interpretations: First, stochastic variation in fire types and properties which are not purposeful and may be influenced by mistakes and/or limitations; Second, the varied properties and contents may indicate averaged behavioral choices made by Neanderthals and can be related to the different desired properties and functions of these fire events and overall site function (Hoare, 2020; Mallol et al., 2007; McCauley et al., 2020). Future research will develop hypotheses to test these scenarios further.

The categories of low and high temperature fires are distinguished in RDM layer 9 as there is little overlap in signals outside of the cave entrance and for clusters within the cave's dripline location during the period in which layer 9 accumulated. The degree and density of calcined fragments remains higher than carbonized/charred material within the cave, although carbonized bone is still present within the high temperature features. Indeed, potentially it is the size of these features within the cave (specifically CF 1) which allowed enough material to reach such high temperatures, an explanatory mechanism for the relationship between the size and temperatures reached. Bones within these large fires additionally could not have achieved white coloration through a series of re-heating events at temperatures under 700 °C, as spectroscopic testing on samples from these squares do verify high temperature alteration with structural and chemical calcination. Finally, these temperature thresholds remain relevant despite the time-averaged palimpsest nature of the deposits, as these temperatures were reached whether the fauna are from a single fire event or averaged over several events.

Temperatures recorded and fuels utilized have relevance for the properties of light and heat of these fire features, with heat transmitted through both convection and radiation, and light emitted solely through radiation (Hoare et al., 2020). Length of fire duration is additionally of interest as larger (and potentially hotter) fires would be easier to maintain as long as there was enough available fuel, and certain activities may require minimum amounts of combustion time (such as smoking fires to dry meat or to keep insects away; Henry et al., 2018). Low temperature fires additionally may be better suitable for domestic activities such as cooking, as temperatures > 700 °C are beyond those needed for cooking.

In addition to temperatures thresholds reached, fire contents additionally can provide information on choices within fire using behaviors. Fires primarily fueled by bone in particular are noted to not have embers, and therefore radiative heat is linked to the combustion time of the bones themselves (Hoare et al., 2020). Future research will use the data generated from this study alongside other complementary datasets, including micromorphological thin sections of the preserved in-situ events, to learn more about the contents of identified features and relationship to bone accumulations. The strength of multiscale approaches is the combination of several independent lines of evidence to narrow the best likelihood of possibilities.

Conclusion

Through the mapping of densities and distributions of burnt bone at different temperature thresholds, verified by spectroscopic methods, piece plotted and screened faunal remains here are proposed as an appropriate tool for establishing differences between burning concentrations and relating accumulations of burnt fauna to behaviors of fire use and maintenance, complementary to lithic analysis and geological approaches. Specific properties which zooarchaeological approaches can address include duration length (Chapter 3), reduction or oxidizing conditions, maximum temperatures reached, and the behaviors which lead hominins to burn bone (use as fuel, burned after butchery and consumption, etc.).

Methodology proposed here to investigate anthropogenic burning through zooarchaeological lens includes the consideration of fauna within three scales of analysis: ≥ 2.5 cm bone (primarily piece plotted) to make species and element identifications; < 2.5cm- 6mm bone (primarily coarse screened material) as burning is overwhelmingly located within the screens due to the mechanical fragility of burnt bone; and micromorphological slides which present the preserved context to describe the general behavior of bone (burnt and unburnt) in relation to the original depositional environment. This study also recommends both traditional zooarchaeological methods of data collection, including count and weight parameters, color coding, and screening for anthropogenic modifications, but also including extensive spectroscopic sampling within assemblages both to verify burning and to include information from the chemical structure of bone which is not macroscopically observable.

Faunal assemblages are crucial to the study of fire using behaviors, as bone as a fire proxy provides significant amounts of valuable information on a finer scale than many lithic or geological analyses, data which are necessary to address goals of reconstructing pyrotechnology and related behaviors. Zooarchaeology has an important and complementary role in advancing standards in reporting fire evidence and has the potential to shed much light on diverse types of fire technology across geographical and temporal periods for any fire using hominin. Standardized study of burnt faunal assemblages on all three scales of analyses presented here would provide unprecedented opportunities to create the comparative perspective needed in advancing knowledge regarding ancient fire using behaviors both within Neanderthal populations and between Neanderthals and contemporaneous African AMH and later UP European AMH.

References

Abdolahzadeh, A., McPherron, S. P., Sandgathe, D. M., Schurr, T. G., Olszewski, D. I., & Dibble, H. L. (2022). Investigating variability in the frequency of fire use in the archaeological record of Late Pleistocene Europe. *Archaeological and Anthropological Sciences*, *14*(4), 1-26.

Aldeias, V., Goldberg, P., Sandgathe, D., Berna, F., Dibble, H. L., McPherron, S. P., ... & Rezek, Z. (2012). Evidence for Neandertal use of fire at Roc de Marsal (France). *Journal of Archaeological Science*, *39*(7), 2414-2423.

Allué, E., Mallol, C., Aldeias, V., Burguet-Coca, A., Cabanes, D., Carrancho, Á., ... & Vaquero, M. (2022). Fire among Neanderthals. In *Updating Neanderthals* (pp. 227-249). Academic Press.

Alperson-Afil, N., Sharon, G., Kislev, M., Melamed, Y., Zohar, I., Ashkenazi, S., ... & Goren-Inbar, N. (2009). Spatial organization of hominin activities at Gesher Benot Ya'aqov, Israel. *science*, *326*(5960), 1677-1680.

Arroyo, A. M., Ruiz, M. L., Bernabeu, G. V., Román, R. S., Morales, M. G., & Straus, L. G. (2008). Archaeological implications of human-derived manganese coatings: a study of blackened bones in El Mirón Cave, Cantabrian Spain. *Journal of Archaeological Science*, *35*(3), 801-813.

Barkai, R., Rosell, J., Blasco, R., & Gopher, A. (2017). Fire for a reason: Barbecue at middle Pleistocene Qesem cave, Israel. *Current Anthropology*, *58*(S16), S314-S328.

Beasley, M. M., Bartelink, E. J., Taylor, L., & Miller, R. M. (2014). Comparison of transmission FTIR, ATR, and DRIFT spectra: implications for assessment of bone bioapatite diagenesis. Journal of Archaeological Science, 46,16-22.

Binford, L. R. (1978). *Nunamiut ethnoarchaeology*. New York: Academic Press.

Backwell, L. R., d'Errico, F., Banks, W. E., de la Peña, P., Sievers, C., Stratford, D., ... & Wadley, L. (2018). New excavations at border cave, KwaZulu-natal, South Africa. *Journal of Field Archaeology*, *43*(6), 417-436.

Boëda, E., Bonilauri, S., Connan, J., Jarvie, D., Mercier, N., Tobey, M., ... & Muhesen, S. (2008). Middle Palaeolithic bitumen use at Umm el Tlel around 70 000 BP. *Antiquity*, *82*(318), 853-861.

Brittingham, A., Hren, M. T., Hartman, G., Wilkinson, K. N., Mallol, C., Gasparyan, B., & Adler, D. S. (2019). Geochemical evidence for the control of fire by Middle Palaeolithic hominins. *Scientific Reports*, *9*(1), 1-7.

Brown, K. S., Marean, C. W., Herries, A. I., Jacobs, Z., Tribolo, C., Braun, D., ... & Bernatchez, J. (2009). Fire as an engineering tool of early modern humans. *Science*, *325*(5942), 859-862.

Bruno, T. J. (1999). Sampling accessories for infrared spectrometry. Applied Spectroscopy Reviews, 34(1-2), 91-120.

Buikstra, J. E., & Swegle, M. (1989). Bone modification due to burning: experimental evidence. *Bone modification*, 247-258.

Castel, J. C., Discamps, E., Soulier, M. C., Sandgathe, D., Dibble, H. L., McPherron, S. J., ... & Turq, A. (2017). Neandertal subsistence strategies during the Quina Mousterian at Roc de Marsal (France). *Quaternary International*, *433*, 140-156.

Chadefaux, C., Vignaud, C., Chalmin, E., Robles-Camacho, J., Arroyo-Cabrales, J., Johnson, E., & Reiche, I. (2009). Color origin and heat evidence of paleontological bones: Case study of blue and gray bones from San Josecito Cave, Mexico. *American Mineralogist*, *94*(1), 27-33.

Chazan, M. (2017). Toward a long prehistory of fire. *Current Anthropology*, *58*(S16), S351-S359.

Clark, A. E. (2016). Time and space in the middle paleolithic: Spatial structure and occupation dynamics of seven open-air sites. *Evolutionary Anthropology: Issues, News, and Reviews*, *25*(3), 153-163.

Clark, J. L., & Ligouis, B. (2010). Burned bone in the Howieson's Poort and post-Howieson's Poort Middle Stone Age deposits at Sibudu (South Africa): behavioral and taphonomic implications. *Journal of Archaeological Science*, *37*(10), 2650-2661.

Costamagno, S., Thery-Parisot, I., Brugal, J. P., & Guibert, R. (2005). Taphonomic consequences of the use of bones as fuel. Experimental data and archaeological applications. *Biosphere to lithosphere: new studies in vertebrate taphonomy*, 51-62.

Costamagno, S., Théry-Parisot, I., Castel, J. C., & Brugal, J. P. (2009). Combustible ou non? Analyse multifactorielle et modèles explicatifs sur des ossements brûlés paléolithiques. *GESTION DES COMBUSTIBLES AU PALÉOLITHIQUE ET AU MÉSOLITHIQUE NOUVEAUX OUTILS, NOUVELLES INTERPRÉTATIONS FUEL MANAGEMENT DURING THE PALAEOLITHIC AND MESOLITHIC PERIOD*, 61.

Dal Sasso, G., Lebon, M., Angelini, I., Maritan, L., Usai, D., & Artioli, G. (2016). Bone diagenesis variability among multiple burial phases at Al Khiday (Sudan) investigated by ATR-FTIR spectroscopy. *Palaeogeography, Palaeoclimatology, Palaeoecology*, *463*, 168-179.

Dal Sasso, G., Asscher, Y., Angelini, I., Nodari, L., & Artioli, G. (2018). A universal curve of apatite crystallinity for the assessment of bone integrity and preservation. *Scientific reports*, *8*(1), 1-13.

Dibble, H. L., Sandgathe, D., Goldberg, P., McPherron, S., & Aldeias, V. (2018). Were Western European Neandertals able to make fire?. *Journal of Paleolithic Archaeology*, *1*(1), 54-79.

Dowker, S. E. P., & Elliott, J. C. (1979). Infrared absorption bands from NCO− and NCN2− in heated carbonate-containing apatites prepared in the presence of NH4+ Ions. *Calcified Tissue International*, *29*(1), 177-178.

Drouet, C., Aufray, M., Rollin-Martinet, S., Vandecandelaère, N., Grossin, D., Rossignol, F., ... & Rey, C. (2018). Nanocrystalline apatites: The fundamental role of water. *American Mineralogist: Journal of Earth and Planetary Materials*, *103*(4), 550-564.

Ellingham, S. T., Thompson, T. J., Islam, M., & Taylor, G. (2015). Estimating temperature exposure of burnt bone—A methodologica

Gallello, G., Kuligowski, J., Pastor, A., Diez, A., & Bernabeu, J. (2013). Biological mineral content in Iberian skeletal cremains for control of diagenetic factors employing multivariate statistics. *Journal of archaeological science*, *40*(5), 2477-2484.

Gallo, G., Fyhrie, M., Paine, C., Ushakov, S. V., Izuho, M., Gunchinsuren, B., ... & Navrotsky, A. (2021). Characterization of structural changes in modern and archaeological burnt bone: Implications for differential preservation bias. *PloS one*, *16*(7), e0254529.

Gifford-Gonzalez, D. (1989). Ethnographic analogues for interpreting modified bones: some cases from East Africa. *Bone modification*, 179-246.

Goldberg, P., & Berna, F. (2010). Micromorphology and context. *Quaternary International*, *214*(1-2), 56-62.

Goldberg, P., Dibble, H., Berna, F., Sandgathe, D., McPherron, S. J., & Turq, A. (2012). New evidence on Neandertal use of fire: examples from Roc de Marsal and Pech de l'Azé IV. *Quaternary International*, *247*, 325-340.

Goldberg, P., Miller, C. E., & Mentzer, S. M. (2017). Recognizing fire in the Paleolithic archaeological record. *Current Anthropology*, *58*(S16), S175-S190

Grunenwald, A., Keyser, C., Sautereau, A. M., Crubézy, E., Ludes, B., & Drouet, C. (2014). Revisiting carbonate quantification in apatite (bio) minerals: a validated FTIR methodology. *Journal of Archaeological Science*, *49*, 134-141.

Guérin, G., Discamps, E., Lahaye, C., Mercier, N., Guibert, P., Turq, A., ... & Soulier, M. C. (2012). Multi-method (TL and OSL), multi-material (quartz and flint) dating of the Mousterian site of Roc de Marsal (Dordogne, France): correlating Neanderthal occupations with the climatic variability of MIS 5–3. *Journal of Archaeological Science*, *39*(10), 3071-3084.

Hedges, R. E. (2002). Bone diagenesis: an overview of processes. Archaeometry, 44(3), 319-328.

Henry, A. G. (2017). Neanderthal cooking and the costs of fire. *Current Anthropology*, *58*(S16), S329-S336.

Henry, A. G., Büdel, T., & Bazin, P. L. (2018). Towards an understanding of the costs of fire. *Quaternary International*, *493*, 96-105.

Hoare, S. (2020). Assessing the function of palaeolithic hearths: experiments on intensity of luminosity and radiative heat outputs from different fuel sources. *Journal of Paleolithic Archaeology*, *3*(4), 537-565.

Hodgkins, J., Marean, C. W., Turq, A., Sandgathe, D., McPherron, S. J., & Dibble, H. (2016). Climate-mediated shifts in Neandertal subsistence behaviors at Pech de l'Azé IV and Roc de Marsal (Dordogne Valley, France). *Journal of human evolution*, *96*, 1-18.

Holcomb, D. W., & Young, R. A. (1980). Thermal decomposition of human tooth enamel. *Calcified Tissue International*, *31*(1), 189-201.

Hollund, H. I., Ariese, F., Fernandes, R., Jans, M. M. E., & Kars, H. (2013). Testing an alternative high-throughput tool for investigating bone diagenesis: FTIR in attenuated total reflection (ATR) mode. Archaeometry, 55(3), 507- 532.

Jaubert, J., Verheyden, S., Genty, D., Soulier, M., Cheng, H., Blamart, D., ... & Santos, F. (2016). Early Neanderthal constructions deep in Bruniquel Cave in southwestern France. *Nature*, *534*(7605), 111-114.

Koller, J., Baumer, U., & Mania, D. (2001). High-tech in the Middle Palaeolithic: Neandertal-manufactured pitch identified. *European Journal of Archaeology*, *4*(3), 385-397.

Lam, Y. M., Chen, X., & Pearson, O. M. (1999). Intertaxonomic variability in patterns of bone density and the differential representation of bovid, cervid, and equid elements in the archaeological record. *American Antiquity*, *64*(2), 343-362.

LeGeros, R. Z. (1983). Carbonate analyses of synthetic, mineral and biological apatites. *J. Dent. Res.*, *62*, 259.

Leierer, L., Jambrina-Enríquez, M., Herrera-Herrera, A. V., Connolly, R., Hernández, C. M., Galván, B., & Mallol, C. (2019). Insights into the timing, intensity and natural setting of Neanderthal occupation from the geoarchaeological study of combustion structures: A micromorphological and biomarker investigation of El Salt, unit Xb, Alcoy, Spain. *PLoS One*, *14*(4), e0214955.

Leierer, L., Alonso, Á. C., Pérez, L., Lagunilla, Á. H., Herrera-Herrera, A. V., Connolly, R., ... & Mallol, C. (2020). It's getting hot in here–Microcontextual study of a potential pit hearth at the Middle Paleolithic site of El Salt, Spain. *Journal of Archaeological Science*, *123*, 105237.

MacDonald, K., Scherjon, F., van Veen, E., Vaesen, K., & Roebroeks, W. (2021). Middle Pleistocene fire use: The first signal of widespread cultural diffusion in human evolution. *Proceedings of the National Academy of Sciences*, *118*(31), e2101108118.

Mallol, C., Marlowe, F. W., Wood, B. M., & Porter, C. C. (2007). Earth, wind, and fire: ethnoarchaeological signals of Hadza fires. Journal of Archaeological Science, 34(12), 2035-2052.

Mallol, C. & Henry, A. (2017). Ethnoarchaeology of Paleolithic fire: methodological considerations. CurrentAnthropology, 58(S16), S217-S229.

Mamede, A. P., Gonçalves, D., Marques, M. P. M., & Batista de Carvalho, L. A. (2018). Burned bones tell their own stories: A review of methodological approaches to assess heat-induced diagenesis. *Applied Spectroscopy Reviews*, *53*(8), 603-635.

Martin, R. B., Burr, D. B., Sharkey, N. A., & Fyhrie, D. P. (2015). Skeletal biology. In *Skeletal tissue mechanics* (pp. 35-93). Springer, New York, NY.

Mayer, I., Jacobsohn, O., Niazov, T., Werckmann, J., Iliescu, M., Richard-Plouet, M., ... & Reinen, D. (2003). Manganese in precipitated hydroxyapatites. *European Journal of Inorganic Chemistry*, *2003*(7), 1445-1451.

Mazza, P. P. A., Martini, F., Sala, B., Magi, M., Colombini, M. P., Giachi, G., ... & Ribechini, E. (2006). A new Palaeolithic discovery: tar-hafted stone tools in a European Mid-Pleistocene bone-bearing bed. *Journal of archaeological science*, *33*(9), 1310-1318.

McCauley, B., Collard, M., & Sandgathe, D. (2020). A cross-cultural survey of on-site fire use by recent hunter-gatherers: Implications for research on Palaeolithic pyrotechnology. *Journal of Paleolithic Archaeology*, *3*(4), 566-584.

Moreau, G., Auguste, P., Locht, J. L., & Patou-Mathis, M. (2021). Detecting human activity areas in Middle Palaeolithic open-air sites in Northern France from the distribution of faunal remains. *Journal of Archaeological Science: Reports*, *40*, 103196.

Murphree, W. C., & Aldeias, V. (2022). The evolution of pyrotechnology in the Upper Palaeolithic of Europe. *Archaeological and Anthropological Sciences*, *14*(10), 1-26.

Nakamoto, K. (2009). *Infrared and Raman spectra of inorganic and coordination compounds, part B: applications in coordination, organometallic, and bioinorganic chemistry*. John Wiley & Sons
Piga, G., Malgosa, A., Thompson, T. J. U., & Enzo, S. (2008). A new calibration of the XRD technique for the study of archaeological burned human remains. *Journal of Archaeological Science*, *35*(8), 2171-2178.

Piga, G., Amarante, A., Makhoul, C., Cunha, E., Malgosa, A., Enzo, S., & Gonçalves, D. (2018). β-Tricalcium phosphate interferes with the assessment of crystallinity in burned skeletal remains. *Journal of Spectroscopy*, *2018*.

Pollock, C. R., Pokines, J. T., & Bethard, J. D. (2018). Organic staining on bone from exposure to wood and other plant materials. *Forensic Science International*, *283*, 200-210.

Reeves, J. S., McPherron, S. P., Aldeias, V., Dibble, H. L., Goldberg, P., Sandgathe, D., & Turq, A. (2019). Measuring spatial structure in time-averaged deposits insights from Roc de Marsal, France. *Archaeological and Anthropological Sciences*, *11*(10), 5743-5762.

Reiche, I., Vignaud, C., & Menu, M. (2000). Heat induced transformation of fossil mastodon ivory into turquoise 'odontolite'. Structural and elemental characterisation. *Solid State Sciences*, *2*(6), 625-636.

Reiche, I., Vignaud, C., Champagnon, B., Panczer, G., Brouder, C., Morin, G., ... & Menu, M. (2001). From mastodon ivory to gemstone: The origin of turquoise color in odontolite. *American Mineralogist*, *86*(11-12), 1519-1524.

Reiche, I., Morin, G., Brouder, C., Solé, V. A., Petit, P. E., Vignaud, C., ... & Menu, M. (2002). Manganese accommodation in fossilised mastodon ivory and heat-induced colour transformation: Evidence by EXAFS. *European journal of mineralogy*, *14*(6), 1069-1073.

Reidsma, F. H., van Hoesel, A., van Os, B. J., Megens, L., & Braadbaart, F. (2016). Charred bone: Physical and chemical changes during laboratory simulated heating under reducing conditions and its relevance for the study of fire use in archaeology. *Journal of Archaeological Science: Reports*, *10*, 282-292.

Rey, C., Collins, B., Goehl, T., Dickson, I. R., & Glimcher, M. J. (1989). The carbonate environment in bone mineral: a resolution-enhanced Fourier transform infrared spectroscopy study. *Calcified tissue international*, *45*(3), 157-164.

Rey, C., Combes, C., Drouet, C., & Glimcher, M. J. (2009). Bone mineral: update on chemical composition and structure. *Osteoporosis international*, *20*(6), 1013-1021.

Robles, J., Arroyo-Cabrales, J., Johnson, E., Allen, B. L., & Izquierdo, G. (2002). Blue bone analyses as a contribution to the study of bone taphonomy in San Josecito Cave, Nuevo Leon, Mexico. *Journal of Cave and Karst Studies*, *64*(2), 145-149.

Roebroeks, W., & Villa, P. (2011). On the earliest evidence for habitual use of fire in Europe. *Proceedings of the National Academy of Sciences*, *108*(13), 5209-5214.

Sandgathe, D. M., Dibble, H. L., Goldberg, P., McPherron, S. P., Turq, A., Niven, L., & Hodgkins, J. (2011). On the role of fire in Neandertal adaptations in Western Europe: evidence from Pech de l'Azé IV and Roc de Marsal, France. *PaleoAnthropology*, *2011*, 216-242.

Schmidt, P. and A. Mackay (2016). "Why Was Silcrete Heat-Treated in the Middle Stone Age? An Early Transformative Technology in the Context of Raw Material Use at Mertenhof Rock Shelter, South Africa." PLOS ONE **11**(2): e0149243.

Schmidt, P., Stynder, D., Conard, N. J., & Parkington, J. E. (2020). When was silcrete heat treatment invented in South Africa?. *Palgrave Communications*, *6*(1), 1-10.

Scott, R. M., Buckley, H. R., Spriggs, M., Valentin, F., & Bedford, S. (2010). Identification of the first reported Lapita cremation in the Pacific Islands using archaeological, forensic and contemporary burning evidence. *Journal of Archaeological Science*, *37*(5), 901-909.

Shahack-Gross, R., Bar-Yosef, O., & Weiner, S. (1997). Black-coloured bones in Hayonim Cave, Israel: differentiating between burning and oxide staining. *Journal of archaeological Science*, *24*(5), 439-44.

Shimelmitz, R., Kuhn, S. L., Jelinek, A. J., Ronen, A., Clark, A. E., & Weinstein-Evron, M. (2014). 'Fire at will': The emergence of habitual fire use 350,000 years ago. *Journal of Human Evolution*, *77*, 196-203.

Shipman, P., Foster, G., & Schoeninger, M. (1984). Burnt bones and teeth: an experimental study of color, morphology, crystal structure and shrinkage. *Journal of archaeological science*, *11*(4), 307-325.

Snoeck, C., Lee-Thorp, J. A., & Schulting, R. J. (2014). From bone to ash: Compositional and structural changes in burned modern and archaeological bone. *Palaeogeography, palaeoclimatology, palaeoecology*, *416*, 55-68.

Spagnolo, V., Marciani, G., Aureli, D., Berna, F., Toniello, G., Astudillo, F., ... & Ronchitelli, A. (2019). Neanderthal activity and resting areas from stratigraphic unit 13 at the Middle Palaeolithic site of Oscurusciuto (Ginosa-Taranto, Southern Italy). *Quaternary Science Reviews*, *217*, 169-193.

Speth, J., & Clark, J. (2006). Hunting and overhunting in the Levantine late Middle Palaeolithic. *Before Farming*, *2006*(3), 1-43.

Sponheimer, M., & Lee-Thorp, J. A. (1999). Oxygen isotopes in enamel carbonate and their ecological significance. *Journal of Archaeological Science*, *26*(6), 723-728.

Stahlschmidt, M. C., Miller, C. E., Ligouis, B., Hambach, U., Goldberg, P., Berna, F., ... & Conard, N. J. (2015). On the evidence for human use and control of fire at Schöningen. *Journal of Human Evolution*, *89*, 181-201.

Stahlschmidt, M. C., Mallol, C., & Miller, C. E. (2020). Fire as an artifact—advances in paleolithic combustion structure studies: Introduction to the special issue. *Journal of Paleolithic Archaeology*, *3*(4), 503-508.

Stiner, M. C., Kuhn, S. L., Weiner, S., & Bar-Yosef, O. (1995). Differential burning, recrystallization, and fragmentation of archaeological bone. *Journal of archaeological science*, *22*(2), 223-237.

Stout, S. D., Cole, M. E., & Agnew, A. M. (2019). Histomorphology: Deciphering the metabolic record. In *Ortner's identification of pathological conditions in human skeletal remains* (pp. 91-167). Academic Press.

Théry-Parisot, I., Costamagno, S., Brugal, J. P., Fosse, P., & Guilbert, R. (2005). The use of bone as fuel during the Palaeolithic, experimental study of bone combustible properties.

Thompson, T. (2004). Recent advances in the study of burned bone and their implications for forensic anthropology.Forensic science international, 146, S203-S205.

Thompson, T. J. U., Gauthier, M., & Islam, M. (2009). The application of a new method of Fourier Transform Infrared Spectroscopy to the analysis of burned bone. *Journal of Archaeological Science*, *36*(3), 910-914.

Thompson, T. J. U., Islam, M., & Bonniere, M. (2013). A new statistical approach for determining the crystallinity of heat-altered bone mineral from FTIR spectra. *Journal of Archaeological Science*, *40*(1), 416-422.

Toffolo, M. B., Brink, J. S., & Berna, F. (2015). Bone diagenesis at the Florisbad spring site, Free State Province (South Africa): Implications for the taphonomy of the Middle and Late Pleistocene faunal assemblages. *Journal of Archaeological Science: Reports*, *4*, 152-163.

Turner, E., Hutson, J., Villaluenga, A., García Moreno, A., & Gaudzinski-Windheuser, S. (2018). Bone staining in waterlogged deposits: a preliminary contribution to the interpretation of near-shore find accumulation at the Schöningen 13II-4 ‘Spear-Horizon’site, Lower Saxony, Germany. *Historical Biology, 30*(6), 767-773.

Vallverdú, J., Vaquero, M., Cáceres, I., Allué, E., Rosell, J., Saladié, P., ... & Carbonell, E. (2010). Sleeping activity area within the site structure of archaic human groups: Evidence from Abric Romaní level N combustion activity areas. *Current Anthropology*, *51*(1), 137-145.

Vallverdú, J., Alonso, S., Bargalló, A., Bartrolí, R., Campeny, G., Carrancho, Á., ... & Carbonell, E. (2012). Combustion structures of archaeological level O and mousterian activity areas with use of fire at the Abric Romaní rockshelter (NE Iberian Peninsula). *Quaternary International*, *247*, 313-324.

Van Casteren, A., Codd, J. R., Kupczik, K., Plasqui, G., Sellers, W. I., & Henry, A. G. (2022). The cost of chewing: The energetics and evolutionary significance of mastication in humans. *Science advances*, *8*(33), eabn8351.

Vaquero, M., Bargalló, A., Chacón, M. G., Romagnoli, F., & Sañudo, P. (2015). Lithic recycling in a Middle Paleolithic expedient context: evidence from the Abric Romaní (Capellades, Spain). *Quaternary International*, *361*, 212-228.

Vidal-Matutano, P., Henry, A., & Théry-Parisot, I. (2017). Dead wood gathering among Neanderthal groups: charcoal evidence from Abric del Pastor and El Salt (Eastern Iberia). *Journal of archaeological science*, *80*, 109-121.

Vidal-Matutano, P., Pérez-Jordà, G., Hernández, C. M., & Galván, B. (2018). Macrobotanical evidence (wood charcoal and seeds) from the Middle Palaeolithic site of El Salt, Eastern Iberia: Palaeoenvironmental data and plant resources catchment areas. *Journal of archaeological science: reports*, *19*, 454-464.

Wadley et al., Fire and grass-bedding construction 200 thousand years ago at Border Cave, South Africa.Science369,863–866 (2020)

Weiner, S., & Bar-Yosef, O. (1990). States of preservation of bones from prehistoric sites in the Near East: a survey. Journal of Archaeological Science, 17(2), 187-196.

White, R., Mensan, R., Clark, A. E., Tartar, E., Marquer, L., Bourrillon, R., ... & Ranlett, S. (2017). Technologies for the control of heat and light in the Vézère Valley Aurignacian. *Current Anthropology*, *58*(S16), S288-S302.

Wiessner, P. W. (2014). Embers of society: Firelight talk among the Ju/’hoansi Bushmen. *Proceedings of the National Academy of Sciences*, *111*(39), 14027-14035.

Wrangham, R. (2009). *Catching fire: how cooking made us human*. Basic books.

Chapter 5

Conclusions and Future Directions

The presence of anthropogenic fire in the MP of Southwest France in relatively temperate periods indicates that pyrotechnology was a part of the behavioral repertoire of at least some Neanderthal populations. This is supported by data from other geographic areas, including Abric del Pastor in Spain, which exhibits evidence of fire in Marine Isotope Stage (MIS) 4. These populations are in lower latitudes and are inferred to represented geographical areas which did not experience the same environmental stresses as the dry and cold presented in French Neanderthal deposits where fire proxies are absent (Dibble et al., 2018; Mallol et al., 2019; Sandgathe et al., 2011). This study expands upon our knowledge of presence of Neanderthal fire in the MP to document specific properties found within the combustion features of Roc de Marsal layer 9, and the relevant aspects of Neanderthal fire technology which produced these fires.

We report here through a zooarchaeological perspective evidence of different types of combustion features in RDM layer 9 (**Chapter 4**). This includes both low-temperature and high-temperature dominated features, which are spatially differentiated within and outside of the RDM cave. These observations have not been described through lithic and geoarchaeological approaches, and here demonstrates the applicability of fauna as a fire proxy (**Chapters 2, 3**). Methodologies recommended by this study include both traditional zooarchaeological approaches such as collecting the weights (g), sizes (mm), macroscopic burning scale and bone tissue type distribution, but also incorporating spectroscopic analyses to verify burning and monitor for different fire conditions.

Chapters 2 and 3 use experiments to build spectroscopic reference libraries to quantify the degree and type of heat induced transformations to bone mineral for better extrapolation to archaeological assemblages of burnt bone. We determine that the timing of organic loss leaves both experimental and archaeological bone heated to temperatures around 300 °C, but under 700 °C, vulnerable to dissolution. This is because bone heated within this range has lost all organic protection, is very porous, and still has small, highly soluble, crystallites (**Chapter 2**). Bones heated above 700 °C receive the energy needed to experience tremendous crystallite growth that results in much less soluble bioapatite minerals and a much lower degree of porosity (**Chapter 2**). Our inferences are supported by average crystallite sizes additionally measured by XRD. These results, previously undescribed, have large consequences for researchers evaluating burned bone in archaeological contexts as we have described the differential preservation of bones burnt to different temperatures. This may produce biased assemblages, especially in depositional environments with water movement, where charred and carbonized bone are more easily destroyed. Conclusions of this study are incorporated into **Chapter 4** to recognize that the lack of high-temperature (> 700 °C) fires outside of the RDM dripline are not due to preservation biases or environmental factors, because the most mechanically fragile, calcined bone is the most thermodynamically stable category of burnt bone.

FTIR-ATR is also used here to describe the elimination of organic components, responsible for the coloration changes in heated bone, in bones that experience temperatures under 700 °C for long durations (**Chapter 3**). XRD measurements are additionally used to verify true calcination via bioapatite crystallite growth. Our experiments result in bones which are depigmented (white and grey in color) at 300 and 550 °C, but are not calcined structurally or chemically (**Chapter 3**). This observation advances the zooarchaeological categorizations of burned bones, which have previously depended on color descriptions (such as the Stiner et al. 1995 heating scale). Once bones have fully had the combusted and charred organic components removed this study also demonstrates that it is still possible to detect bones burnt at high temperatures for long durations through the example of the massively exaggerated crystallite sizes of samples heated at 750 °C for 9 hours (**Chapter 3**). In terms of recognizing archaeological examples of long duration burning, we are able to recommend that researchers test heated bones which are light in color with spectroscopic methods to investigate long duration burning within different archaeological assemblages. Duration is highlighted as a very important variable of interest, as it is related to fire function and fire using behaviors. **Chapter 4** explores this parameter within the RDM layer 9 assemblage, and only four samples were found to indicate spectroscopic signatures which may be related to long duration fire at low temperatures. Along with a recommendation for more sampling within these areas, we additionally propose more experimental work regarding other avenues for similar signatures of discrepancies between coloration and chemical structure of bone (for example, the burning of sun-bleached bone) which could be alternative scenarios for such samples.

Chapter 4 applies these spectroscopic observations from the experimental studies to the faunal assemblage of RDM layer 9, verifying thermal alteration and the temperature thresholds reached. We then spatially analyze the physical zooarchaeological data on the assemblage, and KDE heatmaps identified patterns of feature temperature distributions: high temperature (> 700 °C) within the cave and lower temperature (~ 300-500 °C) outside of the dripline. These inferences remain valid even for time averaged collections, as the palimpsests reflect a large-scale pattern in fire technology (Reeves et al., 2019). Evidence of different types of anthropogenic features, indicative of different technological systems of using and maintaining fire, is complementary to our prior knowledge of combustion features at RDM layer 9, which indicates different types of features throughout the cave interior and exterior (Aldeias et al., 2012; Goldberg et al., 2012). This includes intact and displaced features, well-structured features, stacked features, and features primarily of ash (Aldeias et al., 2012; Goldberg et al., 2012).

This study additionally contributes to Reeves et al. (2019)'s conclusion through analyses of burnt lithic distributions that fire areas were high activity areas, as evidenced here through faunal remains with anthropogenic butchery marks (including scraping and cut marks) found throughout the site and within several accumulations of burnt bone (**Chapter 4**). Other consistent behaviors regarding fire use includes the inference of bone being burnt within the site as a fuel or maintenance (i.e. site cleaning) strategy, supported by both the Costamagno et al. (2005, 2009) combustion indices and the concentration of calcined and blue bone within the cave which potentially represents older faunal assemblages which had undergone diagenetic alteration in the environment before being burnt by Neanderthals (**Chapter 4**).

In addition to estimating and distinguishing different temperature thresholds, bone is additionally used in this study to monitor the atmospheric conditions of heating, long duration times, and the role of bone in the pyrotechnology sequence of fire use and maintenance (**Chapters 3-4**). Bone within RDM layer 9 was not found to have any indication of burning in a reduction atmosphere within the spectroscopic analyses, but more specific sampling in the future utilizing micromorphological observations may be potential avenue for more specific sampling strategies.

Neanderthals exhibited a variety of behaviors regarding their use and maintenance of fire at RDM layer 9 (**Chapter 4**). This may indicate that Neanderthals at this time and geographic area had a comprehensive knowledge of fire, likely is the result of fire that could be produced (control of fire), and produced fires of differing properties to address different functional (i.e. activity specific) or economic (i.e. fuel availability) needs.

Future directions

Combustion feature properties at RDM layer 9 will next be combined on a larger scale with data from lithic, paleobotanical, and geoarchaeological analyses. This includes the further incorporation of micromorphological slides, as the microcontext provides an indispensable line of evidence for the structure and contents of combustion features, and work described in this study demonstrates the applicability even with diagenetic alteration (**Chapter 4).** In this way, a comprehensive and holistic perspective of combustion features at RDM layer 9 may be explored and further questions relevant to Neanderthal fire using behaviors, such as the organic components of fire and the contents of ash-dump features, may be described alongside the faunal evidence.

To specifically address the role of fire technology, work expanding past this manuscript will investigate the chaine operatoire of pyrotechnology within RDM, considering the fire event from construction, maintenance, and final extinguishing. Three aspects of the fire event will be considered for this study, fire temperature, the role of bone as a fire component, and any recorded trampling or hearth rake-out. I will compare between all features in RDM layer 9 with spatial analyses taking into account the Z axis of artifact deposition.

Future experimental projects are also planned to describe finer details of burning scenarios explored in this manuscript. This includes addressing bones burnt with different organic status (i.e. ‘dry’ or sun-bleached bones), the thermal alteration of bone buried at different depths in different substrates, bones within micromorphological slides, and bones exposed to heat for time lengths between 3 and 9 hours to see when duration begins impact assemblages. While these experiments have been and will be developed to investigate burning conditions and archaeological fire properties, the principles described here have also contributed to distinguishing between natural and anthropogenic fires, an essential step for studying fire remains.

Along with more experimental work, I aim to improve methods for quantifying changes in burnt bone and better predicting temperature thresholds and other conditions of burning. These analytical studies will include the use of Near Infrared Spectroscopy (NIR) methods, will consider the transmittance mode of FTIR, and will build models of burning based on all reference collections accumulated for this project.

The methodological approaches developed for this research program have engaged with the first principles of thermal alteration to improve and modernize zooarchaeological interpretations of archaeological burnt bone. Exploring these different scenarios of heating enables a tremendous amount of future research on both the kinetics and composition of bones heated under different circumstances, but also the archaeological application of these methods. This methodology can be utilized both on additional fire features from the Middle Paleolithic, but also archaeological collections from the Upper Paleolithic and other periods in which modern human fire use is of interest (such as expansion and migrations, i.e. the UP assemblage of Tolbor-17 included in **Chapter 2**, and UP Gravettian and Solutrean assemblages from before and during the last glacial maximum).

Overarching aims of my future research program will be to approach archaeological faunal assemblages to speak to fire using behaviors and patterns of behavior. This is especially true for Neanderthals, whose position as hominins closely related to us with a well-documented archaeological record provides excellent opportunities to test different types occupational sites and look for patterns between combustion feature evidence to describe on a greater scale their knowledge of fire control, types of fire use, and methods of fire maintenance. To address this, I will first be comparing the sites of RDM and Pech de l'Azé IV (PIV) to the MP chronological sequence of Le Moustier, a site 20 kilometers from RDM, and an example of a MIS 3 Middle Paleolithic combustion feature from the site of Trou Al'Wesse, Belgium. This will be accomplished by 1) standardizing data collection for the weights, sizes, and macroscopic burning stages of thermally altered bone; 2) a heavy sampling strategy within all stages of burnt bone for spectroscopic analyses of FTIR-ATR and XRD utilizing observations for smarter sampling described in this manuscript; 3) quantification of burning degrees and atmospheres from micromorophological evidence, additionally speaking to depositional behaviors like trampling; 4) the creation of three-dimensional spatial distribution maps to distinguish primary fire locations and the properties of individual features.

To best contextualize Neanderthal fire, however, I believe it is necessary to also test modern human UP fire evidence with the same methodologies, especially if research goals are to understand the similarities and differences between Neanderthals and modern humans. Work towards those goals has already begun with the consideration of the site of Tolbor 17, an Upper Paleolithic (UP) site in Mongolia (**Chapter 2**), and the future work to be done at an IUP site dating to 45 ka in Bulgaria, Bacho Kiro. Due to the extensive presence of Aurignacian sites in the same constrained geographic area as PIV and RDM, future work on the fire evidence within these zooarchaeological assemblages would also be valuable datapoints to contextualize fire use in the Paleolithic and the relative importance and technology for different species of hominins.

The consideration of fire as a technology and bone as an appropriate proxy for the study of that technology, opens opportunities to better understand social and economic lifeways of hominins. My research contributes to our knowledge of fire proxies, and what bone can tell us about pyrotechnology thousands of years ago. The utilization of pyrotechnology to understand behavior of Neanderthals provides a new lens to describe the diverse lifeways of Pleistocene hominins that touches upon the many important aspects of their technological and cultural adaptations, filling in the picture of our human story.

References

Aldeias, V., Goldberg, P., Sandgathe, D., Berna, F., Dibble, H. L., McPherron, S. P., ... & Rezek, Z. (2012). Evidence for Neandertal use of fire at Roc de Marsal (France). *Journal of Archaeological Science*, *39*(7), 2414-2423.

Costamagno, S., Thery-Parisot, I., Brugal, J. P., & Guibert, R. (2005). Taphonomic consequences of the use of bones as fuel. Experimental data and archaeological applications. *Biosphere to lithosphere: new studies in vertebrate taphonomy*, 51-62.

Costamagno, S., Théry-Parisot, I., Castel, J. C., & Brugal, J. P. (2009). Combustible ou non? Analyse multifactorielle et modèles explicatifs sur des ossements brûlés paléolithiques. *GESTION DES COMBUSTIBLES AU PALÉOLITHIQUE ET AU MÉSOLITHIQUE NOUVEAUX OUTILS, NOUVELLES INTERPRÉTATIONS FUEL MANAGEMENT DURING THE PALAEOLITHIC AND MESOLITHIC PERIOD*, 61.

Dibble, H. L., McPherron, S. J., Goldberg, P., & Sandgathe, D. M. (Eds.). (2018). *The Middle Paleolithic Site of Pech de L'Azé IV*. Springer International Publishing.

Goldberg, P., Dibble, H., Berna, F., Sandgathe, D., McPherron, S. J., & Turq, A. (2012). New evidence on Neandertal use of fire: examples from Roc de Marsal and Pech de l'Azé IV. *Quaternary International*, *247*, 325-340.

Hublin, J. J., Sirakov, N., Aldeias, V., Bailey, S., Bard, E., Delvigne, V., ... & Tsanova, T. (2020). Initial upper palaeolithic homo sapiens from bacho kiro cave, Bulgaria. *Nature*, *581*(7808), 299-302.

Mallol, C., Hernández, C., Mercier, N., Falguères, C., Carrancho, Á., Cabanes, D., ... & Galván, B. (2019). Fire and brief human occupations in Iberia during MIS 4: Evidence from Abric del Pastor (Alcoy, Spain). *Scientific reports*, *9*(1), 1-11.

Reeves, J. S., McPherron, S. P., Aldeias, V., Dibble, H. L., Goldberg, P., Sandgathe, D., & Turq, A. (2019). Measuring spatial structure in time-averaged deposits insights from Roc de Marsal, France. *Archaeological and Anthropological Sciences*, *11*(10), 5743-5762.

Stiner, M. C., Kuhn, S. L., Weiner, S., & Bar-Yosef, O. (1995). Differential burning, recrystallization, and fragmentation of archaeological bone. *Journal of archaeological science*, *22*(2), 223-237.

Appendix A: Supplemental Materials for Chapter 2

Table 1: Experimental modern bone FTIR-ATR relevant peak height values.

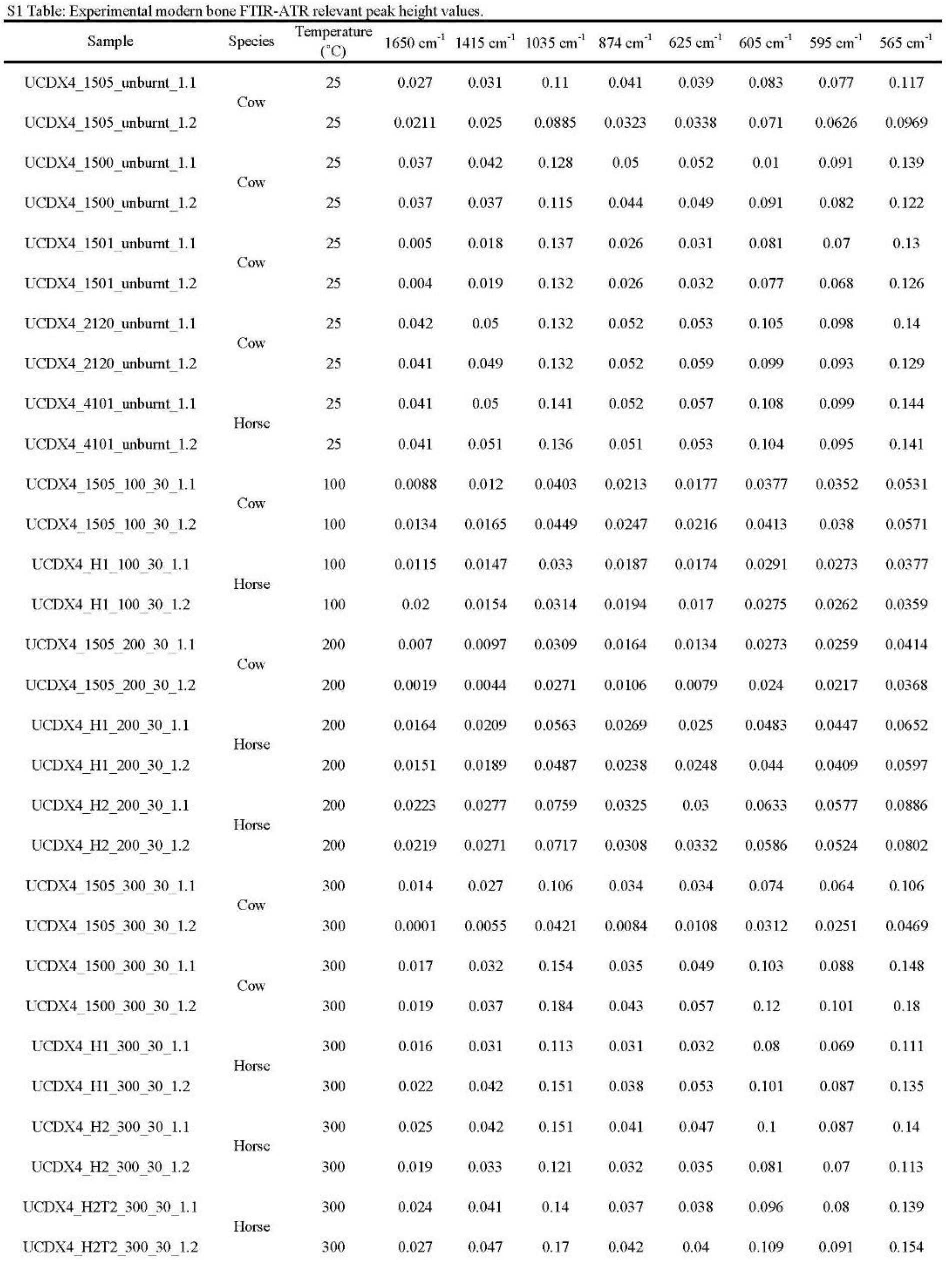

S1 Table: Experimental modern bone FTIR-ATR relevant peak height values.

Sample	Species	Temperature (˚C)	1650 cm^{-1}	1415 cm^{-1}	1035 cm^{-1}	874 cm^{-1}	625 cm^{-1}	605 cm^{-1}	595 cm^{-1}	565 cm^{-1}
UCDX4_1505_unburnt_1.1	Cow	25	0.027	0.031	0.11	0.041	0.039	0.083	0.077	0.117
UCDX4_1505_unburnt_1.2		25	0.0211	0.025	0.0885	0.0323	0.0338	0.071	0.0626	0.0969
UCDX4_1500_unburnt_1.1	Cow	25	0.037	0.042	0.128	0.05	0.052	0.01	0.091	0.139
UCDX4_1500_unburnt_1.2		25	0.037	0.037	0.115	0.044	0.049	0.091	0.082	0.122
UCDX4_1501_unburnt_1.1	Cow	25	0.005	0.018	0.137	0.026	0.031	0.081	0.07	0.13
UCDX4_1501_unburnt_1.2		25	0.004	0.019	0.132	0.026	0.032	0.077	0.068	0.126
UCDX4_2120_unburnt_1.1	Cow	25	0.042	0.05	0.132	0.052	0.053	0.105	0.098	0.14
UCDX4_2120_unburnt_1.2		25	0.041	0.049	0.132	0.052	0.059	0.099	0.093	0.129
UCDX4_4101_unburnt_1.1	Horse	25	0.041	0.05	0.141	0.052	0.057	0.108	0.099	0.144
UCDX4_4101_unburnt_1.2		25	0.041	0.051	0.136	0.051	0.053	0.104	0.095	0.141
UCDX4_1505_100_30_1.1	Cow	100	0.0088	0.012	0.0403	0.0213	0.0177	0.0377	0.0352	0.0531
UCDX4_1505_100_30_1.2		100	0.0134	0.0165	0.0449	0.0247	0.0216	0.0413	0.038	0.0571
UCDX4_H1_100_30_1.1	Horse	100	0.0115	0.0147	0.033	0.0187	0.0174	0.0291	0.0273	0.0377
UCDX4_H1_100_30_1.2		100	0.02	0.0154	0.0314	0.0194	0.017	0.0275	0.0262	0.0359
UCDX4_1505_200_30_1.1	Cow	200	0.007	0.0097	0.0309	0.0164	0.0134	0.0273	0.0259	0.0414
UCDX4_1505_200_30_1.2		200	0.0019	0.0044	0.0271	0.0106	0.0079	0.024	0.0217	0.0368
UCDX4_H1_200_30_1.1	Horse	200	0.0164	0.0209	0.0563	0.0269	0.025	0.0483	0.0447	0.0652
UCDX4_H1_200_30_1.2		200	0.0151	0.0189	0.0487	0.0238	0.0248	0.044	0.0409	0.0597
UCDX4_H2_200_30_1.1	Horse	200	0.0223	0.0277	0.0759	0.0325	0.03	0.0633	0.0577	0.0886
UCDX4_H2_200_30_1.2		200	0.0219	0.0271	0.0717	0.0308	0.0332	0.0586	0.0524	0.0802
UCDX4_1505_300_30_1.1	Cow	300	0.014	0.027	0.106	0.034	0.034	0.074	0.064	0.106
UCDX4_1505_300_30_1.2		300	0.0001	0.0055	0.0421	0.0084	0.0108	0.0312	0.0251	0.0469
UCDX4_1500_300_30_1.1	Cow	300	0.017	0.032	0.154	0.035	0.049	0.103	0.088	0.148
UCDX4_1500_300_30_1.2		300	0.019	0.037	0.184	0.043	0.057	0.12	0.101	0.18
UCDX4_H1_300_30_1.1	Horse	300	0.016	0.031	0.113	0.031	0.032	0.08	0.069	0.111
UCDX4_H1_300_30_1.2		300	0.022	0.042	0.151	0.038	0.053	0.101	0.087	0.135
UCDX4_H2_300_30_1.1	Horse	300	0.025	0.042	0.151	0.041	0.047	0.1	0.087	0.14
UCDX4_H2_300_30_1.2		300	0.019	0.033	0.121	0.032	0.035	0.081	0.07	0.113
UCDX4_H2T2_300_30_1.1	Horse	300	0.024	0.041	0.14	0.037	0.038	0.096	0.08	0.139
UCDX4_H2T2_300_30_1.2		300	0.027	0.047	0.17	0.042	0.04	0.109	0.091	0.154

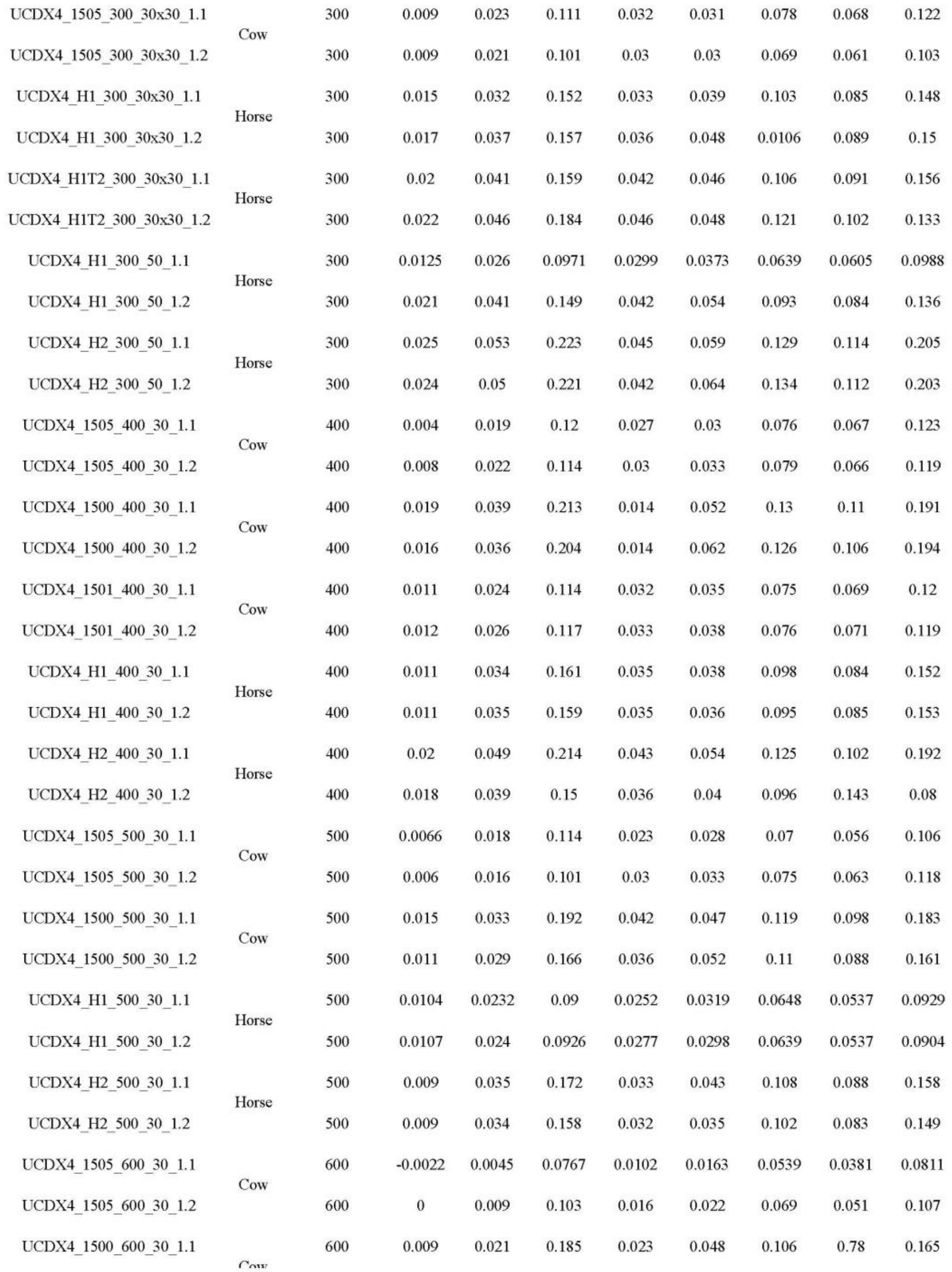

UCDX4_1505_300_30x30_1.1	Cow	300	0.009	0.023	0.111	0.032	0.031	0.078	0.068	0.122
UCDX4_1505_300_30x30_1.2		300	0.009	0.021	0.101	0.03	0.03	0.069	0.061	0.103
UCDX4_H1_300_30x30_1.1	Horse	300	0.015	0.032	0.152	0.033	0.039	0.103	0.085	0.148
UCDX4_H1_300_30x30_1.2		300	0.017	0.037	0.157	0.036	0.048	0.0106	0.089	0.15
UCDX4_H1T2_300_30x30_1.1	Horse	300	0.02	0.041	0.159	0.042	0.046	0.106	0.091	0.156
UCDX4_H1T2_300_30x30_1.2		300	0.022	0.046	0.184	0.046	0.048	0.121	0.102	0.133
UCDX4_H1_300_50_1.1	Horse	300	0.0125	0.026	0.0971	0.0299	0.0373	0.0639	0.0605	0.0988
UCDX4_H1_300_50_1.2		300	0.021	0.041	0.149	0.042	0.054	0.093	0.084	0.136
UCDX4_H2_300_50_1.1	Horse	300	0.025	0.053	0.223	0.045	0.059	0.129	0.114	0.205
UCDX4_H2_300_50_1.2		300	0.024	0.05	0.221	0.042	0.064	0.134	0.112	0.203
UCDX4_1505_400_30_1.1	Cow	400	0.004	0.019	0.12	0.027	0.03	0.076	0.067	0.123
UCDX4_1505_400_30_1.2		400	0.008	0.022	0.114	0.03	0.033	0.079	0.066	0.119
UCDX4_1500_400_30_1.1	Cow	400	0.019	0.039	0.213	0.014	0.052	0.13	0.11	0.191
UCDX4_1500_400_30_1.2		400	0.016	0.036	0.204	0.014	0.062	0.126	0.106	0.194
UCDX4_1501_400_30_1.1	Cow	400	0.011	0.024	0.114	0.032	0.035	0.075	0.069	0.12
UCDX4_1501_400_30_1.2		400	0.012	0.026	0.117	0.033	0.038	0.076	0.071	0.119
UCDX4_H1_400_30_1.1	Horse	400	0.011	0.034	0.161	0.035	0.038	0.098	0.084	0.152
UCDX4_H1_400_30_1.2		400	0.011	0.035	0.159	0.035	0.036	0.095	0.085	0.153
UCDX4_H2_400_30_1.1	Horse	400	0.02	0.049	0.214	0.043	0.054	0.125	0.102	0.192
UCDX4_H2_400_30_1.2		400	0.018	0.039	0.15	0.036	0.04	0.096	0.143	0.08
UCDX4_1505_500_30_1.1	Cow	500	0.0066	0.018	0.114	0.023	0.028	0.07	0.056	0.106
UCDX4_1505_500_30_1.2		500	0.006	0.016	0.101	0.03	0.033	0.075	0.063	0.118
UCDX4_1500_500_30_1.1	Cow	500	0.015	0.033	0.192	0.042	0.047	0.119	0.098	0.183
UCDX4_1500_500_30_1.2		500	0.011	0.029	0.166	0.036	0.052	0.11	0.088	0.161
UCDX4_H1_500_30_1.1	Horse	500	0.0104	0.0232	0.09	0.0252	0.0319	0.0648	0.0537	0.0929
UCDX4_H1_500_30_1.2		500	0.0107	0.024	0.0926	0.0277	0.0298	0.0639	0.0537	0.0904
UCDX4_H2_500_30_1.1	Horse	500	0.009	0.035	0.172	0.033	0.043	0.108	0.088	0.158
UCDX4_H2_500_30_1.2		500	0.009	0.034	0.158	0.032	0.035	0.102	0.083	0.149
UCDX4_1505_600_30_1.1	Cow	600	-0.0022	0.0045	0.0767	0.0102	0.0163	0.0539	0.0381	0.0811
UCDX4_1505_600_30_1.2		600	0	0.009	0.103	0.016	0.022	0.069	0.051	0.107
UCDX4_1500_600_30_1.1	Cow	600	0.009	0.021	0.185	0.023	0.048	0.106	0.78	0.165

UCDX4_1500_600_30_1.2	Cow	600	0.009	0.021	0.185	0.023	0.056	0.112	0.77	0.165
UCDX4_1501_600_30_1.1	Cow	600	0.009	0.021	0.145	0.029	0.037	0.09	0.072	0.142
UCDX4_1501_600_30_1.2		600	0.0034	0.0139	0.0995	0.0182	0.0263	0.0617	0.0482	0.095
UCDX4_H1_600_30_1.1	Horse	600	0.013	0.028	0.122	0.032	0.04	0.085	0.065	0.119
UCDX4_H1_600_30_1.2		600	0.012	0.025	0.108	0.028	0.033	0.077	0.058	0.108
UCDX4_H2_600_30_1.1	Horse	600	0.006	0.032	0.193	0.034	0.04	0.112	0.083	0.176
UCDX4_H2_600_30_1.2		600	0.008	0.036	0.193	0.036	0.043	0.116	0.088	0.18
UCDX4_H4_600_30_1.1	Horse	600	0.01	0.025	0.143	0.027	0.031	0.085	0.061	0.125
UCDX4_H4_600_30_1.2		600	0.011	0.03	0.152	0.03	0.036	0.089	0.68	0.133
UCDX4_1505_700_30_1.1	Cow	700	0	0.005	0.098	0.013	0.021	0.061	0.044	0.097
UCDX4_1505_700_30_1.2		700	0.0018	0.0057	0.0705	0.0112	0.0177	0.051	0.0335	0.0726
UCDX4_1500_700_30_1.1	Cow	700	0.011	0.026	0.318	0.031	0.061	0.166	0.108	0.242
UCDX4_1500_700_30_1.2		700	0.012	0.025	0.0292	0.03	0.056	0.154	0.108	0.242
UCDX4_1501_700_30_1.1	Cow	700	0.005	0.013	0.164	0.02	0.035	0.095	0.071	0.148
UCDX4_1501_700_30_1.2		700	0.004	0.012	0.153	0.019	0.034	0.091	0.068	0.139
UCDX4_H1_700_30_1.1	Horse	700	0.007	0.046	0.423	0.042	0.058	0.242	0.136	0.329
UCDX4_H1T1_700_30_1.1	Horse	700	0.009	0.049	0.0468	0.047	0.062	0.236	0.139	0.344
UCDX4_H1T1_700_30_1.2		700	0.01	0.048	0.0384	0.04	0.061	0.22	0.128	0.307
UCDX4_H2_700_30_1.1	Horse	700	0.013	0.048	0.34	0.042	0.048	0.177	0.121	0.269
UCDX4_H2_700_30_1.2		700	0.014	0.051	0.298	0.042	0.047	0.158	0.112	0.237
UCDX4_1505_700_30x30_1.1	Cow	700	0.004	0.01	0.153	0.02	0.037	0.099	0.063	0.145
UCDX4_1505_700_30x30_1.2		700	0.004	0.01	0.126	0.018	0.032	0.082	0.054	0.121
UCDX4_1501_700_30x30_1.1	Cow	700	0.006	0.016	0.233	0.023	0.052	0.142	0.084	0.142
UCDX4_1501_700_30x30_1.2		700	0.006	0.017	0.214	0.022	0.05	0.134	0.08	0.134
UCDX4_H0_700_30x30_1.1	Horse	700	0.011	0.044	0.4	0.038	0.062	0.213	0.124	0.319
UCDX4_H0_700_30x30_1.2		700	0.012	0.047	0.41	0.041	0.066	0.223	0.138	0.334
UCDX4_H1_700_30x30_1.1	Horse	700	0.011	0.045	0.426	0.048	0.065	0.23	0.136	0.344
UCDX4_H1_700_30x30_1.2		700	0.013	0.042	0.333	0.044	0.058	0.196	0.12	0.277
UCDX4_H2_700_30x30_1.1	Horse	700	0.006	0.048	0.441	0.042	0.059	0.209	0.148	0.357
UCDX4_H2_700_30x30_1.2		700	0.008	0.049	0.448	0.043	0.06	0.237	0.149	0.359
UCDX4_H3_700_30x30_1.1	Horse	700	0.01	0.05	0.532	0.044	0.079	0.0263	0.151	0.409

UCDX4_H3_700_30x30_1.2	Horse	700	0.01	0.048	0.441	0.048	0.072	0.0246	0.141	0.346
UCDX4_H1_700_50_1.1	Horse	700	0.01	0.049	0.443	0.044	0.059	0.233	0.14	0.336
UCDX4_H1_700_50_1.2		700	0.007	0.04	0.293	0.036	0.048	0.18	0.111	0.248
UCDX4_1505_800_30_1.1	Cow	800	0.004	0.01	0.157	0.02	0.044	0.103	0.07	0.147
UCDX4_1505_800_30_1.2		800	0.004	0.01	0.157	0.02	0.033	0.103	0.07	0.147
UCDX4_1501_800_30_1.1	Cow	800	0.009	0.019	0.23	0.029	0.052	0.135	0.093	0.21
UCDX4_1501_800_30_1.2		800	0.009	0.017	0.208	0.027	0.048	0.124	0.083	0.194
UCDX4_H1_800_30_1.1	Horse	800	0.012	0.042	0.448	0.041	0.068	0.24	0.146	0.369
UCDX4_H1_800_30_1.2		800	0.012	0.039	0.398	0.039	0.063	0.222	0.14	0.328
UCDX4_1505_900_30_1.1	Cow	900	0.003	0.006	0.258	0.018	0.048	0.163	0.1	0.242
UCDX4_1505_900_30_1.2		900	0.005	0.008	0.277	0.022	0.051	0.161	0.106	0.26
UCDX4_1500_900_30_1.1	Cow	900	0.011	0.013	0.466	0.021	0.119	0.259	0.138	0.395
UCDX4_1500_900_30_1.2		900	0.01	0.013	0.406	0.018	0.106	0.239	0.137	0.354
UCDX4_H1_900_30_1.1	Horse	900	0.007	0.026	0.446	0.033	0.066	0.152	0.152	0.378
UCDX4_H1_900_30_1.2		900	0.011	0.029	0.467	0.036	0.068	0.156	0.156	0.385
UCDX4_H5_900_30_1.1	Horse	900	0.007	0.031	0.562	0.041	0.064	0.0283	0.177	0.439
UCDX4_H5_900_30_1.2		900	0.006	0.028	0.515	0.039	0.061	0.0267	0.125	0.408
UCDX4_1505_1000_30_1.1	Cow	1000	0.0002	0.001	0.119	0.02	0.024	0.095	0.066	0.135
UCDX4_1505_1000_30_1.2		1000	-0.0013	0	0.101	0.018	0.019	0.082	0.56	0.12
UCDX4_1500_1000_30_1.1	Cow	1000	0	0.013	0.105	0.017	0.061	0.116	0.063	0.159
UCDX4_1500_1000_30_1.2		1000	0.016	0.016	0.279	0.024	0.096	0.188	0.101	0.271
UCDX4_1501_1000_30_1.1	Cow	1000	0.005	0.018	0.137	0.026	0.033	0.086	0.068	0.136
UCDX4_1501_1000_30_1.2		1000	0.004	0.019	0.133	0.026	0.032	0.084	0.067	0.126
UCDX4_H0_1000_30_1.1	Horse	1000	0.012	0.013	0.313	0.024	0.049	0.188	0.127	0.288
UCDX4_H0_1000_30_1.2		1000	0.014	0.015	0.372	0.029	0.057	0.223	0.148	0.33
UCDX4_H1_1000_30_1.1	Horse	1000	0.004	0.007	0.362	0.023	0.052	0.215	0.144	0.336
UCDX4_H1_1000_30_1.2		1000	0.006	0.008	0.316	0.021	0.048	0.205	0.133	0.295
UCDX4_1505_1100_30_1.1	Cow	1100	-0.00249	-0.018	0.0612	0.0212	0.0093	0.0587	0.0463	0.0801
UCDX4_1505_1100_30_1.2		1100	-0.00249	-0.0019	0.0624	0.0176	0.0095	0.06	0.0476	0.081
UCDX4_1500_1100_30_1.1	Cow	1100	0.006	0.006	0.244	0.031	0.043	0.171	0.129	0.235
UCDX4_1500_1100_30_1.2		1100	0.007	0.008	0.288	0.034	0.045	0.196	0.162	0.285

UCDX4_H1_1100_30_1.1	Horse	1100	0.014	0.016	0.303	0.038	0.048	0.195	0.148	0.277
UCDX4_H1_1100_30_1.2		1100	0.013	0.015	0.274	0.024	0.06	0.191	0.148	0.258
UCDX4_1505_1200_30_1.1	Cow	1200	-0.0039	-0.0033	0.0498	0.0249	0.0079	0.0373	0.0441	0.0654
UCDX4_1505_1200_30_1.2		1200	-0.002	-0.0017	0.0586	0.0288	0.0101	0.0559	0.0503	0.0734
UCDX4_1500_1200_30_1.1	Cow	1200	0.013	0.011	0.0249	0.045	0.05	0.183	0.162	0.247
UCDX4_1500_1200_30_1.2		1200	0	0.011	0.209	0.047	0.04	0.162	0.142	0.211
UCDX4_1501_1200_30_1.1	Cow	1200	0.0063	0.061	0.046	0.0268	0.0152	0.0455	0.0424	0.0604
UCDX4_1501_1200_30_1.2		1200	0.0078	0.077	0.053	0.0306	0.0193	0.0499	0.0455	0.0641
UCDX4_H1_1200_30_1.1	Horse	1200	0.0108	0.0109	0.0384	0.0222	0.0228	0.0383	0.0359	0.0502
UCDX4_H1_1200_30_1.2		1200	0.011	0.011	0.0549	0.0286	0.0233	0.0502	0.0454	0.067
UCDX4_H2_1200_30_1.1	Horse	1200	0.015	0.016	0.157	0.048	0.057	0.116	0.108	0.173
UCDX4_H2_1200_30_1.2		1200	0.016	0.017	0.158	0.048	0.045	0.121	0.112	0.176

Table 2: Calculated experimental modern sample values of FTIR C/P, IRSF, and bioapatite crystal size average as measured from XRD.

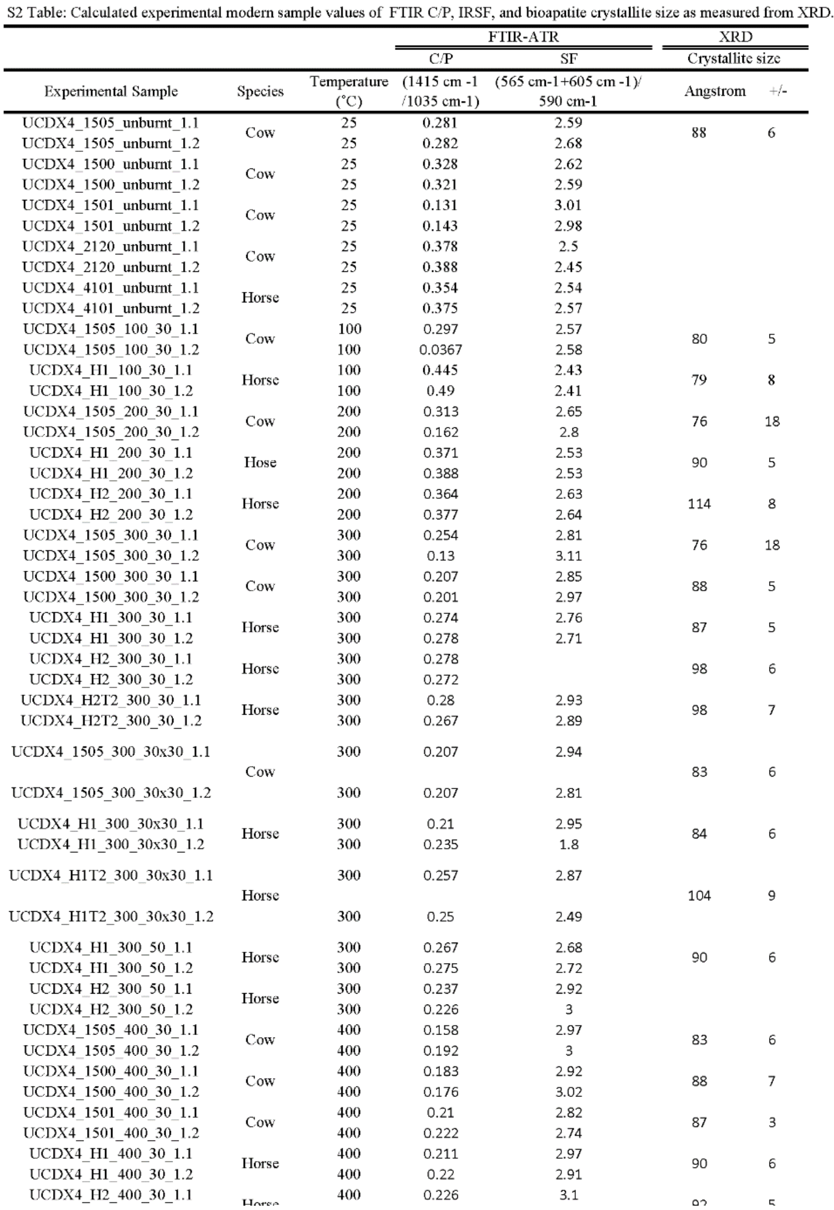

S2 Table: Calculated experimental modern sample values of FTIR C/P, IRSF, and bioapatite crystallite size as measured from XRD.

			FTIR-ATR		XRD	
			C/P	SF	Crystallite size	
Experimental Sample	Species	Temperature (°C)	(1415 cm -1 /1035 cm-1)	(565 cm-1+605 cm -1)/ 590 cm-1	Angstrom	+/-
UCDX4_1505_unburnt_1.1	Cow	25	0.281	2.59	88	6
UCDX4_1505_unburnt_1.2		25	0.282	2.68		
UCDX4_1500_unburnt_1.1	Cow	25	0.328	2.62		
UCDX4_1500_unburnt_1.2		25	0.321	2.59		
UCDX4_1501_unburnt_1.1	Cow	25	0.131	3.01		
UCDX4_1501_unburnt_1.2		25	0.143	2.98		
UCDX4_2120_unburnt_1.1	Cow	25	0.378	2.5		
UCDX4_2120_unburnt_1.2		25	0.388	2.45		
UCDX4_4101_unburnt_1.1	Horse	25	0.354	2.54		
UCDX4_4101_unburnt_1.2		25	0.375	2.57		
UCDX4_1505_100_30_1.1	Cow	100	0.297	2.57	80	5
UCDX4_1505_100_30_1.2		100	0.0367	2.58		
UCDX4_H1_100_30_1.1	Horse	100	0.445	2.43	79	8
UCDX4_H1_100_30_1.2		100	0.49	2.41		
UCDX4_1505_200_30_1.1	Cow	200	0.313	2.65	76	18
UCDX4_1505_200_30_1.2		200	0.162	2.8		
UCDX4_H1_200_30_1.1	Hose	200	0.371	2.53	90	5
UCDX4_H1_200_30_1.2		200	0.388	2.53		
UCDX4_H2_200_30_1.1	Horse	200	0.364	2.63	114	8
UCDX4_H2_200_30_1.2		200	0.377	2.64		
UCDX4_1505_300_30_1.1	Cow	300	0.254	2.81	76	18
UCDX4_1505_300_30_1.2		300	0.13	3.11		
UCDX4_1500_300_30_1.1	Cow	300	0.207	2.85	88	5
UCDX4_1500_300_30_1.2		300	0.201	2.97		
UCDX4_H1_300_30_1.1	Horse	300	0.274	2.76	87	5
UCDX4_H1_300_30_1.2		300	0.278	2.71		
UCDX4_H2_300_30_1.1	Horse	300	0.278		98	6
UCDX4_H2_300_30_1.2		300	0.272			
UCDX4_H2T2_300_30_1.1	Horse	300	0.28	2.93	98	7
UCDX4_H2T2_300_30_1.2		300	0.267	2.89		
UCDX4_1505_300_30x30_1.1	Cow	300	0.207	2.94	83	6
UCDX4_1505_300_30x30_1.2		300	0.207	2.81		
UCDX4_H1_300_30x30_1.1	Horse	300	0.21	2.95	84	6
UCDX4_H1_300_30x30_1.2		300	0.235	1.8		
UCDX4_H1T2_300_30x30_1.1	Horse	300	0.257	2.87	104	9
UCDX4_H1T2_300_30x30_1.2		300	0.25	2.49		
UCDX4_H1_300_50_1.1	Horse	300	0.267	2.68	90	6
UCDX4_H1_300_50_1.2		300	0.275	2.72		
UCDX4_H2_300_50_1.1	Horse	300	0.237	2.92		
UCDX4_H2_300_50_1.2		300	0.226	3		
UCDX4_1505_400_30_1.1	Cow	400	0.158	2.97	83	6
UCDX4_1505_400_30_1.2		400	0.192	3		
UCDX4_1500_400_30_1.1	Cow	400	0.183	2.92	88	7
UCDX4_1500_400_30_1.2		400	0.176	3.02		
UCDX4_1501_400_30_1.1	Cow	400	0.21	2.82	87	3
UCDX4_1501_400_30_1.2		400	0.222	2.74		
UCDX4_H1_400_30_1.1	Horse	400	0.211	2.97	90	6
UCDX4_H1_400_30_1.2		400	0.22	2.91		
UCDX4_H2_400_30_1.1		400	0.226	3.1		

UCDX4_H2_400_30_1.2	Horse	400	0.228	1.23	92	[illegible]
UCDX4_1505_500_30_1.1	Cow	500	0.158	3.14	90	6
UCDX4_1505_500_30_1.2		500	0.157	3.06		
UCDX4_1500_500_30_1.1	Cow	500	0.171	3.08	94	7
UCDX4_1500_500_30_1.2		500	0.174	3.07		
UCDX4_H1_500_30_1.1	Horse	500	0.257	2.93	105	7
UCDX4_H1_500_30_1.2		500	0.259	2.87		
UCDX4_H2_500_30_1.1	Horse	500	0.203	3.02	85	4
UCDX4_H2_500_30_1.2		500	0.215	3.02		
UCDX4_1505_600_30_1.1	Cow	600	0.058	3.54	99	6
UCDX4_1505_600_30_1.2		600	0.157	3.45		
UCDX4_1500_600_30_1.1	Cow	600	0.113	3.47	109	4
UCDX4_1500_600_30_1.2		600	0.113	3.59		
UCDX4_1501_600_30_1.1	Cow	600	0.144	3.2	107	7
UCDX4_1501_600_30_1.2		600	0.139	3.25		
UCDX4_H1_600_30_1.1	Horse	600	0.229	3.13	109	7
UCDX4_H1_600_30_1.2		600	0.231	3.18		
UCDX4_H2_600_30_1.1	Horse	600	0.165	3.46	99	13
UCDX4_H2_600_30_1.2		600	0.186	3.36		
UCDX4_H4_600_30_1.1	Horse	600	0.174	3.44	92	6
UCDX4_H4_600_30_1.2		600	0.197	3.26		
UCDX4_1505_700_30_1.1	Cow	700	0.051	3.59	256	15
UCDX4_1505_700_30_1.2		700	0.08	3.68		
UCDX4_1500_700_30_1.1	Cow	700	0.081	3.77	177	40
UCDX4_1500_700_30_1.2		700	0.085	3.66		
UCDX4_1501_700_30_1.1	Cow	700	0.079	3.42	376	18
UCDX4_1501_700_30_1.2		700	0.078	3.38		
UCDX4_H1_700_30_1.1	Horse	700	0.108	4.19	389	8
UCDX4_H1T1_700_30_1.1	Horse	700	0.104	4.17	462	12
UCDX4_H1T1_700_30_1.2		700	0.125	4.11		
UCDX4_H2_700_30_1.1	Horse	700	0.141	3.68	289	17
UCDX4_H2_700_30_1.2		700	0.171	3.52		
UCDX4_1505_700_30x30_1.1	Cow	700	0.065	3.87	272	21
UCDX4_1505_700_30x30_1.2		700	0.079	3.75		
UCDX4_1501_700_30x30_1.1	Cow	700	0.068	4.1		
UCDX4_1501_700_30x30_1.2		700	0.079	4.01		
UCDX4_H0_700_30x30_1.1	Horse	700	0.11	4.29	653	15
UCDX4_H0_700_30x30_1.2		700	0.114	4.03		
UCDX4_H1_700_30x30_1.1	Horse	700	0.105	4.22	564	13
UCDX4_H1_700_30x30_1.2		700	0.126	3.94		
UCDX4_H2_700_30x30_1.1	Horse	700	0.108	3.82	583	19
UCDX4_H2_700_30x30_1.2		700	0.109	4		
UCDX4_H3_700_30x30_1.1	Horse	700	0.093	2.88	583	17
UCDX4_H3_700_30x30_1.2		700	0.108	2.62		
UCDX4_H1_700_50_1.1	Horse	700	0.11	4.06	350	70
UCDX4_H1_700_50_1.2		700	0.136	3.85		
UCDX4_1505_800_30_1.1	Cow	800	0.063	3.57	561	37
UCDX4_1505_800_30_1.2		800	0.063	3.57		
UCDX4_1501_800_30_1.1	Cow	800	0.082	3.7	551	47
UCDX4_1501_800_30_1.2		800	0.081	3.83		
UCDX4_H1_800_30_1.1	Horse	800	0.093	4.17	641	21
UCDX4_H1_800_30_1.2		800	0.097	3.92		
UCDX4_1505_900_30_1.1	Cow	900	0.023	4.05	868	57
UCDX4_1505_900_30_1.2		900	0.028	3.97		

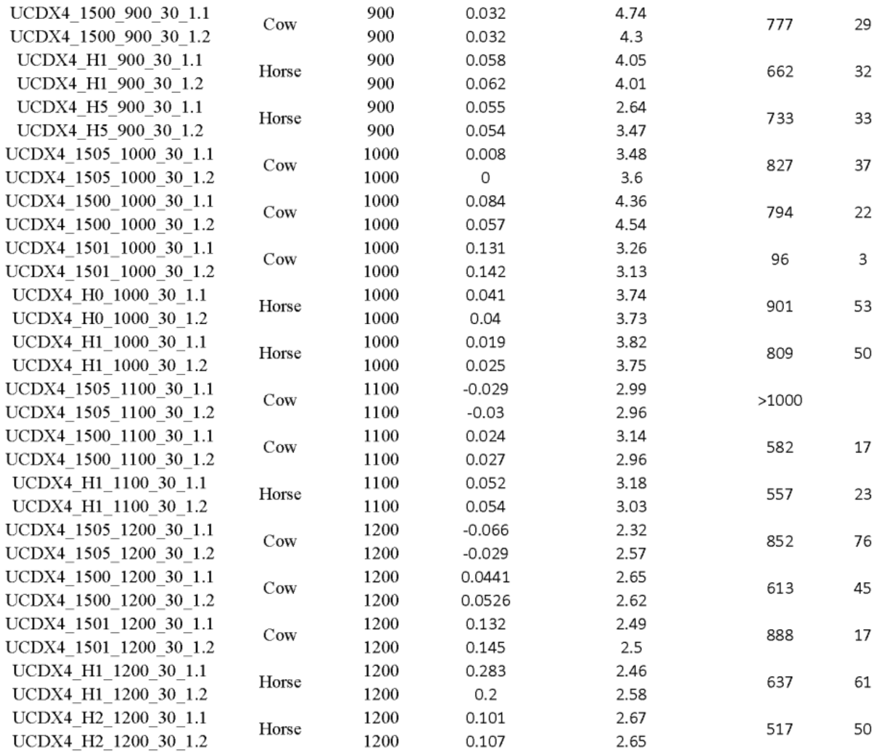

UCDX4_1500_900_30_1.1	Cow	900	0.032	4.74	777	29
UCDX4_1500_900_30_1.2		900	0.032	4.3		
UCDX4_H1_900_30_1.1	Horse	900	0.058	4.05	662	32
UCDX4_H1_900_30_1.2		900	0.062	4.01		
UCDX4_H5_900_30_1.1	Horse	900	0.055	2.64	733	33
UCDX4_H5_900_30_1.2		900	0.054	3.47		
UCDX4_1505_1000_30_1.1	Cow	1000	0.008	3.48	827	37
UCDX4_1505_1000_30_1.2		1000	0	3.6		
UCDX4_1500_1000_30_1.1	Cow	1000	0.084	4.36	794	22
UCDX4_1500_1000_30_1.2		1000	0.057	4.54		
UCDX4_1501_1000_30_1.1	Cow	1000	0.131	3.26	96	3
UCDX4_1501_1000_30_1.2		1000	0.142	3.13		
UCDX4_H0_1000_30_1.1	Horse	1000	0.041	3.74	901	53
UCDX4_H0_1000_30_1.2		1000	0.04	3.73		
UCDX4_H1_1000_30_1.1	Horse	1000	0.019	3.82	809	50
UCDX4_H1_1000_30_1.2		1000	0.025	3.75		
UCDX4_1505_1100_30_1.1	Cow	1100	-0.029	2.99	>1000	
UCDX4_1505_1100_30_1.2		1100	-0.03	2.96		
UCDX4_1500_1100_30_1.1	Cow	1100	0.024	3.14	582	17
UCDX4_1500_1100_30_1.2		1100	0.027	2.96		
UCDX4_H1_1100_30_1.1	Horse	1100	0.052	3.18	557	23
UCDX4_H1_1100_30_1.2		1100	0.054	3.03		
UCDX4_1505_1200_30_1.1	Cow	1200	-0.066	2.32	852	76
UCDX4_1505_1200_30_1.2		1200	-0.029	2.57		
UCDX4_1500_1200_30_1.1	Cow	1200	0.0441	2.65	613	45
UCDX4_1500_1200_30_1.2		1200	0.0526	2.62		
UCDX4_1501_1200_30_1.1	Cow	1200	0.132	2.49	888	17
UCDX4_1501_1200_30_1.2		1200	0.145	2.5		
UCDX4_H1_1200_30_1.1	Horse	1200	0.283	2.46	637	61
UCDX4_H1_1200_30_1.2		1200	0.2	2.58		
UCDX4_H2_1200_30_1.1	Horse	1200	0.101	2.67	517	50
UCDX4_H2_1200_30_1.2		1200	0.107	2.65		

Table 3: FTIR-ATR Unit 3 archaeological sample relevant peak height values.

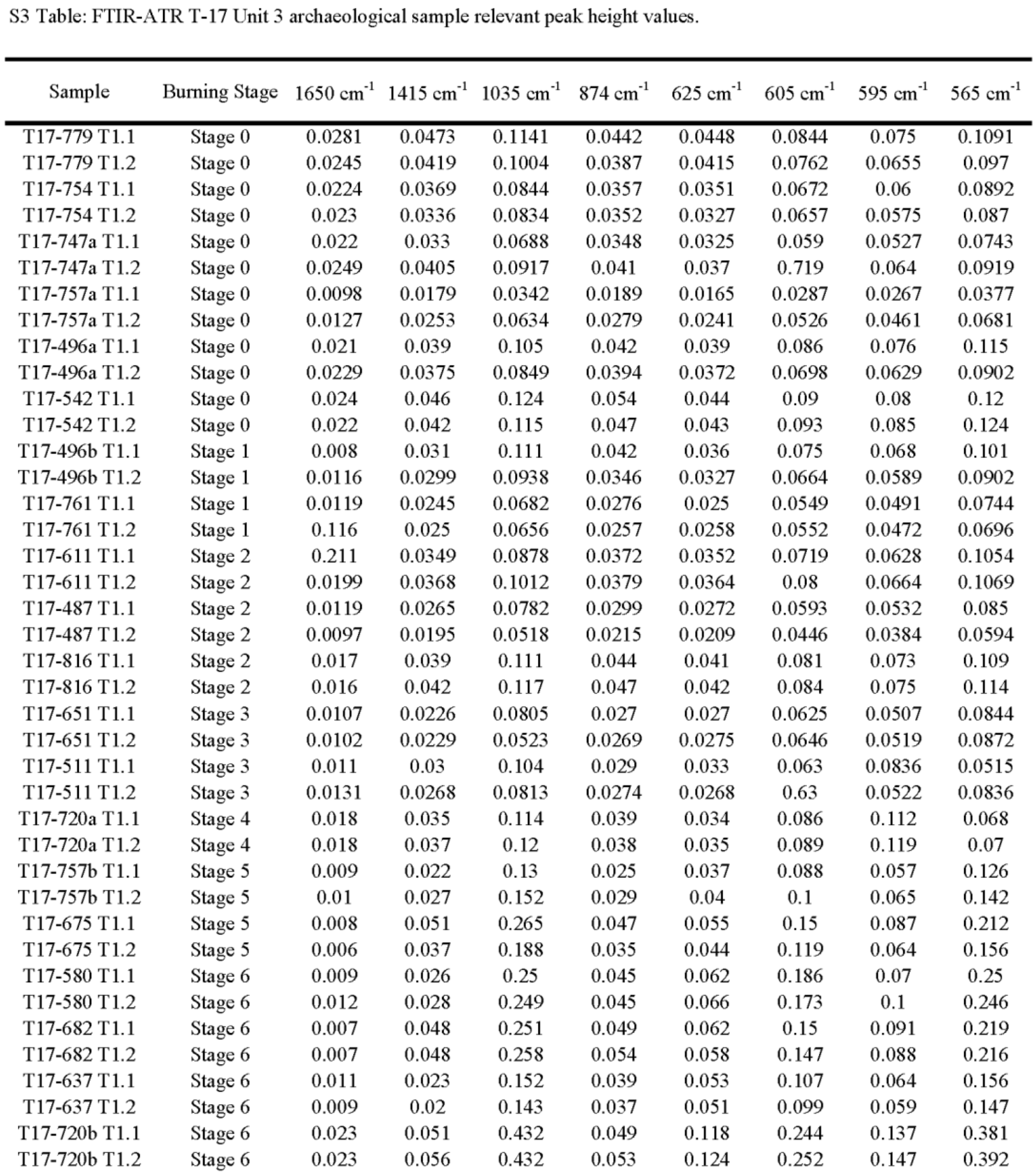

S3 Table: FTIR-ATR T-17 Unit 3 archaeological sample relevant peak height values.

Sample	Burning Stage	1650 cm^{-1}	1415 cm^{-1}	1035 cm^{-1}	874 cm^{-1}	625 cm^{-1}	605 cm^{-1}	595 cm^{-1}	565 cm^{-1}
T17-779 T1.1	Stage 0	0.0281	0.0473	0.1141	0.0442	0.0448	0.0844	0.075	0.1091
T17-779 T1.2	Stage 0	0.0245	0.0419	0.1004	0.0387	0.0415	0.0762	0.0655	0.097
T17-754 T1.1	Stage 0	0.0224	0.0369	0.0844	0.0357	0.0351	0.0672	0.06	0.0892
T17-754 T1.2	Stage 0	0.023	0.0336	0.0834	0.0352	0.0327	0.0657	0.0575	0.087
T17-747a T1.1	Stage 0	0.022	0.033	0.0688	0.0348	0.0325	0.059	0.0527	0.0743
T17-747a T1.2	Stage 0	0.0249	0.0405	0.0917	0.041	0.037	0.719	0.064	0.0919
T17-757a T1.1	Stage 0	0.0098	0.0179	0.0342	0.0189	0.0165	0.0287	0.0267	0.0377
T17-757a T1.2	Stage 0	0.0127	0.0253	0.0634	0.0279	0.0241	0.0526	0.0461	0.0681
T17-496a T1.1	Stage 0	0.021	0.039	0.105	0.042	0.039	0.086	0.076	0.115
T17-496a T1.2	Stage 0	0.0229	0.0375	0.0849	0.0394	0.0372	0.0698	0.0629	0.0902
T17-542 T1.1	Stage 0	0.024	0.046	0.124	0.054	0.044	0.09	0.08	0.12
T17-542 T1.2	Stage 0	0.022	0.042	0.115	0.047	0.043	0.093	0.085	0.124
T17-496b T1.1	Stage 1	0.008	0.031	0.111	0.042	0.036	0.075	0.068	0.101
T17-496b T1.2	Stage 1	0.0116	0.0299	0.0938	0.0346	0.0327	0.0664	0.0589	0.0902
T17-761 T1.1	Stage 1	0.0119	0.0245	0.0682	0.0276	0.025	0.0549	0.0491	0.0744
T17-761 T1.2	Stage 1	0.116	0.025	0.0656	0.0257	0.0258	0.0552	0.0472	0.0696
T17-611 T1.1	Stage 2	0.211	0.0349	0.0878	0.0372	0.0352	0.0719	0.0628	0.1054
T17-611 T1.2	Stage 2	0.0199	0.0368	0.1012	0.0379	0.0364	0.08	0.0664	0.1069
T17-487 T1.1	Stage 2	0.0119	0.0265	0.0782	0.0299	0.0272	0.0593	0.0532	0.085
T17-487 T1.2	Stage 2	0.0097	0.0195	0.0518	0.0215	0.0209	0.0446	0.0384	0.0594
T17-816 T1.1	Stage 2	0.017	0.039	0.111	0.044	0.041	0.081	0.073	0.109
T17-816 T1.2	Stage 2	0.016	0.042	0.117	0.047	0.042	0.084	0.075	0.114
T17-651 T1.1	Stage 3	0.0107	0.0226	0.0805	0.027	0.027	0.0625	0.0507	0.0844
T17-651 T1.2	Stage 3	0.0102	0.0229	0.0523	0.0269	0.0275	0.0646	0.0519	0.0872
T17-511 T1.1	Stage 3	0.011	0.03	0.104	0.029	0.033	0.063	0.0836	0.0515
T17-511 T1.2	Stage 3	0.0131	0.0268	0.0813	0.0274	0.0268	0.63	0.0522	0.0836
T17-720a T1.1	Stage 4	0.018	0.035	0.114	0.039	0.034	0.086	0.112	0.068
T17-720a T1.2	Stage 4	0.018	0.037	0.12	0.038	0.035	0.089	0.119	0.07
T17-757b T1.1	Stage 5	0.009	0.022	0.13	0.025	0.037	0.088	0.057	0.126
T17-757b T1.2	Stage 5	0.01	0.027	0.152	0.029	0.04	0.1	0.065	0.142
T17-675 T1.1	Stage 5	0.008	0.051	0.265	0.047	0.055	0.15	0.087	0.212
T17-675 T1.2	Stage 5	0.006	0.037	0.188	0.035	0.044	0.119	0.064	0.156
T17-580 T1.1	Stage 6	0.009	0.026	0.25	0.045	0.062	0.186	0.07	0.25
T17-580 T1.2	Stage 6	0.012	0.028	0.249	0.045	0.066	0.173	0.1	0.246
T17-682 T1.1	Stage 6	0.007	0.048	0.251	0.049	0.062	0.15	0.091	0.219
T17-682 T1.2	Stage 6	0.007	0.048	0.258	0.054	0.058	0.147	0.088	0.216
T17-637 T1.1	Stage 6	0.011	0.023	0.152	0.039	0.053	0.107	0.064	0.156
T17-637 T1.2	Stage 6	0.009	0.02	0.143	0.037	0.051	0.099	0.059	0.147
T17-720b T1.1	Stage 6	0.023	0.051	0.432	0.049	0.118	0.244	0.137	0.381
T17-720b T1.2	Stage 6	0.023	0.056	0.432	0.053	0.124	0.252	0.147	0.392

Table 4: Calculated archaeological T-17 Unit 3 C/P and IRSF values, and bioapatite crystal size average as measured from XRD.

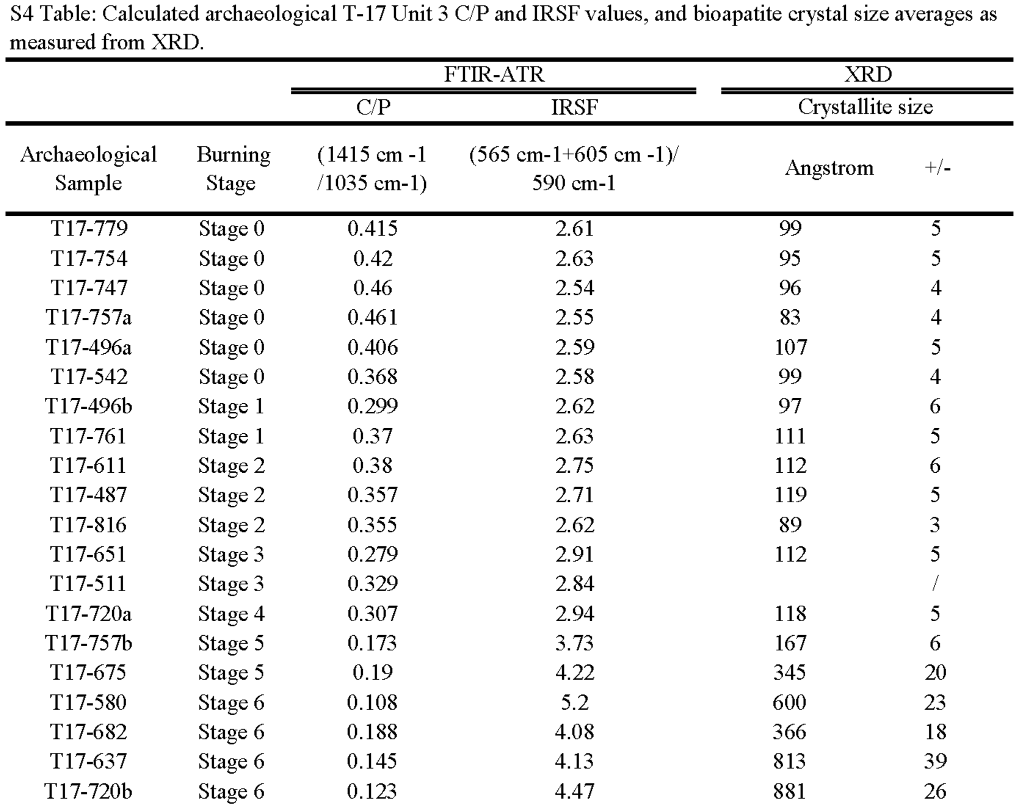

S4 Table: Calculated archaeological T-17 Unit 3 C/P and IRSF values, and bioapatite crystal size averages as measured from XRD.

		FTIR-ATR		XRD	
		C/P	IRSF	Crystallite size	
Archaeological Sample	Burning Stage	(1415 cm -1 /1035 cm-1)	(565 cm-1+605 cm -1)/ 590 cm-1	Angstrom	+/-
T17-779	Stage 0	0.415	2.61	99	5
T17-754	Stage 0	0.42	2.63	95	5
T17-747	Stage 0	0.46	2.54	96	4
T17-757a	Stage 0	0.461	2.55	83	4
T17-496a	Stage 0	0.406	2.59	107	5
T17-542	Stage 0	0.368	2.58	99	4
T17-496b	Stage 1	0.299	2.62	97	6
T17-761	Stage 1	0.37	2.63	111	5
T17-611	Stage 2	0.38	2.75	112	6
T17-487	Stage 2	0.357	2.71	119	5
T17-816	Stage 2	0.355	2.62	89	3
T17-651	Stage 3	0.279	2.91	112	5
T17-511	Stage 3	0.329	2.84		/
T17-720a	Stage 4	0.307	2.94	118	5
T17-757b	Stage 5	0.173	3.73	167	6
T17-675	Stage 5	0.19	4.22	345	20
T17-580	Stage 6	0.108	5.2	600	23
T17-682	Stage 6	0.188	4.08	366	18
T17-637	Stage 6	0.145	4.13	813	39
T17-720b	Stage 6	0.123	4.47	881	26

SE microscopy imaging instrument and magnification details:

Secondary electron (SE) images were acquired for two samples of archaeological bone and three samples of modern bone annealed at different temperatures (300˚, 700˚, and 1200˚C) in a Quattro environmental scanning electron microscope (eSEM), manufactured by ThermoFischer Scientific. The SE images were obtained at an accelerating voltage of either 10kV or 20kV and with an electron beam width, or size spot, of 3.0. Spot 3 is commonly used to attain sufficient signal without compromising resolution. To prevent the buildup of charge on sample surfaces, the SE images were acquired in low vacuum mode with partial pressure of water set at 400 Pa. A low vacuum detector (LVD), which is optimized for this pressure range, was used to measure the SE image signal.

Appendix B: Supplemental Materials for Chapter 3

Table 1: Element, bone label ID, and relevant trials

Bovid Element	Bone Label	Trial utilized
Humerus	A	T1
Femur	B	T1
Humerus	C	T1
Femur	D	T2A, T2B, T3A
Radius	E	T2A, T2B, T3A
Radius	F	T2A, T2B, T3A
Femur	G	T3B, T4, T5
Femur	H	T3B, T4, T5
Femur	I	T3B, T4, T5
Radius	J	T7, T8
Femur	K	T7, T8
Humerus	L	T7, T8

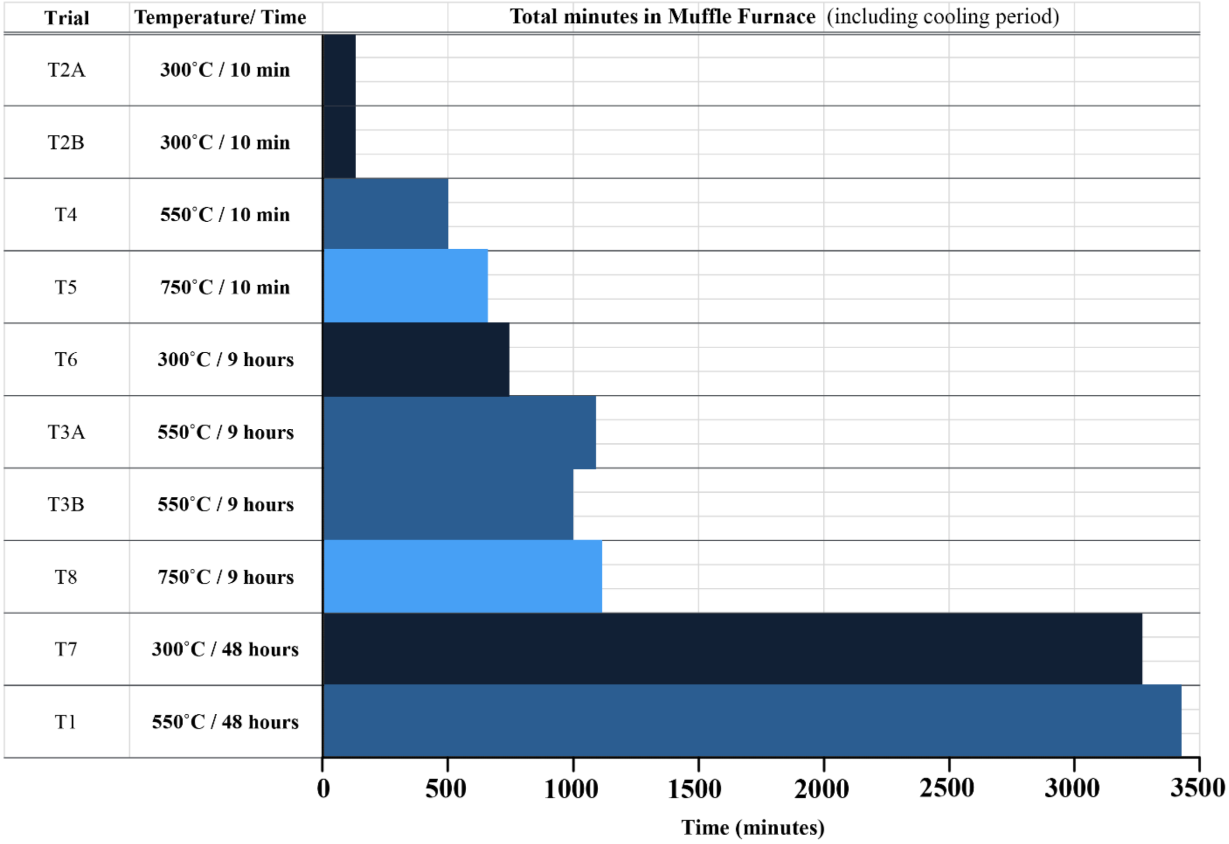

Fig 1: Total time (minutes) for each trial, including the cooling periods inside the muffle furnace.

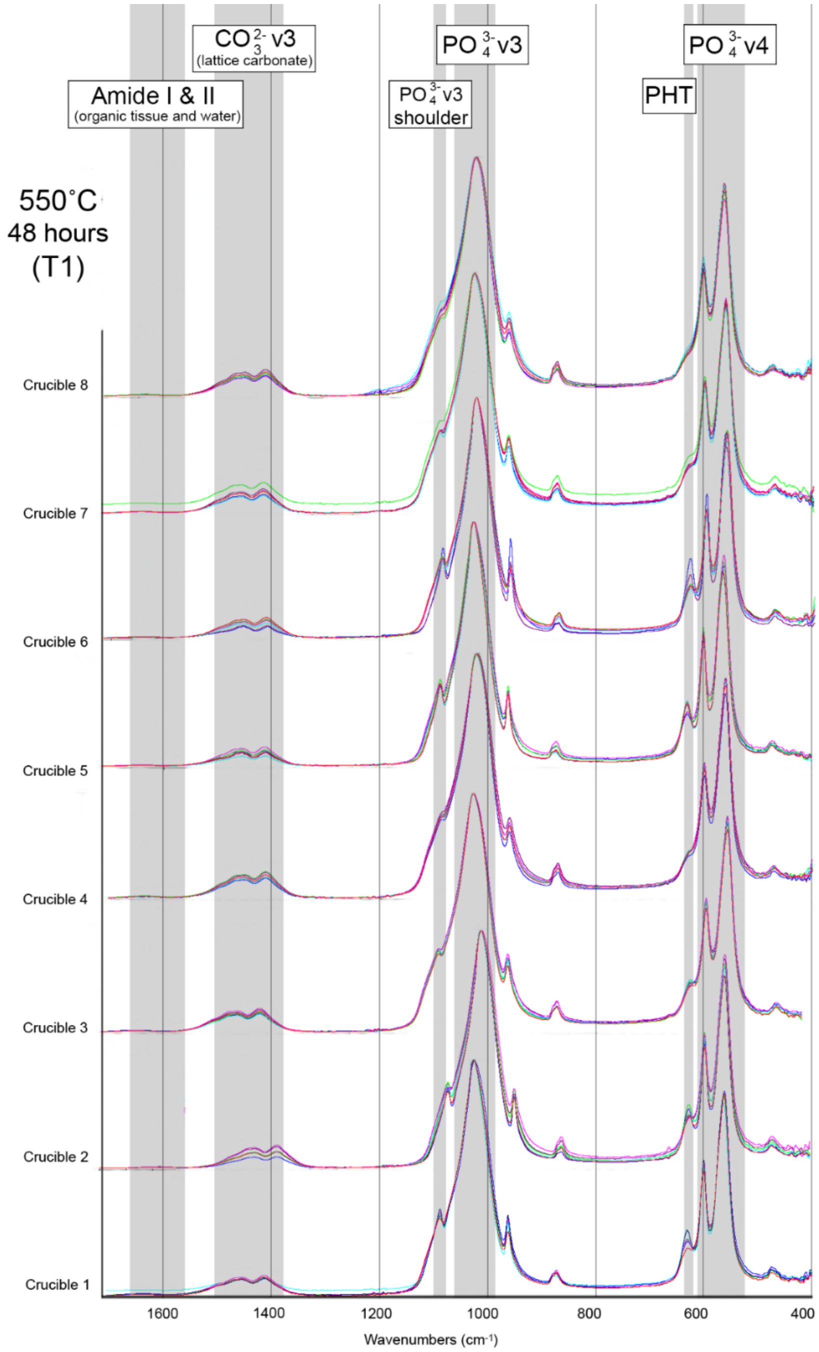

Fig 2. 550°C 48 hour (T1) experiment organized by crucible. Heat induced alterations to the structure and chemistry seen most pronounced in crucibles at back of furnace (crucibles 1,2,5 and 6). Nearly all bone burnt at 300° and 550°C do not have elevated SF and PHT ratios of true calcined bone but heat signatures are represented in full in the 750°C samples (Fig. 4-6; Table 7). The only exceptions to this pattern are samples at both depths of crucibles 1, 2, 5, and 6 from the 550°C 48 hour trial (T1). These samples demonstrate moderately elevated SF and PHT ratios nearing those of the 750°C trials, alongside the 1090cm^{-1} peak shoulder.

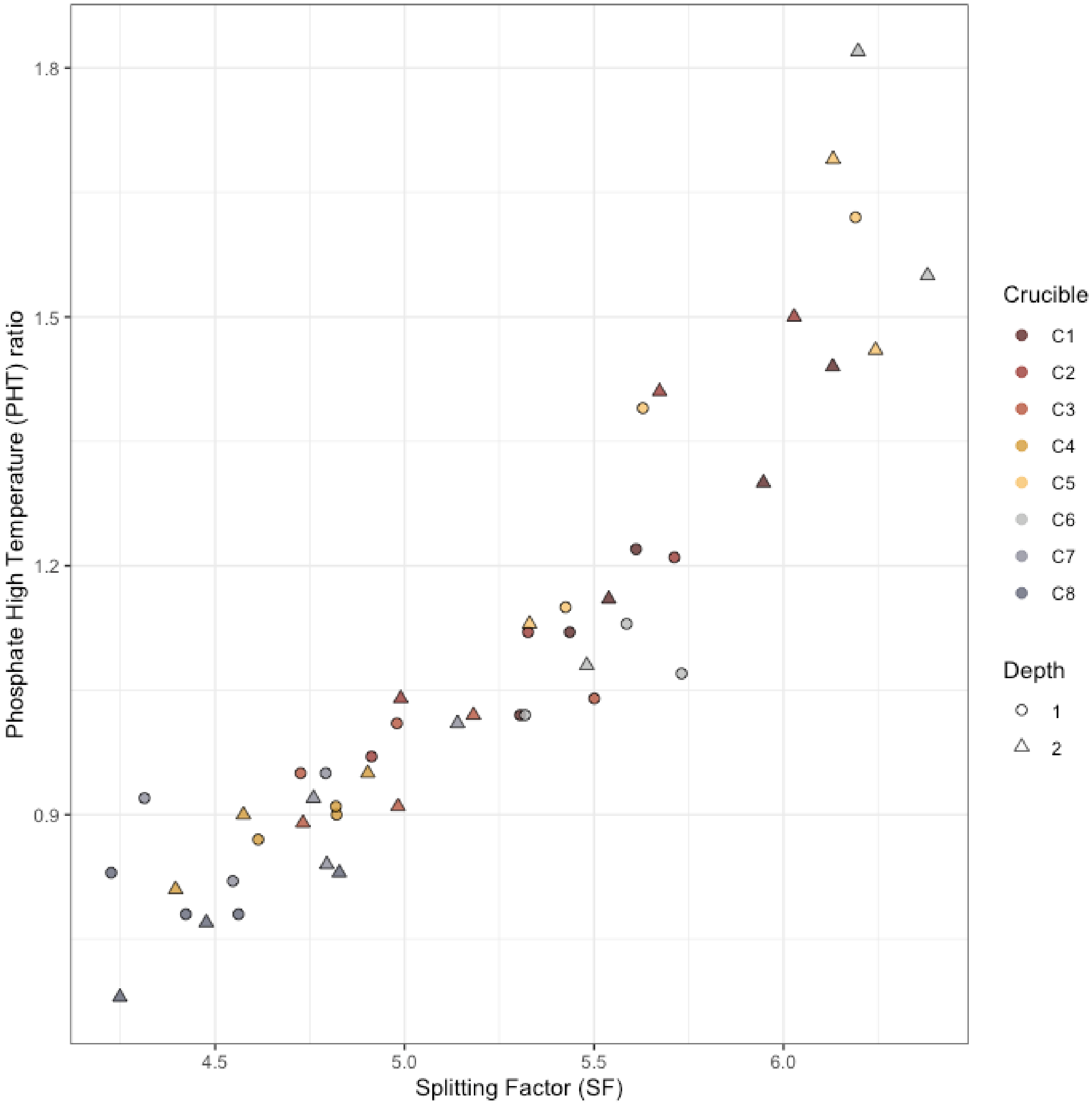

Fig 3. PHT and SF ratio for 550°C 48 hour trial (T1) organized by crucible. Greatest measures of heat alteration noted in crucibles in back of muffle furnace (crucibles 1,2,5 and 6).

Table 2: FTIR data

ID	Trial	Order	G/Mix	Crucible	Depth	Bone	Temperatu	Time	SF	CP	PHT	1650	1035	CO/P
UCDX13_T1_G_C1_0_BONEA	T1	10	G	C1	1	A	550	2880	5.436	0.054	1.12	0.002	0.425	0.004706
UCDX13_T1_G_C1_0_BONEB	T1	10	G	C1	1	B	550	2880	5.305	0.061	1.02	0.009	0.431	0.020882
UCDX13_T1_G_C1_0_BONEC	T1	10	G	C1	1	C	550	2880	5.611	0.053	1.22	-0.001	0.46	-0.002174
UCDX13_T1_G_C1_-2_BONEA	T1	10	G	C1	2	A	550	2880	6.13	0.038	1.44	0.008	0.586	0.013652
UCDX13_T1_G_C1_-2_BONEB	T1	10	G	C1	2	B	550	2880	5.539	0.065	1.16	-0.002	0.434	-0.004608
UCDX13_T1_G_C1_-2_BONEC	T1	10	G	C1	2	C	550	2880	5.947	0.051	1.3	0.007	0.471	0.014862
UCDX13_T1_G_C2_0_BONEA	T1	10	G	C2	1	A	550	2880	5.326	0.049	1.12	-0.01	0.451	-0.022173
UCDX13_T1_G_C2_0_BONEB	T1	10	G	C2	1	B	550	2880	4.913	0.071	0.97	-0.04	0.368	-0.108696
UCDX13_T1_G_C2_0_BONEC	T1	10	G	C2	1	C	550	2880	5.712	0.054	1.21	-0.04	0.591	-0.067682
UCDX13_T1_G_C2_-2_BONEA	T1	10	G	C2	2	A	550	2880	6.028	0.032	1.5	-0.014	0.6	-0.023333
UCDX13_T1_G_C2_-2_BONEB	T1	10	G	C2	2	B	550	2880	4.99	0.07	1.04	-0.04	0.375	-0.106667
UCDX13_T1_G_C2_-2_BONEC	T1	10	G	C2	2	C	550	2880	5.673	0.05	1.41	-0.015	0.446	-0.033632
UCDX13_T1_G_C3_0_BONEA	T1	10	G	C3	1	A	550	2880	4.98	0.056	1.01	-0.001	0.397	-0.002519
UCDX13_T1_G_C3_0_BONEB	T1	10	G	C3	1	B	550	2880	4.726	0.073	0.95	0	0.326	0
UCDX13_T1_G_C3_0_BONEC	T1	10	G	C3	1	C	550	2880	5.501	0.064	1.04	0.008	0.421	0.019002
UCDX13_T1_G_C3_-2_BONEA	T1	10	G	C3	2	A	550	2880	5.182	0.054	0.102	-0.001	0.371	-0.002695
UCDX13_T1_G_C3_-2_BONEB	T1	10	G	C3	2	B	550	2880	4.732	0.076	0.89	-0.001	0.357	-0.002801
UCDX13_T1_G_C3_-2_BONEC	T1	10	G	C3	2	C	550	2880	4.983	0.069	0.91	0.001	0.445	0.002247
UCDX13_T1_G_C4_0_BONEA	T1	10	G	C4	1	A	550	2880	4.821	0.065	0.9	-0.001	0.367	-0.002725
UCDX13_T1_G_C4_0_BONEB	T1	10	G	C4	1	B	550	2880	4.614	0.081	0.87	-0.001	0.34	-0.002941
UCDX13_T1_G_C4_0_BONEC	T1	10	G	C4	1	C	550	2880	4.819	0.074	0.91	0.001	0.405	0.002469
UCDX13_T1_G_C4_-2_BONEA	T1	10	G	C4	2	A	550	2880	4.903	0.064	0.95	0.005	0.445	0.011236
UCDX13_T1_G_C4_-2_BONEB	T1	10	G	C4	2	B	550	2880	4.396	0.08	0.81	0.002	0.323	0.006192
UCDX13_T1_G_C4_-2_BONEC	T1	10	G	C4	2	C	550	2880	4.575	0.084	0.9	0.01	0.361	0.027701
UCDX13_T1_MIX_C5_0_BONEA	T1	10	Mix	C5	1	A	550	2880	5.425	0.047	1.15	-0.002	0.514	-0.003891
UCDX13_T1_MIX_C5_0_BONEB	T1	10	Mix	C5	1	B	550	2880	6.19	0.043	1.62	0.002	0.713	0.002805
UCDX13_T1_MIX_C5_0_BONEC	T1	10	Mix	C5	1	C	550	2880	5.629	0.053	1.39	0.006	0.538	0.011152
UCDX13_T1_MIX_C5_-2_BONEA	T1	10	Mix	C5	2	A	550	2880	6.131	0.029	1.69	0.005	0.668	0.007485
UCDX13_T1_MIX_C5_-2_BONEB	T1	10	Mix	C5	2	B	550	2880	5.33	0.058	1.13	-0.001	0.413	-0.002421
UCDX13_T1_MIX_C5_-2_BONEC	T1	10	Mix	C5	2	C	550	2880	6.243	0.046	1.46	0.007	0.658	0.010638
UCDX13_T1_MIX_C6_0_BONEA	T1	10	Mix	C6	1	A	550	2880	5.731	0.045	1.07	-0.003	0.508	-0.005906
UCDX13_T1_MIX_C6_0_BONEB	T1	10	Mix	C6	1	B	550	2880	5.586	0.056	1.13	-0.004	0.491	-0.008147
UCDX13_T1_MIX_C6_0_BONEC	T1	10	Mix	C6	1	C	550	2880	5.318	0.066	1.02	-0.003	0.437	-0.006865
UCDX13_T1_MIX_C6_-2_BONEA	T1	10	Mix	C6	2	A	550	2880	6.197	0.033	1.82	-0.008	0.593	-0.013491
UCDX13_T1_MIX_C6_-2_BONEB	T1	10	Mix	C6	2	B	550	2880	6.38	0.041	1.55	-0.003	0.689	-0.004354
UCDX13_T1_MIX_C6_-2_BONEC	T1	10	Mix	C6	2	C	550	2880	5.481	0.056	1.08	0.002	0.395	0.005063
UCDX13_T1_MIX_C7_0_BONEA	T1	10	Mix	C7	1	A	550	2880	4.792	0.059	0.95	0.007	0.369	0.01897
UCDX13_T1_MIX_C7_0_BONEB	T1	10	Mix	C7	1	B	550	2880	4.547	0.08	0.82	-0.002	0.393	-0.005089
UCDX13_T1_MIX_C7_0_BONEC	T1	10	Mix	C7	1	C	550	2880	4.314	0.074	0.92	-0.002	0.326	-0.006135
UCDX13_T1_MIX_C7_-2_BONEA	T1	10	Mix	C7	2	A	550	2880	5.14	0.054	1.01	-0.01	0.418	-0.023923
UCDX13_T1_MIX_C7_-2_BONEB	T1	10	Mix	C7	2	B	550	2880	4.795	0.071	0.84	0	0.328	0
UCDX13_T1_MIX_C7_-2_BONEC	T1	10	Mix	C7	2	C	550	2880	4.76	0.068	0.92	0.004	0.356	0.011236
UCDX13_T1_MIX_C8_0_BONEA	T1	10	Mix	C8	1	A	550	2880	4.226	0.057	0.83	-0.003	0.322	-0.009317
UCDX13_T1_MIX_C8_0_BONEB	T1	10	Mix	C8	1	B	550	2880	4.423	0.065	0.78	0.005	0.441	0.011338
UCDX13_T1_MIX_C8_0_BONEC	T1	10	Mix	C8	1	C	550	2880	4.562	0.08	0.78	-0.005	0.405	-0.012346
UCDX13_T1_MIX_C8_-2_BONEA	T1	10	Mix	C8	2	A	550	2880	4.828	0.066	0.83	-0.002	0.423	-0.004728
UCDX13_T1_MIX_C8_-2_BONEB	T1	10	Mix	C8	2	B	550	2880	4.477	0.087	0.77	0.007	0.358	0.019553
UCDX13_T1_MIX_C8_-2_BONEC	T1	10	Mix	C8	2	C	550	2880	4.249	0.075	0.68	-0.003	0.323	-0.009288
UCDX13_T2A_G_C1_0_BONED	T2A	1	G	C1	1	D	300	10	3.413	0.149	N/A	0.023	0.224	0.102679

UCDX13_T2A_G_C1_0_BONEE	T2A	1	G	C1	1	E	300	10	3.41	0.169	N/A	0.023	0.217	0.105991
UCDX13_T2A_G_C1_0_BONEF	T2A	1	G	C1	1	F	300	10	3.429	0.16	N/A	0.024	0.24	0.1
UCDX13_T2A_G_C1_-2_BONED	T2A	1	G	C1	2	D	300	10	3.429	0.14	N/A	0.025	0.23	0.108696
UCDX13_T2A_G_C1_-2_BONEE	T2A	1	G	C1	2	E	300	10	3.267	0.21	N/A	0.028	0.224	0.125
UCDX13_T2A_G_C1_-2_BONEF	T2A	1	G	C1	2	F	300	10	3.367	0.172	N/A	0.031	0.209	0.148325
UCDX13_T2A_G_C2_0_BONED	T2A	1	G	C2	1	D	300	10	3.502	0.148	N/A	0.022	0.119	0.184874
UCDX13_T2A_G_C2_0_BONEE	T2A	1	G	C2	1	E	300	10	3.521	0.184	N/A	0.024	0.124	0.193548
UCDX13_T2A_G_C2_0_BONEF	T2A	1	G	C2	1	F	300	10	3.387	0.175	N/A	0.023	0.198	0.116162
UCDX13_T2A_G_C2_-2_BONED	T2A	1	G	C2	2	D	300	10	3.436	0.16	N/A	0.018	0.169	0.106509
UCDX13_T2A_G_C2_-2_BONEE	T2A	1	G	C2	2	E	300	10	3.458	0.188	N/A	0.022	0.109	0.201835
UCDX13_T2A_G_C2_-2_BONEF	T2A	1	G	C2	2	F	300	10	3.428	0.186	N/A	0.023	0.184	0.125
UCDX13_T2A_G_C3_0_BONED	T2A	1	G	C3	1	D	300	10	3.441	0.165	N/A	0.023	0.164	0.140244
UCDX13_T2A_G_C3_0_BONEE	T2A	1	G	C3	1	E	300	10	3.315	0.197	N/A	0.024	0.167	0.143713
UCDX13_T2A_G_C3_0_BONEF	T2A	1	G	C3	1	F	300	10	3.374	0.173	N/A	0.034	0.194	0.175258
UCDX13_T2A_G_C3_-2_BONED	T2A	1	G	C3	2	D	300	10	3.374	0.177	N/A	0.034	0.176	0.193182
UCDX13_T2A_G_C3_-2_BONEE	T2A	1	G	C3	2	E	300	10	3.342	0.188	N/A	0.031	0.161	0.192547
UCDX13_T2A_G_C3_-2_BONEF	T2A	1	G	C3	2	F	300	10	3.291	0.191	N/A	0.024	0.167	0.143713
UCDX13_T2A_G_C4_0_BONED	T2A	1	G	C4	1	D	300	10	3.298	0.176	N/A	0.019	0.133	0.142857
UCDX13_T2A_G_C4_0_BONEE	T2A	1	G	C4	1	E	300	10	3.364	0.209	N/A	0.03	0.178	0.168539
UCDX13_T2A_G_C4_0_BONEF	T2A	1	G	C4	1	F	300	10	3.261	0.197	N/A	0.028	0.123	0.227642
UCDX13_T2A_G_C4_-2_BONED	T2A	1	G	C4	2	D	300	10	3.235	0.182	N/A	0.037	0.174	0.219697
UCDX13_T2A_G_C4_-2_BONEE	T2A	1	G	C4	2	E	300	10	3.184	0.244	N/A	0.029	0.132	0.219697
UCDX13_T2A_G_C4_-2_BONEF	T2A	1	G	C4	2	F	300	10	3.281	0.2	N/A	0.034	0.142	0.239437
UCDX13_T2A_G_C5_0_BONED	T2A	1	G	C5	1	D	300	10	3.52	0.132	N/A	0.015	0.186	0.080645
UCDX13_T2A_G_C5_0_BONEE	T2A	1	G	C5	1	E	300	10	3.447	0.171	N/A	0.021	0.224	0.09375
UCDX13_T2A_G_C5_0_BONEF	T2A	1	G	C5	1	F	300	10	3.363	0.191	N/A	0.025	0.147	0.170068
UCDX13_T2A_G_C5_-2_BONED	T2A	1	G	C5	2	D	300	10	3.379	0.158	N/A	0.014	0.166	0.084337
UCDX13_T2A_G_C5_-2_BONEE	T2A	1	G	C5	2	E	300	10	3.458	0.182	N/A	0.032	0.277	0.115523
UCDX13_T2A_G_C5_-2_BONEF	T2A	1	G	C5	2	F	300	10	3.406	0.161	N/A	0.02	0.206	0.097087
UCDX13_T2B_MIX_C1_0_BONED	T2B	2	Mix	C1	1	D	300	10	3.57	0.141	N/A	0.029	0.236	0.122881
UCDX13_T2B_MIX_C1_0_BONEE	T2B	2	Mix	C1	1	E	300	10	3.574	0.164	N/A	0.035	0.295	0.118644
UCDX13_T2B_MIX_C1_0_BONEF	T2B	2	Mix	C1	1	F	300	10	3.592	0.147	N/A	0.035	0.295	0.118644
UCDX13_T2B_MIX_C1_-2_BONED	T2B	2	Mix	C1	2	D	300	10	3.449	0.164	N/A	0.016	0.158	0.101266
UCDX13_T2B_MIX_C1_-2_BONEE	T2B	2	Mix	C1	2	E	300	10	3.5	0.192	N/A	0.022	0.183	0.120219
UCDX13_T2B_MIX_C1_-2_BONEF	T2B	2	Mix	C1	2	F	300	10	3.482	0.157	N/A	0.026	0.2	0.13
UCDX13_T2B_MIX_C2_0_BONED	T2B	2	Mix	C2	1	D	300	10	3.455	0.169	N/A	0.027	0.175	0.154286
UCDX13_T2B_MIX_C2_0_BONEE	T2B	2	Mix	C2	1	E	300	10	3.547	0.187	N/A	0.036	0.229	0.157205
UCDX13_T2B_MIX_C2_0_BONEF	T2B	2	Mix	C2	1	F	300	10	3.598	0.16	N/A	0.02	0.207	0.096618
UCDX13_T2B_MIX_C2_-2_BONED	T2B	2	Mix	C2	2	D	300	10	3.575	0.159	N/A	0.019	0.18	0.105556
UCDX13_T2B_MIX_C2_-2_BONEE	T2B	2	Mix	C2	2	E	300	10	3.522	0.199	N/A	0.035	0.185	0.189189
UCDX13_T2B_MIX_C2_-2_BONEF	T2B	2	Mix	C2	2	F	300	10	3.496	0.181	N/A	0.021	0.109	0.192661
UCDX13_T2B_MIX_C3_0_BONED	T2B	2	Mix	C3	1	D	300	10	3.429	0.173	N/A	0.013	0.165	0.078788
UCDX13_T2B_MIX_C3_0_BONEE	T2B	2	Mix	C3	1	E	300	10	3.353	0.215	N/A	0.021	0.151	0.139073
UCDX13_T2B_MIX_C3_0_BONEF	T2B	2	Mix	C3	1	F	300	10	3.469	0.194	N/A	0.02	0.157	0.127389
UCDX13_T2B_MIX_C3_-2_BONED	T2B	2	Mix	C3	2	D	300	10	3.448	0.17	N/A	0.039	0.203	0.192118
UCDX13_T2B_MIX_C3_-2_BONEE	T2B	2	Mix	C3	2	E	300	10	3.345	0.218	N/A	0.031	0.152	0.203947
UCDX13_T2B_MIX_C3_-2_BONEF	T2B	2	Mix	C3	2	F	300	10	3.422	0.204	N/A	0.025	0.157	0.159236
UCDX13_T2B_MIX_C4_0_BONED	T2B	2	Mix	C4	1	D	300	10	3.563	0.181	N/A	0.03	0.148	0.202703
UCDX13_T2B_MIX_C4_0_BONEE	T2B	2	Mix	C4	1	E	300	10	3.373	0.214	N/A	0.025	0.14	0.178571
UCDX13_T2B_MIX_C4_0_BONEF	T2B	2	Mix	C4	1	F	300	10	3.408	0.213	N/A	0.012	0.121	0.099174
UCDX13_T2B_MIX_C4_-2_BONED	T2B	2	Mix	C4	2	D	300	10	3.312	0.187	N/A	0.023	0.12	0.191667

UCDX13_T2B_MIX_C4_-2_BONEE	T2B	2	Mix	C4	2	E	300	10	3.393	0.241	N/A	0.015	0.102	0.147059
UCDX13_T2B_MIX_C4_-2_BONEF	T2B	2	Mix	C4	2	F	300	10	3.313	0.206	N/A	0.028	0.141	0.198582
UCDX13_T2B_MIX_C5_0_BONED	T2B	2	Mix	C5	1	D	300	10	3.55	0.146	N/A	0.021	0.202	0.10396
UCDX13_T2B_MIX_C5_0_BONEE	T2B	2	Mix	C5	1	E	300	10	3.465	0.183	N/A	0.026	0.211	0.123223
UCDX13_T2B_MIX_C5_0_BONEF	T2B	2	Mix	C5	1	F	300	10	3.392	0.165	N/A	0.021	0.218	0.09633
UCDX13_T2B_MIX_C5_-2_BONED	T2B	2	Mix	C5	2	D	300	10	3.48	0.161	N/A	0.023	0.158	0.14557
UCDX13_T2B_MIX_C5_-2_BONEE	T2B	2	Mix	C5	2	E	300	10	3.431	0.187	N/A	0.029	0.2	0.145
UCDX13_T2B_MIX_C5_-2_BONEF	T2B	2	Mix	C5	2	F	300	10	3.497	0.17	N/A	0.031	0.247	0.125506
UCDX13_T3A_G_C1_0_BONED	T3A	6	G	C1	1	D	550	540	4.591	0.054	0.7	-0.007	0.365	-0.019178
UCDX13_T3A_G_C1_0_BONEE	T3A	6	G	C1	1	E	550	540	4.538	0.082	0.78	-0.01	0.285	-0.035088
UCDX13_T3A_G_C1_0_BONEF	T3A	6	G	C1	1	F	550	540	4.431	0.078	0.8	-0.005	0.412	-0.012136
UCDX13_T3A_G_C1_-2_BONED	T3A	6	G	C1	2	D	550	540	4.741	0.054	0.78	-0.009	0.311	-0.028939
UCDX13_T3A_G_C1_-2_BONEE	T3A	6	G	C1	2	E	550	540	4.603	0.076	0.89	-0.003	0.291	-0.010309
UCDX13_T3A_G_C1_-2_BONEF	T3A	6	G	C1	2	F	550	540	4.667	0.069	0.76	-0.009	0.331	-0.02719
UCDX13_T3A_G_C2_0_BONED	T3A	6	G	C2	1	D	550	540	4.579	0.052	0.8	0	0.3	0
UCDX13_T3A_G_C2_0_BONEE	T3A	6	G	C2	1	E	550	540	4.851	0.086	0.81	0.002	0.332	0.006024
UCDX13_T3A_G_C2_0_BONEF	T3A	6	G	C2	1	F	550	540	4.815	0.063	0.4	-0.001	0.309	-0.003236
UCDX13_T3A_G_C2_-2_BONED	T3A	6	G	C2	2	D	550	540	4.706	0.056	0.81	0.006	0.341	0.017595
UCDX13_T3A_G_C2_-2_BONEE	T3A	6	G	C2	2	E	550	540	4.891	0.083	0.73	-0.001	0.419	-0.002387
UCDX13_T3A_G_C2_-2_BONEF	T3A	6	G	C2	2	F	550	540	4.657	0.071	0.68	-0.004	0.34	-0.011765
UCDX13_T3A_G_C3_0_BONED	T3A	6	G	C3	1	D	550	540	4.581	0.052	0.77	0.006	0.322	0.018634
UCDX13_T3A_G_C3_0_BONEE	T3A	6	G	C3	1	E	550	540	4.445	0.084	0.66	-0.004	0.297	-0.013468
UCDX13_T3A_G_C3_0_BONEF	T3A	6	G	C3	1	F	550	540	4.461	0.076	0.69	0.006	0.309	0.019417
UCDX13_T3A_G_C3_-2_BONED	T3A	6	G	C3	2	D	550	540	4.429	0.056	0.68	-0.003	0.261	-0.011494
UCDX13_T3A_G_C3_-2_BONEE	T3A	6	G	C3	2	E	550	540	4.446	0.081	0.78	0	0.354	0
UCDX13_T3A_G_C3_-2_BONEF	T3A	6	G	C3	2	F	550	540	4.366	0.078	0.76	-0.001	0.337	-0.002967
UCDX13_T3A_G_C4_0_BONED	T3A	6	G	C4	1	D	550	540	4.375	0.062	0.7	-0.003	0.284	-0.010563
UCDX13_T3A_G_C4_0_BONEE	T3A	6	G	C4	1	E	550	540	4.321	0.082	0.68	-0.003	0.305	-0.009836
UCDX13_T3A_G_C4_0_BONEF	T3A	6	G	C4	1	F	550	540	4.297	0.075	0.67	-0.002	0.271	-0.00738
UCDX13_T3A_G_C4_-2_BONED	T3A	6	G	C4	2	D	550	540	4.46	0.049	0.66	-0.006	0.355	-0.016901
UCDX13_T3A_G_C4_-2_BONEE	T3A	6	G	C4	2	E	550	540	4.336	0.099	0.75	0.007	0.277	0.025271
UCDX13_T3A_G_C4_-2_BONEF	T3A	6	G	C4	2	F	550	540	4.374	0.077	0.69	0.005	0.376	0.013298
UCDX13_T3A_G_C5_0_BONED	T3A	6	G	C5	1	D	550	540	4.522	0.057	0.83	-0.007	0.233	-0.030043
UCDX13_T3A_G_C5_0_BONEE	T3A	6	G	C5	1	E	550	540	4.338	0.1	0.87	0.006	0.307	0.019544
UCDX13_T3A_G_C5_0_BONEF	T3A	6	G	C5	1	F	550	540	4.704	0.067	0.88	0.003	0.355	0.008451
UCDX13_T3A_G_C5_-2_BONED	T3A	6	G	C5	2	D	550	540	4.791	0.052	0.85	-0.004	0.302	-0.013245
UCDX13_T3A_G_C5_-2_BONEE	T3A	6	G	C5	2	E	550	540	4.853	0.075	0.79	-0.002	0.301	-0.006645
UCDX13_T3A_G_C5_-2_BONEF	T3A	6	G	C5	2	F	550	540	4.73	0.072	0.79	-0.004	0.273	-0.014652
UCDX13_T3B_MIX_C1_0_BONEG	T3B	7	Mix	C1	1	G	550	540	4.522	0.063	0.85	0	0.419	0
UCDX13_T3B_MIX_C1_0_BONEH	T3B	7	Mix	C1	1	H	550	540	4.693	0.057	0.83	-0.001	0.481	-0.002079
UCDX13_T3B_MIX_C1_0_BONEI	T3B	7	Mix	C1	1	I	550	540	4.726	0.083	0.82	0.01	0.508	0.019685
UCDX13_T3B_MIX_C1_-2_BONEG	T3B	7	Mix	C1	2	G	550	540	4.708	0.051	0.82	0.009	0.402	0.022388
UCDX13_T3B_MIX_C1_-2_BONEH	T3B	7	Mix	C1	2	H	550	540	4.86	0.053	0.88	0.01	0.466	0.021459
UCDX13_T3B_MIX_C1_-2_BONEI	T3B	7	Mix	C1	2	I	550	540	5.1	0.07	0.86	0.009	0.527	0.017078
UCDX13_T3B_MIX_C3_0_BONEG	T3B	7	Mix	C3	1	G	550	540	4.667	0.049	0.85	0.008	0.369	0.02168
UCDX13_T3B_MIX_C3_0_BONEH	T3B	7	Mix	C3	1	H	550	540	4.714	0.059	0.86	0.013	0.441	0.029478
UCDX13_T3B_MIX_C3_0_BONEI	T3B	7	Mix	C3	1	I	550	540	4.497	0.079	0.91	0.004	0.324	0.012346
UCDX13_T3B_MIX_C3_-2_BONEG	T3B	7	Mix	C3	2	G	550	540	4.884	0.049	0.92	0.014	0.472	0.029661
UCDX13_T3B_MIX_C3_-2_BONEH	T3B	7	Mix	C3	2	H	550	540	4.605	0.058	0.9	0.012	0.385	0.031169
UCDX13_T3B_MIX_C3_-2_BONEI	T3B	7	Mix	C3	2	I	550	540	4.203	0.096	0.86	0.008	0.311	0.025723
UCDX13_T3B_MIX_C4_0_BONEG	T3B	7	Mix	C4	1	G	550	540	4.366	0.068	0.82	-0.002	0.333	-0.006006

UCDX13_T3B_MIX_C4_0_BONEH	T3B	7	Mix	C4	1	H	550	540	4.474	0.058	0.77	0.006	0.358	0.01676
UCDX13_T3B_MIX_C4_0_BONEI	T3B	7	Mix	C4	1	I	550	540	4.495	0.075	N/A	0.005	0.411	0.012165
UCDX13_T3B_MIX_C4_-2_BONEG	T3B	7	Mix	C4	2	G	550	540	4.618	0.053	0.76	-0.002	0.447	-0.004474
UCDX13_T3B_MIX_C4_-2_BONEH	T3B	7	Mix	C4	2	H	550	540	4.222	0.068	0.79	0.006	0.295	0.020339
UCDX13_T3B_MIX_C4_-2_BONEI	T3B	7	Mix	C4	2	I	550	540	4.279	0.078	0.86	0.002	0.393	0.005089
UCDX13_T3B_MIX_C5_0_BONEG	T3B	7	Mix	C5	1	G	550	540	4.632	0.05	0.9	0.001	0.419	0.002387
UCDX13_T3B_MIX_C5_0_BONEH	T3B	7	Mix	C5	1	H	550	540	4.73	0.059	0.75	0.002	0.398	0.005025
UCDX13_T3B_MIX_C5_0_BONEI	T3B	7	Mix	C5	1	I	550	540	4.612	0.074	0.88	0.002	0.39	0.005128
UCDX13_T3B_MIX_C5_-2_BONEG	T3B	7	Mix	C5	2	G	550	540	4.641	0.053	0.92	0.01	0.355	0.028169
UCDX13_T3B_MIX_C5_-2_BONEH	T3B	7	Mix	C5	2	H	550	540	4.844	0.05	0.94	0.009	0.435	0.02069
UCDX13_T3B_MIX_C5_-2_BONEI	T3B	7	Mix	C5	2	I	550	540	4.752	0.07	0.9	0.011	0.436	0.025229
UCDX13_T4_G_C1_0_BONEG	T4	3	G	C1	1	G	550	10	3.981	0.072	N/A	-0.001	0.345	-0.002899
UCDX13_T4_G_C1_0_BONEH	T4	3	G	C1	1	H	550	10	3.925	0.072	N/A	0	0.36	0
UCDX13_T4_G_C1_0_BONEI	T4	3	G	C1	1	I	550	10	3.953	0.101	N/A	0.002	0.43	0.004651
UCDX13_T4_G_C2_0_BONEG	T4	3	G	C2	1	G	550	10	4.132	0.051	N/A	-0.005	0.287	-0.017422
UCDX13_T4_G_C2_0_BONEH	T4	3	G	C2	1	H	550	10	4.232	0.07	N/A	-0.002	0.431	-0.00464
UCDX13_T4_G_C2_0_BONEI	T4	3	G	C2	1	I	550	10	4.132	0.1	N/A	-0.009	0.401	-0.022444
UCDX13_T4_G_C3_0_BONEG	T4	3	G	C3	1	G	550	10	4.051	0.072	N/A	-0.003	0.362	-0.008287
UCDX13_T4_G_C3_0_BONEH	T4	3	G	C3	1	H	550	10	4.035	0.076	N/A	0	0.316	0
UCDX13_T4_G_C3_0_BONEI	T4	3	G	C3	1	I	550	10	4.093	0.098	N/A	-0.008	0.392	-0.020408
UCDX13_T4_G_C4_0_BONEG	T4	3	G	C4	1	G	550	10	4.051	0.078	N/A	0.007	0.31	0.022581
UCDX13_T4_G_C4_0_BONEH	T4	3	G	C4	1	H	550	10	4.035	0.08	N/A	0.001	0.377	0.002653
UCDX13_T4_G_C4_0_BONEI	T4	3	G	C4	1	I	550	10	3.919	0.101	N/A	0.004	0.394	0.010152
UCDX13_T5_G_C1_0_BONEG	T5	4	G	C1	1	G	750	540	6.786	0.011	1.93	0.001	0.737	0.001357
UCDX13_T5_G_C1_0_BONEH	T5	4	G	C1	1	H	750	540	6.272	0.013	2.02	-0.004	0.649	-0.006163
UCDX13_T5_G_C1_0_BONEI	T5	4	G	C1	1	I	750	540	5.073	-0.019	1.45	0.001	0.304	0.003289
UCDX13_T5_G_C1_-2_BONEG	T5	4	G	C1	2	G	750	540	5.994	0.012	1.89	-0.003	0.551	-0.005445
UCDX13_T5_G_C1_-2_BONEH	T5	4	G	C1	2	H	750	540	6.45	0.015	1.79	-0.003	0.685	-0.00438
UCDX13_T5_G_C1_-2_BONEI	T5	4	G	C1	2	I	750	540	5.62	0.021	1.5	-0.002	0.513	-0.003899
UCDX13_T5_G_C2_0_BONEG	T5	4	G	C2	1	G	750	540	6.238	0.009	2.12	-0.004	0.605	-0.006612
UCDX13_T5_G_C2_0_BONEH	T5	4	G	C2	1	H	750	540	6.246	0.009	2.01	-0.001	0.595	-0.001681
UCDX13_T5_G_C2_0_BONEI	T5	4	G	C2	1	I	750	540	4.73	-0.038	1.4	-0.009	0.214	-0.042056
UCDX13_T5_G_C2_-2_BONEG	T5	4	G	C2	2	G	750	540	6.658	0.01	1.92	-0.002	0.661	-0.003026
UCDX13_T5_G_C2_-2_BONEH	T5	4	G	C2	2	H	750	540	6.423	0.016	1.06	-0.012	0.665	-0.018045
UCDX13_T5_G_C2_-2_BONEI	T5	4	G	C2	2	I	750	540	5.13	0.035	1.34	-0.002	0.349	-0.005731
UCDX13_T5_G_C3_0_BONEG	T5	4	G	C3	1	G	750	540	6.77	0.008	2	0.001	0.56	0.001786
UCDX13_T5_G_C3_0_BONEH	T5	4	G	C3	1	H	750	540	6.507	0.014	2.12	-0.01	0.699	-0.014306
UCDX13_T5_G_C3_0_BONEI	T5	4	G	C3	1	I	750	540	5.401	-0.015	1.58	-0.004	0.43	-0.009302
UCDX13_T5_G_C3_-2_BONEG	T5	4	G	C3	2	G	750	540	6.516	0.013	1.96	-0.009	0.619	-0.01454
UCDX13_T5_G_C3_-2_BONEH	T5	4	G	C3	2	H	750	540	6.201	0.014	1.89	-0.004	0.558	-0.007168
UCDX13_T5_G_C3_-2_BONEI	T5	4	G	C3	2	I	750	540	5.567	0.028	1.39	0.001	0.465	0.002151
UCDX13_T5_G_C4_0_BONEG	T5	4	G	C4	1	G	750	540	6.356	0.003	2	0.007	0.563	0.012433
UCDX13_T5_G_C4_0_BONEH	T5	4	G	C4	1	H	750	540	6.405	0.015	2.2	-0.002	0.624	-0.003205
UCDX13_T5_G_C4_0_BONEI	T5	4	G	C4	1	I	750	540	4.962	-0.025	1.42	0.001	0.237	0.004219
UCDX13_T5_G_C4_-2_BONEG	T5	4	G	C4	2	G	750	540	6.284	0.011	1.8	-0.003	0.584	-0.005137
UCDX13_T5_G_C4_-2_BONEH	T5	4	G	C4	2	H	750	540	6.477	0.014	1.84	0.007	0.617	0.011345
UCDX13_T5_G_C4_-2_BONEI	T5	4	G	C3	2	I	750	540	5.813	0.023	1.4	0.008	0.539	0.014842
UCDX13_T6_G_C1_0_BONEG	T6	5	G	C1	1	G	300	540	3.471	0.094	N/A	0.015	0.211	0.07109
UCDX13_T6_G_C1_0_BONEH	T6	5	G	C1	1	H	300	540	3.43	0.108	N/A	0.013	0.165	0.078788
UCDX13_T6_G_C1_0_BONEI	T6	5	G	C1	1	I	300	540	3.564	0.118	N/A	0.004	0.161	0.024845
UCDX13_T6_G_C2_0_BONEG	T6	5	G	C2	1	G	300	540	3.643	0.109	N/A	0.004	0.381	0.010499

UCDX13_T6_G_C2_0_BONEH	T6	5	G	C2	1	H	300	540	3.642	0.096	N/A	0.013	0.331	0.039275
UCDX13_T6_G_C2_0_BONEI	T6	5	G	C2	1	I	300	540	3.527	0.13	N/A	0.006	0.396	0.015152
UCDX13_T6_G_C3_0_BONEG	T6	5	G	C3	1	G	300	540	3.607	0.107	N/A	0.013	0.305	0.042623
UCDX13_T6_G_C3_0_BONEH	T6	5	G	C3	1	H	300	540	3.536	0.115	N/A	0.011	0.244	0.045082
UCDX13_T6_G_C3_0_BONEI	T6	5	G	C3	1	I	300	540	3.553	0.135	N/A	0.016	0.313	0.051118
UCDX13_T6_G_C4_0_BONEG	T6	5	G	C4	1	G	300	540	3.592	0.106	N/A	0.025	0.267	0.093633
UCDX13_T6_G_C4_0_BONEH	T6	5	G	C4	1	H	300	540	3.556	0.113	N/A	0.02	0.279	0.071685
UCDX13_T6_G_C4_0_BONEI	T6	5	G	C4	1	I	300	540	3.499	0.155	N/A	0.014	0.257	0.054475
UCDX13_T7_G_C1_0_BONEJ	T7	9	G	C1	1	J	300	2880	3.645	0.12	N/A	0.01	0.397	0.025189
UCDX13_T7_G_C1_0_BONEK	T7	9	G	C1	1	K	300	2880	3.617	0.112	N/A	0.008	0.367	0.021798
UCDX13_T7_G_C1_0_BONEL	T7	9	G	C1	1	L	300	2880	3.541	0.128	N/A	0.005	0.309	0.016181
UCDX13_T7_G_C2_0_BONEJ	T7	9	G	C2	1	J	300	2880	3.667	0.12	N/A	-0.002	0.389	-0.005141
UCDX13_T7_G_C2_0_BONEK	T7	9	G	C2	1	K	300	2880	3.513	0.12	N/A	0.005	0.312	0.016026
UCDX13_T7_G_C2_0_BONEL	T7	9	G	C2	1	L	300	2880	3.615	0.117	N/A	-0.002	0.357	-0.005602
UCDX13_T7_G_C3_0_BONEJ	T7	9	G	C3	1	J	300	2880	3.57	0.122	N/A	-0.002	0.364	-0.005495
UCDX13_T7_G_C3_0_BONEK	T7	9	G	C3	1	K	300	2880	3.643	0.121	N/A	0.006	0.391	0.015345
UCDX13_T7_G_C3_0_BONEL	T7	9	G	C3	1	L	300	2880	3.621	0.116	N/A	-0.003	0.34	-0.008824
UCDX13_T7_G_C4_0_BONEJ	T7	9	G	C4	1	J	300	2880	3.491	0.13	N/A	0.009	0.411	0.021898
UCDX13_T7_G_C4_0_BONEK	T7	9	G	C4	1	K	300	2880	3.616	0.115	N/A	-0.002	0.367	-0.00545
UCDX13_T7_G_C4_0_BONEL	T7	9	G	C4	1	L	300	2880	3.642	0.116	N/A	0.007	0.298	0.02349
UCDX13_T8_C1_G_0_BONEJ	T8	8	G	C1	1	J	750	540	4.55	-0.013	1.34	-0.002	0.285	-0.007018
UCDX13_T8_C1_G_0_BONEK	T8	8	G	C1	1	K	750	540	5.301	0.003	1.44	-0.002	0.55	-0.003636
UCDX13_T8_C1_G_0_BONEL	T8	8	G	C1	1	L	750	540	5.087	-0.008	1.38	-0.001	0.39	-0.002564
UCDX13_T8_C2_G_0_BONEJ	T8	8	G	C2	1	J	750	540	4.602	-0.053	1.29	-0.003	0.163	-0.018405
UCDX13_T8_C2_G_0_BONEK	T8	8	G	C2	1	K	750	540	4.906	0.033	1.38	0.009	0.257	0.035019
UCDX13_T8_C2_G_0_BONEL	T8	8	G	C2	1	L	750	540	5.077	-0.028	1.49	0	0.296	0
UCDX13_T8_C3_G_0_BONEJ	T8	8	G	C3	1	J	750	540	4.655	-0.11	1.17	0.017	0.161	0.10559
UCDX13_T8_C3_G_0_BONEK	T8	8	G	C3	1	K	750	540	5.082	-0.021	1.44	0.01	0.343	0.029155
UCDX13_T8_C3_G_0_BONEL	T8	8	G	C3	1	L	750	540	5.076	-0.015	1.47	0.007	0.399	0.017544
UCDX13_T8_C4_G_0_BONEJ	T8	8	G	C4	1	J	750	540	5.351	-0.035	1.38	-0.001	0.22	-0.004545
UCDX13_T8_C4_G_0_BONEK	T8	8	G	C4	1	K	750	540	4.987	-0.023	1.52	0.008	0.376	0.021277
UCDX13_T8_C4_G_0_BONEL	T8	8	G	C4	1	L	750	540	4.647	-0.003	1.61	0.008	0.47	0.017021

Table 3: XRD Data

name	temp	grain size	error
T1C2-0-B	550	20.3	0.2
T1C3-0-C	550	23.5	0.2
T1C4-0-A	550	19.8	0.1
T1C4-A_5-70	550	17	0.1
T3A-C3-0-E	550	16.2	0.2
T3AC5-0-D	550	17	0.2
T6C3-0-I	300	8.7	0.1
T6C4-0-H	300	7.9	0.1
T7GC1-0-L	300	9.8	0.1
T7GC2-0-J	300	10.1	0.1
T7GC3-0-K	300	9.4	0.1
T7GC4-0-K	300	10	0.1
H2_5 200C	200	9	0.5
P0_4 300C@50	300	17.2	1
H1_1 300C	300	8.7	0.5
H1_8 300C 30_30	300	8.4	0.6
H1_12 300C@50	300	9	0.6
H1_17 300 30_30	300	8.4	0.5
H0_2 300C	300	8.3	0.6
H2_1 300C	300	9.8	0.6
H2_10 300C_180	300	9.2	0.5
H1_6 400C	400	9	0.6
H2_2 400C	400	9.2	0.5
H2_4 500C	500	8.5	0.4
H2_8 600C	600	9.9	1.3
H0_4 600C	600	9.2	0
H1_10 700C@50	700	35	7
H0_1 700C	700	46.2	1.2

H1_2 700C	700	38.9	0.8
H2_3 700 30_30	700	58.3	1.9
H0_3 700 30_30	700	56.4	1.3
H1_5 700 30_30	700	65.3	1.5
H0_7 700 30_30	700	58.3	1.7
H1_14 800C	800	64.1	2.1
H0_5 900C	900	73.3	3.3
H1_11 900C	900	66.2	3.2
H0_6 1000C	1000	90.1	5.3
H1_7 1000C	1000	80.9	5
C0_4 1100C	1100	58.2	1.7
H1_4 1100C	1100	55.7	2.3
C0_2 1200C	1200	61.3	4.5
H2_9 1200C	1200	51.7	5

Appendix C: Supplemental Materials for Chapter 4

Table 1. RDM layer 9 samples selected for FTIR-ATR. Burning stage following Stiner et al., (1995) with the addition of stage 5b and 6b to indicate blue coloration on stage 5 and 6 bones.

Square	ID	Burning Stage
J22	89D	ST4
J22	89C	ST6
J22	89B	ST3
J22	89A	ST0
J21	720F	ST6
J21	720E	ST3
J21	720D	ST2
J21	720C	ST0
J21	720B	ST0
J21	720A	ST0
J21	720A	ST0
J20	998I	ST6b
J20	998H	ST6
J20	998G	STb
J20	998F	ST6
J20	998E	ST3
J20	998D	ST4
J20	998B	ST0
J20	998A	ST0
J20	998A	ST0
J18	3855S	ST3
J18	3855R	ST4
J18	3855Q	ST3
J18	3855P	ST5
J18	3855O	ST2
J18	3855N	ST5b
J18	3855M	ST6
J18	3855L	ST5b
J18	3855K	ST4
J18	3855J	ST5
J18	3855i	ST6
J18	3855H	ST5
J18	3855F	duration
J18	3855E	ST2
J18	3855D	ST0
J18	3855C	ST1
J18	3855C	ST0
J18	3855B	ST0
J18	3855A	ST0
I18	1991O	ST6b

I18	1991N	ST6
I18	1991L	ST5
I18	1991K	ST4
I18	1991I	ST4
I18	1991H	ST4
I18	1991G	ST2
I18	1991F	ST2
I18	1991E	ST3
I18	1991D	ST3
I18	1991C	duration
I18	1991B	ST0
I18	1991A	ST0
H19	92O	duration
H19	92N	ST5b
H19	92M	ST6
H19	92L	ST6b
H19	92K	ST5
H19	92J	ST3
H19	92I	ST5
H19	92H	ST6
H19	92G	ST5
H19	92F	ST2
H19	92E	ST2
H19	92D	duration
H19	92C	ST3
H19	92B	ST0
H19	92A	ST0
H19	92A	ST0
H18	3953B	ST6
H18	3953A	ST6
H18	3002N	ST4
H18	3002M	ST5
H18	3002L	ST5
H18	3002K	ST5
H18	3002J	ST4
H18	3002I	ST4
H18	3002H	ST6
H18	3002F	ST3
H18	3002E	ST2
H18	3002D	ST4
H18	3002C	ST4
H18	3002B	ST0
H18	3002A	ST0
H18	3002O	ST4
G18	7245B	ST6
G18	7245A	ST6

G18	7245A	ST6
E18	1626M	ST5
E18	1626L	ST5
E18	1626H	ST3
CF4	251G	ST6b
CF4	251F	ST6
CF4	251E	ST6
CF4	251D	ST6
CF4	251C	ST6
CF4	251B	ST5b
CF4	251B	ST5b
CF4	251A	ST6b
CF1	239N	ST3
CF1	239N	ST3
CF1	239M	ST6
CF1	239L	STB
CF1	239K	ST5
CF1	239J	ST3
CF1	239I	ST2
CF1	239G	ST6b
J18	3855A	ST6b
I18	1991P	ST6
I18	1991M	ST6
I18	1991J	ST4
H18	3002G	ST6
CF1	239F	ST0
CF1	239E	ST1
CF1	239D	STT
CF1	239C	ST0
CF1	239B	ST0
CF1	239A	ST5

Table 2. Conversion between Stiner et al. (1995) burning stages and Costamagno et al. (2005) burning stages

Stiner et al., 1995 stage	Costamagno et al. 2005 stage
0	0
1	1
2	
3	2
4	
5	3
6	4

Table 3: Calculation of combustion index coefficients following Costamagno et al., (2005)

N	**Coefficient**	
Xa x 0	49271 x 0	0
Xb x 1	1472 x 1	1472
Xc x 2*	20778 x 2	41556
Xd x 3	2301 x 3	6903
Xe x 4	10318 x4	41272

*Includes Stiner et al. (1995) stages 2-4

Table 4: PCA scores for the Costamagno et al. (2009) combustion indices for European and African Paleolithic fire examples.

	PC 1	**PC 2**	**PC 3**	**PC 4**
Caminade Foyer	32.329	16.055	10.908	-5.6508
Caminade Sufrace	25.709	3.4819	-8.3305	-15.529
Castanet	2.1703	28.535	7.2958	11.07
Chex Pinaud 2	16.732	33.577	7.5265	33.18
Combette E	-4.9427	-31.043	16.69	14.432
Combette F/G	-2.4791	-25.221	1.9531	13.876
Cuzoul 23	-49.966	46.895	-18.69	6.5491
El Horno 2	-48.964	-39.143	-19.703	24.565
Troubat 8c	-53.171	-32.06	13.209	-12.076
Troubat 10	-66.363	-24.32	-12.495	8.6237
Troubat 11	-50.351	-10.296	-1.6919	-11.45
Troubat 12	-35.124	2.6786	9.1352	-12.085
Troubat 13	-44.474	4.067	-2.648	-3.3806

Pt Cp Barrat Bad.	-76.35	52.753	-4.9809	9.2504
Pt Cp Barrat Sol.	-46.279	16.339	6.0636	-13.041
RDM L.4	-65.018	-12.898	10.282	-11.058
RDM L.9	-17.948	-4.4206	15.051	-25.708
Sibulu AB 1	32.549	-10.655	-3.3944	9.378
Sibulu AB 2	35.232	3.289	4.7943	-4.2187
Sibulu Ash1	33.162	1.2761	10.794	-0.0719
Sibulu Ash2	34.039	0.47134	14.568	3.2864
Sibulu D1	35.39	2.6827	0.48884	-5.24
Sibulu D2	36.26	4.7704	-3.3188	-9.2564
Sibulu D3	36.527	4.5966	-0.0695	-7.3804
Sibulu H1	30.271	-15.115	15.413	22.521
Sibulu H2	37.355	5.0065	-3.3894	-8.9169
Sibulu H3	31.341	-6.2144	10.838	9.0013
Sibulu H4	33.865	-1.3625	-0.8934	-1.3186
Sibulu H6	33.712	-15.331	-44.593	-2.1498
Sibulu P1	35.537	4.2844	1.2955	-6.9644
Sibulu P2	39.25	-2.6787	-32.108	-10.237

Table 5: PC loadings for the indices proposed by Costamagno et al. (2009)

	PC 1	**PC 2**	**PC 3**	**PC 4**
% Spongieux brule	-0.34	0.73235	-0.24313	0.53754
% os brules < 2.5cm	-0.08409	0.22141	0.968	0.082988
% Carbonieses	0.13254	0.61169	-0.06175	-0.77747
% os brules	0.92723	0.20119	0.007458	0.31576

Table 6: Summary statistics for bone indices following Costamagno et al. (2009)

PC	**Eigenvalue**	**% variance**
1	1641.84	66.908
2	441.975	18.011
3	196.628	8.013
4	173.428	7.0675

Table 7: RDM FTIR and mFTIR data

ID	SQUARE	ID	WINDOW	STAGE	SF	CP	DURATION FL	CO 1650	P 1035	CO/P
RDM_J22_89D_St4_test1	J22	89D		ST4	4.635	0.049		0.002	0.146	0.013699
RDM_J22_89C_St6_test1	J22	89C		ST6	4.361	-0.048		-0.005	0.102	-0.04902
RDM_J22_89B_St3_test1	J22	89B		ST3	3.442	0.159		0	0.113	0
RDM_J22_89A_St0_test1	J22	89A		ST0	3.389	0.164		0.007	0.091	0.076923
RDM_J21_720F_St6_test1	J21	720F		ST6	4.4	-0.039		-0.009	0.067	-0.13433
RDM_J21_720E_st3_test1	J21	720E		ST3	3.54	0.151		-0.006	0.089	-0.06742
RDM_J21_720D_St2_test1	J21	720D		ST2	3.759	0.143		0.002	0.121	0.016529
RDM_J21_720C_St0_test1	J21	720C		ST0	3.417	0.162		0.001	0.128	0.007813
RDM_J21_720B_ST0_test1	J21	720B		ST0	4.081	0.102		-0.005	0.123	-0.04065
RDM_J21_720A_ST0_Test1	J21	720A		ST0	3.662	0.213		-0.006	0.107	-0.05607
RDM_J21_720A_St0_test2	J21	720A		ST0	3.645	0.204		-0.006	0.111	-0.05405
RDM_J20_998I_ST6b_test1	J20	998I		ST6b	4.921	0.209		0.005	0.299	0.016722
RDM_J20_998H_St6_Test1	J20	998H		ST6	4.836	0.048		-0.006	0.341	-0.0176
RDM_J20_998G_St6b_test1	J20	998G		STb	4.569	0.33		0.006	0.214	0.028037
RDM_J20_998F_St6_test1	J20	998F		ST6	4.824	0.338		-0.004	0.334	-0.01198
RDM_J20_998E_St3_test1	J20	998E		ST3	3.96	0.16		0.008	0.314	0.025478
RDM_J20_998D_St4_test1	J20	998D		ST4	3.79	0.205		0.022	0.353	0.062323
RDM_J20_998B_St0_test1	J20	998B		ST0	3.57	0.281		0.012	0.178	0.067416
RDM_J20_998A_St0_test1	J20	998A		ST0	3.676	0.306		0.005	0.267	0.018727
RDM_J20_998A_St0_test2	J20	998A		ST0	3.647	0.342		0.005	0.25	0.02
RDM_J18_3855S_St3_test1	J18	3855S		ST3	3.503	0.192		-0.001	0.2	-0.005
RDM_J18_3855R_St4_test1	J18	3855R		ST4	4.488	0.108		-0.002	0.224	-0.00893
RDM_J18_3855Q_St3_test1	J18	3855Q		ST3	3.95	0.179		0.012	0.254	0.047244
RDM_J18_3855P_St5_test1	J18	3855P		ST5	4.463	0.083		-0.006	0.364	-0.01648
RDM_J18_3855O_St2_test1	J18	3855O		ST2	3.786	0.207		0.014	0.315	0.044444
RDM_J18_3855N_St5b_test1	J18	3855N		ST5b	5.028	0.009		-0.009	0.308	-0.02922
RDM_J18_3855M_St6_test1	J18	3855M		ST6	4.692	-0.024		-0.012	0.286	-0.04196
RDM_J18_3855L_St5b_test1	J18	3855L		ST5b	5.258	0.046		0.002	0.412	0.004854
RDM_J18_3855K_st4_test1	J18	3855K		ST4	5.472	0.036		0.005	0.449	0.011136
RDM_J18_3855J_St5_test1	J18	3855J		ST5	5.14	0.009		-0.011	0.379	-0.02902
RDM_J18_3855i_St6_test1	J18	3855i		ST6	4.632	0.007		-0.01	0.289	-0.0346
RDM_J18_3855H_st5_test1	J18	3855H		ST5	4.872	0.036		-0.007	0.298	-0.02349
RDM_J18_3855F_st2or4_test1_IT IS 2	J18	3855F		duration	3.701	0.181		0	0.215	0
RDM_J18_3855E_St2_test1	J18	3855E		ST2	3.925	0.141		0.007	0.242	0.028926
RDM_J18_3855D_St0_test1	J18	3855D		ST0	3.406	0.194		0.009	0.281	0.032028
RDM_J18_3855C_St1_test1	J18	3855C		ST1	3.616	0.159		0.007	0.239	0.029289
RDM_J18_3855C_St0_test1	J18	3855C		ST0	3.621	0.197		0.008	0.263	0.030418
RDM_J18_3855B_St0_test1	J18	3855B		ST0	3.597	0.237		0.001	0.269	0.003717
RDM_J18_3855A_st0_test1	J18	3855A		ST0	3.613	0.169		0.009	0.272	0.033088
RDM_I18_1991O_st6b_test1	I18	1991O		ST6b	4.587	0.021		-0.002	0.201	-0.00995
RDM_I18_1991N_St6_test1	I18	1991N		ST6	4.678	-0.004		-0.003	0.344	-0.00872
RDM_I18_1991L_St5_test1	I18	1991L		ST5	5.267	0.068		-0.002	0.364	-0.00549
RDM_I18_1991K_St4_test1	I18	1991K		ST4	4.793	0.132		0.01	0.314	0.031847
RDM_I18_1991I_St4_test1	I18	1991I		ST4	5.244	0.055		0	0.344	0
RDM_I18_1991H_St4_test1	I18	1991H		ST4	5.085	0.053		0.03	0.327	0.091743
RDM_I18_1991G_St2_test1	I18	1991G		ST2	3.828	0.242		0.009	0.267	0.033708
RDM_I18_1991F_St2_test1	I18	1991F		ST2	3.663	0.388		0.008	0.155	0.051613
RDM_I18_1991E_St3_test1	I18	1991E		ST3	4.024	0.187		0.009	0.294	0.030612
RDM_I18_1991D_St3_test1	I18	1991D		ST3	3.713	0.235		0.004	0.265	0.015094
RDM_I18_1991C_st2or4_test1_ ST2	I18	1991C		duration	3.876	0.224	X	0.004	0.262	0.015267
RDM_I18_1991B_st0_test1	I18	1991B		ST0	3.603	0.233		0.01	0.286	0.034965
RDM_I18_1991A_St0_test1	I18	1991A		ST0	3.455	0.256		0.007	0.245	0.028571
RDM_H19_92O_St4_test1	H19	92O		duration	3.943	0.163	X	0.009	0.314	0.028662
RDM_H19_92N_ST5b_test1	H19	92N		ST5b	5.038	0.055		0	0.352	0
RDM_H19_92M_St6_test1	H19	92M		ST6	4.491	-0.009		-0.003	0.329	-0.00912
RDM_H19_92L_St6b_test1	H19	92L		ST6b	4.712	0.017		-0.003	0.236	-0.01271
RDM_H19_92K_St5_test1	H19	92K		ST5	4.939	0.098		0	0.349	0
RDM_H19_92J_St3_test1	H19	92J		ST3	3.414	0.219		0.014	0.296	0.047297
RDM_H19_92I_St5_test1	H19	92I		ST5	5.018	0.003		-0.002	0.427	-0.00468
RDM_H19_92H_st6_test1	H19	92H		ST6	4.269	-0.017		0.002	0.233	0.008584
RDM_H19_92G_st5_test1	H19	92G		ST5	4.68	0.002	weird spectra	-0.003	0.416	-0.00721
RDM_H19_92F_st2_test1	H19	92F		ST2	3.516	0.241		0	0.233	0
RDM_H19_92E_st2_test1	H19	92E		ST2	3.539	0.209		0.003	0.203	0.014778
RDM_H19_92D_St2or4_test1	H19	92D		duration	3.809	0.165	x	0.015	0.328	0.045732
RDM_H19_92C_St3_test1	H19	92C		ST3	3.523	0.207		0.02	0.283	0.070671

RDM_H19_92B_St0_test1	H19	92B	ST0	3.577	0.227	0.011	0.36	0.030556
RDM_H19_92A_St0_test2	H19	92A	ST0	3.503	0.246	0.1	0.127	0.787402
RDM_H19_92A_St0_test1	H19	92A	ST0	3.499	0.25	0.008	0.191	0.041885
RDM_H18_3953B_St6_test1	H18	3953B	ST6	5.336	-0.015	-0.009	0.179	-0.05028
RDM_H18_3953A_St6_test1	H18	3953A	ST6	4.752	0.026	-0.0037	0.0529	-0.06994
RDM_H18_3002N_St4_test1	H18	3002N	ST4	4.009	0.157	0.006	0.39	0.015385
RDM_H18_3002M_St5_test1	H18	3002M	ST5	4.938	0.016	0	0.341	0
RDM_H18_3002L_St5_test1	H18	3002L	ST5	5.152	0.041	0	0.504	0
RDM_H18_3002K_St5_test1	H18	3002K	ST5	5.199	0.041	0.009	0.575	0.015652
RDM_H18_3002J_st4_test1	H18	3002J	ST4	4.468	0.1	0.01	0.299	0.033445
RDM_H18_3002I_St4_test1	H18	3002I	ST4	5.514	0.037	-0.011	0.495	-0.02222
RDM_H18_3002H_st6_test1	H18	3002H	ST6	5.468	0.032	-0.004	0.54	-0.00741
RDM_H18_3002F_St3_test1	H18	3002F	ST3	3.849	0.147	0.007	0.268	0.026119
RDM_H18_3002E_st2_test1	H18	3002E	ST2	3.849	0.147	0.016	0.355	0.04507
RDM_H18_3002D_st4_test1	H18	3002D	ST4	4.215	0.122	0.01	0.384	0.026042
RDM_H18_3002C_St4_Test1	H18	3002C	ST4	3.966	0.155	0.009	0.333	0.027027
RDM_H18_3002B_St0_test1	H18	3002B	ST0	3.867	0.188	0.021	0.322	0.065217
RDM_H18_3002A_St0_test1	H18	3002A	ST0	3.469	0.225	0.026	0.25	0.104
RDM_H18_3002O_St4or0_test1	H18	3002O	ST0	4.968	0.064	0.002	0.372	0.005376
RDM_G18_7245B_ST6_TEST1	G18	7245B	ST6	4.844	-0.008	-0.004	0.404	-0.0099
RDM_G18_7245A_ST6_TEST1	G18	7245A	ST6	4.956	-0.056	-0.004	0.296	-0.01351
RDM_G18_7245A_ST6_TEST1	G18	7245A	ST6	4.469	0.051	-0.011	0.281	-0.03915
RDM_E18_1626M_ST5_TEST1	E18	1626M	ST5	5.699	0.022	-0.006	0.248	-0.02419
RDM_E18_1626L_ST5_TEST1	E18	1626L	ST5	4.776	0.146	0.007	0.219	0.031963
RDM_E18_1626H_ST3_TEST1	E18	1626H	ST3	3.984	0.15	0.006	0.0928	0.064655
RDM_CF4_251G_ST6B_TEST1	CF4	251G	ST6b	4.888	-0.012	-0.014	0.302	-0.04636
RDM_CF4_251F_ST6_TEST1	CF4	251F	ST6	4.758	0.015	-0.004	0.322	-0.01242
RDM_CF4_251E_ST6_TEST1	CF4	251E	ST6	5.266	0.007	-0.015	0.482	-0.03112
RDM_CF4_251D_ST6_TEST1	CF4	251D	ST6	5.447	0.005	-0.005	0.464	-0.01078
RDM_CF4_251C_ST6_TEST1	CF4	251C	ST6	4.907	0.032	-0.004	0.457	-0.00875
RDM_CF4_251B_ST5b_TEST1	CF4	251B	ST5b	4.795	0.02	-0.008	0.417	-0.01918
RDM_CF4_251B_ST5b_TEST2	CF4	251B	ST5b	4.792	0.012	-0.002	0.432	-0.00463
RDM_CF4_251A_ST6B_TEST1	CF4	251A	ST6b	4.701	-0.018	-0.002	0.287	-0.00697
RDM_CF1_239N_ST3_TEST2	CF1	239N	ST3	3.623	0.11	-0.0054	0.0378	-0.14286
RDM_CF1_239N_ST3_TEST1	CF1	239N	ST3	3.324	0.125	0.0116	0.0604	0.192053
RDM_CF1_239M_ST6_TEST1	CF1	239M	ST6	5.376	0.049	0.003	0.272	0.011029
RDM_CF1_239L_ST5B_TEST1	CF1	239L	STB	5.148	0.103	-0.006	0.158	-0.03797
RDM_CF1_239K_ST5_TEST1	CF1	239K	ST5	4.79	0.03	-0.005	0.226	-0.02212
RDM_CF1_239J_ST3_TEST1	CF1	239J	ST3	3.56	0.161	0.006	0.102	0.058824
RDM_CF1_239I_ST2_TEST1	CF1	239I	ST2	3.53	0.204	0.002	0.095	0.021053
RDM_CF1_239G_ST6B_TEST1	CF1	239G	ST6b	4.539	-0.005	0.002	0.082	0.02439
RDM_J18_3855A_ST6B_TEST1	J18	3855A	ST6b	4.609	0.058	-0.012	0.321	-0.03738
RDM_I18_1991P_ST6_TEST1	I18	1991P	ST6	4.433	0.005	-0.002	0.246	-0.00813
RDM_I18_1991M_ST6_TEST1	I18	1991M	ST6	4.66	0.002	0.007	0.279	0.02509
RDM_I18_1991J_ST4_REST1	I18	1991J	ST4	4.612	0.121	0	0.262	0
RDM_H18_3002G_ST6_TEST1	H18	3002G	ST6	4.348	0.001	-0.012	0.288	-0.04167
RDM_CF1_239F_ST0_TEST1	CF1	239F	ST0	3.278	0.178	0.005	0.11	0.045455
RDM_CF1_239E_ST1_TEST1	CF1	239E	ST1	3.785	0.137	0.003	0.135	0.022222
RDM_CF1_239D_ST_TEST1	CF1	239D	STT	3.503	0.175	0.004	0.099	0.040404
RDM_CF1_239C_ST0_TEST1	CF1	239C	ST0	3.505	0.151	-0.003	0.098	-0.03061
RDM_CF1_239B_ST0_TEST1	CF1	239B	ST0	3.521	0.219	-0.001	0.108	-0.00926
RDM_CF1_239A_ST5_TEST1	CF1	239A	ST5	5.78	0.023	0.002	0.268	0.007463
RDM_MM_506A_WINDOWA_1	MM	506A	1		0.189	-0.045	0.289	-0.15571
RDM_MM_506A_WINDOWA_2	MM	506A	2		0.198	-0.053	0.291	-0.18213
RDM_MM_506A_WINDOWA_3	MM	506A	3		0.183	-0.035	0.443	-0.07901
RDM_MM_506A_WINDOWA_4	MM	506A	4		0.179	-0.038	0.484	-0.07851
RDM_MM_506A_WINDOWA_5	MM	506A	5		0.176	-0.044	0.483	-0.0911
RDM_MM_506A_WINDOWA_6	MM	506A	6		0.21	-0.057	0.214	-0.26636
RDM_MM_506A_WINDOWA_7	MM	506A	7		0.199	-0.041	0.291	-0.14089
RDM_MM_506A_WINDOWA_8	MM	506A	8		0.18	-0.049	0.325	-0.15077
RDM_MM_506A_WINDOWAA_3	MM	506A	3		0.111	-0.031	0.456	-0.06798
RDM_MM_506A_WINDOWAA_4	MM	506A	4		0.106	-0.027	0.486	-0.05556
RDM_MM_506A_WINDOWAA_5	MM	506A	5		0.125	-0.033	0.219	-0.15068
RDM_MM_506A_WINDOWAA_6	MM	506A	6		0.106	-0.013	0.542	-0.02399
RDM_MM_506A_WINDOWAA_7	MM	506A	7		0.084	-0.03	0.426	-0.07042
RDM_MM_506A_WINDOWAA_8	MM	506A	8		0.108	-0.019	0.397	-0.04786

RDM_MM_506A_WINDOWAA_9	MM	506A	9	0.085	-0.032	0.495	-0.06465
RDM_MM_506A_WINDOWAA_10	MM	506A	10	0.1	-0.015	0.491	-0.03055
RDM_MM_506A_WINDOWB_3	MM	506A	3	0.179	-0.014	0.291	-0.04811
RDM_MM_506A_WINDOWB_4	MM	506A	4	0.183	-0.021	0.282	-0.07447
RDM_MM_506A_WINDOWB_8	MM	506A	8	0.172	-0.007	0.498	-0.01406
RDM_MM_506A_WINDOWB_9	MM	506A	9	0.176	-0.018	0.275	-0.06545
RDM_MM_506A_WINDOWC_1	MM	506A	1	0.152	-0.023	0.408	-0.05637
RDM_MM_506A_WINDOWC_2	MM	506A	2	0.156	-0.022	0.444	-0.04955
RDM_MM_506A_WINDOWC_3	MM	506A	3	0.164	-0.033	0.326	-0.10123
RDM_MM_506A_WINDOWC_11	MM	506A	11	0.157	-0.028	0.439	-0.06378
RDM_MM_506A_WINDOWD_16	MM	506A	16	0.161	-0.031	0.363	-0.0854
RDM_MM_506A_WINDOWD_17	MM	506A	17	0.15	-0.028	0.568	-0.0493
RDM_MM_506A_WINDOWD_19	MM	506A	19	0.163	-0.031	0.401	-0.07731
RDM_MM_506A_WINDOWD_20	MM	506A	20	0.151	-0.03	0.506	-0.05929
RDM_MM_506A_WINDOWE_2	MM	506A	2	0.139	-0.033	0.543	-0.06077
RDM_MM_506A_WINDOWE_3	MM	506A	3	0.14	-0.039	0.277	-0.14079
RDM_MM_506A_WINDOWF_4	MM	506A	4	0.107	-0.006	0.49	-0.01224
RDM_MM_506A_WINDOWF_5	MM	506A	5	0.157	-0.028	0.247	-0.11336
RDM_MM_506A_WINDOWI_10	MM	506A	10	0.121	-0.02	0.348	-0.05747
RDM_MM_506A_WINDOWI_12	MM	506A	12	0.116	-0.025	0.401	-0.06234
RDM_MM_506A_WINDOWI_14	MM	506A	14	0.178	-0.021	0.419	-0.05012
RDM_MM_506A_WINDOWJ_4	MM	506A	4	0.117	-0.04	0.28	-0.14286
RDM_MM_506A_WINDOWJ_5	MM	506A	5	0.119	0.001	0.497	0.002012
RDM_MM_506A_WINDOWK_14	MM	506A	14	0.174	-0.039	0.4	-0.0975
RDM_MM_506A_WINDOWK_18	MM	506A	18	0.117	-0.033	0.61	-0.0541
RDM_MM_506A_WINDOWK_20	MM	506A	20	0.156	-0.024	0.413	-0.05811
RDM_MM_506A_WINDOWL_7	MM	506A	7	0.247	-0.009	0.398	-0.02261
RDM_MM_506A_WINDOWL_8	MM	506A	8	0.231	0.231	0.358	0.645251
RDM_MM_506A_WINDOWL_15	MM	506A	15	0.107	-0.005	0.472	-0.01059
RDM_MM_506A_WINDOWN_3	MM	506A	3	0.096	-0.034	0.475	-0.07158
RDM_MM_506A_WINDOWN_6	MM	506A	6	0.093	-0.031	0.666	-0.04655
RDM_MM_506A_WINDOWN_9	MM	506A	9	0.11	-0.034	0.516	-0.06589
RDM_MM_506A_WINDOWO_4	MM	506A	4	0.156	-0.03	0.406	-0.07389
RDM_MM_506A_WINDOWO_6	MM	506A	6	0.136	-0.038	0.338	-0.11243
RDM_MM_506A_WINDOWO_8	MM	506A	8	0.124	-0.045	0.346	-0.13006
RDM_MM_211ASH_WINDOWA_1	MM	211ASH	1	0.123	-0.014	0.065	-0.21538
RDM_MM_211ASH_WINDOWA_7	MM	211ASH	7	0.186	-0.003	0.361	-0.00831
RDM_MM_211ASH_WINDOWC_2	MM	211ASH	2	0.29	0.006	0.179	0.03352
RDM_MM_211ASH_WINDOWC_1	MM	211ASH	1	0.215	-0.009	0.067	-0.13433
RDM_MM_211ASH_WINDOWC_4	MM	211ASH	4	0.233	-0.009	0.131	-0.0687
RDM_MM_211ASH_WINDOWE_11	MM	211ASH	11	0.203	-0.016	0.339	-0.0472
RDM_MM_211ASH_WINDOWE_16	MM	211ASH	16	0.218	-0.014	0.473	-0.0296
RDM_MM_211ASH_WINDOWF_11	MM	211ASH	11	0.264	-0.013	0.258	-0.05039
RDM_MM_211ASH_WINDOWF_16	MM	211ASH	16	0.216	-0.017	0.313	-0.05431
RDM_MM_211ASH_WINDOWF_18	MM	211ASH	18	0.242	-0.007	0.368	-0.01902
RDM_501_WINDOWA_1	MM	501	1	0.043	-0.044	0.398	-0.11055
RDM_501_WINDOWA_2	MM	501	2	0.02	-0.044	0.473	-0.09302
RDM_501_WINDOWA_4	MM	501	4	0.273	-0.048	0.273	-0.17582
RDM_501_WINDOWAA_4	MM	501	4	0.194	0.011	0.424	0.025943
RDM_501_WINDOWAA_5	MM	501	5	0.175	0.006	0.457	0.013129
RDM_501_WINDOWB_2	MM	501	2	0.19	-0.029	0.087	-0.33333
RDM_501_WINDOWB_3	MM	501	3	0.268	-0.016	0.355	-0.04507
RDM_501_WINDOWBB_14	MM	501	14	0.148	-0.016	0.383	-0.04178
RDM_501_WINDOWBB_15	MM	501	15	0.159	-0.015	0.522	-0.02874
RDM_501_WINDOWBB_16	MM	501	16	0.15	-0.018	0.561	-0.03209
RDM_501_WINDOWC_1	MM	501	1	0.243	-0.017	0.419	-0.04057
RDM_501_WINDOWC_2	MM	501	2	0.263	-0.022	0.192	-0.11458
RDM_501_WINDOWC_3	MM	501	3	0.243	-0.026	0.321	-0.081
RDM_501_WINDOWF_5	MM	501	5	0.333	-0.024	0.571	-0.04203
RDM_501_WINDOWF_16	MM	501	16	0.281	-0.025	0.452	-0.05531
RDM_501_WINDOWF_17	MM	501	17	0.26	-0.032	0.612	-0.05229
RDM_501_WINDOWG_2	MM	501	2	0.206	-0.008	0.253	-0.03162
RDM_501_WINDOWG_3	MM	501	3	0.196	-0.019	0.179	-0.10615
RDM_501_WINDOWG_6	MM	501	6	0.193	-0.01	0.347	-0.02882
RDM_501_WINDOWH_1	MM	501	1	0.247	-0.012	0.247	-0.04858
RDM_501_WINDOWH_3	MM	501	3	0.309	-0.009	0.254	-0.03543

RDM_501_WINDOWH_6	MM	501	6	0.18	-0.015	0.311	-0.04823
RDM_501_WINDOWI_6	MM	501	6	0.03	-0.009	0.288	-0.03125
RDM_501_WINDOWI_7	MM	501	7	-0.028	-0.008	0.218	-0.0367
RDM_501_WINDOWI_8	MM	501	8	0.371	-0.008	0.238	-0.03361
RDM_501_WINDOWJ_5	MM	501	5	0.265	-0.003	0.266	-0.01128
RDM_501_WINDOWJ_7	MM	501	7	0.211	-0.003	0.265	-0.01132
RDM_501_WINDOWJ_8	MM	501	8	0.14	-0.007	0.403	-0.01737
RDM_501_WINDOWK_11	MM	501	11	0.192	-0.015	0.279	-0.05376
RDM_501_WINDOWK_12	MM	501	12	0.176	-0.002	0.331	-0.00604
RDM_501_WINDOWL_5	MM	501	5	0.12	0	0.43	0
RDM_501_WINDOWL_6	MM	501	6	0.142	0.001	0.444	0.002252
RDM_501_WINDOWL_7	MM	501	7	0.166	0.002	0.384	0.005208
RDM_501_WINDOWM_5	MM	501	5	0.204	-0.007	0.24	-0.02917
RDM_501_WINDOWM_6	MM	501	6	0.196	0.001	0.296	0.003378
RDM_501_WINDOWM_9	MM	501	9	0.217	-0.005	0.37	-0.01351
RDM_501_WINDOWO_10	MM	501	10	0.142	-0.004	0.316	-0.01266
RDM_501_WINDOWO_11	MM	501	11	0.163	-0.002	0.41	-0.00488
RDM_501_WINDOWO_14	MM	501	14	0.153	-0.003	0.415	-0.00723
RDM_501_WINDOWP_6	MM	501	6	0.279	-0.013	0.254	-0.05118
RDM_501_WINDOWP_7	MM	501	7	0.169	-0.009	0.367	-0.02452
RDM_501_WINDOWP_11	MM	501	11	0.176	-0.005	0.502	-0.00996
RDM_501_WINDOWR_12	MM	501	12	0.33	-0.003	0.177	-0.01695
RDM_501_WINDOWR_13	MM	501	13	-0.002	-0.005	0.486	-0.01029
RDM_501_WINDOWS_1	MM	501	1	0.006	-0.015	0.33	-0.04545
RDM_501_WINDOWT_3	MM	501	3	0.279	-0.007	0.254	-0.02756
RDM_501_WINDOWT_4	MM	501	4	0.255	-0.013	0.386	-0.03368
RDM_501_WINDOWT_5	MM	501	5	0.296	-0.007	0.254	-0.02756
RDM_501_WINDOWU_3	MM	501	3	-0.003	-0.024	0.483	-0.04969
RDM_501_WINDOWU_5	MM	501	5	-0.017	-0.026	0.466	-0.05579
RDM_501_WINDOWU_6	MM	501	6	0.012	-0.025	0.383	-0.06527
RDM_501_WINDOWV_13	MM	501	13	0.106	-0.045	0.318	-0.14151
RDM_501_WINDOWV_14	MM	501	14	0.026	-0.042	0.316	-0.13291
RDM_501_WINDOWV_15	MM	501	15	0.037	-0.048	0.342	-0.14035
RDM_501_WINDOWW_9	MM	501	9	0.055	-0.021	0.32	-0.06563
RDM_501_WINDOWW_10	MM	501	10	0.17	-0.025	0.412	-0.06068
RDM_501_WINDOWW_14	MM	501	14	0.027	-0.025	0.369	-0.06775
RDM_501_WINDOWY_4	MM	501	4	0.194	0.002	0.508	0.003937
RDM_501_WINDOWY_5	MM	501	5	0.166	-0.004	0.424	-0.00943
RDM_501_WINDOWY_6	MM	501	6	0.147	-0.005	0.414	-0.01208
RDM_501_WINDOWZ_3	MM	501	3	0.104	-0.019	0.314	-0.06051
RDM_501_WINDOWZ_5	MM	501	5	0.101	-0.02	0.464	-0.0431
RDM_501_WINDOWZ_10	MM	501	3	0.114	-0.027	0.515	-0.05243

Table 8: RDM FTIR and mFTIR data

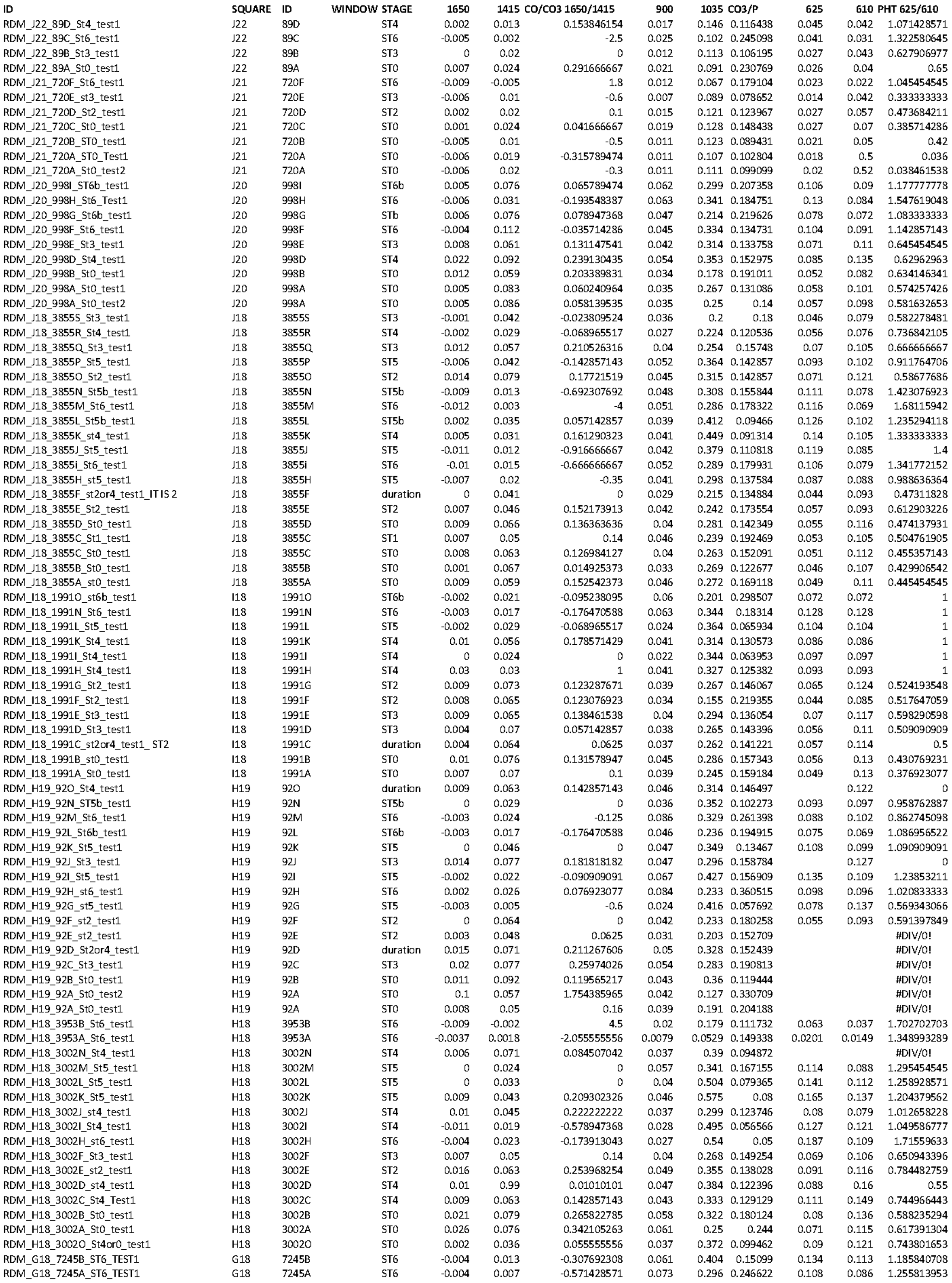

ID	SQUARE	ID	WINDOW	STAGE	1650	1415	CO/CO3 1650/1415	900	1035	CO3/P	625	610	PHT 625/610
RDM_J22_89D_St4_test1	J22	89D		ST4	0.002	0.013	0.153846154	0.017	0.146	0.116438	0.045	0.042	1.071428571
RDM_J22_89C_St6_test1	J22	89C		ST6	-0.005	0.002	-2.5	0.025	0.102	0.245098	0.041	0.031	1.322580645
RDM_J22_89B_St3_test1	J22	89B		ST3	0	0.02	0	0.012	0.113	0.106195	0.027	0.043	0.627906977
RDM_J22_89A_St0_test1	J22	89A		ST0	0.007	0.024	0.291666667	0.021	0.091	0.230769	0.026	0.04	0.65
RDM_J21_720F_St6_test1	J21	720F		ST6	-0.009	-0.005	1.8	0.012	0.067	0.179104	0.023	0.022	1.045454545
RDM_J21_720E_st3_test1	J21	720E		ST3	-0.006	0.01	-0.6	0.007	0.089	0.078652	0.014	0.042	0.333333333
RDM_J21_720D_St2_test1	J21	720D		ST2	0.002	0.02	0.1	0.015	0.121	0.123967	0.027	0.057	0.473684211
RDM_J21_720C_St0_test1	J21	720C		ST0	0.001	0.024	0.041666667	0.019	0.128	0.148438	0.027	0.07	0.385714286
RDM_J21_720B_ST0_test1	J21	720B		ST0	-0.005	0.01	-0.5	0.011	0.123	0.089431	0.021	0.05	0.42
RDM_J21_720A_ST0_Test1	J21	720A		ST0	-0.006	0.019	-0.315789474	0.011	0.107	0.102804	0.018	0.5	0.036
RDM_J21_720A_St0_test2	J21	720A		ST0	-0.006	0.02	-0.3	0.011	0.111	0.099099	0.02	0.52	0.038461538
RDM_J20_998I_ST6b_test1	J20	998I		ST6b	0.005	0.076	0.065789474	0.062	0.299	0.207358	0.106	0.09	1.177777778
RDM_J20_998H_St6_Test1	J20	998H		ST6	-0.006	0.031	-0.193548387	0.063	0.341	0.184751	0.13	0.084	1.547619048
RDM_J20_998G_St6b_test1	J20	998G		STb	0.006	0.076	0.078947368	0.047	0.214	0.219626	0.078	0.072	1.083333333
RDM_J20_998F_St6_test1	J20	998F		ST6	-0.004	0.112	-0.035714286	0.045	0.334	0.134731	0.104	0.091	1.142857143
RDM_J20_998E_St3_test1	J20	998E		ST3	0.008	0.061	0.131147541	0.042	0.314	0.133758	0.071	0.11	0.645454545
RDM_J20_998D_St4_test1	J20	998D		ST4	0.022	0.092	0.239130435	0.054	0.353	0.152975	0.085	0.135	0.62962963
RDM_J20_998B_St0_test1	J20	998B		ST0	0.012	0.059	0.203389831	0.034	0.178	0.191011	0.052	0.082	0.634146341
RDM_J20_998A_St0_test1	J20	998A		ST0	0.005	0.083	0.060240964	0.035	0.267	0.131086	0.058	0.101	0.574257426
RDM_J20_998A_St0_test2	J20	998A		ST0	0.005	0.086	0.058139535	0.035	0.25	0.14	0.057	0.098	0.581632653
RDM_J18_3855S_St3_test1	J18	3855S		ST3	-0.001	0.042	-0.023809524	0.036	0.2	0.18	0.046	0.079	0.582278481
RDM_J18_3855R_St4_test1	J18	3855R		ST4	-0.002	0.029	-0.068965517	0.027	0.224	0.120536	0.056	0.076	0.736842105
RDM_J18_3855Q_St3_test1	J18	3855Q		ST3	0.012	0.057	0.210526316	0.04	0.254	0.15748	0.07	0.105	0.666666667
RDM_J18_3855P_St5_test1	J18	3855P		ST5	-0.006	0.042	-0.142857143	0.052	0.364	0.142857	0.093	0.102	0.911764706
RDM_J18_3855O_St2_test1	J18	3855O		ST2	0.014	0.079	0.17721519	0.045	0.315	0.142857	0.071	0.121	0.58677686
RDM_J18_3855N_St5b_test1	J18	3855N		ST5b	-0.009	0.013	-0.692307692	0.048	0.308	0.155844	0.111	0.078	1.423076923
RDM_J18_3855M_St6_test1	J18	3855M		ST6	-0.012	0.003	-4	0.051	0.286	0.178322	0.116	0.069	1.68115942
RDM_J18_3855L_St5b_test1	J18	3855L		ST5b	0.002	0.035	0.057142857	0.039	0.412	0.09466	0.126	0.102	1.235294118
RDM_J18_3855K_st4_test1	J18	3855K		ST4	0.005	0.031	0.161290323	0.041	0.449	0.091314	0.14	0.105	1.333333333
RDM_J18_3855J_St5_test1	J18	3855J		ST5	-0.011	0.012	-0.916666667	0.042	0.379	0.110818	0.119	0.085	1.4
RDM_J18_3855i_St6_test1	J18	3855i		ST6	-0.01	0.015	-0.666666667	0.052	0.289	0.179931	0.106	0.079	1.341772152
RDM_J18_3855H_st5_test1	J18	3855H		ST5	-0.007	0.02	-0.35	0.041	0.298	0.137584	0.087	0.088	0.988636364
RDM_J18_3855F_st2or4_test1_IT IS 2	J18	3855F		duration	0	0.041	0	0.029	0.215	0.134884	0.044	0.093	0.47311828
RDM_J18_3855E_St2_test1	J18	3855E		ST2	0.007	0.046	0.152173913	0.042	0.242	0.173554	0.057	0.093	0.612903226
RDM_J18_3855D_St0_test1	J18	3855D		ST0	0.009	0.066	0.136363636	0.04	0.281	0.142349	0.055	0.116	0.474137931
RDM_J18_3855C_St1_test1	J18	3855C		ST1	0.007	0.05	0.14	0.046	0.239	0.192469	0.053	0.105	0.504761905
RDM_J18_3855C_St0_test1	J18	3855C		ST0	0.008	0.063	0.126984127	0.04	0.263	0.152091	0.051	0.112	0.455357143
RDM_J18_3855B_St0_test1	J18	3855B		ST0	0.001	0.067	0.014925373	0.033	0.269	0.122677	0.046	0.107	0.429906542
RDM_J18_3855A_st0_test1	J18	3855A		ST0	0.009	0.059	0.152542373	0.046	0.272	0.169118	0.049	0.11	0.445454545
RDM_I18_1991O_st6b_test1	I18	1991O		ST6b	-0.002	0.021	-0.095238095	0.06	0.201	0.298507	0.072	0.072	1
RDM_I18_1991N_St6_test1	I18	1991N		ST6	-0.003	0.017	-0.176470588	0.063	0.344	0.18314	0.128	0.128	1
RDM_I18_1991L_St5_test1	I18	1991L		ST5	-0.002	0.029	-0.068965517	0.024	0.364	0.065934	0.104	0.104	1
RDM_I18_1991K_St4_test1	I18	1991K		ST4	0.01	0.056	0.178571429	0.041	0.314	0.130573	0.086	0.086	1
RDM_I18_1991I_St4_test1	I18	1991I		ST4	0	0.024	0	0.022	0.344	0.063953	0.097	0.097	1
RDM_I18_1991H_St4_test1	I18	1991H		ST4	0.03	0.03	1	0.041	0.327	0.125382	0.093	0.093	1
RDM_I18_1991G_St2_test1	I18	1991G		ST2	0.009	0.073	0.123287671	0.039	0.267	0.146067	0.065	0.124	0.524193548
RDM_I18_1991F_St2_test1	I18	1991F		ST2	0.008	0.065	0.123076923	0.034	0.155	0.219355	0.044	0.085	0.517647059
RDM_I18_1991E_St3_test1	I18	1991E		ST3	0.009	0.065	0.138461538	0.04	0.294	0.136054	0.07	0.117	0.598290598
RDM_I18_1991D_St3_test1	I18	1991D		ST3	0.004	0.07	0.057142857	0.038	0.265	0.143396	0.056	0.11	0.509090909
RDM_I18_1991C_st2or4_test1_ ST2	I18	1991C		duration	0.004	0.064	0.0625	0.037	0.262	0.141221	0.057	0.114	0.5
RDM_I18_1991B_st0_test1	I18	1991B		ST0	0.01	0.076	0.131578947	0.045	0.286	0.157343	0.056	0.13	0.430769231
RDM_I18_1991A_St0_test1	I18	1991A		ST0	0.007	0.07	0.1	0.039	0.245	0.159184	0.049	0.13	0.376923077
RDM_H19_92O_St4_test1	H19	92O		duration	0.009	0.063	0.142857143	0.046	0.314	0.146497		0.122	0
RDM_H19_92N_ST5b_test1	H19	92N		ST5b	0	0.029	0	0.036	0.352	0.102273	0.093	0.097	0.958762887
RDM_H19_92M_St6_test1	H19	92M		ST6	-0.003	0.024	-0.125	0.086	0.329	0.261398	0.088	0.102	0.862745098
RDM_H19_92L_St6b_test1	H19	92L		ST6b	-0.003	0.017	-0.176470588	0.046	0.236	0.194915	0.075	0.069	1.086956522
RDM_H19_92K_St5_test1	H19	92K		ST5	0	0.046	0	0.047	0.349	0.13467	0.108	0.099	1.090909091
RDM_H19_92J_St3_test1	H19	92J		ST3	0.014	0.077	0.181818182	0.047	0.296	0.158784		0.127	0
RDM_H19_92I_St5_test1	H19	92I		ST5	-0.002	0.022	-0.090909091	0.067	0.427	0.156909	0.135	0.109	1.23853211
RDM_H19_92H_st6_test1	H19	92H		ST6	0.002	0.026	0.076923077	0.084	0.233	0.360515	0.098	0.096	1.020833333
RDM_H19_92G_st5_test1	H19	92G		ST5	-0.003	0.005	-0.6	0.024	0.416	0.057692	0.078	0.137	0.569343066
RDM_H19_92F_st2_test1	H19	92F		ST2	0	0.064	0	0.042	0.233	0.180258	0.055	0.093	0.591397849
RDM_H19_92E_st2_test1	H19	92E		ST2	0.003	0.048	0.0625	0.031	0.203	0.152709			#DIV/0!
RDM_H19_92D_St2or4_test1	H19	92D		duration	0.015	0.071	0.211267606	0.05	0.328	0.152439			#DIV/0!
RDM_H19_92C_St3_test1	H19	92C		ST3	0.02	0.077	0.25974026	0.054	0.283	0.190813			#DIV/0!
RDM_H19_92B_St0_test1	H19	92B		ST0	0.011	0.092	0.119565217	0.043	0.36	0.119444			#DIV/0!
RDM_H19_92A_St0_test2	H19	92A		ST0	0.1	0.057	1.754385965	0.042	0.127	0.330709			#DIV/0!
RDM_H19_92A_St0_test1	H19	92A		ST0	0.008	0.05	0.16	0.039	0.191	0.204188			#DIV/0!
RDM_H18_3953B_St6_test1	H18	3953B		ST6	-0.009	-0.002	4.5	0.02	0.179	0.111732	0.063	0.037	1.702702703
RDM_H18_3953A_St6_test1	H18	3953A		ST6	-0.0037	0.0018	-2.055555556	0.0079	0.0529	0.149338	0.0201	0.0149	1.348993289
RDM_H18_3002N_St4_test1	H18	3002N		ST4	0.006	0.071	0.084507042	0.037	0.39	0.094872			#DIV/0!
RDM_H18_3002M_St5_test1	H18	3002M		ST5	0	0.024	0	0.057	0.341	0.167155	0.114	0.088	1.295454545
RDM_H18_3002L_St5_test1	H18	3002L		ST5	0	0.033	0	0.04	0.504	0.079365	0.141	0.112	1.258928571
RDM_H18_3002K_St5_test1	H18	3002K		ST5	0.009	0.043	0.209302326	0.046	0.575	0.08	0.165	0.137	1.204379562
RDM_H18_3002J_st4_test1	H18	3002J		ST4	0.01	0.045	0.222222222	0.037	0.299	0.123746	0.08	0.079	1.012658228
RDM_H18_3002I_St4_test1	H18	3002I		ST4	-0.011	0.019	-0.578947368	0.028	0.495	0.056566	0.127	0.121	1.049586777
RDM_H18_3002H_st6_test1	H18	3002H		ST6	-0.004	0.023	-0.173913043	0.027	0.54	0.05	0.187	0.109	1.71559633
RDM_H18_3002F_St3_test1	H18	3002F		ST3	0.007	0.05	0.14	0.04	0.268	0.149254	0.069	0.106	0.650943396
RDM_H18_3002E_st2_test1	H18	3002E		ST2	0.016	0.063	0.253968254	0.049	0.355	0.138028	0.091	0.116	0.784482759
RDM_H18_3002D_st4_test1	H18	3002D		ST4	0.01	0.99	0.01010101	0.047	0.384	0.122396	0.088	0.16	0.55
RDM_H18_3002C_St4_Test1	H18	3002C		ST4	0.009	0.063	0.142857143	0.043	0.333	0.129129	0.111	0.149	0.744966443
RDM_H18_3002B_St0_test1	H18	3002B		ST0	0.021	0.079	0.265822785	0.058	0.322	0.180124	0.08	0.136	0.588235294
RDM_H18_3002A_St0_test1	H18	3002A		ST0	0.026	0.076	0.342105263	0.061	0.25	0.244	0.071	0.115	0.617391304
RDM_H18_3002O_St4or0_test1	H18	3002O		ST0	0.002	0.036	0.055555556	0.037	0.372	0.099462	0.09	0.121	0.743801653
RDM_G18_7245B_ST6_TEST1	G18	7245B		ST6	-0.004	0.013	-0.307692308	0.061	0.404	0.15099	0.134	0.113	1.185840708
RDM_G18_7245A_ST6_TEST1	G18	7245A		ST6	-0.004	0.007	-0.571428571	0.073	0.296	0.246622	0.108	0.086	1.255813953

RDM_G18_7245A_ST6_TEST1	G18	7245A	ST6	-0.011	0.02	-0.55	0.046	0.281	0.163701	0.088	0.085	1.035294118
RDM_E18_1626M_ST5_TEST1	E18	1626M	ST5	-0.006	0.004	-1.5	0.009	0.248	0.03629	0.075	0.068	1.102941176
RDM_E18_1626L_ST5_TEST1	E18	1626L	ST5	0.007	0.041	0.170731707	0.022	0.219	0.100457	0.061	0.087	0.701149425
RDM_E18_1626H_ST3_TEST1	E18	1626H	ST3	0.006	0.0207	0.289855072	0.0157	0.0928	0.169181			#DIV/0!
RDM_CF4_251G_ST6B_TEST1	CF4	251G	ST6b	-0.014	0.012	-1.166666667	0.067	0.302	0.221854	0.137	0.068	2.014705882
RDM_CF4_251F_ST6_TEST1	CF4	251F	ST6	-0.004	0.023	-0.173913043	0.06	0.322	0.186335	0.152	0.086	1.76744186
RDM_CF4_251E_ST6_TEST1	CF4	251E	ST6	-0.015	0.031	-0.483870968	0.033	0.482	0.068465	0.15	0.094	1.595744681
RDM_CF4_251D_ST6_TEST1	CF4	251D	ST6	-0.005	0.011	-0.454545455	0.035	0.464	0.075431	0.097	0.092	1.054347826
RDM_CF4_251C_ST6_TEST1	CF4	251C	ST6	-0.004	0.031	-0.129032258	0.054	0.457	0.118162	0.083	0.106	0.783018868
RDM_CF4_251B_ST5b_TEST1	CF4	251B	ST5b	-0.008	0.007	-1.142857143	0.022	0.417	0.052758	0.065	0.141	0.460992908
RDM_CF4_251B_ST5b_TEST2	CF4	251B	ST5b	-0.002	0.011	-0.181818182	0.027	0.432	0.0625	0.08	0.148	0.540540541
RDM_CF4_251A_ST6B_TEST1	CF4	251A	ST6b	-0.002	0.021	-0.095238095	0.07	0.287	0.243902	0.094	0.093	1.010752688
RDM_CF1_239N_ST3_TEST2	CF1	239N	ST3	-0.0054	0.0015	-3.6	0.0038	0.0378	0.100529	0.0101	0.0271	0.372693727
RDM_CF1_239N_ST3_TEST1	CF1	239N	ST3	0.0116	0.0197	0.588832487	0.0211	0.0604	0.349338	0.025	0.0449	0.556792873
RDM_CF1_239M_ST6_TEST1	CF1	239M	ST6	0.003	0.021	0.142857143	0.019	0.272	0.069853	0.078	0.065	1.2
RDM_CF1_239L_ST5B_TEST1	CF1	239L	STB	-0.006	0.013	-0.461538462	0.007	0.158	0.044304	0.041	0.039	1.051282051
RDM_CF1_239K_ST5_TEST1	CF1	239K	ST5	-0.005	0.004	-1.25	0.007	0.226	0.030973	0.06	0.063	0.952380952
RDM_CF1_239J_ST3_TEST1	CF1	239J	ST3	0.006	0.023	0.260869565	0.016	0.102	0.156863	0.034	0.029	1.172413793
RDM_CF1_239I_ST2_TEST1	CF1	239I	ST2	0.002	0.023	0.086956522	0.013	0.095	0.136842	0.074	0.058	1.275862069
RDM_CF1_239G_ST6B_TEST1	CF1	239G	ST6b	0.002	0.008	0.25	0.019	0.082	0.231707	0.034	0.031	1.096774194
RDM_J18_3855A_ST6B_TEST1	J18	3855A	ST6b	-0.012	0.028	-0.428571429	0.061	0.321	0.190031	0.087	0.083	1.048192771
RDM_I18_1991P_ST6_TEST1	I18	1991P	ST6	-0.002	0.024	-0.083333333	0.081	0.246	0.329268	0.092	0.078	1.179487179
RDM_I18_1991M_ST6_TEST1	I18	1991M	ST6	0.007	0.025	0.28	0.065	0.279	0.232975	0.115	0.082	1.402439024
RDM_I18_1991J_ST4_REST1	I18	1991J	ST4	0	0.037	0	0.023	0.262	0.087786	0.064	0.079	0.810126582
RDM_H18_3002G_ST6_TEST1	H18	3002G	ST6	-0.012	0.023	-0.52173913	0.08	0.288	0.277778	0.105	0.082	1.280487805
RDM_CF1_239F_ST0_TEST1	CF1	239F	ST0	0.005	0.026	0.192307692	0.017	0.11	0.154545	0.035	0.054	0.648148148
RDM_CF1_239E_ST1_TEST1	CF1	239E	ST1	0.003	0.024	0.125	0.015	0.135	0.111111			#DIV/0!
RDM_CF1_239D_ST_TEST1	CF1	239D	STT	0.004	0.023	0.173913043	0.016	0.099	0.161616	0.028	0.052	0.538461538
RDM_CF1_239C_ST0_TEST1	CF1	239C	ST0	-0.003	0.015	-0.2	0.01	0.098	0.102041	0.025	0.05	0.5
RDM_CF1_239B_ST0_TEST1	CF1	239B	ST0	-0.001	0.024	-0.041666667	0.011	0.108	0.101852	0.028	0.052	0.538461538
RDM_CF1_239A_ST5_TEST1	CF1	239A	ST5	0.002	0.012	0.166666667	0.014	0.268	0.052239	0.091	0.055	1.654545455
RDM_MM_506A_WINDOWA_1	MM	506A	1	-0.045	0.028	-1.607142857	0.039	0.289	0.134948	0.051	0.106	0.481132075
RDM_MM_506A_WINDOWA_2	MM	506A	2	-0.05	0.022	-2.272727273	0.015	0.291	0.051546	0.054	0.117	0.461538462
RDM_MM_506A_WINDOWA_3	MM	506A	3	-0.035	0.061	-0.573770492	0.044	0.443	0.099323	0.066	0.121	0.545454545
RDM_MM_506A_WINDOWA_4	MM	506A	4	-0.038	0.068	-0.558823529	0.051	0.484	0.105372	0.069	0.161	0.428571429
RDM_MM_506A_WINDOWA_5	MM	506A	5	-0.042	0.061	-0.68852459	0.052	0.483	0.10766	0.066	0.164	0.402439024
RDM_MM_506A_WINDOWA_6	MM	506A	6	-0.057	0.006	-9.5	0.006	0.216	0.027778	0.053	0.089	0.595505618
RDM_MM_506A_WINDOWA_7	MM	506A	7	-0.041	0.032	-1.28125	0.025	0.291	0.085911	0.051	0.118	0.43220339
RDM_MM_506A_WINDOWA_8	MM	506A	8	-0.049	0.03	-1.633333333	0.031	0.325	0.095385	0.06	0.112	0.535714286
RDM_MM_506A_WINDOWAA_3	MM	506A	3	-0.031	0.039	-0.794871795	0.047	0.456	0.10307	0.065	0.142	0.457746479
RDM_MM_506A_WINDOWAA_4	MM	506A	4	-0.027	0.038	-0.710526316	0.049	0.486	0.100823	0.064	0.13	0.492307692
RDM_MM_506A_WINDOWAA_5	MM	506A	5	-0.033	0.004	-8.25	0.011	0.219	0.050228	0.047	0.079	0.594936709
RDM_MM_506A_WINDOWAA_6	MM	506A	6	-0.013	0.048	-0.270833333	0.058	0.542	0.107011	0.081	0.146	0.554794521
RDM_MM_506A_WINDOWAA_7	MM	506A	7	-0.03	0.024	-1.25	0.047	0.426	0.110329	0.067	0.121	0.553719008
RDM_MM_506A_WINDOWAA_8	MM	506A	8	-0.019	0.031	-0.612903226	0.043	0.397	0.108312	0.083	0.117	0.709401709
RDM_MM_506A_WINDOWAA_9	MM	506A	9	-0.032	0.031	-1.032258065	0.047	0.495	0.094949	0.081	0.127	0.637795276
RDM_MM_506A_WINDOWAA_10	MM	506A	10	-0.015	0.039	-0.384615385	0.05	0.491	0.101833	0.068	0.141	0.482269504
RDM_MM_506A_WINDOWB_3	MM	506A	3	-0.014	0.047	-0.29787234	0.05	0.291	0.171821	0.07	0.134	0.52238806
RDM_MM_506A_WINDOWB_4	MM	506A	4	-0.021	0.041	-0.512195122	0.042	0.282	0.148936	0.053	0.122	0.43442623
RDM_MM_506A_WINDOWB_8	MM	506A	8	-0.007	0.088	-0.079545455	0.083	0.498	0.166667	0.082	0.16	0.5125
RDM_MM_506A_WINDOWB_9	MM	506A	9	-0.018	0.042	-0.428571429	0.043	0.275	0.156364	0.063	0.108	0.583333333
RDM_MM_506A_WINDOWC_1	MM	506A	1	-0.023	0.054	-0.425925926	0.051	0.408	0.125	0.07	0.114	0.614035088
RDM_MM_506A_WINDOWC_2	MM	506A	2	-0.022	0.065	-0.338461538	0.06	0.444	0.135135	0.064	0.13	0.492307692
RDM_MM_506A_WINDOWC_3	MM	506A	3	-0.033	0.037	-0.891891892	0.032	0.326	0.09816	0.065	0.141	0.460992908
RDM_MM_506A_WINDOWC_11	MM	506A	11	-0.028	0.06	-0.466666667	0.053	0.439	0.120729	0.075	0.128	0.5859375
RDM_MM_506A_WINDOWD_16	MM	506A	16	-0.031	0.044	-0.704545455	0.053	0.363	0.146006	0.062	0.108	0.574074074
RDM_MM_506A_WINDOWD_17	MM	506A	17	-0.028	0.075	-0.373333333	0.071	0.568	0.125	0.083	0.191	0.434554974
RDM_MM_506A_WINDOWD_19	MM	506A	19	-0.031	0.052	-0.596153846	0.055	0.401	0.137157	0.073	0.129	0.565891473
RDM_MM_506A_WINDOWD_20	MM	506A	20	-0.03	0.069	-0.434782609	0.067	0.506	0.132411	0.093	0.185	0.502702703
RDM_MM_506A_WINDOWE_2	MM	506A	2	-0.033	0.062	-0.532258065	0.139	0.543	0.255985	0.082	0.175	0.468571429
RDM_MM_506A_WINDOWE_3	MM	506A	3	-0.039	0.017	-2.294117647	0.033	0.277	0.119134	0.051	0.101	0.504950495
RDM_MM_506A_WINDOWF_4	MM	506A	4	-0.006	0.052	-0.115384615	0.074	0.49	0.15102	0.079	0.152	0.519736842
RDM_MM_506A_WINDOWF_5	MM	506A	5	-0.028	0.022	-1.272727273	0.029	0.247	0.117409	0.05	0.097	0.515463918
RDM_MM_506A_WINDOWI_10	MM	506A	10	-0.02	0.038	-0.526315789	0.053	0.348	0.152299	0.06	0.102	0.588235294
RDM_MM_506A_WINDOWI_12	MM	506A	12	-0.025	0.039	-0.641025641	0.051	0.401	0.127182	0.072	0.147	0.489795918
RDM_MM_506A_WINDOWI_14	MM	506A	14	-0.021	0.067	-0.313432836	0.052	0.419	0.124105	0.079	0.139	0.568345324
RDM_MM_506A_WINDOWJ_4	MM	506A	4	-0.04	0.035	-1.142857143	0.03	0.28	0.107143	0.069	0.112	0.616071429
RDM_MM_506A_WINDOWJ_5	MM	506A	5	0.001	0.077	0.012987013	0.084	0.497	0.169014	0.079	0.156	0.506410256
RDM_MM_506A_WINDOWK_14	MM	506A	14	-0.039	0.05	-0.78	0.036	0.4	0.09	0.074	0.123	0.601626016
RDM_MM_506A_WINDOWK_18	MM	506A	18	-0.033	0.058	-0.568965517	0.066	0.61	0.108197	0.092	0.176	0.522727273
RDM_MM_506A_WINDOWK_20	MM	506A	20	-0.024	0.052	-0.461538462	0.046	0.413	0.11138	0.071	0.132	0.537878788
RDM_MM_506A_WINDOWL_7	MM	506A	7	-0.009	0.095	-0.094736842	0.056	0.398	0.140704	0.067	0.134	0.5
RDM_MM_506A_WINDOWL_8	MM	506A	8	0.231	0.088	2.625	0.069	0.358	0.192737	0.092	0.146	0.630136986
RDM_MM_506A_WINDOWL_15	MM	506A	15	-0.005	0.062	-0.080645161	0.076	0.472	0.161017	0.081	0.144	0.5625
RDM_MM_506A_WINDOWN_3	MM	506A	3	-0.034	0.032	-1.0625	0.049	0.475	0.103158	0.067	0.134	0.5
RDM_MM_506A_WINDOWN_6	MM	506A	6	-0.031	0.055	-0.563636364	0.072	0.666	0.108108	0.082	0.175	0.468571429
RDM_MM_506A_WINDOWN_9	MM	506A	9	-0.034	0.039	-0.871794872	0.045	0.516	0.087209	0.071	0.16	0.44375
RDM_MM_506A_WINDOWO_4	MM	506A	4	-0.03	0.052	-0.576923077	0.06	0.406	0.147783	0.072	0.129	0.558139535
RDM_MM_506A_WINDOWO_6	MM	506A	6	-0.038	0.031	-1.225806452	0.042	0.338	0.12426	0.079	0.14	0.564285714
RDM_MM_506A_WINDOWO_8	MM	506A	8	-0.045	0.024	-1.875	0.047	0.346	0.135838	0.063	0.11	0.572727273
RDM_MM_211ASH_WINDOWA_1	MM	211ASH	1	-0.014	0.004	-3.5	0.005	0.065	0.076923	0.017	0.046	0.369565217
RDM_MM_211ASH_WINDOWA_7	MM	211ASH	7	-0.003	0.07	-0.042857143	0.052	0.361	0.144044	0.062	0.123	0.504065041
RDM_MM_211ASH_WINDOWC_2	MM	211ASH	2	0.006	0.058	0.103448276	0.05	0.179	0.27933	0.044	0.073	0.602739726
RDM_MM_211ASH_WINDOWC_1	MM	211ASH	1	-0.009	0.01	-0.9	0.014	-0.067	-0.20896	0.022	0.044	0.5
RDM_MM_211ASH_WINDOWC_4	MM	211ASH	4	-0.009	0.026	-0.346153846	0.023	0.131	0.175573	0.034	0.058	0.586206897
RDM_MM_211ASH_WINDOWE_11	MM	211ASH	11	-0.016	0.062	-0.258064516	0.047	0.339	0.138643	0.062	0.12	0.516666667
RDM_MM_211ASH_WINDOWE_16	MM	211ASH	16	-0.014	0.094	-0.14893617	0.061	0.473	0.128964	0.078	0.157	0.496815287

RDM_MM_211ASH_WINDOWF_11	MM	211ASH	11	-0.013	0.058	-0.224137931	0.067	0.258	0.25969	0.058	0.097	0.597938144
RDM_MM_211ASH_WINDOWF_16	MM	211ASH	16	-0.017	0.058	-0.293103448	0.041	0.313	0.13099	0.055	0.11	0.5
RDM_MM_211ASH_WINDOWF_18	MM	211ASH	18	-0.007	0.087	-0.08045977	0.062	0.368	0.168478	0.071	0.121	0.58677686
RDM_501_WINDOWA_1	MM	501	1	-0.044	0.013	-3.384615385	0.066	0.398	0.165829	0.087	0.079	1.101265823
RDM_501_WINDOWA_2	MM	501	2	-0.044	0.01	-4.4	0.086	0.473	0.181818	0.107	0.092	1.163043478
RDM_501_WINDOWA_4	MM	501	4	-0.048	0.029	-1.655172414	0.19	0.273	0.695971	0.065	0.051	1.274509804
RDM_501_WINDOWAA_4	MM	501	4	0.011	0.092	0.119565217	0.069	0.424	0.162736	0.08	0.139	0.575539568
RDM_501_WINDOWAA_5	MM	501	5	0.006	0.091	0.065934066	0.073	0.457	0.159737	0.072	0.143	0.503496503
RDM_501_WINDOWB_2	MM	501	2	-0.029	0.01	-2.9	0.002	0.087	0.022989	0.026	0.048	0.541666667
RDM_501_WINDOWB_3	MM	501	3	-0.016	0.088	-0.181818182	0.049	0.355	0.138028	0.07	0.095	0.736842105
RDM_501_WINDOWBB_14	MM	501	14	-0.016	0.052	-0.307692308	0.048	0.383	0.125326	0.069	0.109	0.633027523
RDM_501_WINDOWBB_15	MM	501	15	-0.015	0.078	-0.192307692	0.053	0.522	0.101533	0.074	0.151	0.490066225
RDM_501_WINDOWBB_16	MM	501	16	-0.018	0.078	-0.230769231	0.054	0.561	0.096257	0.076	0.156	0.487179487
RDM_501_WINDOWC_1	MM	501	1	-0.017	0.098	-0.173469388	0.062	0.419	0.147971	0.081	0.136	0.595588235
RDM_501_WINDOWC_2	MM	501	2	-0.022	0.037	-0.594594595	0.024	0.192	0.125	0.046	0.071	0.647887324
RDM_501_WINDOWC_3	MM	501	3	-0.026	0.097	-0.268041237	0.04	0.321	0.124611	0.082	0.109	0.752293578
RDM_501_WINDOWF_5	MM	501	5	-0.024	0.184	-0.130434783	0.084	0.571	0.14711	0.116	0.112	1.035714286
RDM_501_WINDOWF_16	MM	501	16	-0.025	0.12	-0.208333333	0.069	0.452	0.152655	0.095	0.095	1
RDM_501_WINDOWF_17	MM	501	17	-0.032	0.147	-0.217687075	0.074	0.612	0.120915	0.11	0.124	0.887096774
RDM_501_WINDOWG_2	MM	501	2	-0.008	0.055	-0.145454545	0.044	0.253	0.173913	0.052	0.086	0.604651163
RDM_501_WINDOWG_3	MM	501	3	-0.019	0.025	-0.76	0.02	0.179	0.111732	0.041	0.065	0.630769231
RDM_501_WINDOWG_6	MM	501	6	-0.01	0.067	-0.149253731	0.052	0.347	0.149856	0.066	0.118	0.559322034
RDM_501_WINDOWH_1	MM	501	1	-0.012	0.107	-0.112149533	0.065	0.247	0.263158	0.077	0.12	0.641666667
RDM_501_WINDOWH_3	MM	501	3	-0.009	0.109	-0.082568807	0.056	0.254	0.220472	0.069	0.098	0.704081633
RDM_501_WINDOWH_6	MM	501	6	-0.015	0.057	-0.263157895	0.055	0.311	0.176849	0.063	0.102	0.617647059
RDM_501_WINDOWI_6	MM	501	6	-0.009	0.023	-0.391304348	0.063	0.288	0.21875	0.08	0.085	0.941176471
RDM_501_WINDOWI_7	MM	501	7	-0.008	0.009	-0.888888889	0.06	0.218	0.275229	0.073	0.06	1.216666667
RDM_501_WINDOWI_8	MM	501	8	-0.008	0.085	-0.094117647	0.036	0.238	0.151261	0.052	0.079	0.658227848
RDM_501_WINDOWJ_5	MM	501	5	-0.003	0.129	-0.023255814	0.06	0.266	0.225564	0.104	0.131	0.79389313
RDM_501_WINDOWJ_7	MM	501	7	-0.003	0.065	-0.046153846	0.046	0.265	0.173585	0.083	0.102	0.81372549
RDM_501_WINDOWJ_8	MM	501	8	-0.007	0.065	-0.107692308	0.062	0.403	0.153846	0.081	0.102	0.794117647
RDM_501_WINDOWK_11	MM	501	11	-0.015	0.05	-0.3	0.34	0.279	1.218638	0.064	0.085	0.752941176
RDM_501_WINDOWK_12	MM	501	12	-0.002	0.067	-0.029850746	0.058	0.331	0.175227	0.071	0.116	0.612068966
RDM_501_WINDOWL_5	MM	501	5	0	0.081	0	0.076	0.43	0.176744	0.081	0.145	0.55862069
RDM_501_WINDOWL_6	MM	501	6	0.001	0.079	0.012658228	0.07	0.444	0.157658	0.082	0.137	0.598540146
RDM_501_WINDOWL_7	MM	501	7	0.002	0.075	0.026666667	0.066	0.384	0.171875	0.083	0.123	0.674796748
RDM_501_WINDOWM_5	MM	501	5	-0.007	0.05	-0.14	0.038	0.24	0.158333	0.052	0.089	0.584269663
RDM_501_WINDOWM_6	MM	501	6	0.001	0.066	0.015151515	0.051	0.296	0.172297	0.062	0.114	0.543859649
RDM_501_WINDOWM_9	MM	501	9	-0.005	0.082	-0.06097561	0.055	0.37	0.148649	0.072	0.103	0.699029126
RDM_501_WINDOWO_10	MM	501	10	-0.004	0.051	-0.078431373	0.056	0.316	0.177215	0.066	0.1	0.66
RDM_501_WINDOWO_11	MM	501	11	-0.002	0.077	-0.025974026	0.066	0.41	0.160976	0.085	0.127	0.669291339
RDM_501_WINDOWO_14	MM	501	14	-0.003	0.072	-0.041666667	0.063	0.415	0.151807	0.077	0.126	0.611111111
RDM_501_WINDOWP_6	MM	501	6	-0.013	0.066	-0.196969697	0.038	0.254	0.149606	0.054	0.103	0.524271845
RDM_501_WINDOWP_7	MM	501	7	-0.009	0.065	-0.138461538	0.058	0.367	0.158038	0.073	0.137	0.532846715
RDM_501_WINDOWP_11	MM	501	11	-0.005	0.096	-0.052083333	0.069	0.502	0.13745	0.085	0.143	0.594405594
RDM_501_WINDOWR_12	MM	501	12	-0.003	0.056	-0.053571429	0.032	0.177	0.180791	0.068	0.081	0.839506173
RDM_501_WINDOWR_13	MM	501	13	-0.005	0.034	-0.147058824	0.115	0.486	0.236626	0.109	0.091	1.197802198
RDM_501_WINDOWS_1	MM	501	1	-0.015	0.022	-0.681818182	0.083	0.33	0.251515	0.089	0.086	1.034883721
RDM_501_WINDOWT_3	MM	501	3	-0.007	0.07	-0.1	0.038	0.254	0.149606	0.074	0.069	1.072463768
RDM_501_WINDOWT_4	MM	501	4	-0.013	0.095	-0.136842105	0.059	0.386	0.15285	0.09	0.114	0.789473684
RDM_501_WINDOWT_5	MM	501	5	-0.007	0.074	-0.094594595	0.048	0.254	0.188976	0.065	0.059	1.101694915
RDM_501_WINDOWU_3	MM	501	3	-0.024	0.02	-1.2	0.112	0.483	0.231884	0.112	0.116	0.965517241
RDM_501_WINDOWU_5	MM	501	5	-0.026	0.013	-2	0.104	0.466	0.223176	0.107	0.088	1.215909091
RDM_501_WINDOWU_6	MM	501	6	-0.025	0.017	-1.470588235	0.087	0.383	0.227154	0.103	0.101	1.01980198
RDM_501_WINDOWV_13	MM	501	13	-0.045	0.012	-3.75	0.027	0.318	0.084906	0.113	0.077	1.467532468
RDM_501_WINDOWV_14	MM	501	14	-0.042	-0.009	4.666666667	0.041	0.316	0.129747	0.122	0.076	1.605263158
RDM_501_WINDOWV_15	MM	501	15	-0.048	-0.004	12	0.052	0.342	0.152047	0.126	0.071	1.774647887
RDM_501_WINDOWW_9	MM	501	9	-0.021	0.022	-0.954545455	0.063	0.32	0.196875	0.098	0.084	1.166666667
RDM_501_WINDOWW_10	MM	501	10	-0.025	0.075	-0.333333333	0.078	0.412	0.18932	0.111	0.097	1.144329897
RDM_501_WINDOWW_14	MM	501	14	-0.025	0.019	-1.315789474	0.077	0.369	0.208672	0.105	0.088	1.193181818
RDM_501_WINDOWY_4	MM	501	4	0.002	0.109	0.018348624	0.088	0.508	0.173228	0.078	0.155	0.503225806
RDM_501_WINDOWY_5	MM	501	5	-0.004	0.079	-0.050632911	0.07	0.424	0.165094	0.075	0.167	0.449101796
RDM_501_WINDOWY_6	MM	501	6	-0.005	0.071	-0.070422535	0.071	0.414	0.171498	0.071	0.156	0.455128205
RDM_501_WINDOWZ_3	MM	501	3	-0.019	0.026	-0.730769231	0.041	0.314	0.130573	0.068	0.101	0.673267327
RDM_501_WINDOWZ_5	MM	501	5	-0.02	0.044	-0.454545455	0.058	0.464	0.125	0.081	0.112	0.723214286
RDM_501_WINDOWZ_10	MM	501	3	-0.027	0.049	-0.551020408	0.061	0.515	0.118447	0.083	0.129	0.643410853

Table 9: RDM FTIR and mFTIR data

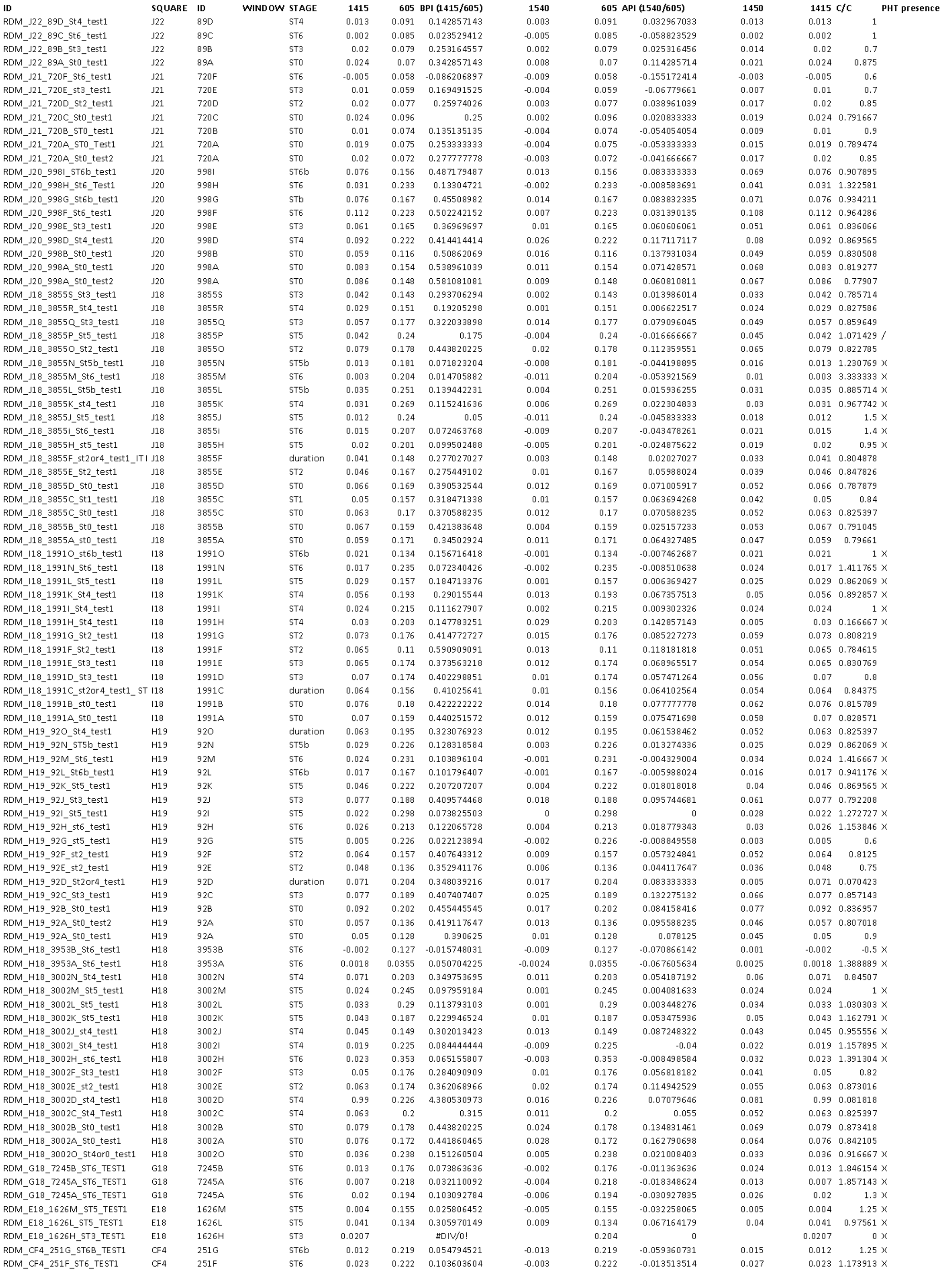

ID	SQUARE	ID	WINDOW	STAGE	1415	605	BPI (1415/605)	1540	605	API (1540/605)	1450	1415	C/C	PHT presence
RDM_J22_89D_St4_test1	J22	89D		ST4	0.013	0.091	0.142857143	0.003	0.091	0.032967033	0.013	0.013	1	
RDM_J22_89C_St6_test1	J22	89C		ST6	0.002	0.085	0.023529412	-0.005	0.085	-0.058823529	0.002	0.002	1	
RDM_J22_89B_St3_test1	J22	89B		ST3	0.02	0.079	0.253164557	0.002	0.079	0.025316456	0.014	0.02	0.7	
RDM_J22_89A_St0_test1	J22	89A		ST0	0.024	0.07	0.342857143	0.008	0.07	0.114285714	0.021	0.024	0.875	
RDM_J21_720F_St6_test1	J21	720F		ST6	-0.005	0.058	-0.086206897	-0.009	0.058	-0.155172414	-0.003	-0.005	0.6	
RDM_J21_720E_st3_test1	J21	720E		ST3	0.01	0.059	0.169491525	-0.004	0.059	-0.06779661	0.007	0.01	0.7	
RDM_J21_720D_St2_test1	J21	720D		ST2	0.02	0.077	0.25974026	0.003	0.077	0.038961039	0.017	0.02	0.85	
RDM_J21_720C_St0_test1	J21	720C		ST0	0.024	0.096	0.25	0.002	0.096	0.020833333	0.019	0.024	0.791667	
RDM_J21_720B_ST0_test1	J21	720B		ST0	0.01	0.074	0.135135135	-0.004	0.074	-0.054054054	0.009	0.01	0.9	
RDM_J21_720A_ST0_Test1	J21	720A		ST0	0.019	0.075	0.253333333	-0.004	0.075	-0.053333333	0.015	0.019	0.789474	
RDM_J21_720A_St0_test2	J21	720A		ST0	0.02	0.072	0.277777778	-0.003	0.072	-0.041666667	0.017	0.02	0.85	
RDM_J20_998I_ST6b_test1	J20	998I		ST6b	0.076	0.156	0.487179487	0.013	0.156	0.083333333	0.069	0.076	0.907895	
RDM_J20_998H_St6_Test1	J20	998H		ST6	0.031	0.233	0.13304721	-0.002	0.233	-0.008583691	0.041	0.031	1.322581	
RDM_J20_998G_St6b_test1	J20	998G		STb	0.076	0.167	0.45508982	0.014	0.167	0.083832335	0.071	0.076	0.934211	
RDM_J20_998F_St6_test1	J20	998F		ST6	0.112	0.223	0.502242152	0.007	0.223	0.031390135	0.108	0.112	0.964286	
RDM_J20_998E_St3_test1	J20	998E		ST3	0.061	0.165	0.36969697	0.01	0.165	0.060606061	0.051	0.061	0.836066	
RDM_J20_998D_St4_test1	J20	998D		ST4	0.092	0.222	0.414414414	0.026	0.222	0.117117117	0.08	0.092	0.869565	
RDM_J20_998B_St0_test1	J20	998B		ST0	0.059	0.116	0.50862069	0.016	0.116	0.137931034	0.049	0.059	0.830508	
RDM_J20_998A_St0_test1	J20	998A		ST0	0.083	0.154	0.538961039	0.011	0.154	0.071428571	0.068	0.083	0.819277	
RDM_J20_998A_St0_test2	J20	998A		ST0	0.086	0.148	0.581081081	0.009	0.148	0.060810811	0.067	0.086	0.77907	
RDM_J18_3855S_St3_test1	J18	3855S		ST3	0.042	0.143	0.293706294	0.002	0.143	0.013986014	0.033	0.042	0.785714	
RDM_J18_3855R_St4_test1	J18	3855R		ST4	0.029	0.151	0.19205298	0.001	0.151	0.006622517	0.024	0.029	0.827586	
RDM_J18_3855Q_St3_test1	J18	3855Q		ST3	0.057	0.177	0.322033898	0.014	0.177	0.079096045	0.049	0.057	0.859649	
RDM_J18_3855P_St5_test1	J18	3855P		ST5	0.042	0.24	0.175	-0.004	0.24	-0.016666667	0.045	0.042	1.071429	/
RDM_J18_3855O_St2_test1	J18	3855O		ST2	0.079	0.178	0.443820225	0.02	0.178	0.112359551	0.065	0.079	0.822785	
RDM_J18_3855N_St5b_test1	J18	3855N		ST5b	0.013	0.181	0.071823204	-0.008	0.181	-0.044198895	0.016	0.013	1.230769	X
RDM_J18_3855M_St6_test1	J18	3855M		ST6	0.003	0.204	0.014705882	-0.011	0.204	-0.053921569	0.01	0.003	3.333333	X
RDM_J18_3855L_St5b_test1	J18	3855L		ST5b	0.035	0.251	0.139442231	0.004	0.251	0.015936255	0.031	0.035	0.885714	X
RDM_J18_3855K_st4_test1	J18	3855K		ST4	0.031	0.269	0.115241636	0.006	0.269	0.022304833	0.03	0.031	0.967742	X
RDM_J18_3855J_St5_test1	J18	3855J		ST5	0.012	0.24	0.05	-0.011	0.24	-0.045833333	0.018	0.012	1.5	X
RDM_J18_3855i_St6_test1	J18	3855i		ST6	0.015	0.207	0.072463768	-0.009	0.207	-0.043478261	0.021	0.015	1.4	X
RDM_J18_3855H_st5_test1	J18	3855H		ST5	0.02	0.201	0.099502488	-0.005	0.201	-0.024875622	0.019	0.02	0.95	X
RDM_J18_3855F_st2or4_test1_IT I	J18	3855F		duration	0.041	0.148	0.277027027	0.003	0.148	0.02027027	0.033	0.041	0.804878	
RDM_J18_3855E_St2_test1	J18	3855E		ST2	0.046	0.167	0.275449102	0.01	0.167	0.05988024	0.039	0.046	0.847826	
RDM_J18_3855D_St0_test1	J18	3855D		ST0	0.066	0.169	0.390532544	0.012	0.169	0.071005917	0.052	0.066	0.787879	
RDM_J18_3855C_St1_test1	J18	3855C		ST1	0.05	0.157	0.318471338	0.01	0.157	0.063694268	0.042	0.05	0.84	
RDM_J18_3855C_St0_test1	J18	3855C		ST0	0.063	0.17	0.370588235	0.012	0.17	0.070588235	0.052	0.063	0.825397	
RDM_J18_3855B_St0_test1	J18	3855B		ST0	0.067	0.159	0.421383648	0.004	0.159	0.025157233	0.053	0.067	0.791045	
RDM_J18_3855A_st0_test1	J18	3855A		ST0	0.059	0.171	0.34502924	0.011	0.171	0.064327485	0.047	0.059	0.79661	
RDM_I18_1991O_st6b_test1	I18	1991O		ST6b	0.021	0.134	0.156716418	-0.001	0.134	-0.007462687	0.021	0.021	1	X
RDM_I18_1991N_St6_test1	I18	1991N		ST6	0.017	0.235	0.072340426	-0.002	0.235	-0.008510638	0.024	0.017	1.411765	X
RDM_I18_1991L_St5_test1	I18	1991L		ST5	0.029	0.157	0.184713376	0.001	0.157	0.006369427	0.025	0.029	0.862069	X
RDM_I18_1991K_St4_test1	I18	1991K		ST4	0.056	0.193	0.29015544	0.013	0.193	0.067357513	0.05	0.056	0.892857	X
RDM_I18_1991I_St4_test1	I18	1991I		ST4	0.024	0.215	0.111627907	0.002	0.215	0.009302326	0.024	0.024	1	X
RDM_I18_1991H_St4_test1	I18	1991H		ST4	0.03	0.203	0.147783251	0.029	0.203	0.142857143	0.005	0.03	0.166667	X
RDM_I18_1991G_St2_test1	I18	1991G		ST2	0.073	0.176	0.414772727	0.015	0.176	0.085227273	0.059	0.073	0.808219	
RDM_I18_1991F_St2_test1	I18	1991F		ST2	0.065	0.11	0.590909091	0.013	0.11	0.118181818	0.051	0.065	0.784615	
RDM_I18_1991E_St3_test1	I18	1991E		ST3	0.065	0.174	0.373563218	0.012	0.174	0.068965517	0.054	0.065	0.830769	
RDM_I18_1991D_St3_test1	I18	1991D		ST3	0.07	0.174	0.402298851	0.01	0.174	0.057471264	0.056	0.07	0.8	
RDM_I18_1991C_st2or4_test1_ ST	I18	1991C		duration	0.064	0.156	0.41025641	0.01	0.156	0.064102564	0.054	0.064	0.84375	
RDM_I18_1991B_st0_test1	I18	1991B		ST0	0.076	0.18	0.422222222	0.014	0.18	0.077777778	0.062	0.076	0.815789	
RDM_I18_1991A_St0_test1	I18	1991A		ST0	0.07	0.159	0.440251572	0.012	0.159	0.075471698	0.058	0.07	0.828571	
RDM_H19_92O_St4_test1	H19	92O		duration	0.063	0.195	0.323076923	0.012	0.195	0.061538462	0.052	0.063	0.825397	
RDM_H19_92N_ST5b_test1	H19	92N		ST5b	0.029	0.226	0.128318584	0.003	0.226	0.013274336	0.025	0.029	0.862069	X
RDM_H19_92M_St6_test1	H19	92M		ST6	0.024	0.231	0.103896104	-0.001	0.231	-0.004329004	0.034	0.024	1.416667	X
RDM_H19_92L_St6b_test1	H19	92L		ST6b	0.017	0.167	0.101796407	-0.001	0.167	-0.005988024	0.016	0.017	0.941176	X
RDM_H19_92K_St5_test1	H19	92K		ST5	0.046	0.222	0.207207207	0.004	0.222	0.018018018	0.04	0.046	0.869565	X
RDM_H19_92J_St3_test1	H19	92J		ST3	0.077	0.188	0.409574468	0.018	0.188	0.095744681	0.061	0.077	0.792208	
RDM_H19_92I_St5_test1	H19	92I		ST5	0.022	0.298	0.073825503	0	0.298	0	0.028	0.022	1.272727	X
RDM_H19_92H_st6_test1	H19	92H		ST6	0.026	0.213	0.122065728	0.004	0.213	0.018779343	0.03	0.026	1.153846	X
RDM_H19_92G_st5_test1	H19	92G		ST5	0.005	0.226	0.022123894	-0.002	0.226	-0.008849558	0.003	0.005	0.6	
RDM_H19_92F_st2_test1	H19	92F		ST2	0.064	0.157	0.407643312	0.009	0.157	0.057324841	0.052	0.064	0.8125	
RDM_H19_92E_st2_test1	H19	92E		ST2	0.048	0.136	0.352941176	0.006	0.136	0.044117647	0.036	0.048	0.75	
RDM_H19_92D_St2or4_test1	H19	92D		duration	0.071	0.204	0.348039216	0.017	0.204	0.083333333	0.005	0.071	0.070423	
RDM_H19_92C_St3_test1	H19	92C		ST3	0.077	0.189	0.407407407	0.025	0.189	0.132275132	0.066	0.077	0.857143	
RDM_H19_92B_St0_test1	H19	92B		ST0	0.092	0.202	0.455445545	0.017	0.202	0.084158416	0.077	0.092	0.836957	
RDM_H19_92A_St0_test2	H19	92A		ST0	0.057	0.136	0.419117647	0.013	0.136	0.095588235	0.046	0.057	0.807018	
RDM_H19_92A_St0_test1	H19	92A		ST0	0.05	0.128	0.390625	0.01	0.128	0.078125	0.045	0.05	0.9	
RDM_H18_3953B_St6_test1	H18	3953B		ST6	-0.002	0.127	-0.015748031	-0.009	0.127	-0.070866142	0.001	-0.002	-0.5	X
RDM_H18_3953A_St6_test1	H18	3953A		ST6	0.0018	0.0355	0.050704225	-0.0024	0.0355	-0.067605634	0.0025	0.0018	1.388889	X
RDM_H18_3002N_St4_test1	H18	3002N		ST4	0.071	0.203	0.349753695	0.011	0.203	0.054187192	0.06	0.071	0.84507	
RDM_H18_3002M_St5_test1	H18	3002M		ST5	0.024	0.245	0.097959184	0.001	0.245	0.004081633	0.024	0.024	1	X
RDM_H18_3002L_St5_test1	H18	3002L		ST5	0.033	0.29	0.113793103	0.001	0.29	0.003448276	0.034	0.033	1.030303	X
RDM_H18_3002K_St5_test1	H18	3002K		ST5	0.043	0.187	0.229946524	0.01	0.187	0.053475936	0.05	0.043	1.162791	X
RDM_H18_3002J_st4_test1	H18	3002J		ST4	0.045	0.149	0.302013423	0.013	0.149	0.087248322	0.043	0.045	0.955556	X
RDM_H18_3002I_St4_test1	H18	3002I		ST4	0.019	0.225	0.084444444	-0.009	0.225	-0.04	0.022	0.019	1.157895	X
RDM_H18_3002H_st6_test1	H18	3002H		ST6	0.023	0.353	0.065155807	-0.003	0.353	-0.008498584	0.032	0.023	1.391304	X
RDM_H18_3002F_St3_test1	H18	3002F		ST3	0.05	0.176	0.284090909	0.01	0.176	0.056818182	0.041	0.05	0.82	
RDM_H18_3002E_st2_test1	H18	3002E		ST2	0.063	0.174	0.362068966	0.02	0.174	0.114942529	0.055	0.063	0.873016	
RDM_H18_3002D_st4_test1	H18	3002D		ST4	0.99	0.226	4.380530973	0.016	0.226	0.07079646	0.081	0.99	0.081818	
RDM_H18_3002C_St4_Test1	H18	3002C		ST4	0.063	0.2	0.315	0.011	0.2	0.055	0.052	0.063	0.825397	
RDM_H18_3002B_St0_test1	H18	3002B		ST0	0.079	0.178	0.443820225	0.024	0.178	0.134831461	0.069	0.079	0.873418	
RDM_H18_3002A_St0_test1	H18	3002A		ST0	0.076	0.172	0.441860465	0.028	0.172	0.162790698	0.064	0.076	0.842105	
RDM_H18_3002O_St4or0_test1	H18	3002O		ST0	0.036	0.238	0.151260504	0.005	0.238	0.021008403	0.033	0.036	0.916667	X
RDM_G18_7245B_ST6_TEST1	G18	7245B		ST6	0.013	0.176	0.073863636	-0.002	0.176	-0.011363636	0.024	0.013	1.846154	X
RDM_G18_7245A_ST6_TEST1	G18	7245A		ST6	0.007	0.218	0.032110092	-0.004	0.218	-0.018348624	0.013	0.007	1.857143	X
RDM_G18_7245A_ST6_TEST1	G18	7245A		ST6	0.02	0.194	0.103092784	-0.006	0.194	-0.030927835	0.026	0.02	1.3	X
RDM_E18_1626M_ST5_TEST1	E18	1626M		ST5	0.004	0.155	0.025806452	-0.005	0.155	-0.032258065	0.005	0.004	1.25	X
RDM_E18_1626L_ST5_TEST1	E18	1626L		ST5	0.041	0.134	0.305970149	0.009	0.134	0.067164179	0.04	0.041	0.97561	X
RDM_E18_1626H_ST3_TEST1	E18	1626H		ST3	0.0207		#DIV/0!		0.204	0		0.0207	0	X
RDM_CF4_251G_ST6B_TEST1	CF4	251G		ST6b	0.012	0.219	0.054794521	-0.013	0.219	-0.059360731	0.015	0.012	1.25	X
RDM_CF4_251F_ST6_TEST1	CF4	251F		ST6	0.023	0.222	0.103603604	-0.003	0.222	-0.013513514	0.027	0.023	1.173913	X

RDM_CF4_251E_ST6_TEST1	CF4	251E	ST6	0.031	0.337	0.091988131	-0.014	0.337	-0.041543027	0.013	0.031	0.419355	X
RDM_CF4_251D_ST6_TEST1	CF4	251D	ST6	0.011	0.281	0.039145907	-0.004	0.281	-0.014234875	0.012	0.011	1.090909	X
RDM_CF4_251C_ST6_TEST1	CF4	251C	ST6	0.031	0.294	0.105442177	-0.001	0.294	-0.003401361	0.044	0.031	1.419355	X
RDM_CF4_251B_ST5b_TEST1	CF4	251B	ST5b	0.007	0.214	0.03271028	-0.005	0.214	-0.023364486	0.004	0.007	0.571429	x
RDM_CF4_251B_ST5b_TEST2	CF4	251B	ST5b	0.011	0.216	0.050925926	0.001	0.216	0.00462963	0.008	0.011	0.727273	
RDM_CF4_251A_ST6B_TEST1	CF4	251A	ST6b	0.021	0.236	0.088983051	-0.001	0.236	-0.004237288	0.022	0.021	1.047619	X
RDM_CF1_239N_ST3_TEST2	CF1	239N	ST3	0.0015	0.0307	0.048859935	-0.0047	0.0307	-0.153094463	0.0001	0.0015	0.066667	
RDM_CF1_239N_ST3_TEST1	CF1	239N	ST3	0.0197	0.0523	0.37667304	0.0123	0.0523	0.235181644	0.0181	0.0197	0.918782	
RDM_CF1_239M_ST6_TEST1	CF1	239M	ST6	0.021	0.134	0.156716418	0.005	0.134	0.037313433	0.024	0.021	1.142857	X
RDM_CF1_239L_ST5B_TEST1	CF1	239L	STB	0.013	0.107	0.121495327	-0.006	0.107	-0.056074766	0.012	0.013	0.923077	X
RDM_CF1_239K_ST5_TEST1	CF1	239K	ST5	0.004	0.139	0.028776978	-0.004	0.139	-0.028776978	0.003	0.004	0.75	X
RDM_CF1_239J_ST3_TEST1	CF1	239J	ST3	0.023	0.081	0.283950617	0.008	0.081	0.098765432	0.02	0.023	0.869565	X
RDM_CF1_239I_ST2_TEST1	CF1	239I	ST2	0.023	0.063	0.365079365	0.004	0.063	0.063492063	0.019	0.023	0.826087	X
RDM_CF1_239G_ST6B_TEST1	CF1	239G	ST6b	0.008	0.075	0.106666667	0.003	0.075	0.04	0.008	0.008	1	X
RDM_J18_3855A_ST6B_TEST1	J18	3855A	ST6b	0.028	0.219	0.127853881	-0.008	0.219	-0.03652968	0.028	0.028	1	
RDM_I18_1991P_ST6_TEST1	I18	1991P	ST6	0.024	0.194	0.12371134	-0.002	0.194	-0.010309278	0.029	0.024	1.208333	
RDM_I18_1991M_ST6_TEST1	I18	1991M	ST6	0.025	0.206	0.121359223	0.008	0.206	0.038834951	0.03	0.025	1.2	
RDM_I18_1991J_ST4_REST1	I18	1991J	ST4	0.037	0.158	0.234177215	0.004	0.158	0.025316456	0.03	0.037	0.810811	
RDM_H18_3002G_ST6_TEST1	H18	3002G	ST6	0.023	0.206	0.111650485	-0.001	0.206	-0.004854369	0.025	0.023	1.086957	
RDM_CF1_239F_ST0_TEST1	CF1	239F	ST0	0.026	0.076	0.342105263	0.007	0.076	0.092105263	0.022	0.026	0.846154	
RDM_CF1_239E_ST1_TEST1	CF1	239E	ST1	0.024	0.088	0.272727273	0.005	0.088	0.056818182	0.021	0.024	0.875	
RDM_CF1_239D_ST_TEST1	CF1	239D	STT	0.023	0.077	0.298701299	0.006	0.077	0.077922078	0.02	0.023	0.869565	
RDM_CF1_239C_ST0_TEST1	CF1	239C	ST0	0.015	0.075	0.2	-0.002	0.075	-0.026666667	0.012	0.015	0.8	
RDM_CF1_239B_ST0_TEST1	CF1	239B	ST0	0.024	0.078	0.307692308	0	0.078	0	0.02	0.024	0.833333	
RDM_CF1_239A_ST5_TEST1	CF1	239A	ST5	0.012	0.164	0.073170732	0.003	0.164	0.018292683	0.012	0.012	1	X
RDM_MM_506A_WINDOWA_1	MM	506A	1	0.028	0.129	0.217054264	-0.032	0.129	-0.248062016	0.013	0.027	0.481481	
RDM_MM_506A_WINDOWA_2	MM	506A	2	0.022	0.127	0.173228346	-0.034	0.127	-0.267716535	0.008	0.022	0.363636	
RDM_MM_506A_WINDOWA_3	MM	506A	3	0.061	0.181	0.337016575	-0.014	0.181	-0.077348066	0.038	0.061	0.622951	
RDM_MM_506A_WINDOWA_4	MM	506A	4	0.068	0.175	0.388571429	-0.02	0.175	-0.114285714	0.039	0.068	0.573529	
RDM_MM_506A_WINDOWA_5	MM	506A	5	0.061	0.198	0.308080808	-0.024	0.198	-0.121212121	0.039	0.061	0.639344	
RDM_MM_506A_WINDOWA_6	MM	506A	6	0.006	0.118	0.050847458	-0.046	0.118	-0.389830508	-0.008	0.006	-1.33333	
RDM_MM_506A_WINDOWA_7	MM	506A	7	0.032	0.13	0.246153846	-0.026	0.13	-0.2	0.015	0.032	0.46875	
RDM_MM_506A_WINDOWA_8	MM	506A	8	0.03	0.153	0.196078431	-0.035	0.153	-0.22875817	0.008	0.03	0.266667	
RDM_MM_506A_WINDOWAA_3	MM	506A	3	0.039	0.155	0.251612903	-0.013	0.155	-0.083870968	0.036	0.041	0.878049	
RDM_MM_506A_WINDOWAA_4	MM	506A	4	0.038	0.183	0.207650273	-0.02	0.183	-0.109289617	0.031	0.038	0.815789	
RDM_MM_506A_WINDOWAA_5	MM	506A	5	0.004	0.095	0.042105263	-0.028	0.095	-0.294736842	0.006	0.004	1.5	
RDM_MM_506A_WINDOWAA_6	MM	506A	6	0.048	0.176	0.272727273	-0.006	0.176	-0.034090909	0.044	0.048	0.916667	
RDM_MM_506A_WINDOWAA_7	MM	506A	7	0.024	0.144	0.166666667	-0.018	0.144	-0.125	0.02	0.024	0.833333	
RDM_MM_506A_WINDOWAA_8	MM	506A	8	0.031	0.171	0.18128655	-0.009	0.171	-0.052631579	0.029	0.031	0.935484	
RDM_MM_506A_WINDOWAA_9	MM	506A	9	0.031	0.156	0.198717949	-0.015	0.156	-0.096153846	0.03	0.031	0.967742	
RDM_MM_506A_WINDOWAA_10	MM	506A	10	0.039	0.154	0.253246753	-0.005	0.154	-0.032467532	0.037	0.039	0.948718	
RDM_MM_506A_WINDOWB_3	MM	506A	3	0.047	0.157	0.299363057	-0.001	0.157	-0.006369427	0.034	0.047	0.723404	
RDM_MM_506A_WINDOWB_4	MM	506A	4	0.041	0.132	0.310606061	-0.01	0.132	-0.075757576	0.029	0.041	0.707317	
RDM_MM_506A_WINDOWB_8	MM	506A	8	0.088	0.176	0.5	0.009	0.176	0.051136364	0.069	0.089	0.775281	
RDM_MM_506A_WINDOWB_9	MM	506A	9	0.042	0.135	0.311111111	-0.007	0.135	-0.051851852	0.031	0.042	0.738095	
RDM_MM_506A_WINDOWC_1	MM	506A	1	0.054	0.157	0.343949045	-0.009	0.157	-0.057324841	0.038	0.054	0.703704	
RDM_MM_506A_WINDOWC_2	MM	506A	2	0.065	0.143	0.454545455	-0.004	0.143	-0.027972028	0.042	0.065	0.646154	
RDM_MM_506A_WINDOWC_3	MM	506A	3	0.037	0.141	0.262411348	-0.02	0.141	-0.141843972	0.024	0.037	0.648649	
RDM_MM_506A_WINDOWC_11	MM	506A	11	0.06	0.157	0.382165605	-0.011	0.157	-0.070063694	0.043	0.06	0.716667	
RDM_MM_506A_WINDOWD_16	MM	506A	16	0.044	0.148	0.297297297	-0.017	0.148	-0.114864865	0.032	0.044	0.727273	
RDM_MM_506A_WINDOWD_17	MM	506A	17	0.075	0.213	0.352112676	-0.1	0.213	-0.469483568	0.052	0.075	0.693333	
RDM_MM_506A_WINDOWD_19	MM	506A	19	0.052	0.16	0.325	-0.014	0.16	-0.0875	0.037	0.052	0.711538	
RDM_MM_506A_WINDOWD_20	MM	506A	20	0.069	0.207	0.333333333	0.014	0.207	0.06763285	0.051	0.069	0.73913	
RDM_MM_506A_WINDOWE_2	MM	506A	2	0.062	0.191	0.32460733	-0.018	0.191	-0.094240838	0.042	0.062	0.677419	
RDM_MM_506A_WINDOWE_3	MM	506A	3	0.017	0.124	0.137096774	-0.03	0.124	-0.241935484	0.009	0.017	0.529412	
RDM_MM_506A_WINDOWF_4	MM	506A	4	0.052	0.171	0.304093567	0	0.171	0	0.043	0.052	0.826923	
RDM_MM_506A_WINDOWF_5	MM	506A	5	0.022	0.131	0.167938931	-0.02	0.131	-0.152671756	0.009	0.022	0.409091	
RDM_MM_506A_WINDOWI_10	MM	506A	10	0.038	0.151	0.251655629	-0.012	0.151	-0.079470199	0.033	0.038	0.868421	
RDM_MM_506A_WINDOWI_12	MM	506A	12	0.039	0.163	0.239263804	-0.015	0.163	-0.09202454	0.027	0.039	0.692308	
RDM_MM_506A_WINDOWI_14	MM	506A	14	0.067	0.17	0.394117647	-0.05	0.17	-0.294117647	0.056	0.067	0.835821	
RDM_MM_506A_WINDOWJ_4	MM	506A	4	0.035	0.145	0.24137931	-0.03	0.145	-0.206896552	0.034	0.035	0.971429	
RDM_MM_506A_WINDOWJ_5	MM	506A	5	0.076	0.175	0.434285714	0.011	0.175	0.062857143	0.07	0.077	0.909091	
RDM_MM_506A_WINDOWK_14	MM	506A	14	0.05	0.154	0.324675325	-0.041	0.154	-0.266233766	0.035	0.049	0.714286	
RDM_MM_506A_WINDOWK_18	MM	506A	18	0.058	0.19	0.305263158	-0.019	0.19	-0.1	0.05	0.058	0.862069	
RDM_MM_506A_WINDOWK_20	MM	506A	20	0.052	0.165	0.315151515	-0.025	0.165	-0.151515152	0.042	0.052	0.807692	
RDM_MM_506A_WINDOWL_7	MM	506A	7	0.095	0.155	0.612903226	0.007	0.155	0.04516129	0.078	0.095	0.821053	
RDM_MM_506A_WINDOWL_8	MM	506A	8	0.088	0.188	0.468085106	0.062	0.188	0.329787234	0.071	0.088	0.806818	
RDM_MM_506A_WINDOWL_15	MM	506A	15	0.062	0.172	0.360465116	0.005	0.172	0.029069767	0.056	0.062	0.903226	
RDM_MM_506A_WINDOWN_3	MM	506A	3	0.032	0.168	0.19047619	-0.025	0.168	-0.148809524	0.025	0.032	0.78125	
RDM_MM_506A_WINDOWN_6	MM	506A	6	0.055	0.217	0.253456221	-0.02	0.217	-0.092165899	0.046	0.053	0.867925	
RDM_MM_506A_WINDOWN_9	MM	506A	9	0.039	0.174	0.224137931	-0.017	0.174	-0.097701149	0.033	0.039	0.846154	
RDM_MM_506A_WINDOWO_4	MM	506A	4	0.052	0.14	0.371428571	-0.011	0.14	-0.078571429	0.036	0.052	0.692308	
RDM_MM_506A_WINDOWO_6	MM	506A	6	0.031	0.151	0.205298013	-0.022	0.151	-0.145695364	0.018	0.031	0.580645	
RDM_MM_506A_WINDOWO_8	MM	506A	8	0.024	0.134	0.179104478	-0.027	0.134	-0.201492537	0.01	0.024	0.416667	
RDM_MM_211ASH_WINDOWA_1	MM	211ASH	1	0.004	0.046	0.086956522	-0.011	0.046	-0.239130435	-0.003	0.004	-0.75	
RDM_MM_211ASH_WINDOWA_7	MM	211ASH	7	0.07	0.123	0.569105691	0.008	0.123	0.06504065	0.057	0.07	0.814286	
RDM_MM_211ASH_WINDOWC_2	MM	211ASH	2	0.058	0.079	0.734177215	0.022	0.079	0.278481013	0.045	0.058	0.775862	
RDM_MM_211ASH_WINDOWC_1	MM	211ASH	1	0.01	0.054	0.185185185	-0.003	0.054	-0.055555556	0.006	0.01	0.6	
RDM_MM_211ASH_WINDOWC_4	MM	211ASH	4	0.026	0.073	0.356164384	-0.02	0.073	-0.273972603	0.018	0.026	0.692308	
RDM_MM_211ASH_WINDOWE_11	MM	211ASH	11	0.062	0.142	0.436619718	-0.005	0.142	-0.035211268	0.045	0.062	0.725806	
RDM_MM_211ASH_WINDOWE_16	MM	211ASH	16	0.094	0.169	0.556213018	0.007	0.169	0.041420118	0.072	0.094	0.765957	
RDM_MM_211ASH_WINDOWF_11	MM	211ASH	11	0.058	0.133	0.436090226	0.002	0.133	0.015037594	0.04	0.059	0.677966	
RDM_MM_211ASH_WINDOWF_16	MM	211ASH	16	0.058	0.137	0.423357664	-0.004	0.137	-0.02919708	0.044	0.058	0.758621	
RDM_MM_211ASH_WINDOWF_18	MM	211ASH	18	0.087	0.133	0.654135338	0.01	0.133	0.07518797	0.07	0.087	0.804598	
RDM_501_WINDOWA_1	MM	501	1	0.013	0.108	0.12037037	-0.032	0.108	-0.296296296	0.008	0.013	0.615385	x
RDM_501_WINDOWA_2	MM	501	2	0.01	0.152	0.065789474	-0.034	0.152	-0.223684211	0.008	0.01	0.8	x
RDM_501_WINDOWA_4	MM	501	4	0.029	0.087	0.333333333	-0.033	0.087	-0.379310345	0.014	0.029	0.482759	x
RDM_501_WINDOWAA_4	MM	501	4	0.092	0.157	0.585987261	0.023	0.157	0.146496815	0.079	0.092	0.858696	
RDM_501_WINDOWAA_5	MM	501	5	0.091	0.168	0.541666667	0.019	0.168	0.113095238	0.074	0.091	0.813187	
RDM_501_WINDOWB_2	MM	501	2	0.01	0.057	0.175438596	-0.023	0.057	-0.403508772	-0.006	0.01	-0.6	
RDM_501_WINDOWB_3	MM	501	3	0.088	0.139	0.633093525	-0.001	0.139	-0.007194245	0.066	0.088	0.75	
RDM_501_WINDOWBB_14	MM	501	14	0.052	0.153	0.339869281	-0.004	0.153	-0.026143791	0.038	0.052	0.730769	
RDM_501_WINDOWBB_15	MM	501	15	0.078	0.181	0.430939227	0.01	0.181	0.055248619	0.054	0.078	0.692308	

RDM_501_WINDOWBB_16	MM	501	16	0.078	0.187	0.417112299	0.004	0.187	0.021390374	0.044	0.078	0.564103
RDM_501_WINDOWC_1	MM	501	1	0.098	0.136	0.720588235	-0.02	0.136	-0.147058824	0.072	0.098	0.734694 x
RDM_501_WINDOWC_2	MM	501	2	0.037	0.081	0.456790123	-0.012	0.081	-0.148148148	0.026	0.037	0.702703 x
RDM_501_WINDOWC_3	MM	501	3	0.097	0.16	0.60625	-0.008	0.16	-0.05	0.07	0.097	0.721649 x
RDM_501_WINDOWF_5	MM	501	5	0.184	0.168	1.095238095	-0.003	0.168	-0.017857143	0.134	0.184	0.728261 x
RDM_501_WINDOWF_16	MM	501	16	0.12	0.143	0.839160839	-0.012	0.143	-0.083916084	0.106	0.12	0.883333 x
RDM_501_WINDOWF_17	MM	501	17	0.147	0.17	0.864705882	-0.011	0.17	-0.064705882	0.137	0.147	0.931973 x
RDM_501_WINDOWG_2	MM	501	2	0.055	0.104	0.528846154	0	0.104	0	0.046	0.055	0.836364
RDM_501_WINDOWG_3	MM	501	3	0.025	0.081	0.308641975	-0.013	0.081	-0.160493827	0.019	0.025	0.76
RDM_501_WINDOWG_6	MM	501	6	0.067	0.148	0.452702703	0	0.148	0	0.051	0.067	0.761194
RDM_501_WINDOWH_1	MM	501	1	0.107	0.165	0.648484848	0.004	0.165	0.024242424	0.082	0.107	0.766355
RDM_501_WINDOWH_3	MM	501	3	0.109	0.144	0.756944444	0.004	0.144	0.027777778	0.082	0.109	0.752294
RDM_501_WINDOWH_6	MM	501	6	0.057	0.116	0.49137931	-0.007	0.116	-0.060344828	0.046	0.057	0.807018
RDM_501_WINDOWI_6	MM	501	6	0.023	0.12	0.191666667	-0.006	0.12	-0.05	0.026	0.023	1.130435 x
RDM_501_WINDOWI_7	MM	501	7	0.009	0.124	0.072580645	-0.006	0.124	-0.048387097	0.014	0.009	1.555556 x
RDM_501_WINDOWI_8	MM	501	8	0.085	0.102	0.833333333	0.004	0.102	0.039215686	0.065	0.085	0.764706 x
RDM_501_WINDOWJ_5	MM	501	5	0.129	0.158	0.816455696	0.104	0.158	0.658227848	0.046	0.054	0.851852 X
RDM_501_WINDOWJ_7	MM	501	7	0.065	0.134	0.485074627	0.003	0.134	0.02238806	0.048	0.065	0.738462 X
RDM_501_WINDOWJ_8	MM	501	8	0.065	0.182	0.357142857	0.003	0.182	0.016483516	0.054	0.065	0.830769 X
RDM_501_WINDOWK_11	MM	501	11	0.05	0.116	0.431034483	-0.004	0.116	-0.034482759	0.04	0.05	0.8
RDM_501_WINDOWK_12	MM	501	12	0.067	0.129	0.519379845	0.009	0.129	0.069767442	0.06	0.067	0.895522
RDM_501_WINDOWL_5	MM	501	5	0.081	0.157	0.515923567	0.018	0.157	0.114649682	0.07	0.081	0.864198
RDM_501_WINDOWL_6	MM	501	6	0.079	0.163	0.484662577	0.017	0.163	0.104294479	0.066	0.079	0.835443
RDM_501_WINDOWL_7	MM	501	7	0.075	0.148	0.506756757	0.019	0.148	0.128378378	0.064	0.075	0.853333
RDM_501_WINDOWM_5	MM	501	5	0.05	0.12	0.416666667	0	0.12	0	0.039	0.05	0.78
RDM_501_WINDOWM_6	MM	501	6	0.066	0.124	0.532258065	0.009	0.124	0.072580645	0.056	0.066	0.848485
RDM_501_WINDOWM_9	MM	501	9	0.082	0.155	0.529032258	0.008	0.155	0.051612903	0.077	0.082	0.939024
RDM_501_WINDOWO_10	MM	501	10	0.051	0.131	0.389312977	0.004	0.131	0.030534351	0.043	0.051	0.843137
RDM_501_WINDOWO_11	MM	501	11	0.077	0.154	0.5	0.012	0.154	0.077922078	0.064	0.077	0.831169
RDM_501_WINDOWO_14	MM	501	14	0.072	0.168	0.428571429	0.009	0.168	0.053571429	0.063	0.072	0.875
RDM_501_WINDOWP_6	MM	501	6	0.066	0.129	0.511627907	0.002	0.129	0.015503876	0.049	0.066	0.742424
RDM_501_WINDOWP_7	MM	501	7	0.065	0.15	0.433333333	0.002	0.15	0.013333333	0.052	0.065	0.8
RDM_501_WINDOWP_11	MM	501	11	0.096	0.171	0.561403509	0.016	0.171	0.093567251	0.08	0.096	0.833333
RDM_501_WINDOWR_12	MM	501	12	0.056	0.081	0.691358025	0.009	0.081	0.111111111	0.043	0.056	0.767857 X
RDM_501_WINDOWR_13	MM	501	13	0.034	0.136	0.25	0.002	0.136	0.014705882	0.032	0.034	0.941176 X
RDM_501_WINDOWS_1	MM	501	1	0.022	0.108	0.203703704	-0.009	0.108	-0.083333333	0.024	0.022	1.090909 X
RDM_501_WINDOWT_3	MM	501	3	0.07	0.077	0.909090909	-0.002	0.077	-0.025974026	0.054	0.07	0.771429 X
RDM_501_WINDOWT_4	MM	501	4	0.095	0.138	0.688405797	0	0.138	0	0.08	0.096	0.833333 X
RDM_501_WINDOWT_5	MM	501	5	0.074	0.101	0.732673267	0.001	0.101	0.00990099	0.056	0.074	0.756757 X
RDM_501_WINDOWU_3	MM	501	3	0.02	0.104	0.192307692	-0.017	0.104	-0.163461538	0.023	0.02	1.15 X
RDM_501_WINDOWU_5	MM	501	5	0.013	0.113	0.115044248	-0.021	0.113	-0.185840708	0.021	0.013	1.615385 X
RDM_501_WINDOWU_6	MM	501	6	0.017	0.141	0.120567376	-0.017	0.141	-0.120567376	0.019	0.017	1.117647 X
RDM_501_WINDOWV_13	MM	501	13	0.012	0.101	0.118811881	-0.034	0.101	-0.336633663	0.005	0.012	0.416667 X
RDM_501_WINDOWV_14	MM	501	14	-0.009	0.076	-0.118421053	-0.034	0.076	-0.447368421	-0.01	-0.009	1.111111 X
RDM_501_WINDOWV_15	MM	501	15	-0.004	0.087	-0.045977011	-0.037	0.087	-0.425287356	-0.009	-0.004	2.25 X
RDM_501_WINDOWW_9	MM	501	9	0.022	0.143	0.153846154	-0.01	0.143	-0.06993007	0.022	0.022	1 X
RDM_501_WINDOWW_10	MM	501	10	0.075	0.159	0.471698113	-0.011	0.159	-0.06918239	0.075	0.069	1.086957 X
RDM_501_WINDOWW_14	MM	501	14	0.019	0.148	0.128378378	-0.018	0.148	-0.121621622	0.017	0.019	0.894737 X
RDM_501_WINDOWY_4	MM	501	4	0.109	0.171	0.637426901	0.025	0.171	0.14619883	0.083	0.109	0.761468
RDM_501_WINDOWY_5	MM	501	5	0.079	0.186	0.424731183	0.012	0.186	0.064516129	0.062	0.079	0.78481
RDM_501_WINDOWY_6	MM	501	6	0.071	0.174	0.408045977	0.009	0.174	0.051724138	0.056	0.071	0.788732
RDM_501_WINDOWZ_3	MM	501	3	0.026	0.135	0.192592593	-0.014	0.135	-0.103703704	0.022	0.026	0.846154 X
RDM_501_WINDOWZ_5	MM	501	5	0.044	0.14	0.314285714	-0.011	0.14	-0.078571429	0.036	0.044	0.818182 X
RDM_501_WINDOWZ_10	MM	501	3	0.049	0.191	0.256544503	-0.019	0.191	-0.09947644	0.033	0.049	0.673469 X

Table 10: RDM FTIR and mFTIR data

ID	SQUARE	ID	WINDOW	STAGE	630	605	OH/P	712	1035	cal/PO4	2010	605	1035	CN/P (2010/605)	CN/P (2010/1035)
RDM_J22_89D_St4_test1	J22	89D		ST4	0.043	0.091	0.472527	0.01	0.146	0.068493	0.004	0.091	0.146	0.043956044	0.02739726
RDM_J22_89C_St6_test1	J22	89C		ST6	0.042	0.085	0.494118	0.03	0.102	0.294118	-0.002	0.085	0.102	-0.023529412	-0.019607843
RDM_J22_89B_St3_test1	J22	89B		ST3	0.025	0.079	0.316456	0.016	0.113	0.141593	-0.003	0.079	0.113	-0.037974684	-0.026548673
RDM_J22_89A_St0_test1	J22	89A		ST0	0.025	0.07	0.357143	0.02	0.091	0.21978	0.008	0.07	0.091	0.114285714	0.087912088
RDM_J21_720F_St6_test1	J21	720F		ST6	0.029	0.058	0.5	-0.004	0.067	-0.0597	-0.007	0.058	0.067	-0.120689655	-0.104477612
RDM_J21_720E_st3_test1	J21	720E		ST3	0.015	0.059	0.254237	0.006	0.089	0.067416	-0.006	0.059	0.089	-0.101694915	-0.06741573
RDM_J21_720D_St2_test1	J21	720D		ST2	0.028	0.077	0.363636	0.015	0.121	0.123967	0.001	0.077	0.121	0.012987013	0.008264463
RDM_J21_720C_St0_test1	J21	720C		ST0	0.027	0.096	0.28125	0.019	0.128	0.148438	0	0.096	0.128	0	0
RDM_J21_720B_ST0_test1	J21	720B		ST0	0.023	0.074	0.310811	0.007	0.123	0.056911	-0.004	0.074	0.123	-0.054054054	-0.032520325
RDM_J21_720A_ST0_Test1	J21	720A		ST0	0.018	0.075	0.24	0.011	0.107	0.102804	-0.005	0.075	0.107	-0.066666667	-0.046728972
RDM_J21_720A_St0_test2	J21	720A		ST0	0.022	0.072	0.305556	0.011	0.111	0.099099	-0.005	0.072	0.111	-0.069444444	-0.045045045
RDM_J20_998I_ST6b_test1	J20	998I		ST6b	0.097	0.156	0.621795	0.033	0.299	0.110368	0.011	0.156	0.299	0.070512821	0.036789298
RDM_J20_998H_St6_Test1	J20	998H		ST6	0.13	0.223	0.58296	0.009	0.341	0.026393	0	0.223	0.341	0	0
RDM_J20_998G_St6b_test1	J20	998G		STb	0.075	0.167	0.449102	0.034	0.214	0.158879	0.011	0.167	0.214	0.065868263	0.051401869
RDM_J20_998F_St6_test1	J20	998F		ST6	0.1	0.223	0.44843	0.025	0.334	0.07485	0.003	0.223	0.334	0.013452915	0.008982036
RDM_J20_998E_St3_test1	J20	998E		ST3	0.067	0.165	0.406061	0.038	0.314	0.121019	0.004	0.197	0.314	0.020304569	0.012738854
RDM_J20_998D_St4_test1	J20	998D		ST4	0.081	0.222	0.364865	0.058	0.353	0.164306	0.015	0.222	0.353	0.067567568	0.042492918
RDM_J20_998B_St0_test1	J20	998B		ST0	0.051	0.116	0.439655	0.038	0.178	0.213483	0.012	0.116	0.178	0.103448276	0.06741573
RDM_J20_998A_St0_test1	J20	998A		ST0	0.058	0.154	0.376623	0.054	0.267	0.202247	-0.001	0.154	0.267	-0.006493506	-0.003745318
RDM_J20_998A_St0_test2	J20	998A		ST0	0.057	0.148	0.385135	0.051	0.25	0.204	0	0.148	0.25	0	0
RDM_J18_3855S_St3_test1	J18	3855S		ST3	0.0444	0.143	0.31049	0.026	0.2	0.13	-0.004	0.143	0.2	-0.027972028	-0.02
RDM_J18_3855R_St4_test1	J18	3855R		ST4	0.056	0.151	0.370861	0.018	0.224	0.080357	0	0.151	0.224	0	0
RDM_J18_3855Q_St3_test1	J18	3855Q		ST3	0.068	0.177	0.384181	0.038	0.254	0.149606	0.005	0.177	0.254	0.028248588	0.019685039
RDM_J18_3855P_St5_test1	J18	3855P		ST5	0.089	0.24	0.370833	0.014	0.364	0.038462	0	0.24	0.364	0	0
RDM_J18_3855O_St2_test1	J18	3855O		ST2	0.07	0.178	0.393258	0.05	0.315	0.15873	0.006	0.178	0.315	0.033707865	0.019047619
RDM_J18_3855N_St5b_test1	J18	3855N		ST5b	0.105	0.181	0.58011	0.006	0.308	0.019481	-0.001	0.181	0.308	-0.005524862	-0.003246753
RDM_J18_3855M_St6_test1	J18	3855M		ST6	0.109	0.204	0.534314	0.001	0.286	0.003497	-0.005	0.204	0.286	-0.024509804	-0.017482517
RDM_J18_3855L_St5b_test1	J18	3855L		ST5b	0.121	0.251	0.482072	0.019	0.412	0.046117	0.003	0.251	0.412	0.011952191	0.007281553
RDM_J18_3855K_st4_test1	J18	3855K		ST4	0.14	0.269	0.520446	0.025	0.449	0.055679	0.009	0.269	0.449	0.033457249	0.020044543
RDM_J18_3855J_St5_test1	J18	3855J		ST5	0.114	0.24	0.475	0.005	0.379	0.013193	-0.006	0.24	0.379	-0.025	-0.015831135
RDM_J18_3855i_St6_test1	J18	3855i		ST6	0.106	0.207	0.512077	0.006	0.289	0.020761	-0.001	0.207	0.289	-0.004830918	-0.003460208
RDM_J18_3855H_st5_test1	J18	3855H		ST5	0.087	0.201	0.432836	0.011	0.298	0.036913	-0.002	0.201	0.298	-0.009950249	-0.006711409
RDM_J18_3855F_st2or4_test1	J18	3855F		duration	0.044	0.148	0.297297	0.027	0.215	0.125581	-0.005	0.148	0.215	-0.033783784	-0.023255814
RDM_J18_3855E_St2_test1	J18	3855E		ST2	0.06	0.167	0.359281	0.033	0.242	0.136364	0.004	0.167	0.242	0.023952096	0.016528926
RDM_J18_3855D_St0_test1	J18	3855D		ST0	0.057	0.169	0.337278	0.04	0.281	0.142349	0.004	0.169	0.281	0.023668639	0.014234875
RDM_J18_3855C_St1_test1	J18	3855C		ST1	0.051	0.157	0.324841	0.037	0.239	0.154812	0.003	0.157	0.239	0.01910828	0.012552301
RDM_J18_3855C_St0_test1	J18	3855C		ST0	0.053	0.17	0.311765	0.039	0.263	0.148289	0.004	0.17	0.263	0.023529412	0.015209125
RDM_J18_3855B_St0_test1	J18	3855B		ST0	0.053	0.159	0.333333	0.036	0.269	0.133829	-0.005	0.158	0.269	-0.03164557	-0.018587361
RDM_J18_3855A_st0_test1	J18	3855A		ST0	0.054	0.171	0.315789	0.037	0.272	0.136029	0.003	0.171	0.272	0.01754386	0.011029412
RDM_I18_1991O_st6b_test1	I18	1991O		ST6b	0.076	0.134	0.567164	0.013	0.201	0.064677	0.005	0.134	0.201	0.037313433	0.024875622
RDM_I18_1991N_St6_test1	I18	1991N		ST6	0.136	0.235	0.578723	0.014	0.344	0.040698	0	0.235	0.344	0	0
RDM_I18_1991L_St5_test1	I18	1991L		ST5	0.109	0.157	0.694268	0.013	0.364	0.035714	0.004	0.157	0.364	0.025477707	0.010989011
RDM_I18_1991K_St4_test1	I18	1991K		ST4	0.089	0.193	0.46114	0.033	0.314	0.105096	0.015	0.193	0.314	0.077720207	0.047770701
RDM_I18_1991I_St4_test1	I18	1991I		ST4	0.097	0.215	0.451163	0.014	0.344	0.040698	0.001	0.215	0.344	0.004651163	0.002906977
RDM_I18_1991H_St4_test1	I18	1991H		ST4	0.096	0.203	0.472906	0.022	0.327	0.067278	0.005	0.203	0.327	0.024630542	0.01529052
RDM_I18_1991G_St2_test1	I18	1991G		ST2	0.067	0.176	0.380682	0.042	0.267	0.157303	0.002	0.176	0.267	0.011363636	0.007490637
RDM_I18_1991F_St2_test1	I18	1991F		ST2	0.044	0.11	0.4	0.038	0.155	0.245161	0.005	0.11	0.155	0.045454545	0.032258065
RDM_I18_1991E_St3_test1	I18	1991E		ST3	0.073	0.174	0.41954	0.037	0.294	0.12585	0.004	0.174	0.294	0.022988506	0.013605442
RDM_I18_1991D_St3_test1	I18	1991D		ST3	0.059	0.174	0.33908	0.035	0.265	0.132075	0.004	0.174	0.265	0.022988506	0.01509434
RDM_I18_1991C_st2or4_test1	I18	1991C		duration	0.059	0.156	0.378205	0.031	0.262	0.118321	0.006	0.156	0.262	0.038461538	0.022900763
RDM_I18_1991B_st0_test1	I18	1991B		ST0	0.06	0.18	0.333333	0.044	0.286	0.153846	0.002	0.18	0.286	0.011111111	0.006993007
RDM_I18_1991A_St0_test1	I18	1991A		ST0	0.055	0.159	0.345912	0.04	0.245	0.163265	0.006	0.159	0.245	0.037735849	0.024489796
RDM_H19_92O_St4_test1	H19	92O		duration	0.065	0.195	0.333333	0.037	0.314	0.117834	0.009	0.195	0.314	0.046153846	0.02866242
RDM_H19_92N_ST5b_test1	H19	92N		ST5b	0.093	0.226	0.411504	0.016	0.352	0.045455	0.007	0.226	0.352	0.030973451	0.019886364
RDM_H19_92M_St6_test1	H19	92M		ST6	0.088	0.231	0.380952	0.013	0.329	0.039514	0.028	0.231	0.329	0.121212121	0.085106383
RDM_H19_92L_St6b_test1	H19	92L		ST6b	0.085	0.167	0.508982	0.009	0.236	0.038136	0.001	0.167	0.236	0.005988024	0.004237288
RDM_H19_92K_St5_test1	H19	92K		ST5	0.108	0.222	0.486486	0.018	0.349	0.051576	0.008	0.222	0.349	0.036036036	0.022922636
RDM_H19_92J_St3_test1	H19	92J		ST3	0.062	0.188	0.329787	0.046	0.296	0.155405	0.01	0.188	0.296	0.053191489	0.033783784
RDM_H19_92I_St5_test1	H19	92I		ST5	0.141	0.298	0.473154	0.022	0.427	0.051522	0.026	0.298	0.427	0.087248322	0.06088993
RDM_H19_92H_st6_test1	H19	92H		ST6	0.098	0.213	0.460094	0.017	0.233	0.072961	0.015	0.213	0.233	0.070422535	0.064377682
RDM_H19_92G_st5_test1	H19	92G		ST5	0.073	0.226	0.323009	0.008	0.416	0.019231	0.007	0.226	0.416	0.030973451	0.016826923
RDM_H19_92F_st2_test1	H19	92F		ST2	0.048	0.157	0.305732	0.031	0.233	0.133047	0.007	0.157	0.233	0.044585987	0.030042918
RDM_H19_92E_st2_test1	H19	92E		ST2	0.043	0.136	0.316176	0.028	0.203	0.137931	0.004	0.136	0.203	0.029411765	0.019704433
RDM_H19_92D_St2or4_test1	H19	92D		duration	0.076	0.204	0.372549	0.044	0.328	0.134146	0.012	0.204	0.328	0.058823529	0.036585366
RDM_H19_92C_St3_test1	H19	92C		ST3	0.066	0.189	0.349206	0.051	0.283	0.180212	0.016	0.189	0.283	0.084656085	0.056537102
RDM_H19_92B_St0_test1	H19	92B		ST0	0.061	0.202	0.30198	0.048	0.36	0.133333	0.008	0.202	0.36	0.03960396	0.022222222
RDM_H19_92A_St0_test2	H19	92A		ST0	0.041	0.136	0.301471	0.032	0.127	0.251969	0.005	0.041	0.127	0.12195122	0.039370079
RDM_H19_92A_St0_test1	H19	92A		ST0	0.038	0.128	0.296875	0.033	0.191	0.172775	0.005	0.128	0.191	0.0390625	0.02617801
RDM_H18_3953B_St6_test1	H18	3953B		ST6	0.068	0.127	0.535433	-0.003	0.179	-0.01676	-0.004	0.127	0.179	-0.031496063	-0.022346369
RDM_H18_3953A_St6_test1	H18	3953A		ST6	0.0217	0.0335	0.647761	0.0002	0.0529	0.003781	-0.0002	0.0335	0.0529	-0.005970149	-0.003780718
RDM_H18_3002N_St4_test1	H18	3002N		ST4	0.075	0.203	0.369458	0.033	0.39	0.084615	0.005	0.203	0.39	0.024630542	0.012820513
RDM_H18_3002M_St5_test1	H18	3002M		ST5	0.114	0.245	0.465306	0.016	0.341	0.046921	0.008	0.245	0.341	0.032653061	0.023460411
RDM_H18_3002L_St5_test1	H18	3002L		ST5	0.119	0.29	0.410345	0.016	0.504	0.031746	0.007	0.29	0.504	0.024137931	0.013888889
RDM_H18_3002K_St5_test1	H18	3002K		ST5	0.136	0.187	0.727273	0.026	0.575	0.045217	0.019	0.187	0.575	0.101604278	0.033043478
RDM_H18_3002J_st4_test1	H18	3002J		ST4	0.076	0.149	0.510067	0.026	0.299	0.086957	0.013	0.149	0.299	0.087248322	0.043478261
RDM_H18_3002I_St4_test1	H18	3002I		ST4	0.117	0.225	0.52	0.008	0.495	0.016162	-0.009	0.225	0.495	-0.04	-0.018181818
RDM_H18_3002H_st6_test1	H18	3002H		ST6	0.156	0.353	0.441926	0.01	0.54	0.018519	0.004	0.353	0.54	0.011331445	0.007407407
RDM_H18_3002F_St3_test1	H18	3002F		ST3	0.059	0.176	0.335227	0.034	0.268	0.126866	0.006	0.176	0.268	0.034090909	0.02238806
RDM_H18_3002E_st2_test1	H18	3002E		ST2	0.083	0.174	0.477011	0.041	0.355	0.115493	0.014	0.174	0.355	0.08045977	0.03943662
RDM_H18_3002D_st4_test1	H18	3002D		ST4	0.072	0.226	0.318584	0.051	0.384	0.132813	0.003	0.226	0.384	0.013274336	0.0078125
RDM_H18_3002C_St4_Test1	H18	3002C		ST4	0.075	0.2	0.375	0.038	0.333	0.114114	0.008	0.2	0.333	0.04	0.024024024
RDM_H18_3002B_St0_test1	H18	3002B		ST0	0.069	0.178	0.38764	0.052	0.322	0.161491	0.015	0.178	0.322	0.084269663	0.046583851
RDM_H18_3002A_St0_test1	H18	3002A		ST0	0.065	0.172	0.377907	0.057	0.25	0.228	0.018	0.172	0.25	0.104651163	0.072
RDM_H18_3002O_St4or0_test	H18	3002O		ST0	0.099	0.238	0.415966	0.021	0.372	0.056452	0.005	0.238	0.372	0.021008403	0.01344086
RDM_G18_7245B_ST6_TEST1	G18	7245B		ST6	0.147	0.176	0.835227	0.01	0.404	0.024752	0.006	0.294	0.404	0.020408163	0.014851485
RDM_G18_7245A_ST6_TEST1	G18	7245A		ST6	0.129	0.218	0.591743	0.009	0.296	0.030405	0.001	0.218	0.296	0.004587156	0.003378378
RDM_G18_7245A_ST6_TEST1	G18	7245A		ST6	0.096	0.194	0.494845	0.006	0.281	0.021352	-0.003	0.194	0.281	-0.015463918	-0.010676157
RDM_E18_1626M_ST5_TEST1	E18	1626M		ST5	0.075	0.155	0.483871	0.002	0.248	0.008065	0	0.155	0.248	0	0
RDM_E18_1626L_ST5_TEST1	E18	1626L		ST5	0.064	0.134	0.477612	0.019	0.219	0.086758	0.012	0.134	0.219	0.089552239	0.054794521
RDM_E18_1626H_ST3_TEST1	E18	1626H		ST3			#DIV/0!			#DIV/0!			0.0928	#DIV/0!	0
RDM_CF4_251G_ST6B_TEST1	CF4	251G		ST6b	0.091	0.219	0.415525	0.004	0.302	0.013245	-0.009	0.219	0.302	-0.04109589	-0.029801325
RDM_CF4_251F_ST6_TEST1	CF4	251F		ST6	0.105	0.222	0.472973	0.014	0.322	0.043478	0.003	0.222	0.322	0.013513514	0.00931677

RDM_CF4_251E_ST6_TEST1	CF4	251E	ST6	0.181	0.337	0.537092	0.001	0.482	0.002075	-0.013	0.337	0.482	-0.038575668	-0.026970954
RDM_CF4_251D_ST6_TEST1	CF4	251D	ST6	0.17	0.281	0.604982	0.01	0.464	0.021552	0.003	0.281	0.464	0.010676157	0.006465517
RDM_CF4_251C_ST6_TEST1	CF4	251C	ST6	0.156	0.294	0.530612	0.013	0.457	0.028446	0.002	0.294	0.457	0.006802721	0.004376368
RDM_CF4_251B_ST5b_TEST1	CF4	251B	ST5b	0.046	0.214	0.214953	0.008	0.417	0.019185	0	0.214	0.417	0	0
RDM_CF4_251B_ST5b_TEST2	CF4	251B	ST5b	0.068	0.216	0.314815	0.012	0.432	0.027778	0.008	0.216	0.432	0.037037037	0.018518519
RDM_CF4_251A_ST6B_TEST1	CF4	251A	ST6b	0.101	0.236	0.427966	0.016	0.287	0.055749	0.002	0.236	0.287	0.008474576	0.006968641
RDM_CF1_239N_ST3_TEST2	CF1	239N	ST3	0.0078	0.0307	0.254072	0.0022	0.0378	0.058201	-0.0036	0.0307	0.0378	-0.117263844	-0.095238095
RDM_CF1_239N_ST3_TEST1	CF1	239N	ST3	0.0235	0.0523	0.449331	0.0179	0.0604	0.296358	0.0114	0.0523	0.0604	0.217973231	0.188741722
RDM_CF1_239M_ST6_TEST1	CF1	239M	ST6	0.078	0.134	0.58209	0.012	0.272	0.044118	0.007	0.134	0.272	0.052238806	0.025735294
RDM_CF1_239L_ST5B_TEST1	CF1	239L	STB	0.042	0.107	0.392523	0.004	0.158	0.025316	-0.006	0.107	0.158	-0.056074766	-0.037974684
RDM_CF1_239K_ST5_TEST1	CF1	239K	ST5	0.056	0.139	0.402878	0.005	0.226	0.022124	-0.002	0.139	0.226	-0.014388489	-0.008849558
RDM_CF1_239J_ST3_TEST1	CF1	239J	ST3	0.028	0.081	0.345679	0.018	0.102	0.176471	0.004	0.081	0.102	0.049382716	0.039215686
RDM_CF1_239I_ST2_TEST1	CF1	239I	ST2	0.022	0.063	0.349206	0.014	0.095	0.147368	0.002	0.063	0.095	0.031746032	0.021052632
RDM_CF1_239G_ST6B_TEST1	CF1	239G	ST6b	0.036	0.075	0.48	0.008	0.082	0.097561	0.003	0.075	0.082	0.04	0.036585366
RDM_J18_3855A_ST6B_TEST1	J18	3855A	ST6b	0.087	0.219	0.39726	0.008	0.321	0.024922	-0.007	0.219	0.321	-0.03196347	-0.021806854
RDM_I18_1991P_ST6_TEST1	I18	1991P	ST6	0.086	0.194	0.443299	0.013	0.246	0.052846	0.001	0.194	0.246	0.005154639	0.004065041
RDM_I18_1991M_ST6_TEST1	I18	1991M	ST6	0.115	0.206	0.558252	0.021	0.279	0.075269	0.011	0.206	0.279	0.053398058	0.039426523
RDM_I18_1991J_ST4_REST1	I18	1991J	ST4	0.064	0.158	0.405063	0.016	0.262	0.061069	0	0.158	0.262	0	0
RDM_H18_3002G_ST6_TEST1	H18	3002G	ST6	0.105	0.206	0.509709	0.014	0.288	0.048611	0.007	0.206	0.288	0.033980583	0.024305556
RDM_CF1_239F_ST0_TEST1	CF1	239F	ST0	0.031	0.076	0.407895	0.018	0.11	0.163636	0.006	0.076	0.11	0.078947368	0.054545455
RDM_CF1_239E_ST1_TEST1	CF1	239E	ST1	0.031	0.088	0.352273	0.016	0.135	0.118519	0.005	0.088	0.135	0.056818182	0.037037037
RDM_CF1_239D_ST_TEST1	CF1	239D	STT	0.027	0.077	0.350649	0.017	0.099	0.171717	0.004	0.077	0.099	0.051948052	0.04040404
RDM_CF1_239C_ST0_TEST1	CF1	239C	ST0	0.021	0.075	0.28	0.01	0.098	0.102041	-0.003	0.075	0.098	-0.04	-0.030612245
RDM_CF1_239B_ST0_TEST1	CF1	239B	ST0	0.023	0.078	0.294872	0.013	0.108	0.12037	-0.002	0.078	0.108	-0.025641026	-0.018518519
RDM_CF1_239A_ST5_TEST1	CF1	239A	ST5	0.091	0.164	0.554878	0.009	0.268	0.033582	0.004	0.164	0.268	0.024390244	0.014925373
RDM_MM_506A_WINDOWA_	MM	506A	1	0.044	0.129	0.341085	0.043	0.289	0.148789	-0.061	0.129	0.289	-0.472868217	-0.211072664
RDM_MM_506A_WINDOWA_	MM	506A	2	0.046	0.127	0.362205	0.033	0.291	0.113402	-0.073	0.127	0.291	-0.57480315	-0.250859107
RDM_MM_506A_WINDOWA_	MM	506A	3	0.061	0.181	0.337017	0.059	0.443	0.133183	-0.058	0.181	0.443	-0.320441989	-0.130925508
RDM_MM_506A_WINDOWA_	MM	506A	4	0.066	0.175	0.377143	0.076	0.484	0.157025	-0.061	0.175	0.484	-0.348571429	-0.126033058
RDM_MM_506A_WINDOWA_	MM	506A	5	0.063	0.198	0.318182	0.057	0.483	0.118012	-0.067	0.198	0.483	-0.338383838	-0.138716356
RDM_MM_506A_WINDOWA_	MM	506A	6	0.03	0.118	0.254237	0.015	0.216	0.069444	-0.074	0.118	0.216	-0.627118644	-0.342592593
RDM_MM_506A_WINDOWA_	MM	506A	7	0.048	0.13	0.369231	0.045	0.291	0.154639	-0.061	0.13	0.291	-0.469230769	-0.209621993
RDM_MM_506A_WINDOWA_	MM	506A	8	0.046	0.153	0.300654	0.04	0.325	0.123077	-0.066	0.153	0.325	-0.431372549	-0.203076923
RDM_MM_506A_WINDOWAA	MM	506A	3	0.05	0.155	0.322581	0.077	0.456	0.16886	-0.047	0.155	0.456	-0.303225806	-0.103070175
RDM_MM_506A_WINDOWAA	MM	506A	4	0.054	0.183	0.295082	0.088	0.486	0.18107	-0.049	0.183	0.486	-0.267759563	-0.100823045
RDM_MM_506A_WINDOWAA	MM	506A	5	0.031	0.095	0.326316	0.053	0.219	0.242009	-0.046	0.095	0.219	-0.484210526	-0.210045662
RDM_MM_506A_WINDOWAA	MM	506A	6	0.07	0.176	0.397727	0.096	0.542	0.177122	-0.048	0.176	0.542	-0.272727273	-0.088560886
RDM_MM_506A_WINDOWAA	MM	506A	7	0.067	0.144	0.465278	0.078	0.426	0.183099	-0.048	0.144	0.426	-0.333333333	-0.112676056
RDM_MM_506A_WINDOWAA	MM	506A	8	0.062	0.171	0.362573	0.085	0.397	0.214106	-0.043	0.171	0.397	-0.251461988	-0.108312343
RDM_MM_506A_WINDOWAA	MM	506A	9	0.055	0.156	0.352564	0.088	0.495	0.177778	-0.048	0.156	0.495	-0.307692308	-0.096969697
RDM_MM_506A_WINDOWAA	MM	506A	10	0.083	0.154	0.538961	0.1	0.491	0.203666	-0.047	0.154	0.491	-0.305194805	-0.095723014
RDM_MM_506A_WINDOWB_	MM	506A	3	0.059	0.157	0.375796	0.057	0.291	0.195876	-0.031	0.157	0.291	-0.197452229	-0.10652921
RDM_MM_506A_WINDOWB_	MM	506A	4	0.047	0.132	0.356061	0.046	0.282	0.163121	-0.036	0.132	0.282	-0.272727273	-0.127659574
RDM_MM_506A_WINDOWB_	MM	506A	8	0.065	0.176	0.369318	0.071	0.498	0.14257	-0.028	0.176	0.498	-0.159090909	-0.0562249
RDM_MM_506A_WINDOWB_	MM	506A	9	0.045	0.135	0.333333	0.046	0.275	0.167273	-0.03	0.135	0.275	-0.222222222	-0.109090909
RDM_MM_506A_WINDOWC_	MM	506A	1	0.049	0.157	0.312102	0.042	0.408	0.102941	-0.039	0.157	0.408	-0.248407643	-0.095588235
RDM_MM_506A_WINDOWC_	MM	506A	2	0.057	0.143	0.398601	0.049	0.444	0.11036	-0.036	0.143	0.444	-0.251748252	-0.081081081
RDM_MM_506A_WINDOWC_	MM	506A	3	0.046	0.141	0.326241	0.033	0.326	0.101227	-0.045	0.141	0.326	-0.319148936	-0.13803681
RDM_MM_506A_WINDOWC_	MM	506A	11	0.057	0.157	0.363057	0.051	0.439	0.116173	-0.041	0.157	0.439	-0.261146497	-0.093394077
RDM_MM_506A_WINDOWD_	MM	506A	16	0.044	0.148	0.297297	0.043	0.363	0.118457	-0.045	0.148	0.363	-0.304054054	-0.123966942
RDM_MM_506A_WINDOWD_	MM	506A	17	0.068	0.213	0.319249	0.073	0.568	0.128521	-0.05	0.213	0.568	-0.234741784	-0.088028169
RDM_MM_506A_WINDOWD_	MM	506A	19	0.053	0.16	0.33125	0.054	0.401	0.134663	-0.048	0.16	0.401	-0.3	-0.119700748
RDM_MM_506A_WINDOWD_	MM	506A	20	0.058	0.207	0.280193	0.079	0.506	0.156126	-0.049	0.207	0.506	-0.236714976	-0.096837945
RDM_MM_506A_WINDOWE_	MM	506A	2	0.071	0.191	0.371728	0.076	0.543	0.139963	-0.059	0.191	0.543	-0.308900524	-0.108655617
RDM_MM_506A_WINDOWE_	MM	506A	3	0.043	0.124	0.346774	0.051	0.277	0.184116	-0.055	0.124	0.277	-0.443548387	-0.198555957
RDM_MM_506A_WINDOWF_	MM	506A	4	0.071	0.171	0.415205	0.07	0.49	0.142857	-0.039	0.171	0.49	-0.228070175	-0.079591837
RDM_MM_506A_WINDOWF_	MM	506A	5	0.037	0.131	0.282443	0.044	0.247	0.178138	-0.044	0.131	0.247	-0.335877863	-0.178137652
RDM_MM_506A_WINDOWI_1	MM	506A	10	0.057	0.151	0.377483	0.076	0.348	0.218391	-0.036	0.151	0.348	-0.238410596	-0.103448276
RDM_MM_506A_WINDOWI_1	MM	506A	12	0.062	0.163	0.380368	0.079	0.401	0.197007	-0.04	0.163	0.401	-0.245398773	-0.099750623
RDM_MM_506A_WINDOWI_1	MM	506A	14	0.058	0.17	0.341176	0.077	0.419	0.183771	-0.038	0.17	0.419	-0.223529412	-0.090692124
RDM_MM_506A_WINDOWJ_	MM	506A	4	0.054	0.145	0.372414	0.065	0.38	0.171053	-0.055	0.115	0.28	-0.47826087	-0.196428571
RDM_MM_506A_WINDOWJ_	MM	506A	5	0.063	0.175	0.36	0.081	0.497	0.162978	-0.014	0.175	0.497	-0.08	-0.028169014
RDM_MM_506A_WINDOWK_	MM	506A	14	0.063	0.154	0.409091	0.094	0.4	0.235	-0.054	0.154	0.4	-0.350649351	-0.135
RDM_MM_506A_WINDOWK_	MM	506A	18	0.078	0.19	0.410526	0.087	0.61	0.142623	-0.06	0.19	0.61	-0.315789474	-0.098360656
RDM_MM_506A_WINDOWK_	MM	506A	20	0.061	0.165	0.369697	0.064	0.413	0.154964	-0.046	0.165	0.413	-0.278787879	-0.111380145
RDM_MM_506A_WINDOWL_	MM	506A	7	0.063	0.155	0.406452	0.083	0.398	0.208543	-0.025	0.155	0.398	-0.161290323	-0.06281407
RDM_MM_506A_WINDOWL_	MM	506A	8	0.081	0.188	0.430851	0.057	0.358	0.159218	-0.018	0.188	0.358	-0.095744681	-0.05027933
RDM_MM_506A_WINDOWL_	MM	506A	15	0.073	0.172	0.424419	0.101	0.472	0.213983	-0.021	0.172	0.472	-0.122093023	-0.044491525
RDM_MM_506A_WINDOWN_	MM	506A	3	0.057	0.168	0.339286	0.069	0.475	0.145263	-0.056	0.168	0.475	-0.333333333	-0.117894737
RDM_MM_506A_WINDOWN_	MM	506A	6	0.075	0.217	0.345622	0.075	0.666	0.112613	-0.059	0.217	0.666	-0.271889401	-0.088588589
RDM_MM_506A_WINDOWN_	MM	506A	9	0.068	0.174	0.390805	0.078	0.516	0.151163	-0.055	0.174	0.516	-0.316091954	-0.106589147
RDM_MM_506A_WINDOWO_	MM	506A	4	0.067	0.14	0.478571	0.057	0.406	0.140394	-0.047	0.14	0.406	-0.335714286	-0.115763547
RDM_MM_506A_WINDOWO_	MM	506A	6	0.069	0.151	0.456954	0.069	0.338	0.204142	-0.052	0.151	0.338	-0.344370861	-0.153846154
RDM_MM_506A_WINDOWO_	MM	506A	8	0.047	0.134	0.350746	0.052	0.346	0.150289	-0.059	0.134	0.346	-0.440298507	-0.170520231
RDM_MM_211ASH_WINDOW	MM	211ASH	1	0.013	0.046	0.282609	0.007	0.065	0.107692	-0.016	0.046	0.065	-0.347826087	-0.246153846
RDM_MM_211ASH_WINDOW	MM	211ASH	7	0.052	0.123	0.422764	0.042	0.361	0.116343	-0.02	0.123	0.361	-0.162601626	-0.055401662
RDM_MM_211ASH_WINDOW	MM	211ASH	2	0.032	0.079	0.405063	0.062	0.179	0.346369	0.003	0.079	0.179	0.037974684	0.016759777
RDM_MM_211ASH_WINDOW	MM	211ASH	1	0.014	0.054	0.259259	0.021	0.067	0.313433	-0.012	0.054	0.067	-0.222222222	-0.179104478
RDM_MM_211ASH_WINDOW	MM	211ASH	4	0.025	0.073	0.342466	0.041	0.131	0.312977	-0.017	0.073	0.131	-0.232876712	-0.129770992
RDM_MM_211ASH_WINDOW	MM	211ASH	11	0.058	0.142	0.408451	0.062	0.339	0.182891	-0.033	0.142	0.339	-0.232394366	-0.097345133
RDM_MM_211ASH_WINDOW	MM	211ASH	16	0.062	0.169	0.366864	0.092	0.473	0.194503	-0.04	0.169	0.473	-0.236686391	-0.084566596
RDM_MM_211ASH_WINDOW	MM	211ASH	11	0.046	0.133	0.345865	0.07	0.258	0.271318	-0.032	0.133	0.258	-0.240601504	-0.124031008
RDM_MM_211ASH_WINDOW	MM	211ASH	16	0.048	0.137	0.350365	0.06	0.313	0.191693	-0.034	0.137	0.313	-0.248175182	-0.108626198
RDM_MM_211ASH_WINDOW	MM	211ASH	18	0.049	0.133	0.368421	0.63	0.368	1.711957	-0.027	0.133	0.368	-0.203007519	-0.073369565
RDM_501_WINDOWA_1	MM	501	1	0.086	0.108	0.796296	0.003	0.398	0.007538	-0.046	0.108	0.398	-0.425925926	-0.115577889
RDM_501_WINDOWA_2	MM	501	2	0.101	0.152	0.664474	0.008	0.473	0.016913	-0.046	0.152	0.473	-0.302631579	-0.097251586
RDM_501_WINDOWA_4	MM	501	4	0.063	0.087	0.724138	0.01	0.273	0.03663	-0.052	0.087	0.273	-0.597701149	-0.19047619
RDM_501_WINDOWAA_4	MM	501	4	0.02	0.157	0.127389	0.122	0.424	0.287736	-0.014	0.157	0.424	-0.089171975	-0.033018868
RDM_501_WINDOWAA_5	MM	501	5	0.067	0.168	0.39881	0.099	0.457	0.21663	-0.014	0.168	0.457	-0.083333333	-0.030634573
RDM_501_WINDOWB_2	MM	501	2	0.024	0.057	0.421053	0.012	0.087	0.137931	-0.031	0.057	0.087	-0.543859649	-0.356321839
RDM_501_WINDOWB_3	MM	501	3	0.065	0.139	0.467626	0.056	0.355	0.157746	-0.027	0.139	0.355	-0.194244604	-0.076056338
RDM_501_WINDOWBB_14	MM	501	14	0.056	0.153	0.366013	0.078	0.383	0.203655	-0.034	0.153	0.383	-0.222222222	-0.088772846
RDM_501_WINDOWBB_15	MM	501	15	0.064	0.181	0.353591	0.087	0.522	0.166667	-0.036	0.181	0.522	-0.198895028	-0.068965517

RDM_501_WINDOWBB_16	MM	501	16	0.071	0.187	0.379679	0.091	0.561	0.16221	-0.038	0.187	0.561	-0.203208556	-0.067736185
RDM_501_WINDOWC_1	MM	501	1	0.064	0.136	0.470588	0.064	0.419	0.152745	-0.028	0.136	0.419	-0.205882353	-0.066825776
RDM_501_WINDOWC_2	MM	501	2	0.041	0.081	0.506173	0.028	0.192	0.145833	-0.027	0.081	0.192	-0.333333333	-0.140625
RDM_501_WINDOWC_3	MM	501	3	0.077	0.16	0.48125	0.065	0.321	0.202492	-0.033	0.16	0.321	-0.20625	-0.102803738
RDM_501_WINDOWF_5	MM	501	5	0.106	0.168	0.630952	0.067	0.571	0.117338	-0.01		0.571	#DIV/0!	-0.017513135
RDM_501_WINDOWF_16	MM	501	16	0.085	0.143	0.594406	0.041	0.452	0.090708	-0.03	0.143	0.452	-0.20979021	-0.066371681
RDM_501_WINDOWF_17	MM	501	17	0.108	0.17	0.635294	0.021	0.612	0.034314	-0.038	0.17	0.612	-0.223529412	-0.062091503
RDM_501_WINDOWG_2	MM	501	2	0.048	0.104	0.461538	0.061	0.253	0.241107	-0.016	0.104	0.253	-0.153846154	-0.063241107
RDM_501_WINDOWG_3	MM	501	3	0.033	0.081	0.407407	0.043	0.179	0.240223	-0.027	0.081	0.179	-0.333333333	-0.150837989
RDM_501_WINDOWG_6	MM	501	6	0.064	0.148	0.432432	0.086	0.347	0.247839	-0.02	0.148	0.347	-0.135135135	-0.057636888
RDM_501_WINDOWH_1	MM	501	1	0.066	0.165	0.4	0.059	0.247	0.238866	-0.022	0.165	0.247	-0.133333333	-0.089068826
RDM_501_WINDOWH_3	MM	501	3	0.059	0.144	0.409722	0.067	0.254	0.26378	-0.02	0.144	0.254	-0.138888889	-0.078740157
RDM_501_WINDOWH_6	MM	501	6	0.059	0.116	0.508621	0.058	0.311	0.186495	-0.024	0.116	0.311	-0.206896552	-0.077170418
RDM_501_WINDOWI_6	MM	501	6	0.074	0.12	0.616667	0.034	0.288	0.118056	-0.013	0.12	0.288	-0.108333333	-0.045138889
RDM_501_WINDOWI_7	MM	501	7	0.073	0.124	0.58871	0.036	0.218	0.165138	-0.011	0.124	0.218	-0.088709677	-0.050458716
RDM_501_WINDOWI_8	MM	501	8	0.05	0.102	0.490196	0.041	0.238	0.172269	-0.013	0.102	0.238	-0.12745098	-0.054621849
RDM_501_WINDOWJ_5	MM	501	5	0.099	0.158	0.626582	0.075	0.266	0.281955	-0.016	0.158	0.266	-0.101265823	-0.060150376
RDM_501_WINDOWJ_7	MM	501	7	0.08	0.134	0.597015	0.102	0.408	0.25	-0.016	0.134	0.408	-0.119402985	-0.039215686
RDM_501_WINDOWJ_8	MM	501	8	0.082	0.182	0.450549	0.082	0.403	0.203474	-0.016	0.182	0.403	-0.087912088	-0.039702233
RDM_501_WINDOWK_11	MM	501	11	0.047	0.116	0.405172	0.062	0.279	0.222222	-0.022	0.116	0.279	-0.189655172	-0.078853047
RDM_501_WINDOWK_12	MM	501	12	0.067	0.129	0.51938	0.084	0.331	0.253776	-0.009	0.129	0.331	-0.069767442	-0.027190332
RDM_501_WINDOWL_5	MM	501	5	0.078	0.157	0.496815	0.102	0.43	0.237209	-0.1	0.157	0.43	-0.636942675	-0.23255814
RDM_501_WINDOWL_6	MM	501	6	0.071	0.163	0.435583	0.101	0.444	0.227477	-0.009	0.163	0.444	-0.055214724	-0.02027027
RDM_501_WINDOWL_7	MM	501	7	0.07	0.148	0.472973	0.081	0.384	0.210938	-0.009	0.148	0.384	-0.060810811	-0.0234375
RDM_501_WINDOWM_5	MM	501	5	0.041	0.12	0.341667	0.059	0.24	0.245833	-0.013	0.12	0.24	-0.108333333	-0.054166667
RDM_501_WINDOWM_6	MM	501	6	0.058	0.124	0.467742	0.084	0.296	0.283784	-0.007	0.124	0.296	-0.056451613	-0.023648649
RDM_501_WINDOWM_9	MM	501	9	0.062	0.155	0.4	0.085	0.37	0.22973	-0.019	0.155	0.37	-0.122580645	-0.051351351
RDM_501_WINDOWO_10	MM	501	10	0.053	0.131	0.40458	0.065	0.316	0.205696	-0.016	0.131	0.316	-0.122137405	-0.050632911
RDM_501_WINDOWO_11	MM	501	11	0.066	0.154	0.428571	0.088	0.41	0.214634	-0.016	0.154	0.41	-0.103896104	-0.03902439
RDM_501_WINDOWO_14	MM	501	14	0.067	0.168	0.39881	0.087	0.415	0.209639	-0.017	0.168	0.415	-0.101190476	-0.040963855
RDM_501_WINDOWP_6	MM	501	6	0.045	0.129	0.348837	0.067	0.254	0.26378	-0.024	0.129	0.254	-0.186046512	-0.094488189
RDM_501_WINDOWP_7	MM	501	7	0.06	0.15	0.4	0.09	0.367	0.245232	-0.022	0.15	0.367	-0.146666667	-0.059945504
RDM_501_WINDOWP_11	MM	501	11	0.072	0.171	0.421053	0.122	0.502	0.243028	-0.018	0.171	0.502	-0.105263158	-0.035856574
RDM_501_WINDOWR_12	MM	501	12	0.066	0.081	0.814815	0.055	0.177	0.310734	-0.006	0.081	0.177	-0.074074074	-0.033898305
RDM_501_WINDOWR_13	MM	501	13	0.113	0.136	0.830882	0.043	0.486	0.088477	0.013	0.136	0.486	0.095588235	0.026748971
RDM_501_WINDOWS_1	MM	501	1	0.075	0.108	0.694444	0.018	0.33	0.054545	-0.01	0.108	0.33	-0.092592593	-0.03030303
RDM_501_WINDOWT_3	MM	501	3	0.068	0.077	0.883117	0.028	0.254	0.110236	-0.012	0.077	0.254	-0.155844156	-0.047244094
RDM_501_WINDOWT_4	MM	501	4	0.086	0.138	0.623188	0.019	0.386	0.049223	-0.02	0.138	0.386	-0.144927536	-0.051813472
RDM_501_WINDOWT_5	MM	501	5	0.064	0.101	0.633663	0.023	0.254	0.090551	-0.012	0.101	0.254	-0.118811881	-0.047244094
RDM_501_WINDOWU_3	MM	501	3	0.091	0.104	0.875	0.009	0.483	0.018634	-0.024	0.104	0.483	-0.230769231	-0.049689441
RDM_501_WINDOWU_5	MM	501	5	0.095	0.113	0.840708	0.029	0.466	0.062232	-0.028	0.113	0.466	-0.247787611	-0.060085837
RDM_501_WINDOWU_6	MM	501	6	0.09	0.141	0.638298	0.011	0.383	0.028721	-0.025	0.141	0.383	-0.177304965	-0.065274151
RDM_501_WINDOWV_13	MM	501	13	0.083	0.101	0.821782	0.025	0.318	0.078616	-0.049	0.101	0.318	-0.485148515	-0.15408805
RDM_501_WINDOWV_14	MM	501	14	0.09	0.076	1.184211	0.026	0.316	0.082278	-0.046	0.076	0.316	-0.605263158	-0.14556962
RDM_501_WINDOWV_15	MM	501	15	0.09	0.087	1.034483	-0.003	0.342	-0.00877	-0.049	0.087	0.342	-0.563218391	-0.143274854
RDM_501_WINDOWW_9	MM	501	9	0.089	0.143	0.622378	0.013	0.32	0.040625	-0.024	0.143	0.32	-0.167832168	-0.075
RDM_501_WINDOWW_10	MM	501	10	0.106	0.159	0.666667	0.018	0.412	0.043689	-0.025	0.159	0.412	-0.157232704	-0.060679612
RDM_501_WINDOWW_14	MM	501	14	0.1	0.148	0.675676	0.007	0.369	0.01897	-0.027	0.148	0.369	-0.182432432	-0.073170732
RDM_501_WINDOWY_4	MM	501	4	0.069	0.171	0.403509	0.081	0.508	0.159449	-0.019	0.171	0.508	-0.111111111	-0.037401575
RDM_501_WINDOWY_5	MM	501	5	0.067	0.186	0.360215	0.108	0.424	0.254717	-0.02	0.186	0.424	-0.107526882	-0.047169811
RDM_501_WINDOWY_6	MM	501	6	0.064	0.174	0.367816	0.075	0.414	0.181159	-0.016	0.174	0.414	-0.091954023	-0.038647343
RDM_501_WINDOWZ_3	MM	501	3	0.059	0.135	0.437037	0.04	0.314	0.127389	-0.035	0.135	0.314	-0.259259259	-0.111464968
RDM_501_WINDOWZ_5	MM	501	5	0.061	0.14	0.435714	0.025	0.464	0.053879	-0.036	0.14	0.464	-0.257142857	-0.077586207
RDM_501_WINDOWZ_10	MM	501	3	0.078	0.191	0.408377	0.072	0.515	0.139806	-0.042	0.191	0.515	-0.219895288	-0.081553398

Table 11: RDM FTIR and mFTIR data

ID	SQUARE	ID	WINDOW	STAGE	878	1035	Co3/P with 878	CALCITE	1726 s	712 calcite corrected	712 calcite uncorrect	1090 shoulder	875 carbonate band
RDM_J22_89D_St4_test1	J22	89D		ST4	0.023	0.146	0.157534247					x	X
RDM_J22_89C_St6_test1	J22	89C		ST6	0.027	0.102	0.264705882					x	X
RDM_J22_89B_St3_test1	J22	89B		ST3	0.025	0.113	0.221238938						X
RDM_J22_89A_St0_test1	J22	89A		ST0	0.029	0.091	0.318681319						X
RDM_J21_720F_St6_test1	J21	720F		ST6	0.011	0.067	0.164179104						X
RDM_J21_720E_st3_test1	J21	720E		ST3	0.012	0.089	0.134831461						X
RDM_J21_720D_St2_test1	J21	720D		ST2	0.026	0.121	0.214876033						X
RDM_J21_720C_St0_test1	J21	720C		ST0	0.03	0.128	0.234375						X
RDM_J21_720B_ST0_test1	J21	720B		ST0	0.018	0.123	0.146341463						X
RDM_J21_720A_ST0_Test1	J21	720A		ST0	0.023	0.107	0.214953271						X
RDM_J21_720A_St0_test2	J21	720A		ST0	0.025	0.111	0.225225225					x	X
RDM_J20_998I_ST6b_test1	J20	998I		ST6b	0.119	0.299	0.397993311			0.011	0.033	x	X
RDM_J20_998H_St6_Test1	J20	998H		ST6	0.087	0.341	0.255131965					x	X
RDM_J20_998G_St6b_test1	J20	998G		STb	0.089	0.214	0.41588785			0.014	0.034	x	X
RDM_J20_998F_St6_test1	J20	998F		ST6	0.141	0.334	0.422155689			0.021	0.036	x	X
RDM_J20_998E_St3_test1	J20	998E		ST3	0.068	0.314	0.21656051						X
RDM_J20_998D_St4_test1	J20	998D		ST4	0.097	0.353	0.274787535						X
RDM_J20_998B_St0_test1	J20	998B		ST0	0.065	0.178	0.365168539			0.003	0.038		X
RDM_J20_998A_St0_test1	J20	998A		ST0	0.094	0.267	0.352059925			0.008	0.051		X
RDM_J20_998A_St0_test2	J20	998A		ST0	0.097	0.25	0.388			0.009	0.051		X
RDM_J18_3855S_St3_test1	J18	3855S		ST3	0.06	0.2	0.3						x
RDM_J18_3855R_St4_test1	J18	3855R		ST4	0.046	0.224	0.205357143					x	X
RDM_J18_3855Q_St3_test1	J18	3855Q		ST3	0.067	0.254	0.263779528						X
RDM_J18_3855P_St5_test1	J18	3855P		ST5	0.083	0.364	0.228021978					x	X
RDM_J18_3855O_St2_test1	J18	3855O		ST2	0.084	0.315	0.266666667						X
RDM_J18_3855N_St5b_test1	J18	3855N		ST5b	0.057	0.308	0.185064935					x	X
RDM_J18_3855M_St6_test1	J18	3855M		ST6	0.053	0.286	0.185314685					x	X
RDM_J18_3855L_St5b_test1	J18	3855L		ST5b	0.053	0.412	0.128640777					x	X
RDM_J18_3855K_st4_test1	J18	3855K		ST4	0.053	0.449	0.118040089					x	X
RDM_J18_3855J_St5_test1	J18	3855J		ST5	0.049	0.379	0.129287599					x	X
RDM_J18_3855i_St6_test1	J18	3855i		ST6	0.058	0.289	0.200692042					x	X
RDM_J18_3855H_st5_test1	J18	3855H		ST5	0.052	0.298	0.174496644					x	X
RDM_J18_3855F_st2or4_test1	J18	3855F		duration	0.048	0.215	0.223255814						X
RDM_J18_3855E_St2_test1	J18	3855E		ST2	0.062	0.242	0.256198347						X
RDM_J18_3855D_St0_test1	J18	3855D		ST0	0.069	0.281	0.245551601						X
RDM_J18_3855C_St1_test1	J18	3855C		ST1	0.068	0.239	0.284518828						X
RDM_J18_3855C_St0_test1	J18	3855C		ST0	0.073	0.263	0.27756654						X
RDM_J18_3855B_St0_test1	J18	3855B		ST0	0.068	0.269	0.252788104						X
RDM_J18_3855A_st0_test1	J18	3855A		ST0	0.037	0.272	0.136029412						X
RDM_I18_1991O_st6b_test1	I18	1991O		ST6b	0.06	0.201	0.298507463						X
RDM_I18_1991N_St6_test1	I18	1991N		ST6	0.062	0.344	0.180232558						X
RDM_I18_1991L_St5_test1	I18	1991L		ST5	0.042	0.364	0.115384615						X
RDM_I18_1991K_St4_test1	I18	1991K		ST4	0.068	0.314	0.21656051						X
RDM_I18_1991I_St4_test1	I18	1991I		ST4	0.034	0.344	0.098837209						X
RDM_I18_1991H_St4_test1	I18	1991H		ST4	0.05	0.327	0.152905199						X
RDM_I18_1991G_St2_test1	I18	1991G		ST2	0.074	0.267	0.277153558						X
RDM_I18_1991F_St2_test1	I18	1991F		ST2	0.067	0.155	0.432258065	x		0.007	0.038		X
RDM_I18_1991E_St3_test1	I18	1991E		ST3	0.075	0.294	0.255102041						X
RDM_I18_1991D_St3_test1	I18	1991D		ST3	0.078	0.265	0.294339623						X
RDM_I18_1991C_st2or4_test1	I18	1991C		duration	0.078	0.262	0.297709924						X
RDM_I18_1991B_st0_test1	I18	1991B		ST0	0.088	0.286	0.307692308						X
RDM_I18_1991A_St0_test1	I18	1991A		ST0	0.079	0.245	0.32244898						X
RDM_H19_92O_St4_test1	H19	92O		duration	0.074	0.314	0.23566879						X
RDM_H19_92N_ST5b_test1	H19	92N		ST5b	0.047	0.352	0.133522727					x	X
RDM_H19_92M_St6_test1	H19	92M		ST6	0.082	0.329	0.249240122	x		0.009	0.023	x	X
RDM_H19_92L_St6b_test1	H19	92L		ST6b	0.049	0.236	0.207627119					x	X
RDM_H19_92K_St5_test1	H19	92K		ST5	0.077	0.349	0.220630372					x	X
RDM_H19_92J_St3_test1	H19	92J		ST3	0.08	0.296	0.27027027						X
RDM_H19_92I_St5_test1	H19	92I		ST5	0.07	0.427	0.163934426	x		0.004	0.018	x	X
RDM_H19_92H_st6_test1	H19	92H		ST6	0.085	0.233	0.364806867					x	X
RDM_H19_92G_st5_test1	H19	92G		ST5	0.022	0.416	0.052884615						
RDM_H19_92F_st2_test1	H19	92F		ST2	0.077	0.233	0.330472103						X
RDM_H19_92E_st2_test1	H19	92E		ST2	0.056	0.203	0.275862069						X
RDM_H19_92D_St2or4_test1	H19	92D		duration	0.081	0.328	0.24695122						X
RDM_H19_92C_St3_test1	H19	92C		ST3	0.085	0.283	0.300353357						X
RDM_H19_92B_St0_test1	H19	92B		ST0	0.094	0.36	0.261111111						X
RDM_H19_92A_St0_test2	H19	92A		ST0	0.064	0.127	0.503937008						X
RDM_H19_92A_St0_test1	H19	92A		ST0	0.062	0.191	0.32460733						X
RDM_H18_3953B_St6_test1	H18	3953B		ST6	0.017	0.179	0.094972067						X
RDM_H18_3953A_St6_test1	H18	3953A		ST6	0.0088	0.0529	0.166351607					x	X
RDM_H18_3002N_St4_test1	H18	3002N		ST4	0.073	0.39	0.187179487						X
RDM_H18_3002M_St5_test1	H18	3002M		ST5	0.064	0.341	0.187683284					x	X
RDM_H18_3002L_St5_test1	H18	3002L		ST5	0.061	0.504	0.121031746					x	X
RDM_H18_3002K_St5_test1	H18	3002K		ST5	0.062	0.575	0.107826087						X
RDM_H18_3002J_st4_test1	H18	3002J		ST4	0.058	0.299	0.193979933					x	X
RDM_H18_3002I_St4_test1	H18	3002I		ST4	-0.009	0.495	-0.018181818					x	X
RDM_H18_3002H_st6_test1	H18	3002H		ST6	0.037	0.54	0.068518519					x	X
RDM_H18_3002F_St3_test1	H18	3002F		ST3	0.057	0.268	0.212686567						X
RDM_H18_3002E_st2_test1	H18	3002E		ST2	0.075	0.355	0.211267606						X
RDM_H18_3002D_st4_test1	H18	3002D		ST4	0.103	0.384	0.268229167						X
RDM_H18_3002C_St4_Test1	H18	3002C		ST4	0.076	0.333	0.228228228						X
RDM_H18_3002B_St0_test1	H18	3002B		ST0	0.093	0.322	0.288819876						X
RDM_H18_3002A_St0_test1	H18	3002A		ST0	0.084	0.25	0.336						X
RDM_H18_3002O_St4or0_test	H18	3002O		ST0	0.055	0.372	0.147849462					x	X
RDM_G18_7245B_ST6_TEST1	G18	7245B		ST6	0.061	0.404	0.150990099					x	X
RDM_G18_7245A_ST6_TEST1	G18	7245A		ST6	0.066	0.296	0.222972973					x	X
RDM_G18_7245A_ST6_TEST1	G18	7245A		ST6	0.06	0.281	0.213523132					x	X
RDM_E18_1626M_ST5_TEST1	E18	1626M		ST5	0.015	0.248	0.060483871					x	X
RDM_E18_1626L_ST5_TEST1	E18	1626L		ST5	0.048	0.219	0.219178082	x		0.005	0.024	x	X
RDM_E18_1626H_ST3_TEST1	E18	1626H		ST3	0.071	0.0928	0.765086207					x	X
RDM_CF4_251G_ST6B_TEST1	CF4	251G		ST6b		0.302	0					x	X
RDM_CF4_251F_ST6_TEST1	CF4	251F		ST6	0.07	0.322	0.217391304					x	X

RDM_CF4_251E_ST6_TEST1	CF4	251E		ST6	0.036	0.482	0.074688797					x	X
RDM_CF4_251D_ST6_TEST1	CF4	251D		ST6	0.038	0.464	0.081896552					x	X
RDM_CF4_251C_ST6_TEST1	CF4	251C		ST6	0.074	0.457	0.161925602					x	X
RDM_CF4_251B_ST5b_TEST1	CF4	251B		ST5b	0.028	0.417	0.067146283					x	
RDM_CF4_251B_ST5b_TEST2	CF4	251B		ST5b	0.032	0.432	0.074074074					x	
RDM_CF4_251A_ST6B_TEST1	CF4	251A		ST6b	0.074	0.287	0.257839721					x	
RDM_CF1_239N_ST3_TEST2	CF1	239N		ST3	0.007	0.0378	0.185185185						
RDM_CF1_239N_ST3_TEST1	CF1	239N		ST3	0.0239	0.0604	0.395695364						
RDM_CF1_239M_ST6_TEST1	CF1	239M		ST6	0.028	0.272	0.102941176					x	
RDM_CF1_239L_ST5B_TEST1	CF1	239L		STB	0.023	0.158	0.14556962					x	
RDM_CF1_239K_ST5_TEST1	CF1	239K		ST5	0.012	0.226	0.053097345					x	
RDM_CF1_239J_ST3_TEST1	CF1	239J		ST3	0.026	0.102	0.254901961						
RDM_CF1_239I_ST2_TEST1	CF1	239I		ST2	0.025	0.095	0.263157895						
RDM_CF1_239G_ST6B_TEST1	CF1	239G		ST6b	0.02	0.082	0.243902439					x	
RDM_J18_3855A_ST6B_TEST1	J18	3855A		ST6b	0.076	0.321	0.236760125					x	
RDM_I18_1991P_ST6_TEST1	I18	1991P		ST6	0.077	0.246	0.31300813					x	
RDM_I18_1991M_ST6_TEST1	I18	1991M		ST6	0.063	0.279	0.225806452					x	
RDM_I18_1991J_ST4_REST1	I18	1991J		ST4	0.043	0.262	0.164122137					x	
RDM_H18_3002G_ST6_TEST1	H18	3002G		ST6	0.076	0.288	0.263888889					x	
RDM_CF1_239F_ST0_TEST1	CF1	239F		ST0	0.024	0.11	0.218181818						
RDM_CF1_239E_ST1_TEST1	CF1	239E		ST1	0.024	0.135	0.177777778						
RDM_CF1_239D_ST_TEST1	CF1	239D		STT	0.027	0.099	0.272727273						
RDM_CF1_239C_ST0_TEST1	CF1	239C		ST0	0.018	0.098	0.183673469						
RDM_CF1_239B_ST0_TEST1	CF1	239B		ST0	0.027	0.108	0.25						
RDM_CF1_239A_ST5_TEST1	CF1	239A		ST5	0.018	0.268	0.067164179					x	
RDM_MM_506A_WINDOWA_	MM	506A	1		0.067	0.289	0.23183391		X				
RDM_MM_506A_WINDOWA_	MM	506A	2		0.038	0.291	0.130584192		X				
RDM_MM_506A_WINDOWA_	MM	506A	3		0.085	0.443	0.191873589		X				
RDM_MM_506A_WINDOWA_	MM	506A	4		0.083	0.484	0.171487603	X	X	0.024	0.076		
RDM_MM_506A_WINDOWA_	MM	506A	5		0.085	0.483	0.175983437		X				
RDM_MM_506A_WINDOWA_	MM	506A	6		0.029	0.216	0.134259259		X				
RDM_MM_506A_WINDOWA_	MM	506A	7		0.051	0.291	0.175257732	X	X	0.012	0.045		
RDM_MM_506A_WINDOWA_	MM	506A	8		0.052	0.325	0.16		X				
RDM_MM_506A_WINDOWAA	MM	506A	3		0.073	0.456	0.160087719	X	X	0.038	0.077		
RDM_MM_506A_WINDOWAA	MM	506A	4		0.069	0.486	0.141975309	x	x	0.046	0.088		
RDM_MM_506A_WINDOWAA	MM	506A	5		0.026	0.219	0.118721461	x	x	0.034	0.053		
RDM_MM_506A_WINDOWAA	MM	506A	6		0.091	0.542	0.167896679	x	x	0.049	0.096		
RDM_MM_506A_WINDOWAA	MM	506A	7		0.071	0.426	0.166666667	x	x	0.034	0.078		
RDM_MM_506A_WINDOWAA	MM	506A	8		0.065	0.397	0.16372796	x	x	0.043	0.085		
RDM_MM_506A_WINDOWAA	MM	506A	9		0.076	0.495	0.153535354	x	x	0.051	0.088		
RDM_MM_506A_WINDOWAA	MM	506A	10		0.075	0.491	0.152749491	x	x	0.056	0.1		
RDM_MM_506A_WINDOWB_	MM	506A	3		0.079	0.291	0.271477663	x	x	0.01	0.057		
RDM_MM_506A_WINDOWB_	MM	506A	4		0.069	0.282	0.244680851	X	X	0.009	0.046		
RDM_MM_506A_WINDOWB_	MM	506A	8		0.115	0.498	0.230923695	X	X	0.011	0.071		
RDM_MM_506A_WINDOWB_	MM	506A	9		0.067	0.275	0.243636364	X	X	0.01	0.046		
RDM_MM_506A_WINDOWC_	MM	506A	1		0.089	0.408	0.218137255		X				
RDM_MM_506A_WINDOWC_	MM	506A	2		0.096	0.444	0.216216216		X				
RDM_MM_506A_WINDOWC_	MM	506A	3		0.065	0.326	0.199386503		X				
RDM_MM_506A_WINDOWC_	MM	506A	11		0.087	0.439	0.198177677		X				
RDM_MM_506A_WINDOWD_	MM	506A	16		0.086	0.363	0.236914601		X				
RDM_MM_506A_WINDOWD_	MM	506A	17		0.118	0.568	0.207746479	X	X	0.019	0.073		
RDM_MM_506A_WINDOWD_	MM	506A	19		0.09	0.401	0.224438903	X	X	0.01	0.054		
RDM_MM_506A_WINDOWD_	MM	506A	20		0.11	0.506	0.217391304	X	X	0.03	0.079		
RDM_MM_506A_WINDOWE_	MM	506A	2		0.112	0.543	0.20626151	X	X	0.025	0.076		
RDM_MM_506A_WINDOWE_	MM	506A	3		0.048	0.277	0.173285199	X	X	0.026	0.051		
RDM_MM_506A_WINDOWF_	MM	506A	4		0.101	0.49	0.206122449	X	X	0.017	0.07		
RDM_MM_506A_WINDOWF_	MM	506A	5		0.048	0.247	0.194331984	X	X	0.015	0.044		
RDM_MM_506A_WINDOWI_1	MM	506A	10		0.077	0.348	0.221264368	X	X	0.03	0.076		
RDM_MM_506A_WINDOWI_1	MM	506A	12		0.073	0.401	0.182044888	X	X	0.039	0.079		
RDM_MM_506A_WINDOWI_1	MM	506A	14		0.1	0.419	0.238663484	X	X	0.035	0.077		
RDM_MM_506A_WINDOWJ_	MM	506A	4		0.056	0.28	0.2	X	X	0.033	0.073		
RDM_MM_506A_WINDOWJ_	MM	506A	5		0.113	0.497	0.227364185	X	X	0.028	0.081		
RDM_MM_506A_WINDOWK_	MM	506A	14		0.073	0.4	0.1825	X	X	0.053	0.094		
RDM_MM_506A_WINDOWK_	MM	506A	18		0.103	0.61	0.168852459	X	X	0.031	0.087		
RDM_MM_506A_WINDOWK_	MM	506A	20		0.072	0.413	0.17433414	X	X	0.023	0.064		
RDM_MM_506A_WINDOWL_	MM	506A	7		0.115	0.398	0.288944724	X	X	0.034	0.083		
RDM_MM_506A_WINDOWL_	MM	506A	8		0.027	0.358	0.075418994	X		0.05	0.12		
RDM_MM_506A_WINDOWL_	MM	506A	15		0.103	0.472	0.218220339	X	X	0.046	0.101		
RDM_MM_506A_WINDOWN_	MM	506A	3		0.08	0.475	0.168421053	X	X	0.029	0.069		
RDM_MM_506A_WINDOWN_	MM	506A	6		0.109	0.666	0.163663664	X	X	0.025	0.075		
RDM_MM_506A_WINDOWN_	MM	506A	9		0.078	0.516	0.151162791	X	X	0.033	0.078		
RDM_MM_506A_WINDOWO_	MM	506A	4		0.083	0.406	0.204433498	X	X	0.012	0.06		
RDM_MM_506A_WINDOWO_	MM	506A	6		0.062	0.338	0.183431953	X	X	0.02	0.069		
RDM_MM_506A_WINDOWO_	MM	506A	8		0.065	0.346	0.187861272	X	X	0.015	0.052		
RDM_MM_211ASH_WINDOW	MM	211ASH	1		0.014	0.065	0.215384615						
RDM_MM_211ASH_WINDOW	MM	211ASH	7		0.078	0.361	0.216066482						
RDM_MM_211ASH_WINDOW	MM	211ASH	2		0.069	0.179	0.38547486	X	X	0.023	0.062		
RDM_MM_211ASH_WINDOW	MM	211ASH	1		0.023	0.067	0.343283582	X	X	0.008	0.021		
RDM_MM_211ASH_WINDOW	MM	211ASH	4		0.039	0.131	0.297709924	X	X	0.021	0.041		
RDM_MM_211ASH_WINDOW	MM	211ASH	11		0.086	0.339	0.253687316	X	X	0.019	0.062		
RDM_MM_211ASH_WINDOW	MM	211ASH	16		0.111	0.473	0.234672304	X	X	0.036	0.092		
RDM_MM_211ASH_WINDOW	MM	211ASH	11		0.071	0.258	0.275193798	X	X	0.027	0.07		
RDM_MM_211ASH_WINDOW	MM	211ASH	16		0.074	0.313	0.236421725	X	X	0.024	0.06		
RDM_MM_211ASH_WINDOW	MM	211ASH	18		0.098	0.368	0.266304348	X	X	0.018	0.063		
RDM_501_WINDOWA_1	MM	501	1		0.085	0.398	0.213567839						
RDM_501_WINDOWA_2	MM	501	2		0.113	0.473	0.238900634						
RDM_501_WINDOWA_4	MM	501	4		0.082	0.273	0.3003663	X	X	0.013	0.01		
RDM_501_WINDOWAA_4	MM	501	4		0.102	0.424	0.240566038	X	X	0.063	0.122		
RDM_501_WINDOWAA_5	MM	501	5		0.108	0.457	0.236323851	X	X	0.038	0.099		
RDM_501_WINDOWB_2	MM	501	2		0.025	0.087	0.287356322	X	X	0.013	0.012		
RDM_501_WINDOWB_3	MM	501	3		0.033	0.355	0.092957746	X	X	0.016	0.049		
RDM_501_WINDOWBB_14	MM	501	14		0.071	0.383	0.18537859	X	X	0.037	0.078		
RDM_501_WINDOWBB_15	MM	501	15		0.089	0.522	0.170498084	X	X	0.04	0.087		

RDM_501_WINDOWBB_16	MM	501	16	0.093	0.561	0.165775401	X	X	0.043	0.091	
RDM_501_WINDOWC_1	MM	501	1	0.127	0.419	0.303102625	X	X	0.035	0.064	
RDM_501_WINDOWC_2	MM	501	2	0.06	0.192	0.3125	X	X	0.016	0.028	
RDM_501_WINDOWC_3	MM	501	3	0.118	0.321	0.367601246	X	X	0.042	0.065	
RDM_501_WINDOWF_5	MM	501	5	0.251	0.571	0.439579685	X	X	0.022	0.047	x
RDM_501_WINDOWF_16	MM	501	16	0.185	0.452	0.409292035	X	X	0.021	0.041	x
RDM_501_WINDOWF_17	MM	501	17	0.193	0.612	0.315359477	X	X	0.005	0.021	x
RDM_501_WINDOWG_2	MM	501	2	0.069	0.253	0.272727273	x	x	0.035	0.061	
RDM_501_WINDOWG_3	MM	501	3	0.043	0.179	0.240223464	x	x	0.029	0.043	
RDM_501_WINDOWG_6	MM	501	6	0.089	0.347	0.25648415	x	x	0.054	0.086	
RDM_501_WINDOWH_1	MM	501	1	0.135	0.247	0.546558704	x	x	0.059	0.097	
RDM_501_WINDOWH_3	MM	501	3	0.122	0.254	0.480314961	x	x	0.035	0.067	
RDM_501_WINDOWH_6	MM	501	6	0.091	0.311	0.292604502	x	x	0.03	0.058	
RDM_501_WINDOWI_6	MM	501	6	0.075	0.288	0.260416667	x	x	0.018	0.034	x
RDM_501_WINDOWI_7	MM	501	7	0.063	0.218	0.288990826	x	x	0.022	0.036	x
RDM_501_WINDOWI_8	MM	501	8	0.093	0.238	0.390756303	X	X	0.016	0.041	x
RDM_501_WINDOWJ_5	MM	501	5	0.111	0.266	0.417293233	X	X	0.037	0.084	X
RDM_501_WINDOWJ_7	MM	501	7	0.102	0.408	0.25	X	X	0.044	0.073	X
RDM_501_WINDOWJ_8	MM	501	8	0.095	0.407	0.233415233	X	X	0.053	0.082	X
RDM_501_WINDOWK_11	MM	501	11	0.067	0.279	0.240143369	X	X	0.053	0.074	
RDM_501_WINDOWK_12	MM	501	12	0.091	0.331	0.274924471	X	X	0.053	0.084	
RDM_501_WINDOWL_5	MM	501	5	0.103	0.43	0.239534884	X	X	0.057	0.102	
RDM_501_WINDOWL_6	MM	501	6	0.105	0.444	0.236486486	X	X	0.057	0.101	
RDM_501_WINDOWL_7	MM	501	7	0.084	0.384	0.21875	X	X	0.038	0.081	
RDM_501_WINDOWM_5	MM	501	5	0.065	0.24	0.270833333	X	X	0.033	0.059	
RDM_501_WINDOWM_6	MM	501	6	0.088	0.296	0.297297297	X	X	0.048	0.084	
RDM_501_WINDOWM_9	MM	501	9	0.081	0.37	0.218918919	X	X	0.042	0.085	
RDM_501_WINDOWO_10	MM	501	10	0.078	0.316	0.246835443	X	X	0.028	0.065	
RDM_501_WINDOWO_11	MM	501	11	0.093	0.41	0.226829268	X	X	0.044	0.088	
RDM_501_WINDOWO_14	MM	501	14	0.099	0.415	0.238554217	X	X	0.042	0.087	
RDM_501_WINDOWP_6	MM	501	6	0.074	0.254	0.291338583	X	X	0.035	0.067	
RDM_501_WINDOWP_7	MM	501	7	0.09	0.367	0.245231608	X	X	0.052	0.09	
RDM_501_WINDOWP_11	MM	501	11	0.105	0.502	0.209163347	X	X	0.075	0.122	
RDM_501_WINDOWR_12	MM	501	12	0.06	0.177	0.338983051	x	x	0.018	0.05	X
RDM_501_WINDOWR_13	MM	501	13	0.131	0.486	0.269547325	X	X	0.016	0.043	X
RDM_501_WINDOWS_1	MM	501	1	0.098	0.33	0.296969697					X
RDM_501_WINDOWT_3	MM	501	3	0.093	0.254	0.366141732	X	X	0.002	0.024	X
RDM_501_WINDOWT_4	MM	501	4	0.131	0.386	0.339378238	X	X	0.01	0.03	
RDM_501_WINDOWT_5	MM	501	5	0.106	0.254	0.417322835	X	X	-0.001	0.023	X
RDM_501_WINDOWU_3	MM	501	3	0.122	0.483	0.252587992					
RDM_501_WINDOWU_5	MM	501	5	0.113	0.466	0.24248927					
RDM_501_WINDOWU_6	MM	501	6	0.097	0.383	0.253263708					
RDM_501_WINDOWV_13	MM	501	13	0.054	0.318	0.169811321	X	X	0.027	0.025	
RDM_501_WINDOWV_14	MM	501	14	0.056	0.316	0.17721519	X	X	0.006	0.004	X
RDM_501_WINDOWV_15	MM	501	15	0.069	0.342	0.201754386	X	X	0.003	-0.003	X
RDM_501_WINDOWW_9	MM	501	9	0.09	0.32	0.28125	X	X	0.005	0.013	X
RDM_501_WINDOWW_10	MM	501	10	0.138	0.412	0.334951456	X	X	0.005	0.018	X
RDM_501_WINDOWW_14	MM	501	14	0.096	0.369	0.260162602					
RDM_501_WINDOWY_4	MM	501	4	0.136	0.508	0.267716535	X	X	0.024	0.081	
RDM_501_WINDOWY_5	MM	501	5	0.111	0.424	0.261792453	X	X	0.058	0.108	
RDM_501_WINDOWY_6	MM	501	6	0.099	0.414	0.239130435	X	X	0.029	0.075	
RDM_501_WINDOWZ_3	MM	501	3	0.063	0.314	0.200636943	X	X	0.022	0.04	X
RDM_501_WINDOWZ_5	MM	501	5	0.079	0.464	0.170258621	X	X	0.028	0.025	X
RDM_501_WINDOWZ_10	MM	501	3	0.086	0.515	0.166990291	X	X	0.048	0.072	X